INFORMATION TO USERS

This manuscript has been reproduced from the microfilm master. UMI films the text directly from the original or copy submitted. Thus, some thesis and dissertation copies are in typewriter face, while others may be from any type of computer printer.

The quality of this reproduction is dependent upon the quality of the copy submitted. Broken or indistinct print, colored or poor quality illustrations and photographs, print bleedthrough, substandard margins, and improper alignment can adversely affect reproduction.

In the unlikely event that the author did not send UMI a complete manuscript and there are missing pages, these will be noted. Also, if unauthorized copyright material had to be removed, a note will indicate the deletion.

Oversize materials (e.g., maps, drawings, charts) are reproduced by sectioning the original, beginning at the upper left-hand corner and continuing from left to right in equal sections with small overlaps.

Photographs included in the original manuscript have been reproduced xerographically in this copy. Higher quality 6" x 9" black and white photographic prints are available for any photographs or illustrations appearing in this copy for an additional charge. Contact UMI directly to order.

Bell & Howell Information and Learning
300 North Zeeb Road, Ann Arbor, MI 48106-1346 USA
800-521-0600

UMI®

DISSERTATION

ENERGY TRANSFER IN ION-RYDBERG CHARGE EXCHANGE

Submitted by
Daniel Scott Fisher
Department of Physics

In partial fulfillment of the requirements
for the Degree of Doctor of Philosophy
Colorado State University
Fort Collins, Colorado
Fall 2000

COLORADO STATE UNIVERSITY

August 24, 2000

WE HEREBY RECOMMEND THAT THE DISSERTATION PREPARED UNDER OUR SUPERVISION BY DANIEL SCOTT FISHER ENTITLED ENERGY TRANSFER IN ION-RYDBERG CHARGE EXCHANGE BE ACCEPTED AS FULFILLING IN PART REQUIREMENTS FOR THE DEGREE OF DOCTOR OF PHILOSOPHY.

Committee on graduate work

Siu Au Lee

[illegible]

William M. Fairbank, Jr.

Stephen R. Lundeen

Adviser

James R. Sites

Department Head

ABSTRACT OF DISSERTATION

ENERGY TRANSFER IN ION-RYDBERG CHARGE EXCHANGE

The charge transfer process between slow ions and Rydberg atoms was studied using resonant laser excitation to detect specific energy states of the collision products. The collisions were studied for ions of charge q = 2 - 11 at a velocity of v = 0.100 a.u. and for velocities v = 0.031 - 0.130 a.u. at a charge of q = 3. The Rydberg target was excited by three lasers into a final state where the primary quantum number could be varied from n_t = 7 to n_t = 26.

The apparatus used to implement the detection scheme is discussed in detail. The apparatus includes a device to remove the primary ion beam prior to the detector while transmitting the q-1 charge transfer beam. The development and characterization of this device are described in detail. Also described is the flexible low noise detector developed to measure the laser excited state in the collision product.

The data collected show a clear resonance in the capture cross section to a

particular energy state as the binding energy of the Rydberg target is varied. The resonance varies significantly over the range of charges and velocities studied and agrees very well with the classical trajectory Monte Carlo (CTMC) theory over nearly the entire range of measurements. Only at the lowest and highest velocities studied are any significant disagreements seen. The measurement shows a slightly larger width than CTMC theory at the lowest two velocities studied, v = 0.031 and 0.046 a.u. At the highest velocity studied v=0.130 a.u. significant disagreement with CTMC theory is seen. However, the measured resonance position clearly disagrees with the predictions of the classical over barrier (COB) model. The variation of width with both charge and velocity is similar to what would be expected from a simple uncertainty principle argument, however the overall agreement with CTMC suggests a quantum mechanical argument may not be necessary to explain this behavior.

Daniel Scott Fisher
Physics Department
Colorado State University
Fort Collins CO 80523
Fall 2000

Acknowledgments

I would like to thank all the people who helped with and provided support during the research and writing of this dissertation. First, Steve Lundeen, my advisor and friend for his insight, assistance, and patience while completing this research. Charles Fehrenbach for his assistance in building and maintaining the experimental apparatus, his expertise with the Rydberg target, and his insight. Eric Hessels for his ability to see fundamental answers to questions and for his willingness to work long hours helping to make these measurements. Brett DePaola for providing the CTMC code with which we made our calculations, and for his help while at Kansas State University. The rest of our experimental group in particular Phil Jacobson, Gerald Stevens, and Robert Komara for their friendship, assistance, and helpful conversations. The technical and clerical staff of Colorado State University, Kansas State University, and the J. R. Macdonald Lab for their support. Finally my family and friends for the encouragement and support they gave throughout my studies, which has made it a very pleasant and rewarding experience.

Table of Contents

List of Tables

List of Figures

Chapter 1 : The process of ion-Rydberg charge exchange

1.1 Introduction

Ion-atom collisions have been studied for some time because of their fundamental interest and for practical reasons. Understanding these collisions is important to many areas of science including astrophysics, atmospheric science, chemistry, material science, and plasma physics. In particular much recent research has dealt with the collisions of highly charged ions with ground state atoms [1, 2]. The collisions by highly charged ions differ from collisions by singly charged ions in a number of ways. One important difference is that highly charged ions generally capture electrons to highly excited states. The radiative decay of these captured states to the ground state can result in a substantial conversion of energy to photons. For example, fully ionized Fe which captures an electron from H ($1s$) will tend to capture into a state about 9.2 keV above its ground state. Thus, it is possible that 9.2 keV will be converted to photons through radiative decay. This is equal to the approximate average kinetic energy per particle in a hot fusion plasma. This conversion of kinetic energy to photons may be an important cooling mechanism in these plasmas, since these photons are not restricted to remain in the plasma.

Another feature of the capture by highly charged ions is that it is quasi-resonant and produces a narrow range of excited states on the ion. This feature of these collisions is of interest as an x-ray gain medium because of the population inversion in the ion it represents. Some practical x-ray laser schemes based on this effect generate a plasma by employing a high-power laser incident on a planar target. The plasma created expands away from the surface into a neutral buffer gas surrounding the planar target. In this gas enhanced x-ray emission is seen from population inversion believed to be from charge capture collisions[3, 4].

The collisions of singly charged ions and highly excited, or Rydberg states of atoms have also been investigated in detail [5, 6, 7]. These collisions are of interest because they have enormous capture cross sections, scaling as n_t^4 at low velocities, where n_t is the principle quantum number of the Rydberg target.

The intersection of these two types of collisions, the study of the collisions of highly charged ions and excited Rydberg targets, is the focus of this dissertation. These collisions promise to have features in common with each of the above collision processes. Most importantly these collisions combine the potential for large radiative energy losses, with the rapidly increasing cross sections (n_t^4) of Rydberg targets. This combination increases the importance of these collisions disproportionately to their relative population in a hot plasma.

This raises a few questions, however. Can these rather fragile Rydberg states exist in a hot plasma where highly charged ions would be present? To determine

if such states might be present in a hot plasma we can start by using the Saha equation [8]. This equation describes the equilibrium distribution of hydrogen gas in various ionization states, including neutral states using a Boltzmann like distribution. For an atomic hydrogen plasma the distribution between neutral and ionized states is,

$$\frac{n_{\text{Proton}} n_{\text{Electron}}}{n_H} = \left(\frac{1}{2\pi}\right)^{\frac{3}{2}} \left(\frac{1}{a_o}\right)^3 \left(\frac{kT}{e^2/a_o}\right)^{\frac{3}{2}} e^{-\frac{1}{2}\left(\frac{e^2/a_o}{kT}\right)} \qquad (1.1.1)$$

where n_{Proton}, n_{Electron}, and n_H are the number density of protons, electrons, and neutral hydrogen, a_o is the Bohr radius, e is the electron charge, k is the Boltzmann constant and T is the temperature of the plasma. For example in a 10 keV plasma with a particle density of 10^{20} m^{-3}(typical of a fusion plasma) this gives a neutral hydrogen density of about 1.7×10^6 m^{-3}. Thus, neutral atoms exist even in a very hot plasma. Furthermore, the derivation of the Saha equation predicts statistical populations in the excited states of the atom using the same Boltzmann like distribution. Thus these states would be present with densities n^2 times larger than the ground state density, up to the state which becomes unstable due to the electric fields in the plasma. So now we must examine what fields are experienced in such plasmas. Although the overall plasma is neutral, some electric fields are produced by local inhomogeneties of the particles in the plasma. The field an atom in the plasma experiences locally can be estimated using the mean Holtsmark field [9],

which is the mean of a probability distribution which characterizes the strengths of the electric microfields in an infinite isotropic one component plasma, a description of a plasma in which particles of a single kind move against a smooth background of matter with the opposite charge. The average microfield calculated in this way is,

$$\bar{E}_{\mu} \cong 3\frac{Ze}{R^2} \tag{1.1.2}$$

where Z is the charge of the positive component of the plasma, e is the electron charge, and R is the average separation between particles. In our example of a hydrogen plasma with a particle density of 10^{20} m^{-3} this field is 1000 V cm^{-1}. Additionally we need to examine the motional field experienced and determine if it is larger than the electric micro-fields we have estimated. A typical tokamak fusion plasma the magnetic containment fields used are about 50 kG, a field of this size with the plasma at an energy of 10 keV gives a motional electric field of 70,000 V cm^{-1}. This field ionizes states of neutral hydrogen down to about $n = 9$. Also this field is much larger than the estimated microfields in the plasma.

This still leaves a number of excited states of the atom available for collisions. However, for sufficiently large velocities the capture cross section of the excited state begins to decrease rapidly. Since the cross section decreases at high velocity we now need to decide if the capture cross sections from excited states at the velocities present in a tokamak plasma are large enough to be significant. As will

be described in Section 1.2.2 CTMC predicts that at high velocities the capture cross section drops as $n^{-1.6}$. However from the Saha equation we know that the density of excited states increases as n^2 because of the degeneracy of states. Thus the density of excited states may increase more rapidly than the total cross section falls at higher velocities. Thus, excited state collisions with ions may play a more important role in very hot plasmas than ground state collisions. All of these factors are further enhanced in favor of the excited state collisions when the plasma environment is less extreme than in a tokamak plasma, and the fields and velocities are lower, for instance in an inertial fusion plasma.

1.2 Theoretical models of ion-Rydberg charge exchange

1.2.1 The classical over barrier model

A simple model of the ion-atom collision process, the classical over barrier (COB) model [10] gives insight into the general features of these collisions, explaining why these collisions have relatively large cross sections, and capture resonantly to excited states of the projectile. In this model the capture process is treated as a one electron, three-body problem ignoring any possible effects of the other electrons on either the ion or Rydberg atom. As the ion approaches the atom during a collision the combined potential wells of the ion and atom affect the electron originally on the target atom. The combined potential of the ion and the

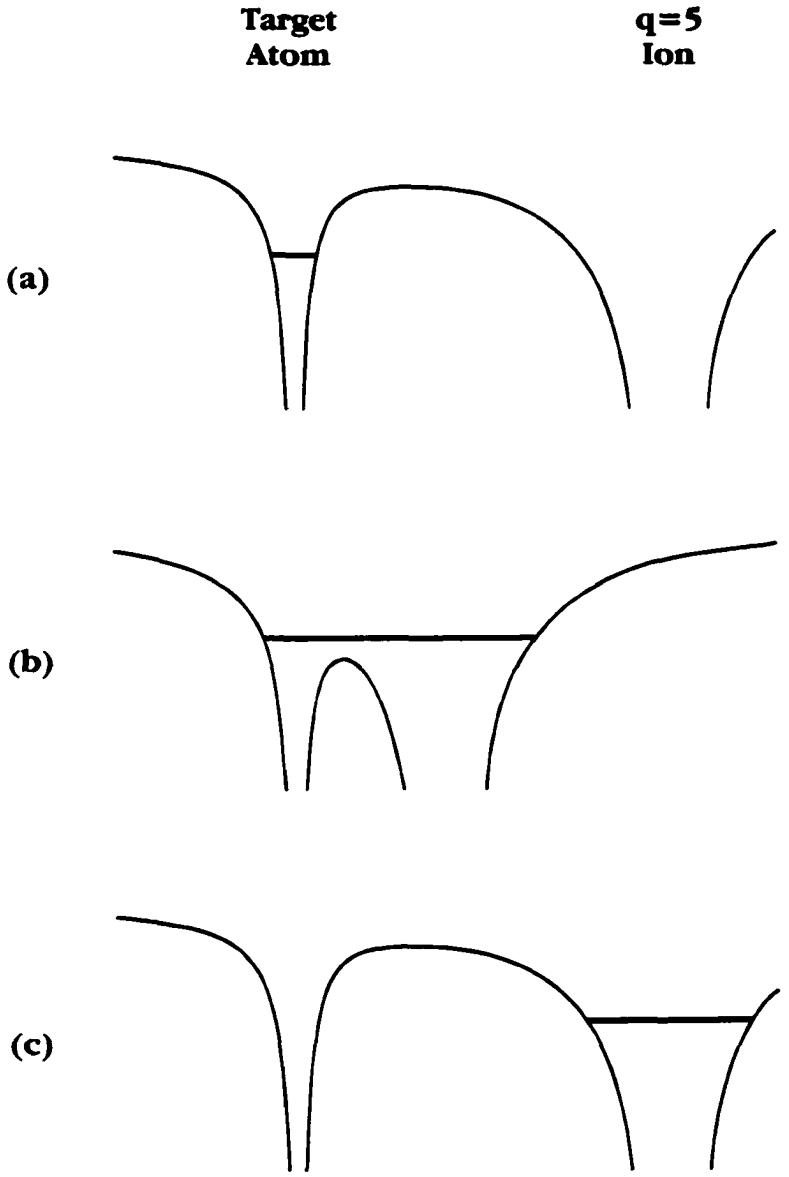

Figure (1.2.1) : **Figure showing the capture process in the COB model.** This figure shows the ion approaching an atom with an excited bound state (a), to the point where the combined potential well is such that the "potential wall" between the atom and the ion is lower than the bound state of the atom (b). After the ion passes its point of closest approach the electron originally bound to the atom has a possibility of being bound to either the atom or the ion, panel (c) shows it bound to the ion.

atom is shown in Fig. 1.2.1 (a). The "potential wall" goes to lower energies as the ion approaches the atom. If the ion gets close enough the "potential wall" between the atom and the ion goes below the energy of the electron bound to the target atom and the electron is shared by the ion-atom system. As the ion and atom separate the "wall" moves up again and it is possible for the electron to be captured to a state of the ion. This is shown in Fig. 1.2.1 (b) and (c). This model implies that the electron will be captured into a state on the ion of about the same binding energy as the original energy on the target atom. Despite its simplicity this model gives a qualitative understanding of the most important features of these collisions. For example using this model it becomes obvious why a multiply-charged ion capturing an electron from a ground state atom captures to an excited state: the capture occurs into states of about the same binding energy, and only high$n$-states on the multiply-charged ion have binding energies similar to the ground state of the atom. The capture process has a large cross section which increases with charge because the potential well of the ion deepens with charge and causes a lower saddle point for the same distance as the charge increases.

This simple model also gives predictions about the nature of collision of ions and Rydberg atoms. For singly charged ions colliding with Rydberg atoms this model predicts that the capture will occur into states of about the same binding energy, that multiple capture will occur with a much smaller cross section than single capture, and the cross section for single capture will be very large. The large

cross section is due to the binding energy of the target atom being quite small (meV). Thus, the "wall" doesn't need to be lowered very much to capture the loosely bound electron. As a result, the capture can occur at a much larger radius than ground state capture. The model also predicts the features of multiply charged ions collisions with Rydberg atoms. Specifically these cross sections will be even larger (because of the excited state and the deeper potential well of the ion), and the capture will occur to much higher n-states of the ion.

Using this model, quantitative results for the capture radius and the most probable final state energy can also be found. Using the potential well of each ion with the electron starting in its specified level, the most probable final level is found simply by conservation of energy at the point where the electron crosses over the saddle point. The combined potentials of the ion and the Rydberg atom core is calculated and the derivative is taken to find the saddle point along the internuclear axis. The combined potential is along the line from atom to ion is,

$$V(z) = -e^2\left(\frac{1}{z} + \frac{q}{(R-z)}\right) \tag{1.2.1}$$

where z is measured from the position of the atom (the origin), R is the separation of the atom and the ion centers, e is the electron charge, and q is the charge of the ion. The position of the saddle point, where the derivative of this combined potential is zero, is equal to,

$$z = \frac{R}{\left(1+\sqrt{q}\right)} \tag{1.2.2}$$

Thus the potential of the saddle point can be determined by putting this position into the original potential equation which gives,

$$V_{Saddle} = -\frac{e^2}{R}\left(1+\sqrt{q}\right)^2 \tag{1.2.3}$$

If the zero field binding energy of the electron on the target atom is used and capture is determined by when the initial energy of the electron (including its negative potential energy due to its proximity to the ion) is equal to the saddle point potential it gives,

$$-e^2\left(\frac{1}{2a_o n_t^2}+\frac{q}{R}\right) = V_{Saddle} = -\frac{e^2}{R}\left(1+\sqrt{q}\right)^2 \tag{1.2.4}$$

where n_t is the n-state of the target atom and a_o is the Bohr radius. Which solving for R gives a capture radius of,

$$R_c = 2a_o n_t^2\left(1+2\sqrt{q}\right) \tag{1.2.5}$$

where R_c is the distance at which capture can occur.

Using this capture radius and inserting it into the potentials of the electron on the ion and atom system,

$$-e^2\left(\frac{1}{2a_o n_t^2}-\frac{q}{R}\right) = -e^2\left(\frac{q^2}{2a_o n_p^2}-\frac{1}{R}\right) \tag{1.2.6}$$

gives the final state of the electron on the ion as,

$$n_p = qn_t\left(\frac{q+2\sqrt{q}}{1+2\sqrt{q}}\right)^{\frac{1}{2}} \tag{1.2.7}$$

where n_p is the n-state of the captured electron on the ion. Thus the state of the captured electron is excited on the ion. The binding energy of the product state as,

$$E_p = E_t\frac{q+2\sqrt{q}}{1+2\sqrt{q}} \tag{1.2.8}$$

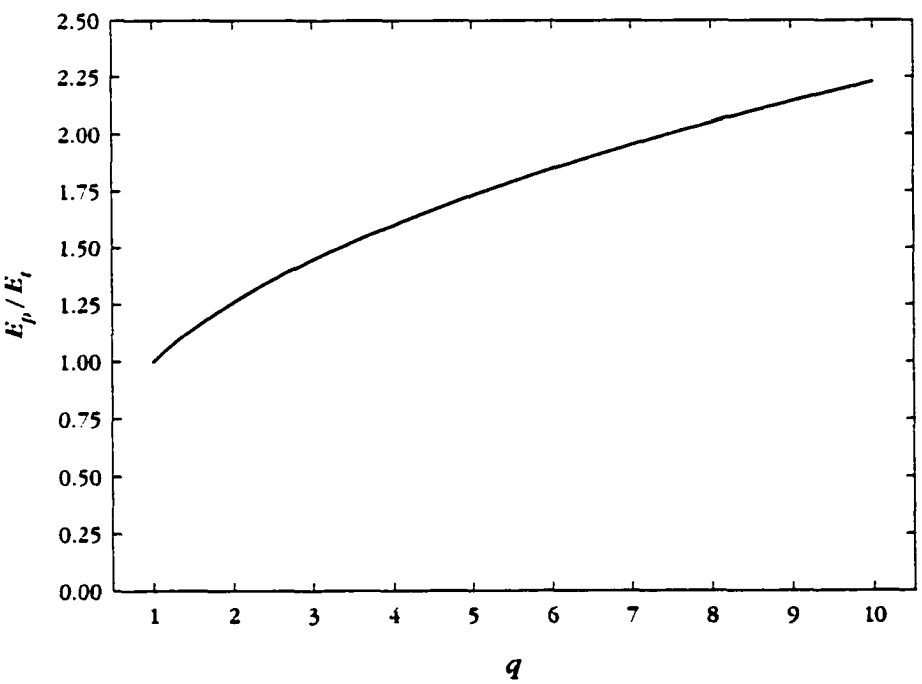

Figure (1.2.2) : **Predicted ratio of E_p to E_t as determined by the COB model.** This figure shows the variation with charge of the ratio of the product to the target binding energy predicted by the COB model, as given by Eqn. 1.2.8.

where E_p is the calculated final binding energy of the captured electron on the ion and E_t is the initial binding energy on the target atom ($1/2a_o n_t^2$). This shows that the COB model predicts a captured state binding energy somewhat larger than the binding energy on the target atom when $q > 1$. A plot of this dependance versus q is shown in Fig. 1.2.2. Testing this prediction is one of the main aims of this dissertation.

The prediction of the COB model that $E_p > E_t$ can also be understood by applying the conservation of energy to the collision. After charge capture by a

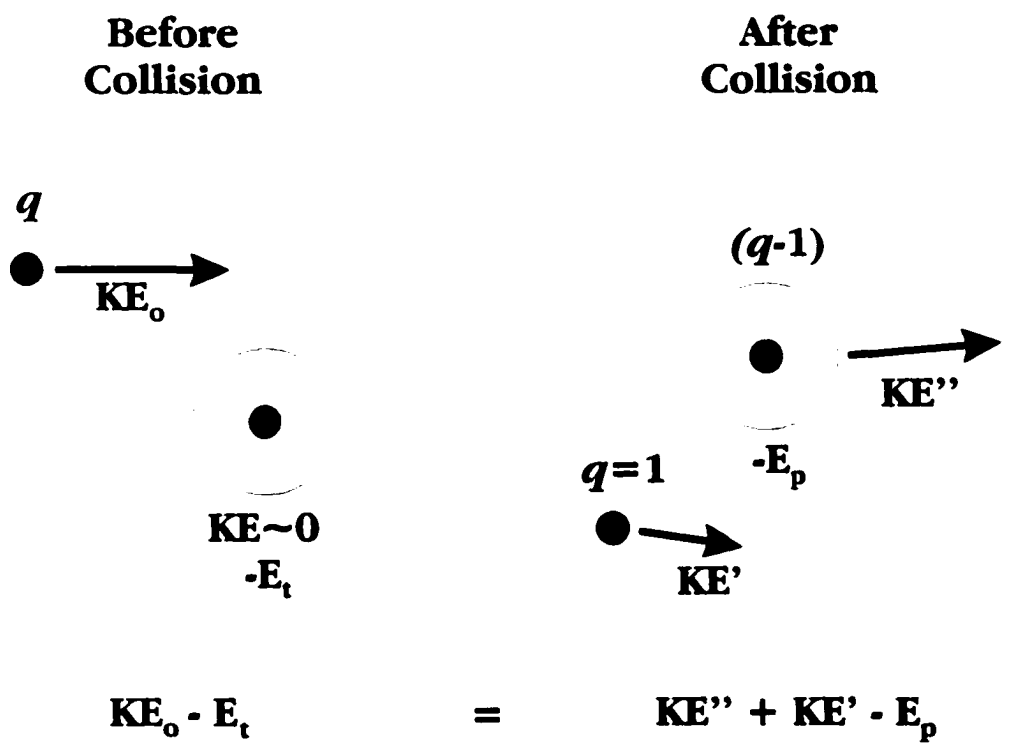

Figure (1.2.3) : **Energy conservation in the collision process.** This shows the conservation in the collision.

multiply-charged ion, both the ion and the ionized Rydberg atom are charged. They will therefore repel each other and gain kinetic energy. The amount of kinetic energy released is equal to,

$$\Delta KE = \frac{e^2(q-1)}{R_c} \tag{1.2.9}$$

where R_c is the capture radius. Overall conservation of energy requires that,

$$KE_o - E_t = KE'' + KE' - E_p \tag{1.2.10}$$

as shown in Fig. 1.2.3. The final kinetic energy is equal to the initial kinetic energy plus the additional energy released because of the coulomb repulsion after capture thus,

$$KE_o + \frac{(q-1)e^2}{R_c} = KE'' + KE' \tag{1.2.11}$$

By using this relation and the conservation of energy in Eqn. 1.2.10, we find that this predicts that,

$$E_p = E_t + \frac{(q-1)e^2}{R_c} \tag{1.2.12}$$

Thus this requires that the binding energy of the captured electron is increased during capture by this amount, and that $E_p > E_t$. Substituting Eqn. 1.2.5 into Eqn. 1.2.12 confirms Eqn. 1.2.8.

This model in itself makes no quantitative or qualitative estimation of the width

of the resonance only the distance at which the charge exchange occurs, and thus what level the captured electron goes into. One implication of the classical model, however, is that the resonance width should be very small at low enough velocities. For sufficiently slow collisions the electron would be shared between the two potential wells but always with a precisely defined energy.

1.2.2 CTMC

Currently the only theoretical model of collisions of ions and Rydberg atoms that provides detailed predictions treats the collision system as three interacting classical particles. This calculation, the classical trajectory Monte Carlo, or CTMC, model[11], simulates the target state by a classical orbit whose energy and angular momentum match the given target state. The orientation of this orbit to the collision plane and the impact parameter of the ion are randomly generated and the CTMC code then integrates the classical equations of motion of the electron, ion, and target cores as the ion approaches from very far away to determine what happens to the electron throughout the collision. Long after the collision has occurred and the two heavy particles are well separated, the code checks to see what the final state of the electron is, if it is still on the target core, free of both ions, or captured by the projectile ion. If it has been captured by the projectile ion it determines its binding energy to the ion, and the n-state to which that energy

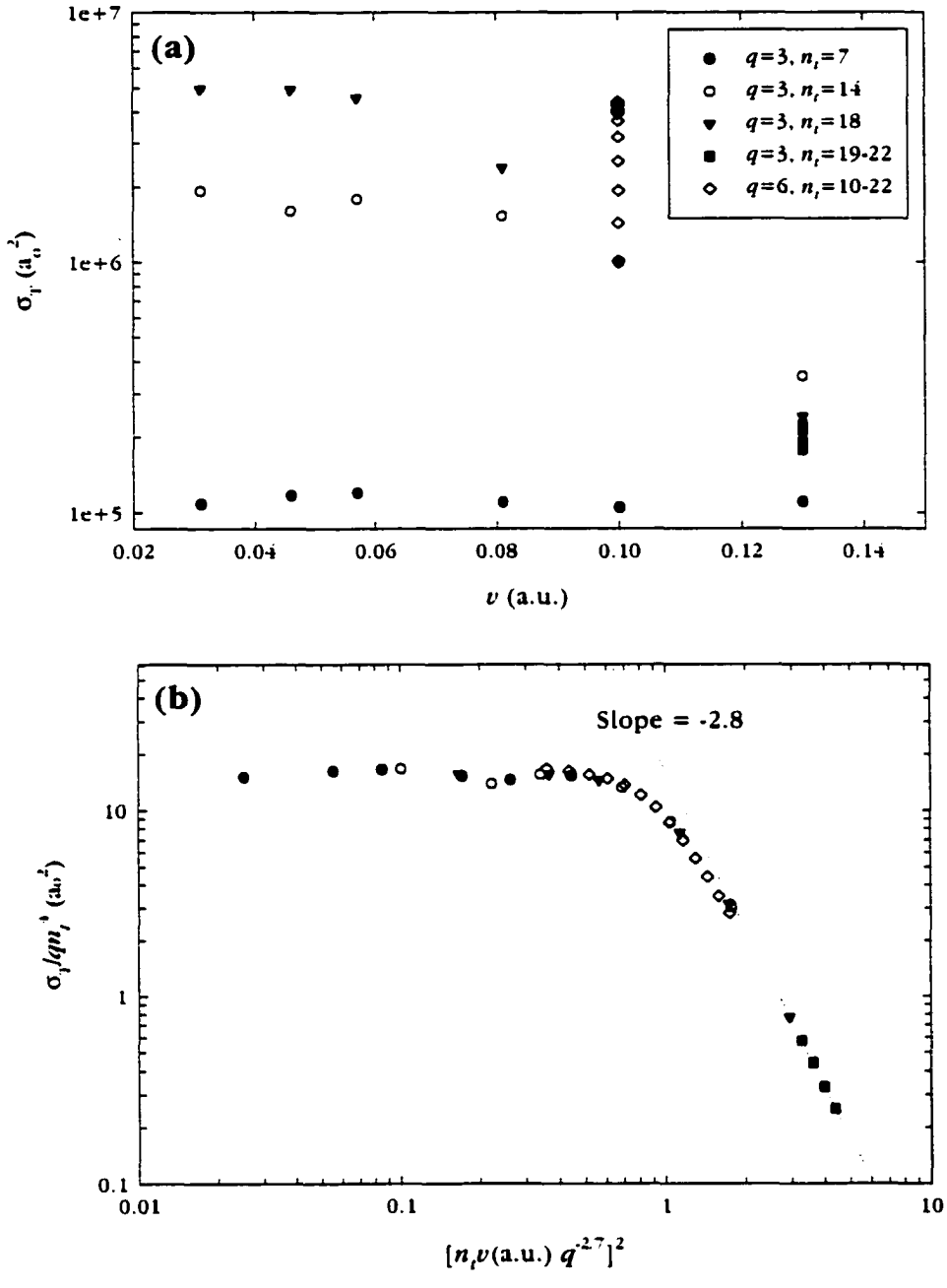

Figure (1.2.4) : **Unscaled and scaled total cross sections for q = 3 and 6.** Panel (a) shows the unscaled q = 3 and 6 total cross sections for a number of targets and velocities. For q = 3 the filled circles show the values for n_t = 7, the open circles are for n_t = 14, the triangles are for n_t = 18 and the filled squares show the values for n_t = 19 - 22. The values for q = 6 are shown as open diamonds for n_t = 10 - 22. Panel (b) show these same total cross sections with the scaling given on the axes. The dotted line is a linear regression of the four rightmost points, and has a slope of -2.8.

corresponds. The final l-state is determined by noting the angular momentum of the captured electron with respect to the projectile ion. From this data, with enough repetitions from random initial conditions, one can estimate the cross sections for various outcomes of the collision, and the total capture cross section for the collision.

Using code provided by Brett DePaola (which was originally coded by Olson[12]) for the CTMC calculations we set the parameters of the collisions of interest to us and calculated the results of these collisions. After running these calculations for a number of different charged ions and velocities a number of trends in the results can be seen. First the total capture cross section is proportional to qn^4 at low velocities. At higher velocities the cross section drops off rapidly. This relationship is shown very dramatically in Fig. 1.2.4 (a) and (b). Figure 1.2.4 (a) shows the unscaled total cross sections for $q = 3$ for a number of targets and velocities and for $q = 6$ for a number of targets, and appear to be completely unrelated curves. However, when the cross sections are divided by $q\,n_t^4$ and plotted versus $[n_t v \text{ (a.u.)}\ q^{-2/7}]^2$, the scaled curves fall on a "universal" curve as seen in Fig. 1.2.4 (b). This curve shows several features of interest. First there is a flat region in the "low" velocity region of this curve, this means that below a velocity of about $(q^{2/7}/n_t)$ a.u. the scaled total capture cross section is approximately constant

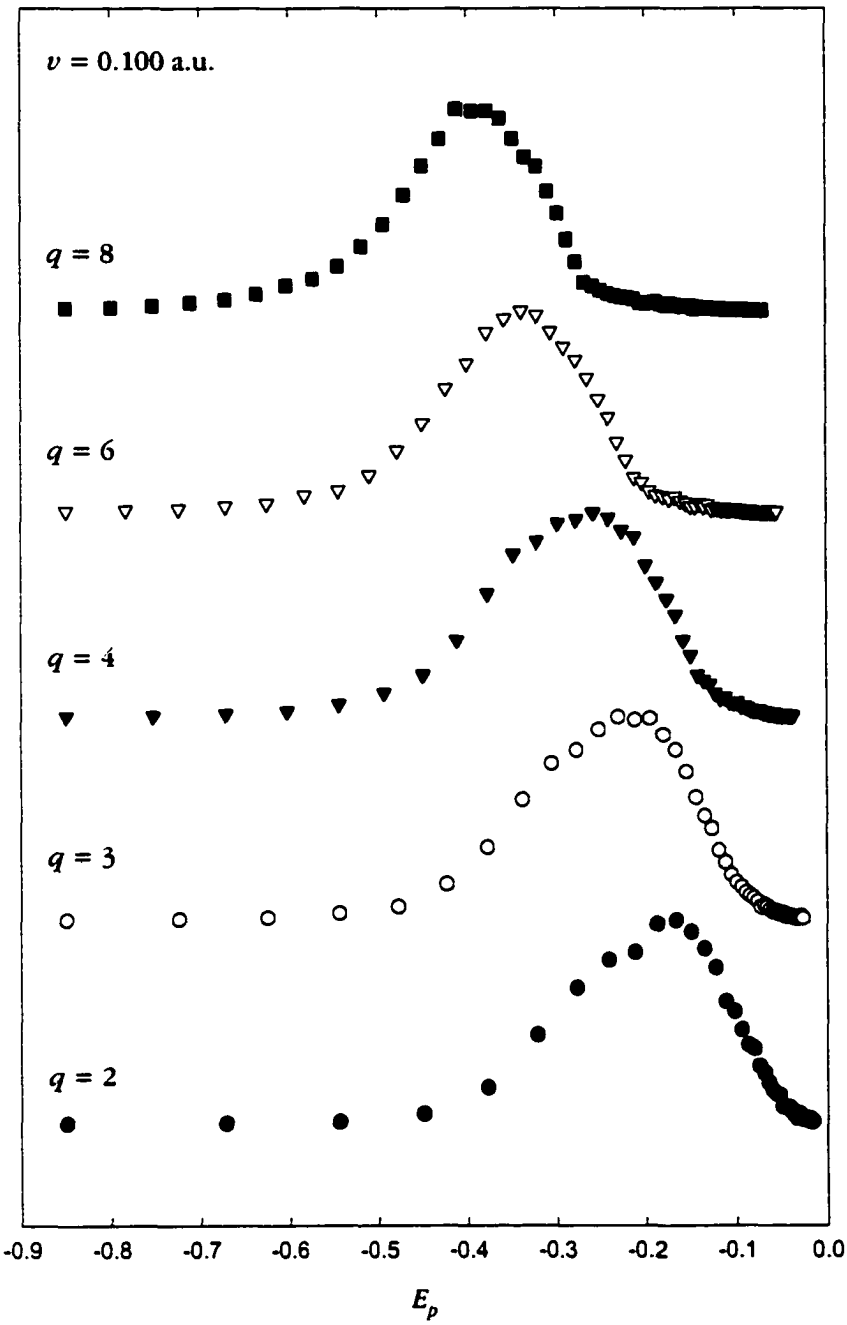

Figure (1.2.5) : **Final State distributions as a function of charge.** This figure shows how the final state distributions calculated by CTMC vary with charge for n_t = 10. The charge of each projectile is listed on the right. All projectiles have a velocity of 0.100 a.u.

and equal to approximately 15 a_o^2. Above this velocity the cross section quickly

drops, as shown by the slope indicated in the figure by the dotted line. At fixed velocity, the cross section drops like $n^{-1.6}$ in this region. At fixed n, it drops like $v^{-5.6}$.

CTMC calculations, like the COB model, predict that the position of the final state population shifts with the charge of the projectile capturing the electron, this

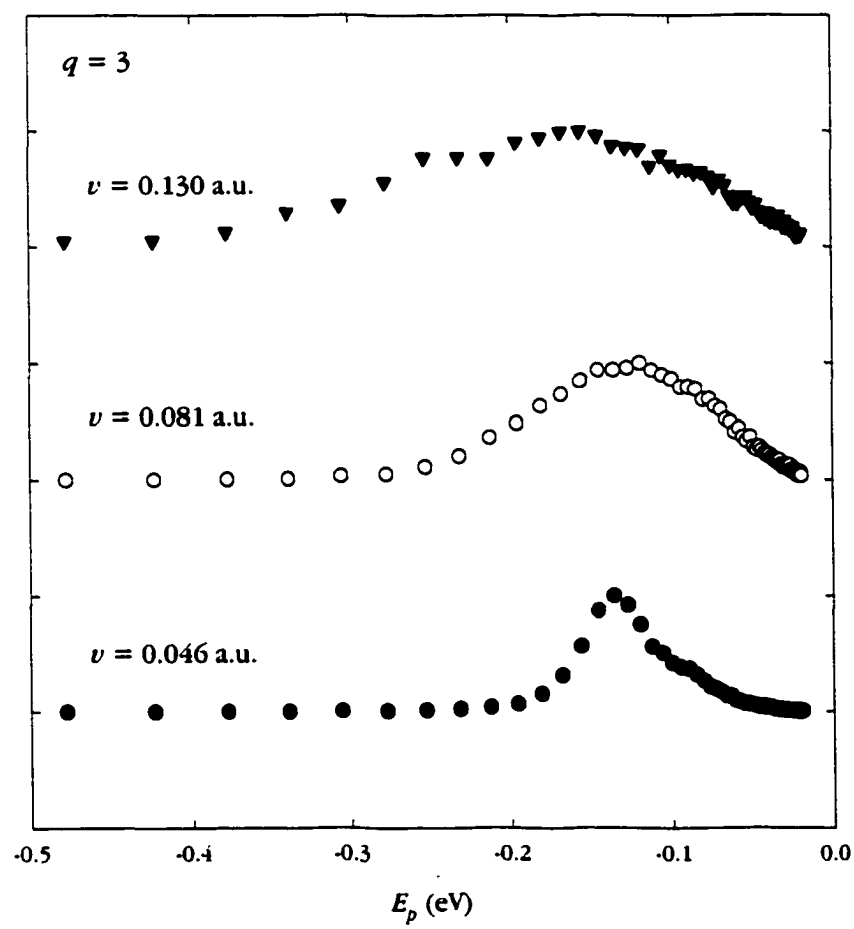

Figure (1.2.6) : **Final state distribution as a function of velocity.** This figure shows how the final state distributions calculated by CTMC vary with velocity for $n_t = 10$. The velocity for each projectile is given at the right. All projectiles have a charge $q = 3$.

can be seen in Fig. 1.2.2. CTMC predicts that the most probable final state approximately follows the approximate functional form $n_p = q^{3/4} n_t$, or the final state binding energy is $E_p = q^{1/2} E_t$ [6]. Unlike the COB model which fails to predict a width for the capture resonance, CTMC does predict a product state resonance width. The predicted width is approximately constant with q, as shown in Fig. 1.2.5, and a nearly linear function of velocity shown in Fig. 1.2.6. There are currently no quantum mechanical calculations for the collision of ions with highly excited states. The large number of states involved in such a calculation causes the problem to quickly become intractable as the n-state of the target increases. In the absence of careful experimental studies, the limitations of the CTMC approach are not yet known.

1.3 Previous experiments

The earliest studies of collisions of Rydberg states and singly charged ions were done in merged beam experiments performed by Bayfield and Koch[13]. These experiments looked at the collisions of a proton beam with a neutral hydrogen beam produced by neutralization of a proton beam in a Xe gas cell. The remaining proton beam was deflected by a set of field plates and another set of plates was used to select the Rydberg states by modulating an axial electric field to select n-states in a band from about 44 to 50. However, this experiment only studied the total capture cross sections and did not determine the final state distribution of the capture population.

The charge transfer population distribution of collisions of ions and Rydberg atoms have only recently been studied. Tunable lasers have made it possible to

create a target of Rydberg atoms dense enough to measure properties of the collision products. The pioneering studies of the final state distributions of the capture population of ion-Rydberg atom resonant charge exchange collisions were done by MacAdam and coworkers [5]. In a series of experiments, a beam of ions crossed a thermal alkali beam excited to Rydberg levels by pulsed lasers, and the final state of the charge exchange product was analyzed by Stark ionization. With this method the capture products are ionized in a carefully controlled electric field to determine their distribution in final n. The experimentally obtained ion flux versus ionizing field is mapped into an n distribution by assuming a one to one correspondence between the field at which an atom ionizes and the n-state in which it started. The problem with this assumption is that the actual route to Stark ionization can be much more complicated. The actual ionization field for levels sharing the same principal quantum number can vary by as much as a factor of three, depending on the values of l and m, and the slew rate of the ionizing field. The Stark ionization technique can only infer the n distribution by making assumptions regarding the l and m distributions and this precludes a precise experimental test of theoretical n-distribution predictions. Distributions in n derived in this way were obtained by MacAdam in studies of collisions by Na^+ on Na(nS or nD) for a few n's in the range 24-34 and a range of ion velocity of approximately 0.9 to 1.7 times the matching velocity. The results of these experiments generally confirm the resonant nature of the capture, but differ in detail from predictions of CTMC calculations. Whether this indicates a deficiency in the predictions, or the difficulty in obtaining an unambiguous n distribution from

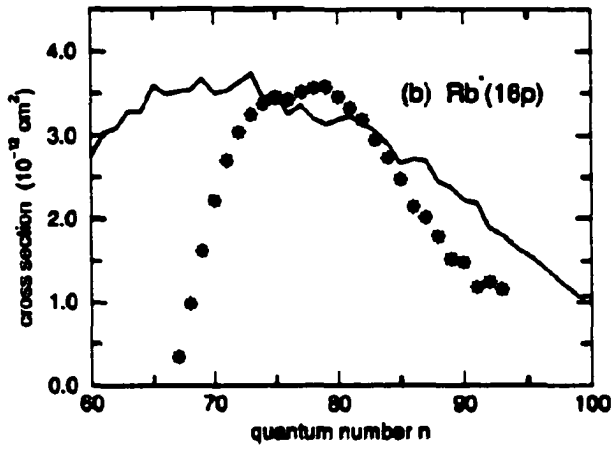

Figure (1.3.1): **Disagreement between CTMC and measurement in Pesnelle experiment.** This figure shows the clear disagreement between the Pesnelle measurement and CTMC theory reported in their paper[14]. The line shows the CTMC calculated capture cross section and the * show the measurement using a classical field ionization model where $F_C = q^3/(16\,n^4)$.

Stark ionization data is not yet clear.

Recent experiments by Pesnelle et. al. [14, 15] also used Stark field ionization to determine the final n-state distributions in charge capture collisions. These experiments studied collisions of q=8 ions on Rydberg atoms. A thermal Rb beam excited by a single UV laser to the $n_t P$ state ($15 <= n_t <= 25$) was crossed with a Kr^{8+} ion beam and the product Kr^{7+} beam was analyzed with a Stark ionization detector. The experimental results show an n distribution that is substantially narrower than the CTMC predictions. This is clearly seen in their figures and reported in their paper. As an example, one of these figures is shown here as Fig. 1.3.1. Additionally, as in the studies with singly charged ions, the inherent

ambiguity involved in inferring n alone from the Stark ionization field clouds the interpretation of the experimental results, which at face value seem to show clear deviations from the predictions of CTMC.

1.4 Our measurement technique

Our study is designed to overcome the ambiguities inherent in the previous experiments due to the limitations of the selective field ionization method. We accomplish this by selecting a single n-state from the charge capture final state distribution and detecting it uniquely using laser excitation. However, this detection method is only practical for a narrow range of final state energies much smaller than the total final state energy distribution, due to the limited range of available laser frequencies. Thus, a new approach for examining the charge capture resonance is needed. The highly resonant population in the final state depends on the initial binding energy of the Rydberg target and the peak position of the distribution changes as the energy of the Rydberg target is changed. Thus, our tuneable Rydberg target provides a way to overcome the limited range of detectable final states. It can be set to a number of different states over a wide range of binding energies, and we can examine how the population in one particular final state varies with the target binding energy. This is depicted in Fig. 1.4.1 showing a single final state measured as the target energy is varied. As can be seen in this depiction, the population in the measured state varies as the target energy is varied. If the total target thickness were independent of n_t, then the size of the laser excitation signal as a function of n_t would directly map the cross section for capture into a specific final state as a function of the target energy. This would map the

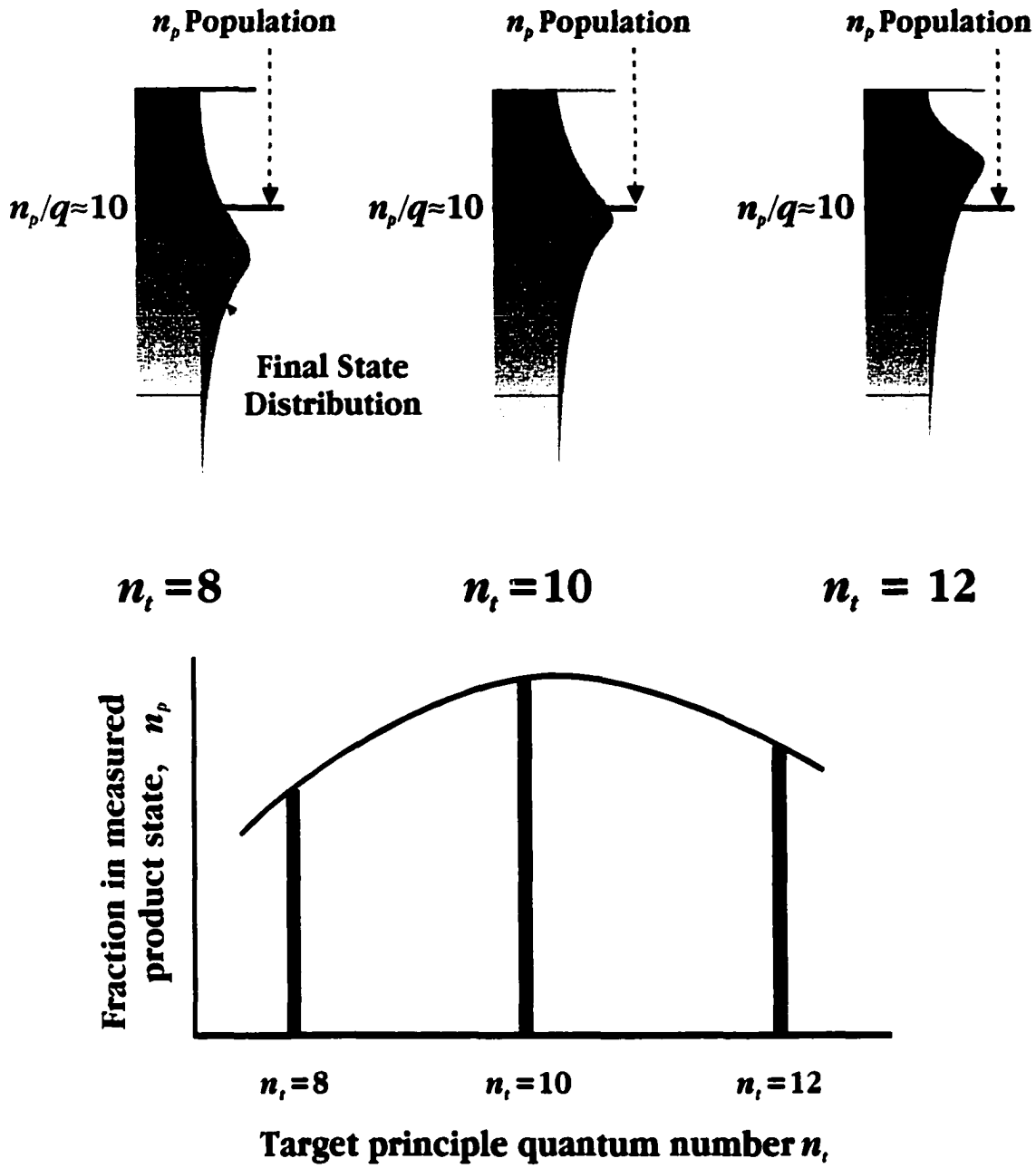

Figure (1.4.1) : **How we use the target state to examine the product state distribution.** This figure shows how we obtain information about the product state distribution by varying the target state of the collision.

charge capture resonance in the space of initial state energy, rather than in final state energy. In practice, it is not practical to control the relative target thickness as n_t is varied. An alternative is to measure the ratio of the laser excitation signal to

the total charge transfer beam intensity. This quantity is independent of target thickness and still reflects the underlying capture resonance.

The scheme for detecting a particular final state involves laser excitation to a very high excited state, which is subsequently Stark ionized. We refer to this

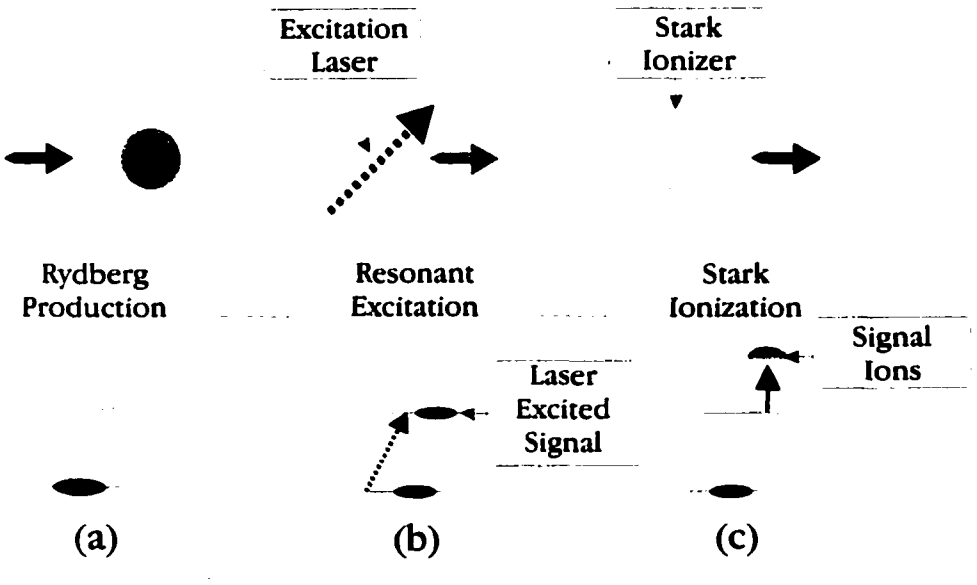

Figure (1.4.2) : **Schematic of RESIS process.** This is a schematic representation of the three steps involved in the RESIS process. The upper part of each panel illustrates the physical process, while the lower portion shows its effect on the atomic level population. The first step shown in panel (a) is populating the Rydberg state through a collision of the ion beam and an atom. The second step shown in panel (b) is to resonantly excite the populated state of interest to a very high lying Rydberg state. The final step shown in panel (c) is to detect the resonantly excited population by Stark ioniziation. Part (b) and (c) compromise the Resonant Excitation Stark Ionization Spectroscopy method.

method as Resonant Excitation Stark Ionization Spectroscopy, or RESIS. The RESIS method in general involves two processes shown schematically in Fig.1.4.2. First

a laser is used to resonantly excite a specific Rydberg state of the charge transfer ion beam to a much higher state. At this point it is necessary to quickly introduce the notation we use to describe the laser excitations. As an example of our notation, a primary ion beam C^{3+} has q=3 this is the identifier we will use to identify a particular measurement along with the velocity v. After the capture of an electron this becomes the capture beam C^{2+*}. Our notation (which is standard) for a transition of the captured electron from the n=29 to the n=71 state in this ion after capture is C III 29-71, where C III stands for the third ionization state of carbon or C^{2+} (C I being neutral carbon). A number of transitions of C III are illustrated in 1.4.3 with a CO_2 laser energy spectrum shown below. As can be seen in the figure the CO_2 laser can excite each lower state to a number of different upper states. These laser excited states are then Stark ionized and the resulting ion current is measured. Thus, Stark ionization plays a role in the RESIS detection process but is not the selective element. This method does not require knowledge of the distribution of the l, m_l states within the n_p state for comparison to theory, and thus provides an unambiguous quantitative test of theory.

We have used this measurement technique previously to measure the resonance in the product state as the target state is varied for q=1 in helium for v=0.100 a.u. and have reported the results of this study [16]. Following this measurement we extended the technique for ions where the capture beam was charged q > 1, and made a measurement for q=2-4 in carbon at v=0.100 a.u. and a velocity study of v=0.031, 0.57, and 0.100 a.u. at q=3. The results from this study are reported elsewhere [17] and also included in this dissertation. This dissertation reports the

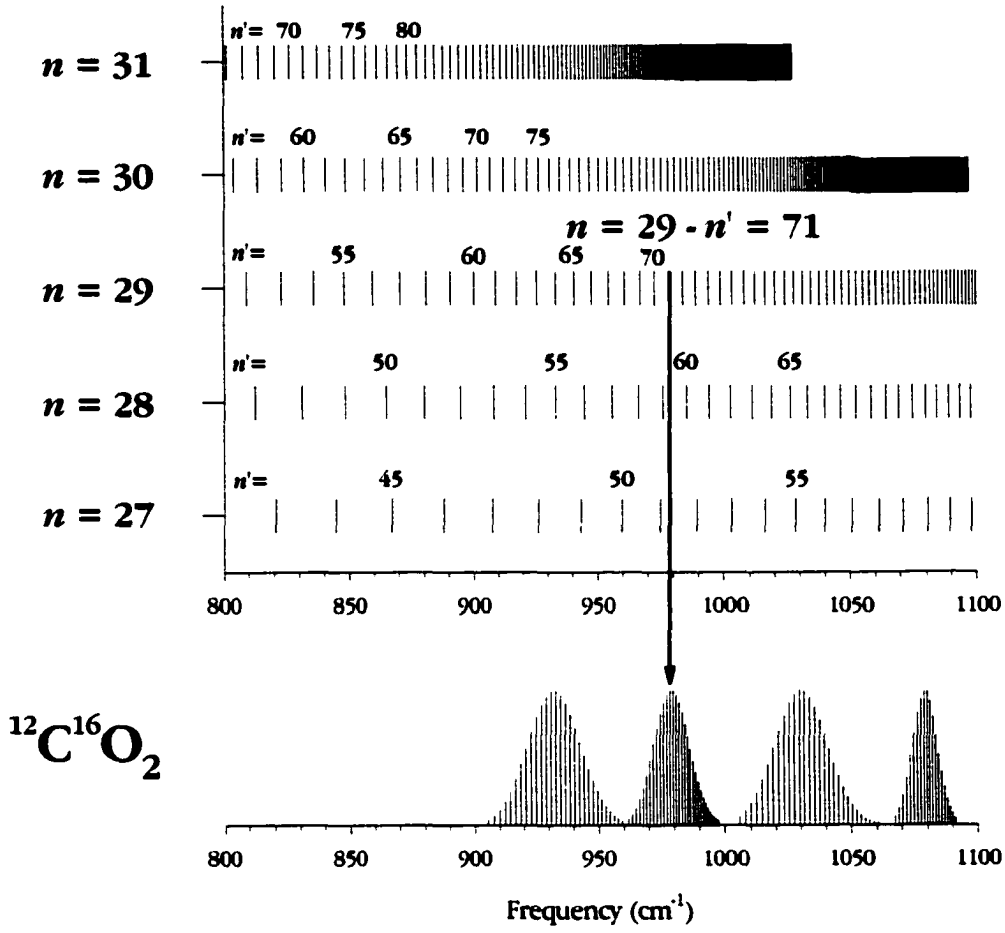

Figure (1.4.3) : **CO_2 spectrum and C III transitions.** The upper part of this figure shows the energies of various transitions of C III. The lower state of the transition is listed to the left and each line indicates the energy of a transition to an upper state n'. A few of these upper states are labeled for each lower state. The lower part of the figure shows the energies of CO_2 laser lines available. Note that the CO_2 laser energies overlap a number of the transitions shown. One particular transition of C III is indicated, the $n=29-n'=71$ transition. Note that this lies near the energy of one of the CO_2 laser lines.

extension of these measurements to $q=11$ and some additional velocity measurements at $q=3$.

1.5 Organization of rest of thesis

The rest of this thesis is organized into two parts. Chapter two describes the experimental apparatus used and the technique used to make the measurements for the ions in this study. This includes the details of how the RESIS technique was extended to charged Rydberg states. It also includes details of the typical operation of the various pieces of the experimental apparatus. Finally chapter three details the measurement procedure, the results of the measurement, and comparisons to the CTMC and COB models of the collision.

Chapter 2 : Experimental apparatus

2.1 Overview and introduction to the experimental apparatus

A schematic diagram of the entire apparatus is shown in Fig. 2.1.1. This diagram shows five distinct regions of interest. The first region is the ion source which produces and accelerates the primary ion beam. The next is the Rydberg target, the collisions of ions with the Rydberg atoms in this target are the focus of this study. The operation of the Rydberg target is described in section 2.3. The third region is the repeller region. The repeller is a device used to block, or repel, the primary ion beam from the rest of the beamline and empty the upper states of the laser transition to reduce noise in the signal. The design and construction of this device was an integral part of this research. Consequently, its design and operational characteristics are described in detail in section 2.4. The final two regions implement the RESIS method to detect the population in a particular final state. The fourth region is the laser interaction region, or LIR. In the LIR Rydberg states populated in the collisions at the target are excited to a very high n-state using a Doppler tuned CO_2 laser. This technique like the Rydberg target, has been used in many previous experiments, and will be described briefly in section 2.5. The fifth and final region is the Rydberg detector. In this region, the excited state

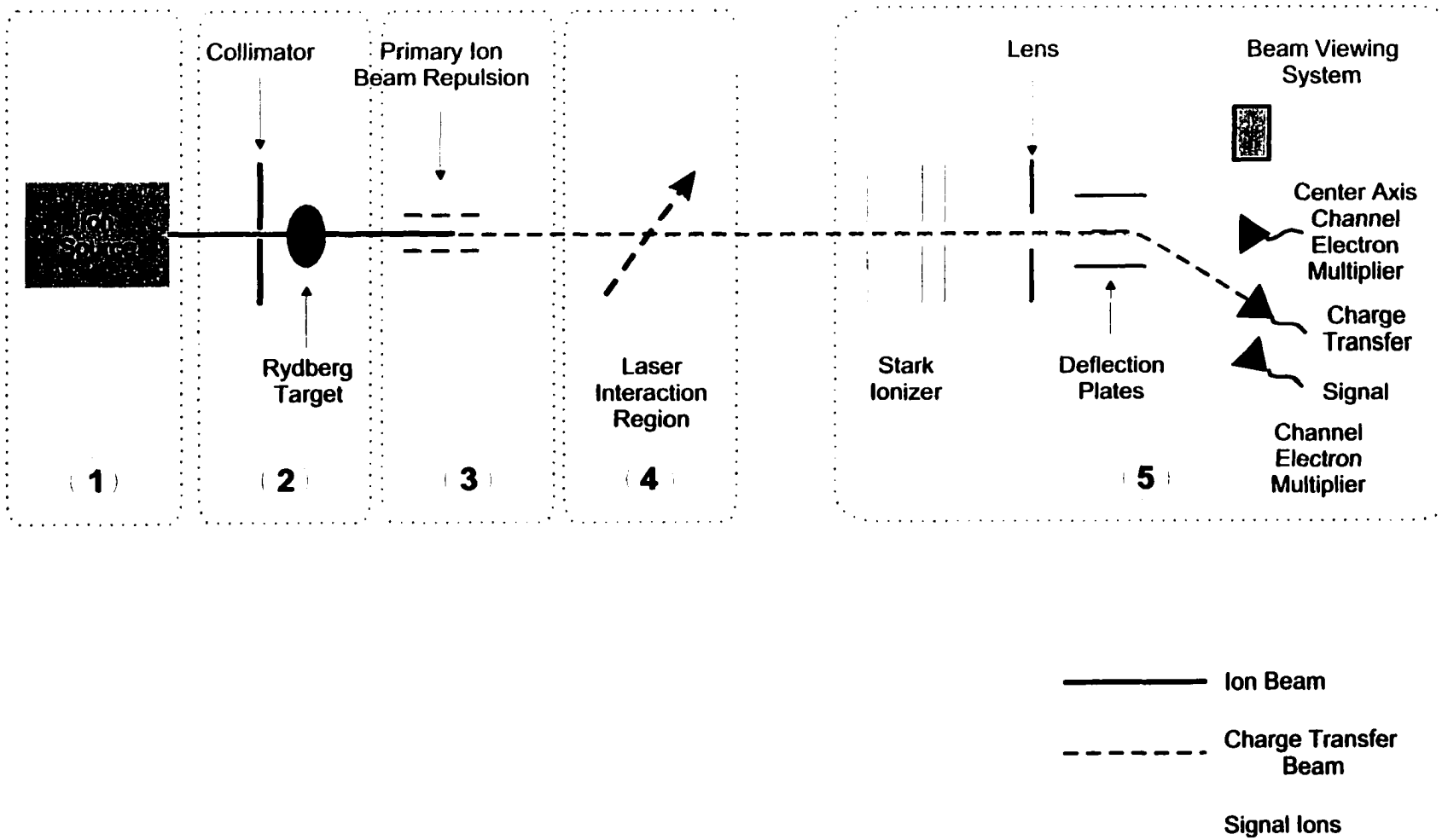

Figure (2.1.1) : <u>Schematic diagram of experimental beamline.</u> This is a schematic diagram of the beamline used to make RESIS measurements in this experiment.

is Stark ionized. After Stark ionization the signal is focused and selected using electrostatic elements. The signal current is then measured. This signal current and the measurement of the total charge transfer beam current are used to analyze the population distribution resulting from the charge capture event. The design and operation of the Rydberg detector are described in section 2.6.

2.2 CRYEBIS Ion source

This experiment required a source of multiply charged ions at a number of different velocities. Fortunately, such a source exists at Kansas State University at the J. R. MacDonald laboratory. The source we used is the CryEBIS, or cryogenic electron beam ion source [18]. This source produces a wide range of different beam species and charges at relatively high particle currents. It is a source of nearly monoenergetic ions with a sophisticated set of ion optics capable of delivering the ion beam to an experimental beam line with a wide range of possible beam energies. The source was maintained and operated by MacDonald laboratory staff. Generally we only needed to do a small tuning of the beam to get the ion beam incident on our target.

The beams used for this study were C^{2+}, C^{4+}, Ne^{6+}, Ar^{8+}, and Ar^{11+} at v = 0.100 a.u., C^{3+} at v = 0.130 a.u., 0.100 a.u., and 0.081 a.u., Ar^{3+} at v = 0.057 a.u., 0.043 a.u., Xe^{3+} at v = 0.031 a.u. (1 a.u. = c/137, or 0.25 keV/amu). This wide range of charges and velocities available from the CryEBIS ion source made it possible to study the effects of varying each on the resonant charge capture.

The primary factor in choosing these particular ions was that the ion have an S-state core. This is important because ions with S-state cores have much simpler

Rydberg fine structure than ions with non S-state cores. Of secondary importance in the choice of specific ions was choosing ions of different masses and the same charge state. This was convenient for the study of different velocities since choosing ions with these characteristics and using the same accelerating potential makes it possible to do virtually no retuning of the repeller and detection ion optics between the ions of different mass. This is possible because the electrostatic ion optics only depend on the energy per charge and not on the velocity. Thus by changing the mass of the ion it is possible to quickly get a wide range of velocities needing only to retune the ion source between ions. This allows data to be taken easily for the C^{3+} at v=0.100, Ar^{3+} at v=0.057, and Xe^{3+} at 0.031 series and the C^{3+} at v=0.081 and Ar^{3+} at v=0.046. These two conditions set restrictions on which ions we eventually used. The operation of the source determined which of these ions were easiest to use. For instance the for q=6 at v=0.100 a number of ions satisfy the two conditions. However Ne^{6+} was chosen since the source produced significantly more beam current than a C^{6+} beam for example, because Ne^{6+} is not fully ionized.

2.3 Rydberg target

2.3.1 Introduction

The Rydberg target used in this experiment has been used previously in a number of other experiments by our group [19, 20, 21, 22, 23]. Most of our current understanding of the target is based on the measurements and the theory developed in the course of these previous experiments. Only the basic ideas needed to understand the target in the context of our experiment will be discussed here. For a more detailed discussion of the Rydberg target one should refer to

Francis Deck's dissertation, the first full description of our Rydberg target, and other publications dealing with the theory of our Rydberg target [19, 20, 21].

The excitation of the Rydberg target is a three-step excitation from the ground state of Rb to a selected upper state. Figure 2.3.1 shows the excitation path for the three steps of the excitation. The first step of the excitation is from the ground state, $5S_{1/2}$, to the $5P_{3/2}$ state. This transition requires a wavelength of 780.241 nm. A diode laser with a power of about 30 mW, and a spectral width of about 50 MHz is used to excite this transition. The next step of the excitation is from the $5P_{3/2}$ to the $4D_{5/2}$ state. An F-center laser with a power of about 30 mW and a spectral width of approximately 10 MHz at a wavelength of 1529.37 nm is used for this step of the excitation. The final step of the excitation selects the target state and is from the $4D_{5/2}$ state to one of a number of different $n_tF_{7/2}$ states. A Ti:Sapphire laser is used for this excitation, and wavelengths from 705.565 nm to 827.371 nm are used for the different final states as shown in Fig. 2.3.1. The power of the laser varies from about 200 mW near 830 nm to about 50 mW near 705 nm.

The excitation frequencies, as measured on a wavemeter (Burleigh Model WA-20), from the $4D_{5/2}$ state to each of the final states of the Rydberg target used in this experiment, are listed in Table 2.3.1. The measured frequencies for the final step of the excitation were fit to a quantum defect model using the equation,

$$h\nu = E(n_t F) - E\left(4D_{5/2}\right) = \left[E_{Ionization} - E\left(4D_{5/2}\right)\right] - \frac{R_{Rb}}{(n-\delta)^2} \qquad (2.3.1)$$

where the energies are measured from the ground state in cm^{-1}, $E(n_tF)$ is the F

state energy, $E(4D_{5/2})$ is the D state energy, $E_{ionization}$ is the ionization energy, R_{Rb} is the Rydberg for ^{85}Rb, and δ is the quantum defect. The fit of the measured values to this equation gives $\delta = 0.01499(8)$ and $E_{ionization}$-$E(4D_{5/2}) = 14335.50(2)$ cm^{-1}. This gives the predicted frequencies listed in Table 2.3.1. The states fit the quantum defect model quite well with a maximum deviation between the predicted and

Table 2.3.1: **^{85}Rb final state frequencies.** This table shows the frequencies for the final transition of the laser excitation for the Rb Rydberg target and the predicted values found by fitting the data to a quantum defect model giving $\delta = 0.01499(8)$ and $E_{ionization}$-$E(4D_{5/2}) = 14335.50(2)$ cm^{-1}. Note the largest deviation between the measured and predicted frequencies is only 0.11 cm^{-1} or 3300 MHz.

Final target state	Measured Frequency(cm^{-1})	Predicted Frequency(cm^{-1})
7F	12086.47	12086.36
8F	12614.37	12614.42
9F	12976.13	12976.20
10F	13234.76	13234.84
11F	13426.05	13426.11
12F	13571.49	13571.53
13F	13684.65	13684.67
14F	13774.41	13774.42
15F	13846.81	13846.81
16F	13906.05	13906.04
17F	13955.14	13955.12
18F	13996.27	13996.24
20F	14060.79	14060.75
22F	14108.51	14108.46
26F	14173.04	14172.98

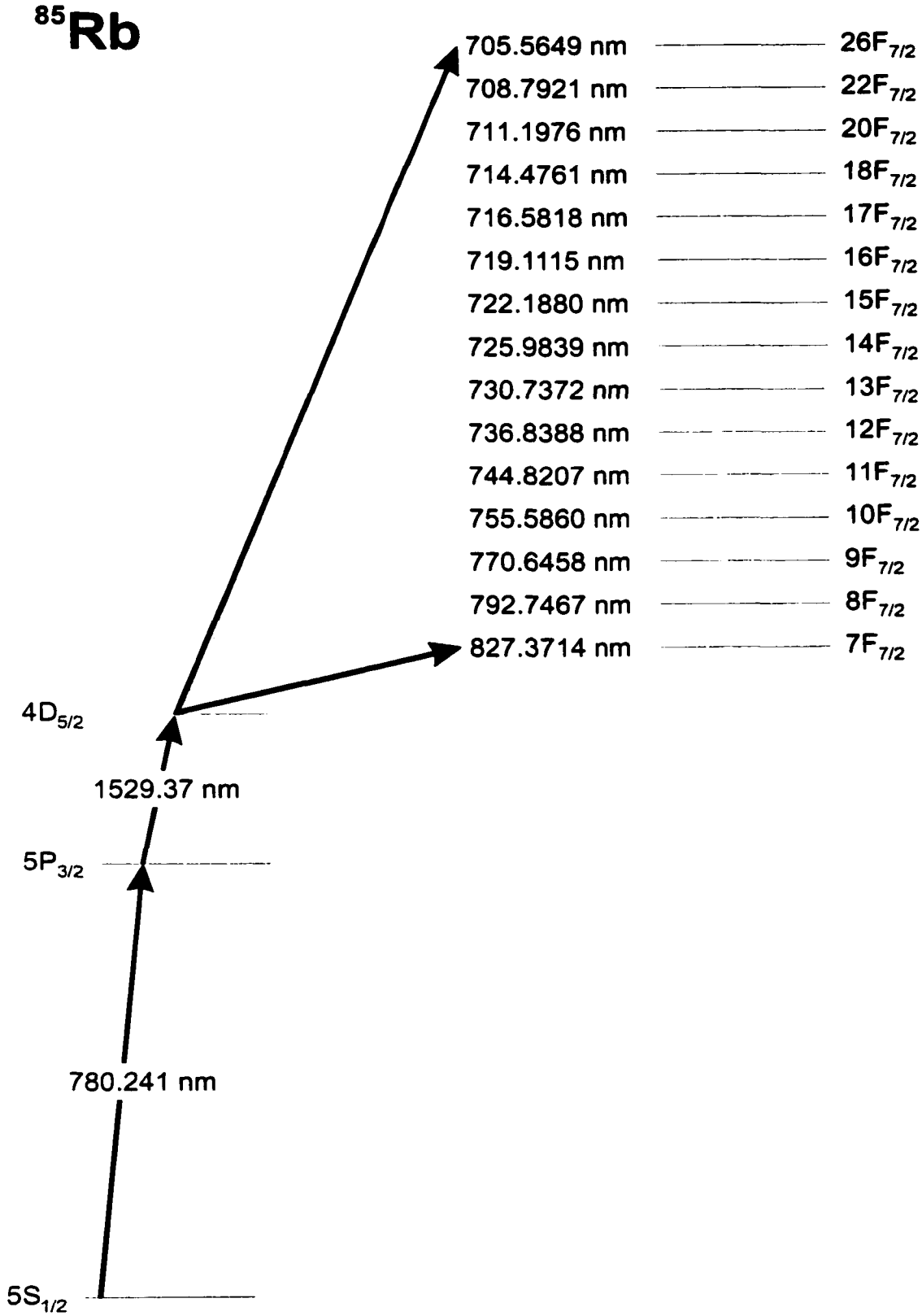

Figure (2.3.1) : **^{85}Rb basic excitation structure.** This shows the simplest description of the Rydberg target excitation path.

measured frequencies of only 0.11 cm^{-1} or 3300 MHz, confirming that these are the n_tF states. The final target states used in this experiment were limited to a range of n_t between 7 and 26.

The final step of the excitation is the primary difference between the operation of the Rydberg target for this experiment and our previous experiments. In this experiment the tuning range of the target has been extended. There is a wide range of final states, n_t = 7-26, accessible compared to previous experiments with our target, which used only one or two final states (F. Deck, n_t=8 and 10 [16] M. T. Huang n_t=10 [18]). The wide tuning range is critical to this experiment, which relies on tuning the target binding energy and measuring the related change in the rate of capture to one particular n level on the projectile. Complications because of the fine and hyperfine structure, and sharing of the final state population were examined in some detail. The reason these complications were studied was our reliance on the binding energy and final state of the target. Some effort was also made to study the variation in target density and the stability of the target with time. We have measured the total excited state population in the final state of a particular n_t = 10 Rydberg target using this excitation scheme. We have estimated the population of this target to be $2x10^8$ excited atoms in a spherical volume of about 3.6 mm diameter. This gives a target density of approximately 10^9 cm^{-3}. This high density and the large capture cross section, approximately 10^{-11} cm^2 (or $3.5x10^5$ a_0^2), for charge capture results in a substantial charge transfer beam on the order of 1% of the primary ion beam incident on the Rydberg target.

The density of the n_tF atoms in the target produced using the above excitation

scheme is sufficient for all n_t to produce a large gain on the transition from the n_tF state to the $(n_t+1)D$ level which lies just below it, resulting in rapid sharing of the excited population between the two levels. This sharing, through a mirrorless maser transition, has been described in detail for the 10F target[20]. This population sharing between the n_tF and the $(n_t+1)D$ levels is observed in all of the targets through the blue fluorescence of the decay from the $(n_t+1)D$ state to the $5P_{3/2}$ state.

2.3.2 Experimental equipment

The chamber containing the Rb Rydberg target is mounted ~2 m from the exit of the final switching magnet of the ion source connected to it by a magnetically shielded 4" stainless steel vacuum nipple to reduce the deflection of the ion beam by the earth's field. The target chamber is illustrated in Fig. 2.3.2. The ion beam enters the target chamber through a small (~3mm diameter) aperture about 2 mm from the target. This ensures that any ions leaving the aperture intersect the target. The chamber itself is a six way cross, two flanges are 6" Dependex (on the top and bottom) and the other four are 4" Dependex.. The chamber is divided into two separate chambers, one containing the oven, the lower chamber, and the upper chamber where the target excitation occurs. Above the target is a liquid nitrogen cooled "cap" used to collect and solidify the Rb after it leaves the excitation/collision region. Below the target is a plate of copper with an aperture between the upper and lower chambers used to collimate the Rb beam just before the excitation. This plate is mounted on a stainless steel "top hat" and together they separate the upper and lower chambers. The copper plate is heated above the condensation

temperature of Rb to prevent liquid Rb from accumulating in the aperture and clogging it. The power for the heating the plate and oven are fed through the lower chamber and the wires to the plate are run through apertures between the lower and the upper chamber. The oven and the "top hat" temperatures are monitored with K type thermocouples. The Rb oven is filled from the top by removing the "cap" and the collimation plate after the oven has cooled and using a custom

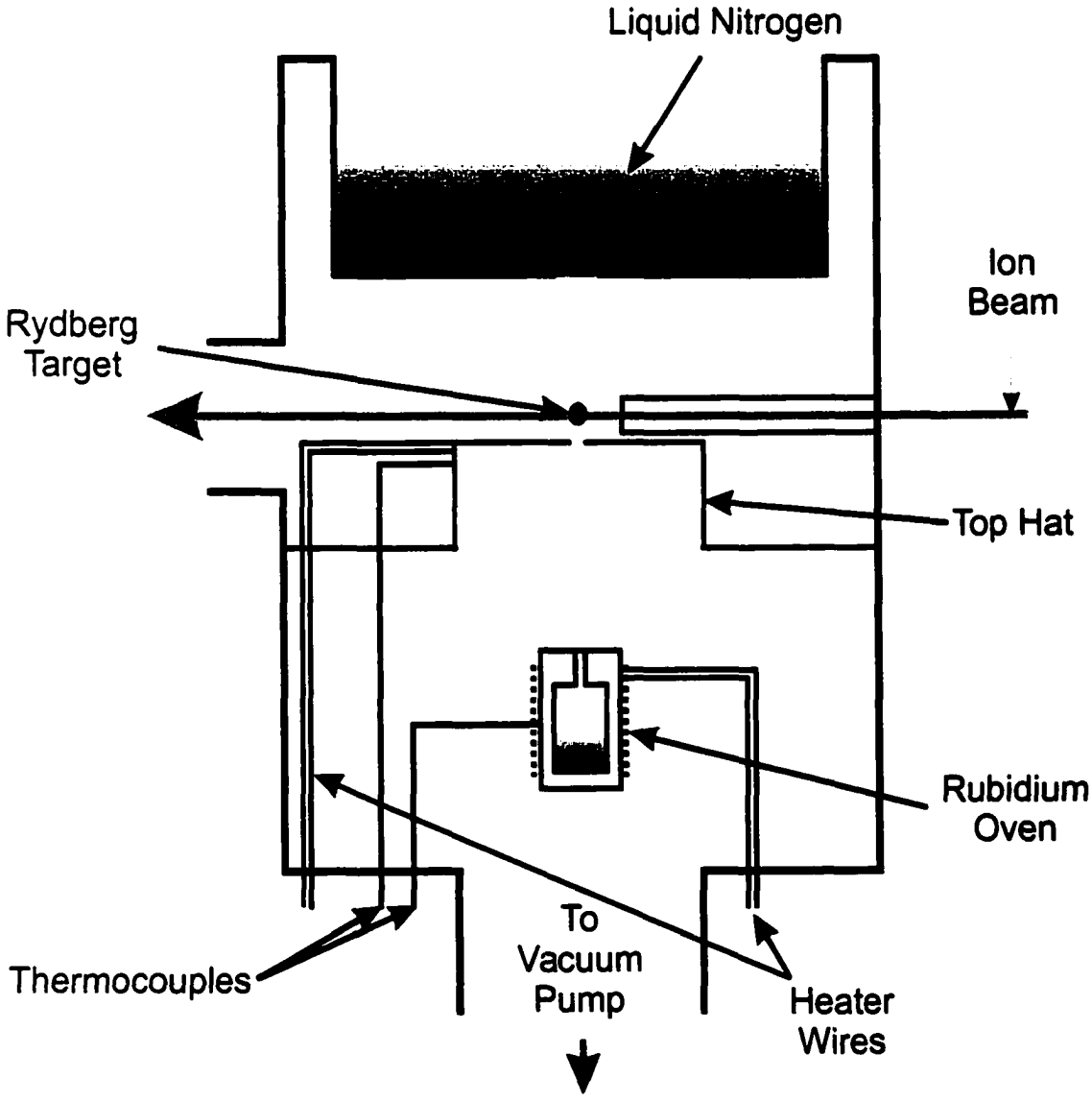

Figure (2.3.2) : **Rydberg target chamber.** This shows the Rydberg target chamber.

spanner wrench to unscrew the top of the oven body. The old Rb ampule is then removed and a new one is inserted into the oven body. When the Rb is replaced, the windows into the upper chamber are cleaned and any solidified Rb is removed from the "cap".

The lasers enter the chamber through two windows mounted on the two 4" Dependex flanges perpendicular to the ion beam propagation direction. These windows are made of quartz allowing the measurement of any ultraviolet light emitted by the target. Two 1' x 2' optical surfaces are mounted on either side of the Rydberg target chamber. These are used to mount the optics for steering and focusing the three lasers used to excite the Rydberg target, and the detectors

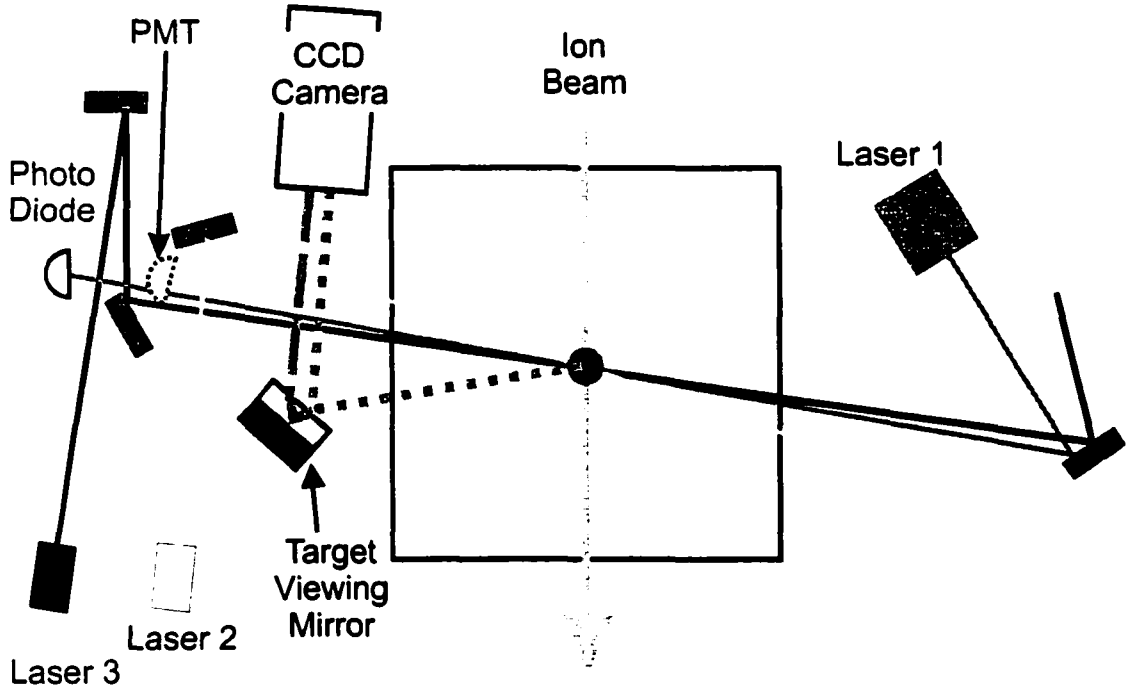

Figure (2.3.3) : **Rydberg target optical layout.** This shows the optical layout to excite the Rydberg target. The unlabeled grey boxes are mirrors. The boxes labeled as Laser 2 and 3 are the positions of the ends of the optical fibers used to transport the lasers to the target chamber. The photomultiplier tube, labeled as PMT is above the plane of the lasers. The purpose of the target viewing mirror is explained in detail in the text.

monitoring the Rydberg target. Two of the lasers used for the excitation of the target are transported to the Rydberg target chamber through separate multi-mode optical fibers and are then shaped and directed into the target chamber. The diode laser used for the first excitation is mounted on one of the optical tables. The three lasers are directed to a point coincident with each other. The point where all three lasers intersect each other and the thermal rubidium beam determines the location of the target. The target is positioned to be directly in front of the entrance aperture of the target chamber.

The approximate positions of the optical elements with respect to the chamber are shown in Fig. 2.3.3, the grey unlabeled elements are mirrors. The rectangles labeled as lasers two and three in the figure are the positions of the ends of the fibers used to transport these lasers from the optical table where they are mounted. As can be seen in the figure, the lasers are nearly collinear with the largest angle of approximately 10° between lasers two and three. The photomultiplier tube, or PMT, is placed above the plane of the lasers and measures the blue fluorescence of the target.

Also shown in the figure is the CCD camera used to visually monitor the target. An interesting aside about the visual monitoring of the target is that it is set up to monitor both the first laser fluorescence and the blue fluorescence of the target with a single camera. To accomplish this, a mirror with a blue filter on top of it, labeled in the figure as the target viewing mirror, directs the image of the target to the CCD camera. The first laser fluorescence is reflected from the first surface of the filter and is imaged slightly displaced from the blue fluorescence which passes

through the filter and is reflected from the mirror. This allows a "split-screen" view of the two different indicators of the target with only a single camera, and allows simultaneous visual monitoring of the fluorescence of both transitions.

The three lasers are locked to their respective transition frequencies using phase locked feedback loops. The first laser, modulated with a frequency of 244 Hz, is locked to the absorption of the Rb measured by the photodiode on the opposite side of the target chamber. The second and third lasers are locked by maximizing the blue fluorescence of the target detected by the photomultiplier tube. To lock to the blue fluorescence, the lasers are frequency modulated at 637 Hz for the second laser and 2150 Hz for the third laser. Relying on the blue fluorescence from the $(n_t+1)D$ state to lock the lasers to their resonance frequencies can limit the range of usable target states. This locking method was first used, and is optimal for the lower n-state targets where the blue fluorescence is very strong. For high-n targets the blue fluorescence becomes quite weak, partly because the lifetime of the state becomes very long. A different locking method might be useful to improve stability of the laser frequencies for these high-n targets.

The Ti:Sapphire laser used for the final excitation currently limits the range of target final states available. As n_t increases the frequency for the final transition approaches the edge of the gain region of the Ti:Sapphire crystal. As the frequency needed moves to the edge of the gain region the overall power is reduced, and the tuning of the laser becomes non-continuous, limited to narrow islands of available frequencies. The Ti:sapphire laser is fine tuned to the final excitation frequency of the target through the use of two intercavity etalons, one thin and one thick whose

free spectral ranges are 225 GHz and 10 GHz respectively after coarse tuning with a birefringent filter.

An ingenious way to partly overcome the non-continuous tuning range of the Ti:Sapphire laser at these frequencies was implemented by Charles Fehrenbach, the post-doc on the project. A small power resistor was placed on the coarse etalon and a current was run through it to control the temperature of the etalon. By changing this temperature, the island of frequencies to which the laser was limited could be moved and the desired transition frequency could be reached. This allowed the extension of the data set from a maximum of an $18F$ target to a maximum of a $26F$ target.

This method is rather slow and uncertain and a faster more reliable method of tuning these frequencies would be desirable to more efficiently tune these extremely high-n targets. However the range of targets available with the current equipment is large enough for the current investigation, and thus never became a critical issue to this experiment.

2.3.3 Complications to the simple excitation scheme

The simple excitation scheme presented in the introduction is useful to understand the basic excitation process, but in reality there are a number of factors which complicate the excitation. The simplest of these complications is that the rubidium atoms in the thermal beam are of two different isotopes, ^{87}Rb and ^{85}Rb, with natural abundances of 28% and 72% respectively. The higher natural abundance of ^{85}Rb leads directly to a higher target density in the excited state so this isotope was chosen for excitation to the Rydberg state. It is possible to excite the

^{85}Rb selectively because the difference between the ground state hyperfine structures of the two isotopes are much larger than the width of the transition. A more complicated factor affecting the simple excitation scheme is the fine and hyperfine structure of the Rb excited states.

The three lower states and their fine and hyperfine structure, as calculated by

Table 2.3.2: ***F* state fine structure.** This table shows the frequencies of the F state fine structure splitting calculated by extrapolating the average of the 6F and 7F measurements by Farely and Gupta[21] (486 MHz and 347 MHz respectively) for all but the 7F state. The lifetime of each of the states is also given.

State	$E(nF_{7/2})$-$E(nF_{5/2})$ (MHz)	Lifetime (μs)
7F	347(*)	0.24
8F	219	0.36
9F	154	0.51
10F	112	0.70
11F	84	0.93
12F	65	1.21
13F	51	1.54
14F	41	1.92
15F	33	2.36
16F	28	2.87
17F	23	3.44
18F	19	4.08
20F	14	5.60
22F	11	7.45
26F	7	12.30

Deck[16], are shown in Fig. 2.3.4. These states are common to all targets regardless of the final target state. The n_tF fine state structure varies with n_t, and is summarized in Table 2.3.2 (by extrapolating values measured by Farely and Gupta [24])along with the lifetimes of these states. These fine structure splittings are calculated using the same method as Deck[16] used to calculate the $8F$ and $10F$ structure. None of the hyperfine splittings for the n_tF states of Rb have been measured, but the structure is expected to be no larger than 10 MHz.

The desired excitation path is from the $5S_{1/2}$(F=3) state, to the $5P_{3/2}$(F=4) state, to the $4D_{5/2}$(F=5) state, and finally to the $n_tF_{7/2}$(F=6) state By selecting the states with the highest F and J quantum numbers for the first two steps of the excitation, and the selection rules permit decay only to the level from which the population was excited, because no other $S_{1/2}$ or $P_{3/2}$ levels are accessible. These first two steps are therefore referred to as "cycling transitions". The final step excites the $n_tF_{7/2}$ (F=6) state. This state must decay to a lower $nD_{5/2}$ (F=5) state, preferring to go to the lowest such state, the $4D_{5/2}$. However there are a number of higher $nD_{5/2}$ states to which decays are also allowed. Each of these should eventually decay back to the $5S_{1/2}$ (F=3) state. Additionally, the natural "maser oscillation" transfers nearly 50% of the $n_tF_{7/2}$ (F=6) population to the $(n_t+1)D_{5/2}$ (F=5) level. Thus ideally, there are five well-defined levels which contain the majority of the Rydberg target excited population. However the laser excitation linewidth, ~150 MHz mostly due to Doppler broadening [16], is larger than the energy difference separating some nearby states. Thus, there is the possibility of exciting states outside the desired excitation path. The relative excitation probabilities for all the allowed transitions

along the intended excitation path are calculated using the method described by Deck [19] and are shown in Fig. 2.3.4. These relative values only apply in the limit when the laser excitation width is much larger than the separation between the states in question. If the width is smaller than the separation, these values only give the relative strengths when all transitions are on resonance.

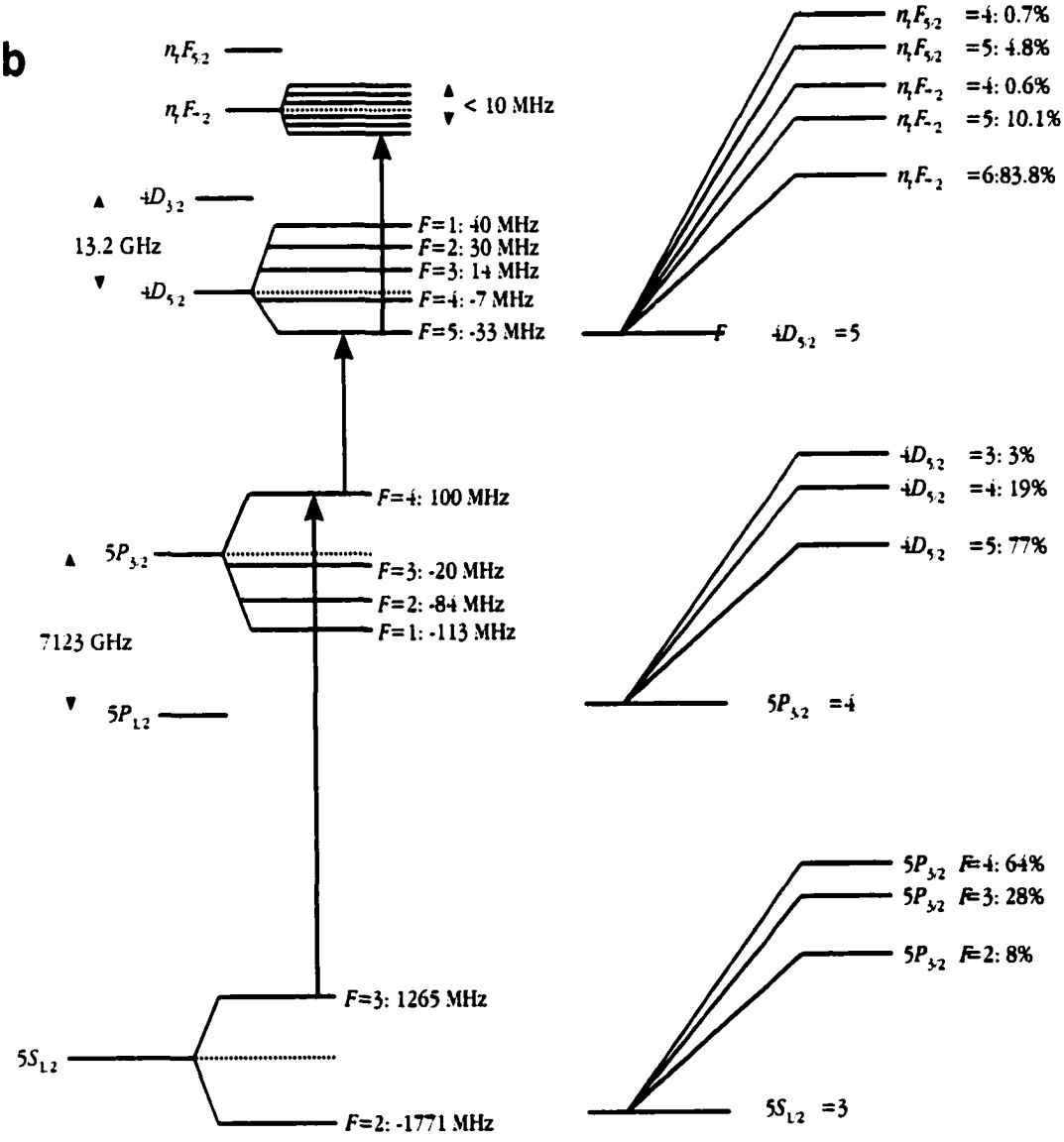

Figure (2.3.4) : **^{85}Rb structure and transition strengths.** This shows the hyperfine structure ^{85}Rb. The dotted lines are the position of the fine structure lines and the frequencies given are the differences from these positions for each of the states.

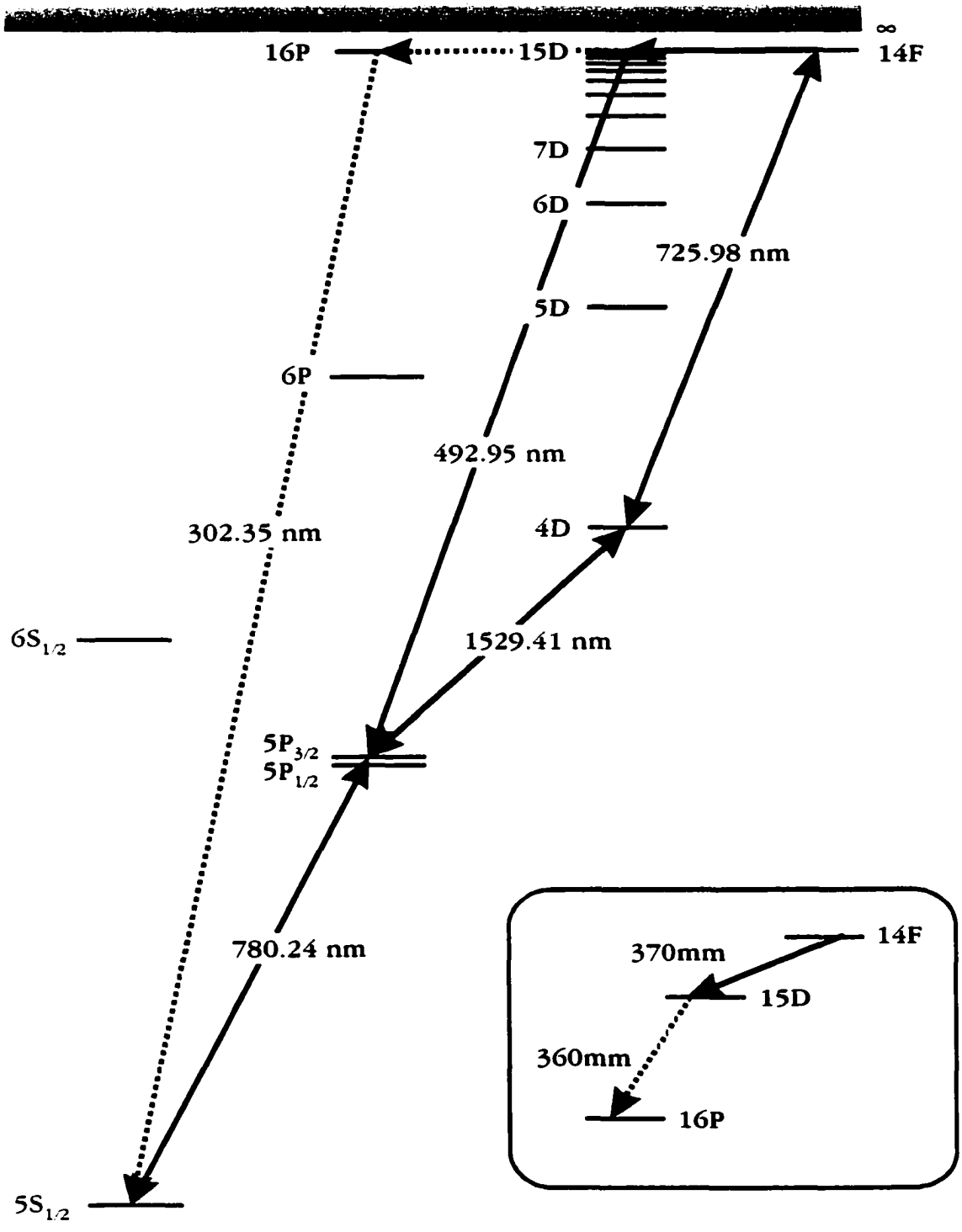

Figure (2.3.5) : **^{85}Rb excitation and decay paths.** This shows the relevant structure and the desired excitation path for a 14*F* target. It also shows the sharing between the 14*F* and 15*D* state and the subsequent decay to the 5*P* state. The dotted arrows show the possible population sharing into the 16*P* state and the subsequent decay if such sharing occurs. The structure shown is to scale.

The relative excitation probabilities for the fine structure transitions are only given for the $4D_{5/2}$ to $n_t F$ transition because this is the only transition where the fine structure can be small enough not to be fully resolved by the ~150 MHz linewidth of the excitation. Both the separation between states and the relative excitation probabilities help keep the population on the desired excitation path. For the first two transitions the fine structure is fully resolved, and the hyperfine transitions are partially resolved and also strongly favor the desired excitation path. The final transition is unresolved but favors the desired excitation path very strongly, at least 83% of the transition should reach the desired final state from the $4D_{5/2}(F=5)$ state. This keeps the majority of the population on the desired excitation path to the final target state. This path is important for maximizing the strength of the target, because any population lost from the desired excitation path can decay to the $5S_{1/2}(F=2)$ ground state and will be lost from the excitation ladder and the target.

The final target state has a much longer lifetime than the other states in the excitation path, any decays out of the "wrong" fine structure state occur at a much lower rate than other losses from the desired excitation path. Any population in the "wrong" fine structure final state should not affect our measurement directly because the difference in energy of the fine structure is small, however it may affect the maximum density of the target. Thus the amount of time the Rb atoms spend in the target is important to the final state density. At 200 °C this time is approximately 8 μs. Thus, losses out of the "wrong" fine structure state, to the unconnected $5S_{1/2}(F=2)$ state, are reduced in importance as the n_t of the target state increases. This is because the lifetime of the final state increases to times equal to

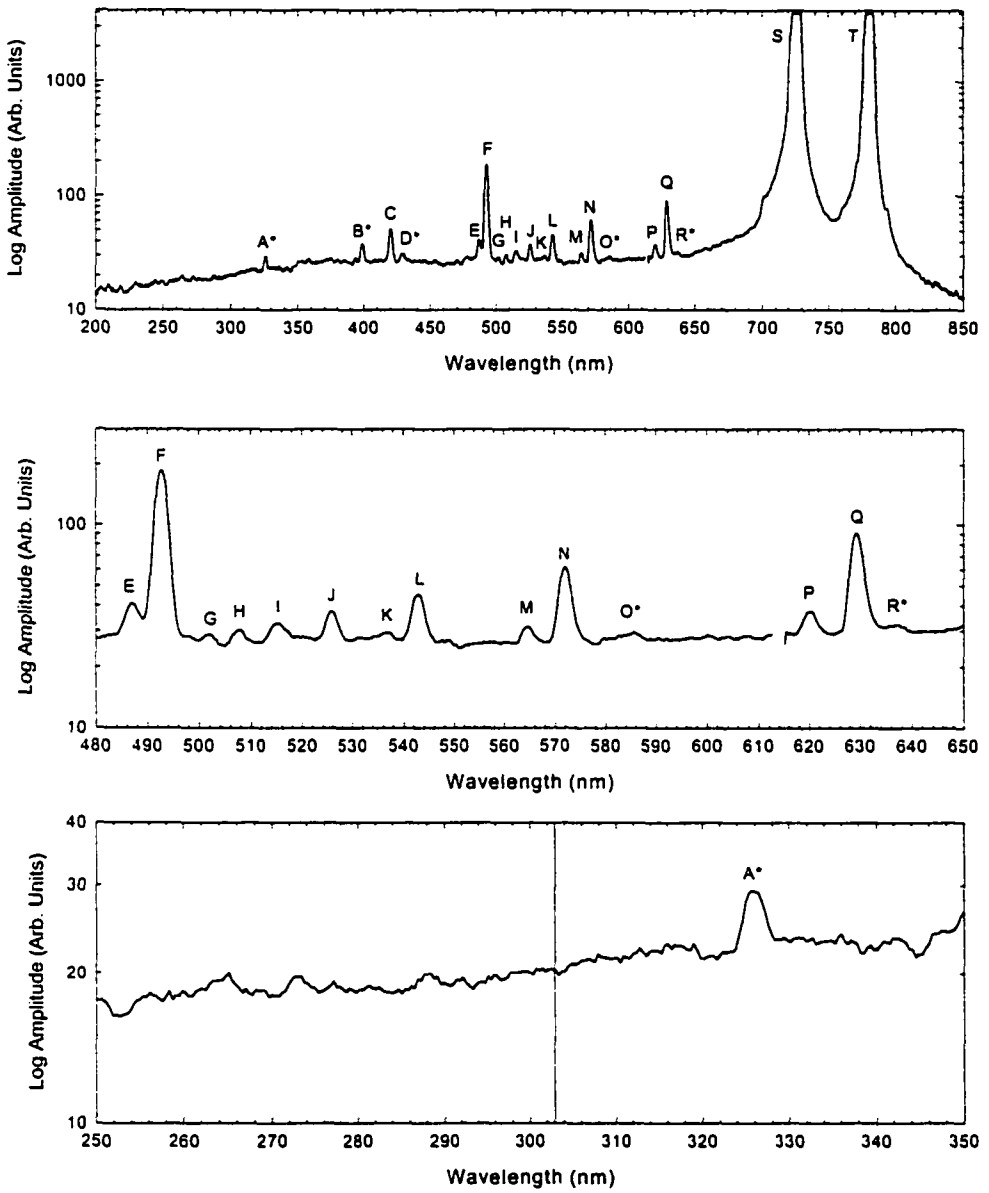

Figure (2.3.6) : **Target spectrum of 14*F* Rydberg target.** This is a spectrum of a 14F Rydberg target. The spectral lines are all labeled with a letter and the frequencies are listed in Table 2.3.3. The labels followed by an asterisk are unidentified lines. The middle figure shows an expanded view of the *nD*-5*P* state series. Note the 15*D*-5*P* state breaks the trend in amplitude, this is because the population is shared through a mirrorless maser transition with the 14*F* state population. The bottom figure shows the region where the 16*P*-5*S* state transition would occur if sufficient 16*P* state population were present, no line appears near that frequency.

Table 2.3.3: **Line identification of 14*F* target spectrum.** This table lists the transitions, the wavelengths measured, and the wavelengths of the transitions from the tabulated energies of Rb I for the 14*F* target spectrum taken and displayed in Fig. 2.3.6.

Label	Transition	Measured Wavelength(nm)	Tabulated Wavelength(nm)
A*	?	325.7	NA
B*	?	398.9	NA
C	$6P$-$5S$	420.1	421.0
D*	?	429.5	NA
E	$15D$-$5P_{1/2}$	486.9	487.2
F	$15D$-$5P_{3/2}$	492.9	493.0
G	$12D$-$5P_{3/2}$ $11D$-$5P_{1/2}$	501.9	501.6 502.3
H	$11D$-$5P_{3/2}$ $10D$-$5P_{1/2}$	507.9	507.7 508.9
I	$10D$-$5P_{3/2}$	515.5	515.2
J	$9D$-$5P_{3/2}$	525.6	526.2
K	$8D$-$5P_{1/2}$	536.3	536.4
L	$8D$-$5P_{3/2}$	543.2	543.3
M	$7D$-$5P_{1/2}$	564.4	564.9
N	$7D$-$5P_{3/2}$	572.3	572.6
O*	?		
P	$6D$-$5P_{1/2}$	620.2	620.8
Q	$6D$-$5P_{3/2}$	629.5	630.0
R*	?	636.8	NA
S	$4D$-$14F$	727.8	726.0
T	$5S_{1/2}$-$5P_{3/2}$	781.0	780.2

or exceeding the time the atoms remain in the target as n_t increases. The lifetimes of the target states are given in Table 2.3.2.

As stated earlier the density of the n_tF atoms is sufficient for all n_t to produce a large gain on the transition from the n_tF state to the $(n_t+1)D$ level which lies just below it, resulting in rapid sharing of the excited population between the two levels. The description of this population sharing [17] also suggests the possibility of further population sharing to other nearby states, for example from the $(n_t+1)D$ state to the $(n_t+2)P$ state. Figure 2.3.5 shows the desired excitation path, the sharing to the $(n_t+1)D$ state and the decay to the $5P$ state for a $14F$ target. It also shows the possible sharing to the $(n_t+2)P$ state and the decay that would characterize this sharing. According to the model of this sharing, whether such additional sharing occurs depends on the total excited state population and the separation between the states involved. These shared populations could produce small but possibly noticeable changes in the product state distribution and should be accounted for in comparisons to theoretical models if these populations exist.

As a check on both the target excitation path and the population sharing in the upper state, the fluorescence spectrum of the target was measured using a broad range spectrometer (OceanOptics Model S2000). The spectra were studied in detail for a number of the targets used in the measurements.

A typical spectra from an $n_t=14$ target is shown in Fig. 2.3.6. There are a number of interesting things to note in this spectrum. The first is the population in the $(n_t+1)D$ state compared to that in the other nD states, especially the $6D$ state. The (n_t+1)D state is significantly populated by the population sharing described

above and it population can be estimated by examination of the amplitude of the strong 15*D* to 5*P* decay, transition F. This fluorescence is much stronger than that from the rest of the *nD* states for this target, in fact about a factor of about 2.5 larger than the next largest *nD* state transition (transition Q, 6*D*-5*P*). Because the 6*D* state is fed by the n_tF state its population can be used to estimate the n_tF population. By examining the ratio of the $(n_t+1)D$ state amplitude to the 6*D* state amplitude correcting for the difference in the lifetimes and the branching ratios we find the population of the $(n_t+1)D$ state, $N_{(nt+1)D}$ is modeled as,

$$N_{(n_t+1)D} = \frac{A_{(n_t+1)D}}{b_{(n_t+1)D\rightarrow 5P_{3/2}}}\tau_{(n_t+1)D} \qquad (2.3.2)$$

where $A_{(nt+1)D}$ is the $(n_t+1)D$ to 5P3/2 transition amplitude (transition F), $b_{(nt+1)D\text{-}>5P3/2}$ is the branching ratio to the $5P_{3/2}$ state, and $\tau_{(nt+1)D}$ is the $(n_t+1)D$ state lifetime. The population of the n_tF state is estimated from the 6*D* state from the following,

$$N_{n_tF} = \frac{A_{6D}}{b_{n_tF\rightarrow 6D}}\tau_{n_tF} \qquad (2.3.3)$$

where A6*D* is the 6*D* to $5P_{3/2}$ transition amplitude (transition Q), $b_{ntF\text{->}6D}$ is the branching ratio into the 6*D* state, and τ_{ntF} is the n_tF state lifetime. Finding the ratio of these populations for all of the targets we find that the relative population in the $(n_t+1)D$ state decreases rapidly above $n_t=12$, as seen in Fig. 2.3.7. This strongly suggests that the sharing mechanism into the $(n_t+1)D$ state is being disrupted for

high target states. This is especially surprising since the predicted necessary threshold decreases rapidly with increasing target.

One clue to what is occurring can be seen by examining the ratio of the $(n_t+1)D$ to $5P_{3/2}$ transition amplitude to the $(n_t+1)D$ to $5P_{1/2}$ transition amplitude. As the

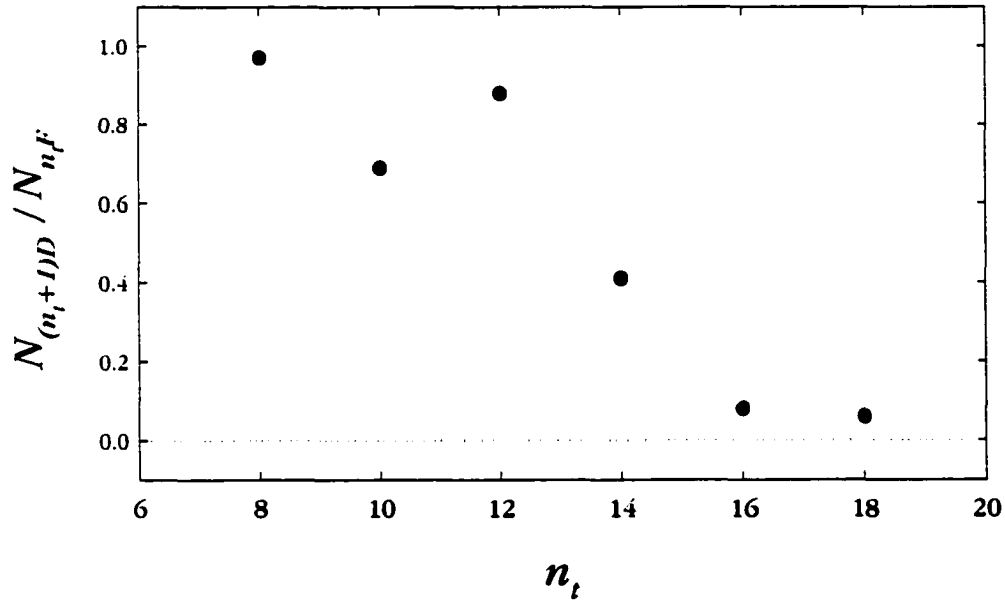

Figure (2.3.7): **Ratio of the $(n_t+1)D$ population to the n_tF state population.** This figure shows the strong decrease of the population in the $(n_t+1)D$ state relative to the n_tF state population as the target state increases.

target n increases this ratio decreases rapidly as can be seen in Fig. 2.3.8. At most, the excitation of the $n_tF_{5/2}$ state is expected to be 1/15 of the excitation of the $n_tF_{7/2}$ state (see Fig. 2.3.4). Thus, even if both the states were efficiently transferred to the $(n_t+1)D_{5/2,3/2}$ state by the maser transition, the relative strength of the fluorescence to $5P_{3/2}$ and $5P_{1/2}$ would not fall below 15. However, for $n_t=16$ and 18 targets, this

ratio is less than 15. This suggests a process other than a radiative process is populating these states, or mixing the n_tF fine structure. Two possible mechanisms are collisions or stray fields.

Most of the other lines visible in the fluorescence spectrum of the $14F$ target are

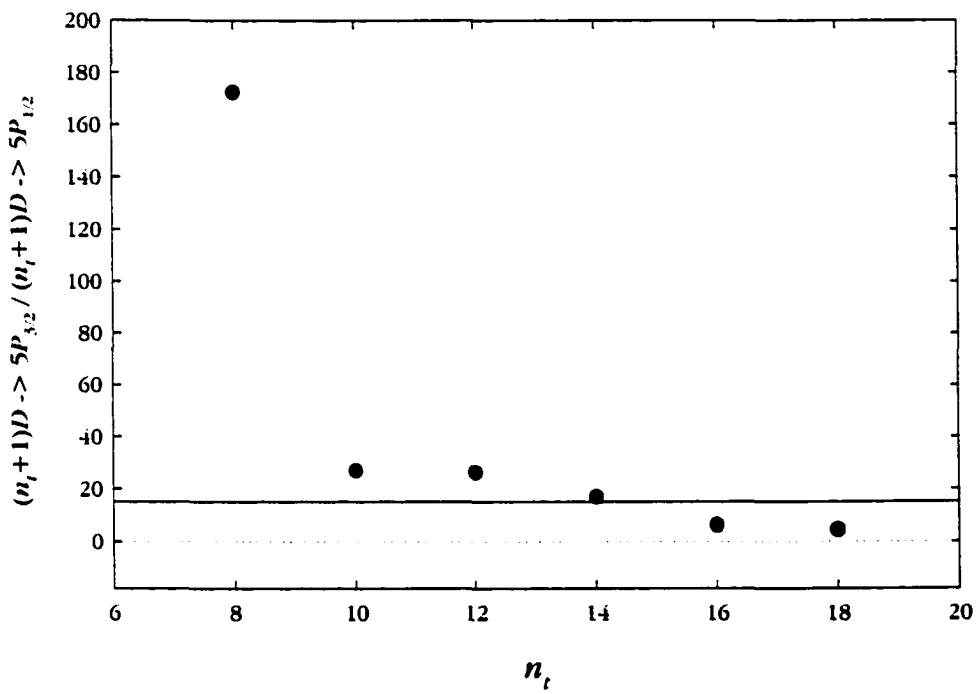

Figure (2.3.8): **Ratio of the $(n_t+1)D$ to $5P_{3/2}$ transition to the $(n_t+1)D$ to $5P_{1/2}$ transition amplitudes.** As can be seen the ratio of these transitions decreases rapidly as the target increases. The solid horizontal line indicates a ratio of 15, the minimum possible ratio if the $(n_t+1)D$ state is populated only through radiative processes from the n_tF state.

decays of nD to nP levels populated in the non-cycling decay of the $14F$ state and these are expanded in the middle panel of the figure. The presence of nD to $nP_{1/2}$ states indicates the presence of some population in the $n_tF_{5/2}$ state although the relative size of the fluorescence shows there is much less population in this decay

path than the desired path, about a factor of 6 between the two $6D$-$5P$ transitions. However, this is more than is expected from the relative strengths of the exciting transitions, which predict no more than 1/15. This again suggests that a process other than direct excitation may be contributing to the population of the "wrong" fine structure states. The spectra do not give any direct information about how well the hyperfine state is controlled but because the separations are smaller than the fine structure, it is likely that some excitation occurs to hyperfine states not on the desired excitation path.

One of the most important things to notice in the $14F$ spectrum for this experiment is the lack of any transition at 302.84 nm, which is the wavelength of the $16P$ to $5S$ transition. This region is expanded for close inspection in Fig. 2.3.6 in the bottom panel. This indicates that further population sharing to the $16P$ state does not occur for this target. Only the $8F$ target spectrum, see Appendix A, shows any fluorescence at the wavelength of the $(n_t+2)P$ state decay. This spectrum shows a peak at 315.7 nm consistent with a $10P$ to $5S$ transition (315.84 nm). However this peak is only 1/200th the size of the $9D$ fluorescence peak, combining this with the difference in lifetimes the population in the $10P$ state is a factor of 300 smaller than the $9D$ population. This means that none of the targets show a significant population in the $(n_t+2)P$ state. With the large $(n_t+1)D$ population from the sharing with the n_tF state it was expected that population might be further shared into the $(n_t+2)P$ state, but this is clearly not seen in the spectra. It is not currently understood why there is no population sharing into the $(n_t+2)P$ state as might be expected from theory[17]. All of the target spectra measured are shown in

Appendix A with the lines identified.

All of these observations lead to the conclusion that the target state, while being a mix of different fine and hyperfine states, is well defined in energy. The population in the nD states to which decay occurs is much smaller than the population in the n_tF and $(n_t + 1)D$ state, which have by far the majority of the highly excited population in the target. In particular the nD states populated by cascades and the population sharing with the $(n_t + 2)P$ state are not significant to the target population.

Two states which are populated significantly are the $5P_{3/2}$ and the $4D_{5/2}$ state, which are on the desired excitation path. The capture cross section of these states is generally much lower than that from the excited states. For example, C^{3+} at $v = 0.100$ a.u. has capture cross sections of $6.6\text{x}10^{-14}$ cm^2 and $1.1\text{x}10^{-13}$ cm^2 for the $5P_{3/2}$ and $4D_{5/2}$ states respectively. These cross sections are about two orders of magnitude smaller than a typical capture cross section of the excited state, $1.3\text{x}10^{-11}$ cm^2 for $n_t = 10$. These relatively small cross sections mean the capture from these lower states are generally insignificant to the total capture. However, in cases where the capture cross sections from the final excited state are small, or where the excited state population is small compared to the lower states population these states might need to be considered. This question will be considered in detail in chapter three in the analysis of the measurement.

2.3.4 Other target considerations

There are a couple of other parameters of the target which are only peripherally related to the considerations discussed above. One of these is the target thickness

and how it varies with the target state selected. Another is the stability of the target and what was done to correct for variations in the target thickness during the measurement. This is of some importance because the measurement of the signal and the charge transfer beam are made one after the other rather than at the same time, and any fluctuations it the target during the measurement could affect their ratio, the quantity we are measuring.

The density of a particular target can be estimated one of two different ways. The first way estimates the density by using the measured charge transfer beam, the total primary ion beam, and the calculated total CTMC cross sections using the standard formula for calculating cross sections,

$$I = I_0\left(1 - e^{-\sigma \rho l}\right) \tag{2.3.4}$$

where I is the charge transfer current, I_0 is the primary ion beam current, σ is the capture cross section, ρ is the target density, and l is the length of the target. The second method for estimating the relative target density is by measuring the blue fluorescence and using the tabulated values for the decay rate from the $(n_t+1)D$ state to the $5P$ state.

Figure 2.3.10 shows the calculation of the relative target density based on both methods for a He^+ primary ion beam in panel (a) and for C^{4+} primary ion beam in panel (b). Also shown is the relative target density from only the capture beam current for a C^{3+} primary ion beam in panel (c). As can be seen in the figure for both ions and methods of calculation the pattern is generally the same, the target density increases rapidly from n_t = 7 to 9 and then remains relatively constant.

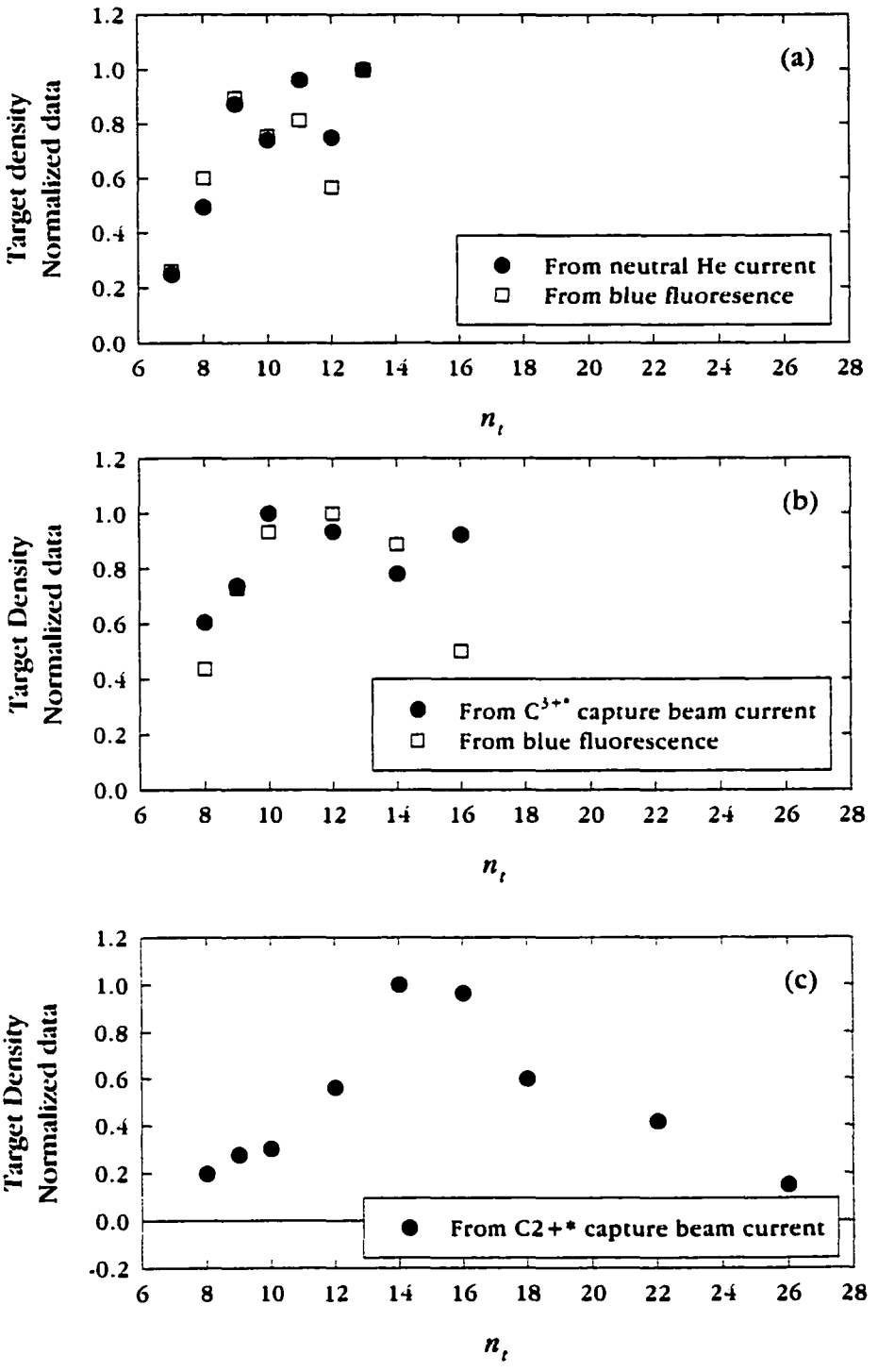

Figure (2.3.9) : **Target density measurements.** This shows the target density measurements calculated from the capture beam current and the blue fluorescence for He^{+} and C^{4+} primary ion beams.

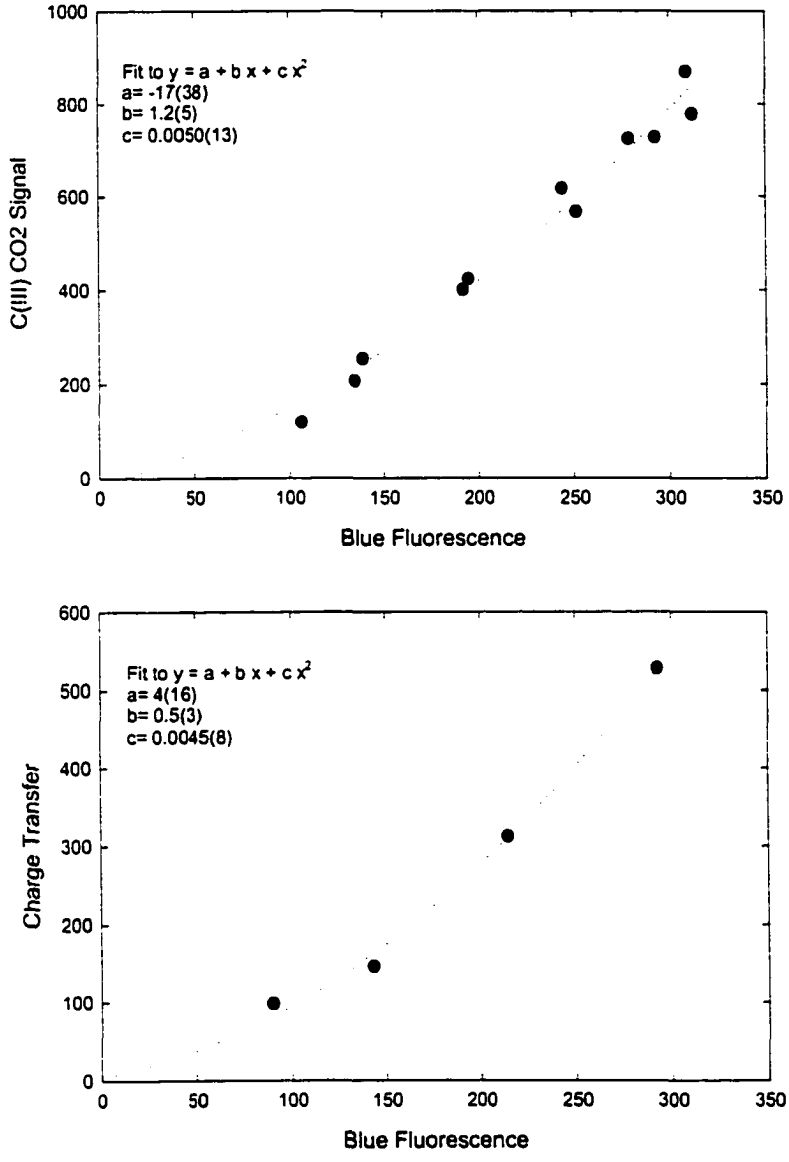

Figure (2.3.10) : **Dependance of the signal and charge transfer beams on the blue fluorescence of target.** This shows the linearity of the signal and charge transfer with the target density as measured by the blue fluorescence.

However in panel (c) we can see that for higher target states the target density decreases rather rapidly. This decrease in target density at the highest targets is important because of the relative populations of the n_t target population to the lower state in the excitation path, this will be discussed in detail in chapter three when the measurement is analyzed in detail.

The target stability is another area of concern for the experiment. The charge transfer and the signal beams are not being measured at the same time, and thus the stability of the target over the small amount of time needed to change between the two beams is critical to this method of measurement. The short term stability of the target is made possible partly through the frequency locking of the three excitation lasers described above in section 2.3.2. Since only the decaying $(n_t+1)D$ state of the target produces any blue light this fluorescence is completely dependant on the lasers being tuned to the target excitation frequencies. By locking the lasers in this manner and carefully monitoring and recording the amount of blue fluorescence of the target the stability of the target is monitored. The stability with the locks is quite sufficient over the small amount of time it takes to make a single measurement of the signal and charge transfer beams, typically five minutes or less. Only small fluctuations in the target blue fluorescence are measured over each signal and charge transfer measurement. The effects of these small fluctuations were reduced by normalizing all of the signals to the blue fluorescence level at the time the signal was measured. This procedure reduced the apparent scatter in the data caused by the small fluctuations in the target strength. A linear normalization of the data was chosen based on the measurements shown in Fig. 2.3.10 showing the relationship

between the signal and charge transfer versus the blue fluorescence of the target. For this data the Ti:Sapphire laser had various attenuators placed in the path before the fiber launchers giving a range laser power for the final excitation without changing the tuning of the laser. As can be seen it is nearly linear over the entire range of the data and since the corrections made in the data set are only for small fluctuations of the blue fluorescence, a linear correction should be quite adequate to correct these fluctuations.

2.3.5 Conclusions

The Rydberg target fulfills all of the requirements necessary to perform this experiment. It is very dense and produces a substantial charge transfer beam making the signal detection easier. It is stable on the time scale of the individual measurements and can be corrected for any small fluctuations within a measurement. The target state is well defined in binding energy. Finally, and perhaps most important to this experiment the Rydberg target can be tuned over a wide range of binding energies, allowing the examination of the capture population as a function of the target energy using a fixed final state energy.

2.4 Repeller

2.4.1 Introduction

After the Rydberg target, the beams enter a device we call the repeller, which serves a dual purpose. Its first function is to block, or repel, the primary ion beam, while transporting the charge transfer beam to the detector. Its second function is to reduce the background by ionizing states near the upper state of the laser

excitation. In previous experiments by our group these functions were relatively easy to accomplish because the charge transfer beam was neutral. The background was ionized in an electric field which could be set at an arbitrary value and the primary ion beam was simply deflected away. To perform these functions when the charge transfer beam is charged poses a significant design challenge. Additionally, this experiment requires that the repeller does not significantly change the population of the n-state being measured. Thus the field in the repeller must be chosen so that it does not mix the population of the$n$-state being probed with other n-states. This section describes our current solution to these challenges, and describes the theory used to determine the effect of the applied fields on the beams.

2.4.2 Ion optics and primary ion beam removal

The primary ion beam is several orders of magnitude larger than the charge

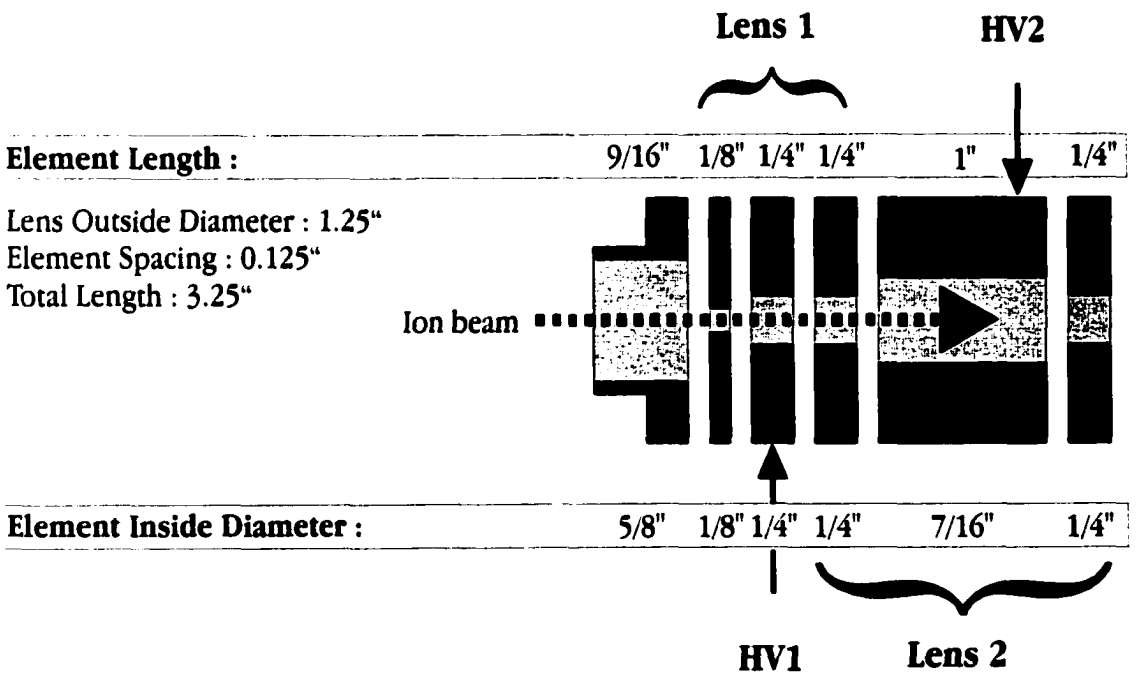

Figure (2.4.1):**Schematic of the repeller.** The repeller has the dimensions as shown in the figure. All of the elements are grounded except for HV1 and HV2. These are the two lens high voltages.

capture population of a particular state. Thus to make it easier to obtain a reasonable signal to noise for the measurement it is a high priority to prevent the primary ion beam from entering the detector. To optimize the signal to noise the repeller must reduce the primary ion beam as much as possible without sacrificing a significant amount of the charge transfer beam. This is the primary design goal of the repeller.

After the target the charge transfer beam and the primary ion beam have

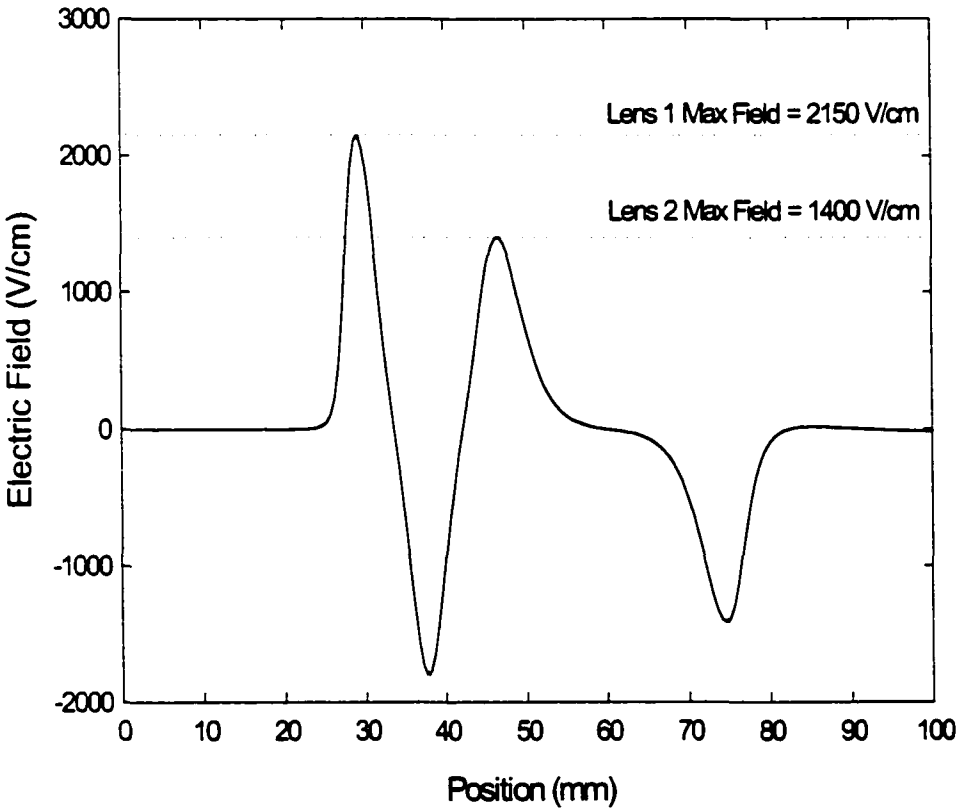

Figure (2.4.2) : **Field profile of the repeller:** This shows the field as a function of position in the repeller when both lens elements are set at 1000 V. The maximum field for Lens 1 gives an effective distance of 4.65 mm. The maximum field for Lens 2 gives an effective distance of 7.14 mm.

essentially the same total kinetic energy but differ in charge. Thus electrostatic focusing elements will affect the two beams differently, and it is possible to separate the two beams. The lenses affect the primary ion beam more strongly than the charge transfer beam because it has a smaller energy per charge. The simplest way to remove the primary ion beam is to set the voltage on one of the lenses higher than the energy per charge of the primary ion beam thus blocking its passage, "repelling" it. The charge transfer beam having a higher energy per charge passes through the lens element, though it may be focused in the process. In this way the ion optics of the repeller can be used to block the primary ion beam and transmit the charge transfer beam. However, the design and implementation of the electrostatic ion optics of the repeller are critical to how well the repeller performs its intended functions. Following the repeller is a pair of x-y deflection plates to correct for any deflection of the beam by the lenses of the repeller.

The device we used as a repeller is manufactured as a deceleration element by Colutron Corporation (PN#400-L). We rewired this device to function as a double einzel lens with a common central grounded element. The geometry and electrical connections of this device are shown in Fig. 2.4.1. A plot of the electric fields in the repeller calculated using SIMION, a standard computer software package for analyzing electrostatic devices, is shown in Fig. 2.4.2. The maximum field for each of the lenses allows the calculation of the effective distance for each lens, defined by:

$$d_{eff} = \frac{V}{E_{Max}} \qquad (2.4.1)$$

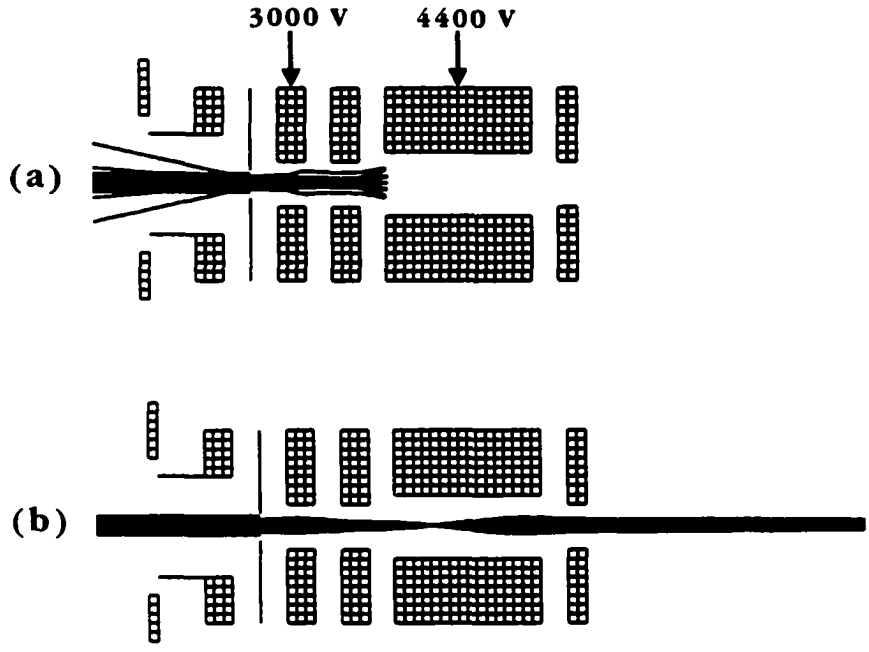

Figure (2.4.3): **SIMION simulation of low charge ion beams in the repeller.** The passage of an Ar^{3+} primary ion beam (a) and an Ar^{2+} charge transfer ion beam (b) through the repeller is shown above. Both beams have an energy of 10 keV. The primary ion beam is completely blocked. The charge transfer beam is well focused on the detector entrance off the page to the right.

where E_{max} is the maximum field generated by the lens and V is the voltage applied to the lens. The effective distance is 4.65 mm for Lens 1 and 7.14 mm for Lens 2. The maximum slew rate, the rate at which the electric field changes with time, can also be calculated for the repeller using the distance between the positions where the field is 10% and 90% of the maximum field, the straight portion of the curve. We will define this distance as d_{slew}, and using 80% of the maximum electric field, and the velocity of the primary ion beam, v, this gives a maximum slew rate of,

$$S_{Max} = \frac{0.8\left(\frac{V}{d_{eff}}\right)}{\left(\frac{d_{Slew}}{v}\right)} \qquad (2.4.2)$$

where d_{Slew} is 2.0 mm for this geometry.The repeller's effect on ion trajectories was evaluated using SIMION [25]. A simulation of the operation of the repeller for an Ar^{3+} primary ion beam with a total energy of 10 keV is shown in Fig. 2.4.3. The voltages for the lens elements were adjusted in the simulation to maximize the transmission of the charge transfer beam to the detector. Panel (a), a simulation of the primary ion beam, shows that the repeller completely blocks it at the second

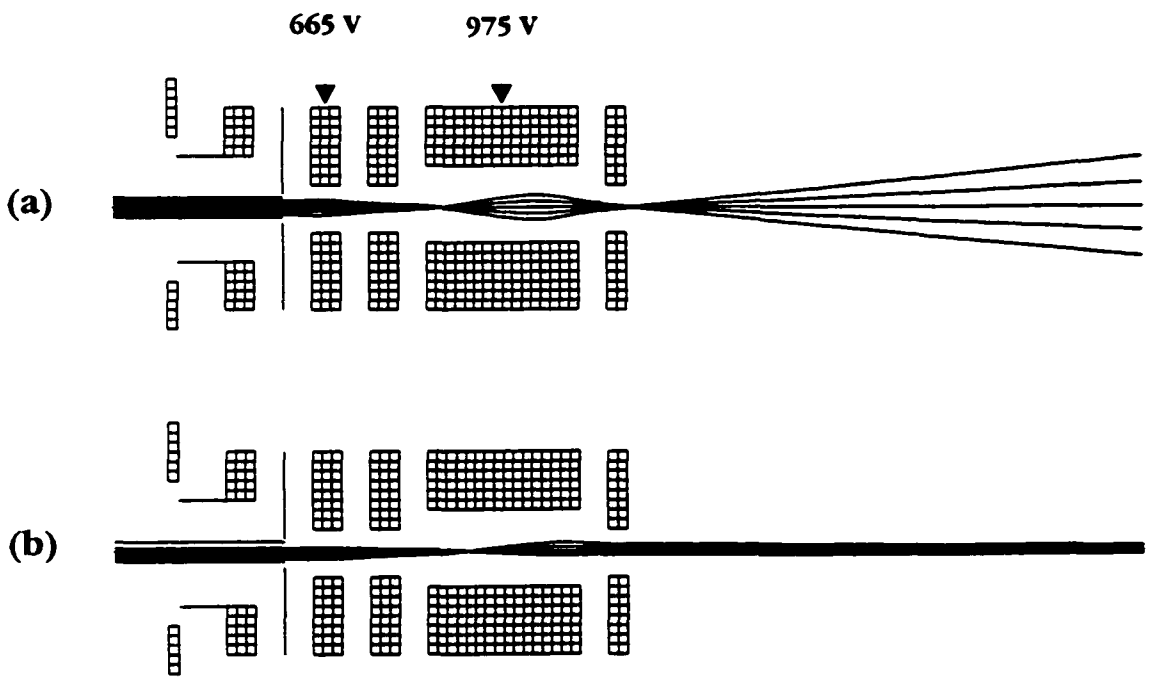

Figure (2.4.4) : **SIMION simulation of high charge ion beams in the repeller.** The passage of an Ar^{10+} primary ion beam (a) and an Ar^{9+} charge transfer ion beam (b) through the repeller is shown above. Both beams have an energy of 10 keV. The primary ion beam is not completely blocked but is strongly defocused. The charge transfer ion beam is well-focused on the detector entrance off the page to the right.

lens. The voltage of the second lens, 4400 V, is larger than the energy per charge of the primary ion beam, 3333 V, thus it is expected that the beam will be blocked and the simulation verifies this. The first lens voltage, 3000 V, is then chosen to focus the charge transfer beam to a spot at the detector entrance. The simulation of the charge transfer beam shown in panel (b) of Fig. 2.4.3 shows this.

For higher charges, the optimum settings for transmission of the charge transfer beam no longer completely blocks the primary ion beam, but instead defocuses it strongly. This can be seen in Fig. 2.4.4, which shows a simulation of an Ar^{10+} primary ion beam with a total energy of 10 keV. At the optimum voltages the primary ion beam diverges rapidly after the repeller (a), while the charge transfer beam is well focused at the detector entrance (b).

The voltages needed to maximize the transmission of the charge transfer beam were found experimentally for a range of charge states and velocities. These values for the voltages agree well with simulations done with SIMION. Using the results of these measurements and simulations the following rules of thumb for the two repeller lens voltages were found,

$$V_{Lens1} = 0.60\frac{KE}{q-1} \tag{2.4.3}$$

$$V_{Lens2} = 0.82\frac{KE}{q-1} \tag{2.4.4}$$

where KE is the total kinetic energy of the beam in eV and q is the charge of the primary ion beam.

The comparison between these rules of thumb and the experimental voltages for

maximum charge transfer transmission versus charge for various ions and velocities are shown in Fig. 2.4.5. The values of the voltages for the experimental settings for maximum charge transfer beam transmission are given in Table 2.4.1 along with the ions used for each measurement. As can be seen in the figure the rules of thumb for the lens voltages agree well with the experimental settings for a wide range of charges and energies. Thus, these rules of thumb give a very good starting point for finding the optimum repeller voltages for a particular beam.

For the lower charge states, another method of operation of the same device was sometimes used to reduce the electric field applied to the beam. In this mode of operation the voltage applied to the first lens is negative rather than positive. This reduces the focusing strength of the lens and at its optimum settings reduces

Table 2.4.1: **Experimental and rule of thumb settings of the repeller.** This table shows the experimental settings for the maximum charge transfer beam compared to the values of the lens potentials determined by the empirical, or "rule of thumb" formulas for the repeller.

		Experimental Value		Rule of thumb	
Ion	KE	V_{Lens1}	V_{Lens2}	V_{Lens1}	V_{Lens2}
Ar^{5+}	10000	1100	2180	1500	2050
Ar^{7+}	10000	1100	1340	1000	1367
Ar^{9+}	10000	700	1060	667	911
Ar^{11+}	10000	600	813	600	820
Ar^{5+}	4545	700	918	545	745
C^{4+}	3250	681	875	650	888
Ne^{6+}	5500	657	912	660	902
Ar^{8+}	10000	996	1107	857	1171

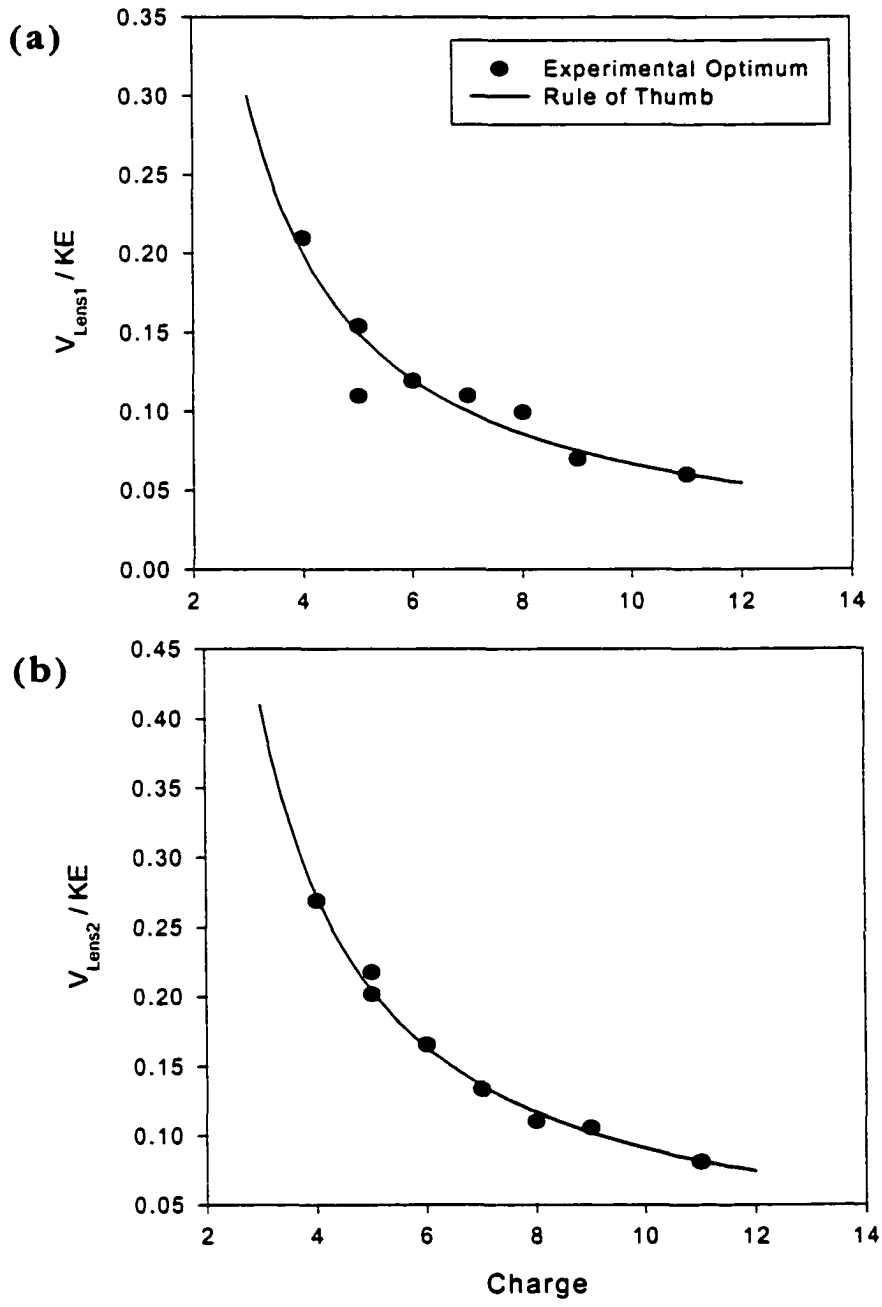

Figure (2.4.5) : **Plot of operating and rule of thumb voltages for the repeller.** These plots show the rule of thumb voltages as solid curves for (a) lens 1 and (b) lens 2. The optimal settings were determined experimentally and are shown as solid points. The voltages were divided by the KE of the beam to compare different ions and velocities. The rule of thumb and the experimental values are in reasonable agreement for the points shown.

the electric field applied to the beam. This mode of operation doesn't completely fulfill the primary design objective of blocking the primary ion beam. It does however reduce the amount of the primary ion beam entering the detector by defocusing it to a large spot size at the detector entrance. A simulation of the operation of the repeller using this method is shown in Fig. 2.4.6. In panel (a) the focusing of a C^{3+} primary ion beam of energy 3250 eV is shown at the optimum settings using a negative voltage on the first lens element. The primary ion beam is weakly focused by the first lens, and then more strongly focused by the second lens resulting in a focal point well before the detector entrance. In panel (b) of Fig. 2.4.6 the focusing of the charge transfer beam, C^{2+}, at the same energy as the primary ion beam is shown. Both lens elements act on the charge transfer beam to gently focus it to a spot at the entrance of the detector.

Experimental data for the settings of the repeller for maximum transmission of the charge transfer beam were taken and the following rules of thumb for the lens voltages were found from that data,

$$V_{Lens1} = -0.25\frac{KE}{q-1} \tag{2.4.5}$$

$$V_{Lens2} = 0.17\frac{KE}{q\text{-}1} \tag{2.4.6}$$

where KE is the total kinetic energy of the beam in eV. The degree of agreement between the experimental and the rule of thumb values for the voltages for this mode of operation was comparable to that in Fig. 2.4.5. The effective distances in

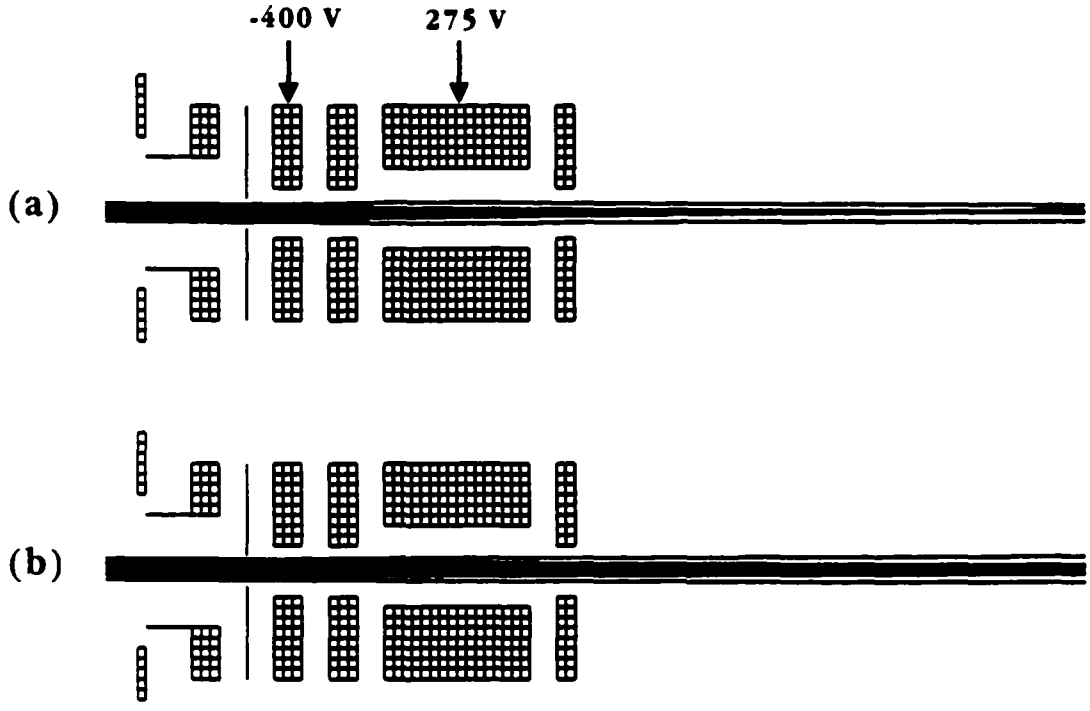

Figure (2.4.6): **SIMION simulation of ion beams in the repeller using a negative potential on the first lens.** The passage of a C^{3+} primary ion beam (a) and a C^{2+} charge transfer ion beam (b) through the repeller is shown above. Both beams have an energy of 3250 eV. Note the repeller does not stop the primary ion beam using this configuration of voltages on the repeller, but instead defocuses it at the detector entrance reducing the amount entering the detector.

the repeller are the same as before since only the voltages applied were changed not the geometry. Thus significantly lower fields are applied to the beam since the voltages applied are much lower than the first method of operation. At high charge, $q > 4$, the operation of the repeller in this manner fails to sufficiently reduce the primary ion beam and the background in the detector.

The removal of the primary beam is not difficult for a wide range of charges and

velocities. The rules of thumb found in this section appear to work over the entire range of ion charges and velocities used in this experiment and there is no obvious reason why they should fail to extend beyond the ranges in this experiment. However, the removal of the primary ion beam is just one of the two functions of the repeller and the second function, removal of the background, complicates the design considerably. Requiring the lower state of the laser transition to remain unmixed, also creates significant problems as will be discussed in detail below.

2.4.3 Background removal by the repeller

Before we can examine the removal of background by the repeller we need to briefly discuss Stark ionization. It is often assumed that Stark ionization of a Rydberg state of a given n occurs at a unique electric field. A more detailed consideration (see Appendix B) concludes that there are a wide range of fields at which Stark ionization can occur, even for states of the same principal quantum number n. The precise ionization field depends on the additional quantum numbers of the state (l, m) or (n_1, n_2, m) and the rate at which the field turns-on, or the slew rate of the ionizing field. For "rapid" entry the ionization is "diabatic" and for a given n state occurs over the range of fields,

$$\frac{1}{9}\frac{e}{a_o}\frac{q^3}{n^4} \le F_{Ionization}^{Diabatic} \le \frac{2}{9}\frac{e}{a_o}\frac{q^3}{n^4} \tag{2.4.7}$$

For "slow" entry into the field, ionization occurs "adiabatically" at

$$F_{Ionization}^{Adiabatic} \approx \frac{1}{16}\frac{e}{a_o}\frac{q^3}{n^4}. \tag{2.4.8}$$

The critical slew rate determines whether the entry to the field is "rapid" or "slow" for high l ($l \geq 3$) this rate is approximately,

$$S_{Crit} \cong \frac{1}{40}\alpha_d^2 \frac{q^9}{n^{10}l^{10}} \ (a.u.) \qquad (2.4.9)$$

for ionization of a single Rydberg electron outside a core ion of charge q and dipole polarizability α_d. Table 2.4.2 shows a sample of the ions and transitions used for this measurement. The ionization of the upper state of the laser transition is expected to be nearly completely diabatic for all these ions.

Table 2.4.2 : **Critical slew rates of various ions.** Slew rates and Critical Slew rates for the upper states of the laser transition for various ions. S_{Crit} is calculated for the upper state of the laser transition, n_u, for l=3 (lower l's are not well approximated by Eqn. 2.4.9).

Ion	α_s	n_u	v (cm s^{-1})	F_R	S_{Crit} (Vcm^{-1}s^{-1})	S_R (Vcm^{-1}s^{-1})
C II	3.56	51	2.19x10^7	1482	4.9x10^6	1.1x10^{11}
C III	4	100	1.77x10^7	2142	2.8x10^5	1.5x10^{11}
C III	4	71	2.19x10^7	1254	8.7x10^6	1.3x10^{11}
C III	4	71	2.85x10^7	1422	8.7x10^6	1.6x10^{11}
C IV	0.009	85	2.19x10^7	1434	9.7x10^1	1.2x10^{11}
Ne VI	0.428	133	2.19x10^7	1419	9.6x10^4	1.2x10^{11}
Ar VIII	0.062	161	2.19x10^7	2189	4.0x10^3	1.9x10^{11}
Ar XI	0.019	200	2.19x10^7	1290	7.5x10^2	1.1x10^{11}
Ar III	3.52	100	1.01x10^7	1387	2.2x10^5	5.6x10^{10}
Ar III	3.52	71	1.23x10^7	1254	6.7x10^6	6.2x10^{10}
Xe III	10.25	71	6.79x10^6	873	5.7x10^7	2.4x10^{10}

If we assume diabatic ionization we can model the effect of the repeller on the

background rate in the detector that arises from population in states near the upper state of the laser transition. To understand this, we must first briefly consider the operation of the detector. As discussed in Chapter 1, the detector contains an electrode held at potential "V_D" between two grounded electrodes. The ratio of the separations between the plates is 3 to 1. The separation between the first and center plate is the larger of the two separations and is referred to as the long gap, and the second smaller separation is referred to as the short gap. Any Rydberg states which Stark ionize at a field of,

$$F_{Long} = \frac{V_D}{3a} \tag{2.4.10}$$

where V_D is the voltage on the center plate of the Stark ionizer and a is the distance of the smaller separation, will ionize as soon as they enter the long gap where the potential is approximately zero. These ions will leave the ionizer at about the same speed at which they entered. On the other hand, Rydberg states which ionize only at the higher field,

$$F_{Short} = \frac{V_D}{a} \tag{2.4.11}$$

will ionize as soon as they enter the short gap. There the potential is $\pm V_S$ and when these ions leave the ionizer their kinetic energy will be increased or decreased by,

$$\Delta KE = qV_D \tag{2.4.12}$$

and this different speed distinguishes them from other ions that may remain after the repeller, or which have been formed by other processes. All such ions with this speed and charge are collected as "signal".

The Stark ionizer in the detector will ionize and detect any Rydberg state which is, (a) not ionized at field of $V_D/3a$ and (b) is ionized at a field of V_D/a. There is a range of principal quantum numbers or binding energies that satisfy this criterion. For simplicity we will assume that the probability of ionizing a Rydberg state with principal quantum number n and binding energy E_B is:

$$\begin{aligned} P(|E_B|,F) &= 0 \qquad \text{if} \quad |E_B| \geq F_0 \\ P(|E_B|,F) &= 1 \qquad \text{if} \quad |E_B| \leq \frac{F_0}{\sqrt{2}} \\ P(|E_B|,F) &= 3.414\left[1-\frac{|E_B|}{F_0}\right] \qquad \text{otherwise} \end{aligned} \tag{2.4.13}$$

where F_0 is defined as,

$$F_0 \equiv 3\sqrt{qF(\text{a.u.})}\cdot R_\infty \tag{2.4.14}$$

and R_∞ is the Rydberg and an a.u. of electric field is $5.142\text{x}10^9$ V cm^{-1}. This ionization probability is shown as a function of E_B in Fig. 2.4.7.

Thus, the probability of detecting a Rydberg state of binding energy $|E_B|$ as a "signal" ion in the detector is,

$$P_{Detect}(|E_B|) = \left[1-P\left(|E_b|,\frac{V_D}{3a}\right)\right]\left[P\left(E_B,\frac{V_D}{a}\right)\right] \tag{2.4.15}$$

which is the probability of ionizing in the short gap, and not in the long gap. Figure 2.4.8(a) shows $P_{Detect}(|E_B|)$ for V_D/a=1214 V/cm, which is the field used in this experiment to detect the C III 29-71 transition. This figure also shows the C III capture population distribution expected as a dotted curve, for a C^{3+} primary ion beam at v = 0.100 a.u. incident on a 12F Rydberg target. Clearly there is some

overlap between the states that are expected to be populated and those that will be detected. This gives rise to a background signal in the detector even in the absence of CO_2 laser excitation of the 29-71 transition.

In order to reduce that background the repeller applies a field,

$$F_R = \frac{V_R}{d_{eff}}. \tag{2.4.16}$$

Using the same simplified model of diabatic ionization the states not ionizing in the

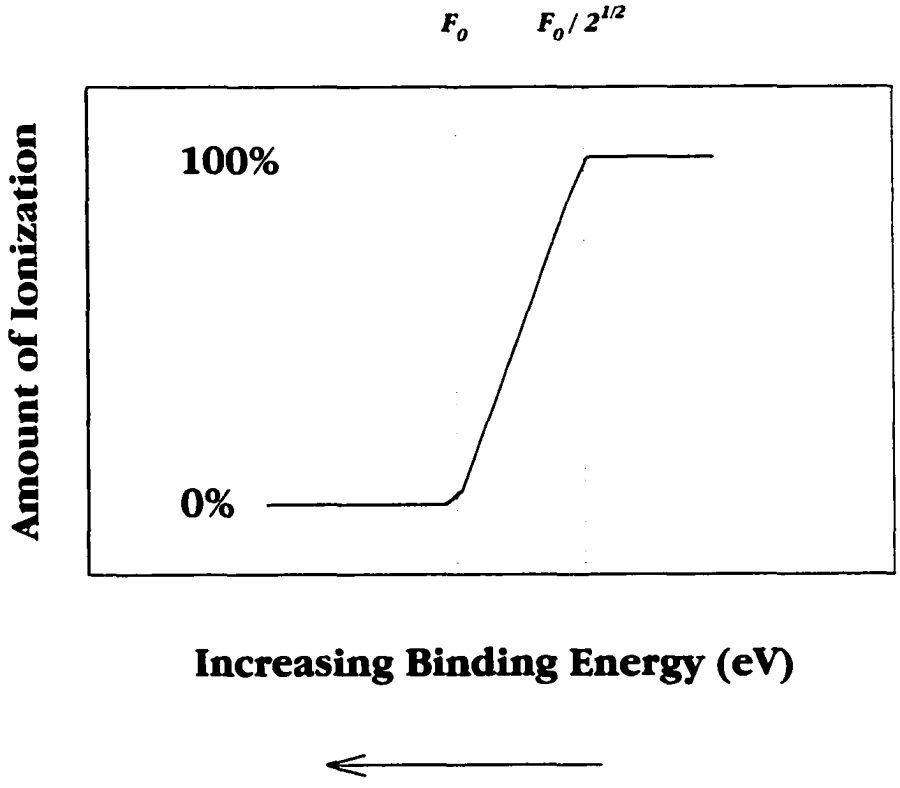

Figure (2.4.7) : **Model of ionization.** This figure shows the simple function $P(|E_B|,F)$ given in Eqn. 2.4.13 used to model the ionization probability of a Rydberg state. The two vertical lines indicate the electric fields where the model begins ionizing the state and completely ionizes the state being examined. The field is described by F_0, defined in Eqn. 2.4.14.

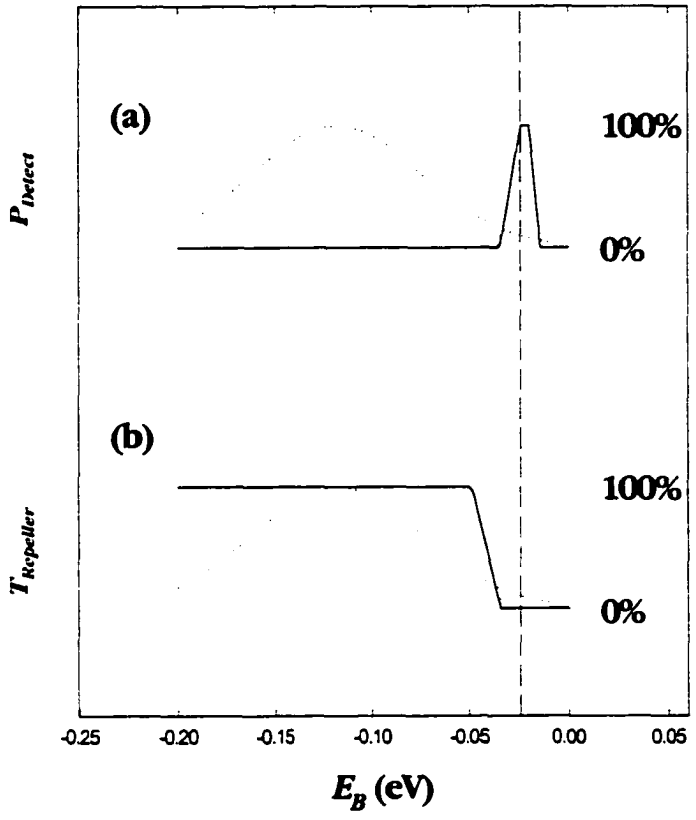

Figure (2.4.8) : **Model of ionization in repeller and detector.** This figure shows a specific example of the ionization model described in the text. The solid line shown in (a) is $P_{Detect}(E_B)$ for a detector field of 1214 V cm^{-1}, which is sufficient to ionize a C III n = 71 state. The vertical dashed line in the figure indicates the binding energy of this state. The smooth dotted curve is a model of the expected capture population distribution for C^{3+} v = 0.100 a.u. incident on a 12F target. The portion of the curve under the detection "window" is the background with no repeller ionization. The solid line shown in (b) is the probability of transmission through the repeller when the field set to is twice that in the detector (2428 V cm^{-1} in this case). The dotted vertical line is present to make visual alignment of the two curves easier. Clearly for this setting of the repeller the model predicts that the background is completely eliminated.

repeller, which are transmitted to the detector, would be expected to vary with binding energy E_B according to,

$$T_{\text{Repeller}} = \left[1 - P\left(|E_B|, \frac{V_R}{d_{eff}}\right)\right] \tag{2.4.17}$$

This curve is shown in Fig. 2.4.8(b), taking

$$\frac{V_R}{d_{eff}} = 2\frac{V_D}{a} \tag{2.4.18}$$

The dotted vertical line in the figure is only present to make visual alignment of the two curves easier. Thus the probability of detecting a state populated prior to the repeller is simply the product of these two probabilities, P_{Detect} and $T_{Repeller}$. For the curves shown it is obvious that this combined probability is zero for fields in the repeller twice as large or larger than the detector field. This means that according to this simple model there should be no background detected. For the more general case where the repeller field is less than twice the detector field there will be background determined by,

$$B = \sum_n N(n) P_{Detect} T_{Repeller} \tag{2.4.19}$$

where $N(n)$ is the amount of population for each product n and is summed over all product states populated. When the n states are very close together, as is the case for the region detected in this experiment this can be approximated by,

$$B \approx \overline{N}(n_u)\frac{A(V_R, V_D)}{\delta E(n_u)} \tag{2.4.20}$$

where $A(V_R,V_D)$ is the area under the curve,

$$P_{Detect}(E,V_R,V_D)=\left[1-P\left(|E|,\frac{V_R}{d_{eff}}\right)\right]\left[1-P\left(|E|,\frac{V_D}{3a}\right)\right]P\left(|E|,\frac{V_D}{a}\right) \quad (2.4.21)$$

$\delta E(n_u)$ is the energy separation between adjacent states near n_u.

$$\delta E(n_u)=2\frac{q^2}{n_u^3}R_\infty \quad (2.4.22)$$

and $\overline{N}(n_u)$ is the average population per state near n_u. Figure 2.4.9 shows the value of $A(V_R,V_D)$ and predicts a zero background $F_R > 2F_D$. The factor of two is due to the range of fields over which states of common n may ionize. Note however that the rise is quite slow until a ratio of less than one. As an example, consider two cases where the same upper state was studied for several targets for C III 29-71 at υ=0.100 a.u, that are shown in Fig. 2.4.10. The measurement shown is of the background to total charge capture beam ratio.

The model described above predicts that for the two cases measuring the same upper state,

$$\frac{B_A}{B_B}=\frac{A_A}{A_B} \quad (2.4.23)$$

where B_A and B_B are the two background rates and A_A and A_B are the area $A(V_R,V_D)$ for each case. For these two cases the ratio of the two areas is computed to be,

$$\frac{A_A}{A_B}=5.9 \quad (2.4.24)$$

and the measured ratio of the background averaged for all of the target states is,

$$\frac{B_A}{B_B} = 4.5 \qquad (2.4.25)$$

these agree quite well. Additionally Fig. 2.4.10 shows the background to charge transfer ratio for what should be a completely closed window for C II 19-51 at

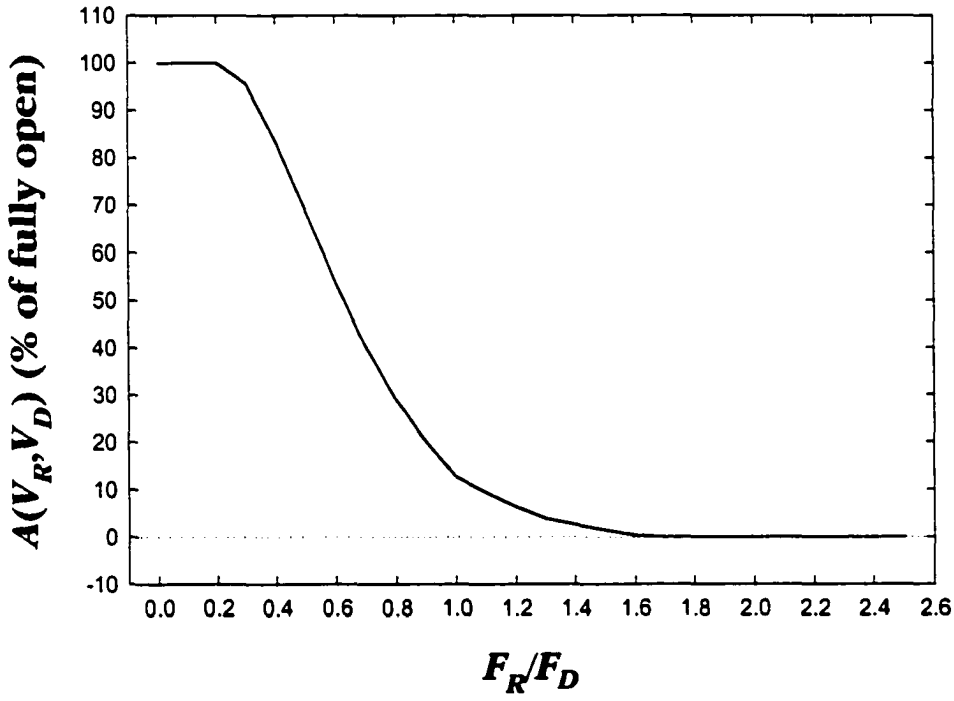

Figure (2.4.9) : **$A(V_R,V_D)$ as a function of the repeller to detector field ratio.** This shows how the area of the open window varies with the ratio of the repeller to detector field. Note the amount of open window does not start to significantly increase until below 1.0 or $F_R=F_D$.

$v=0.100$ a.u. This is quite flat over the entire range of target states for which it was measured. This further supports this window model. When the population from the charge transfer collision moves toward the detection window as the target state

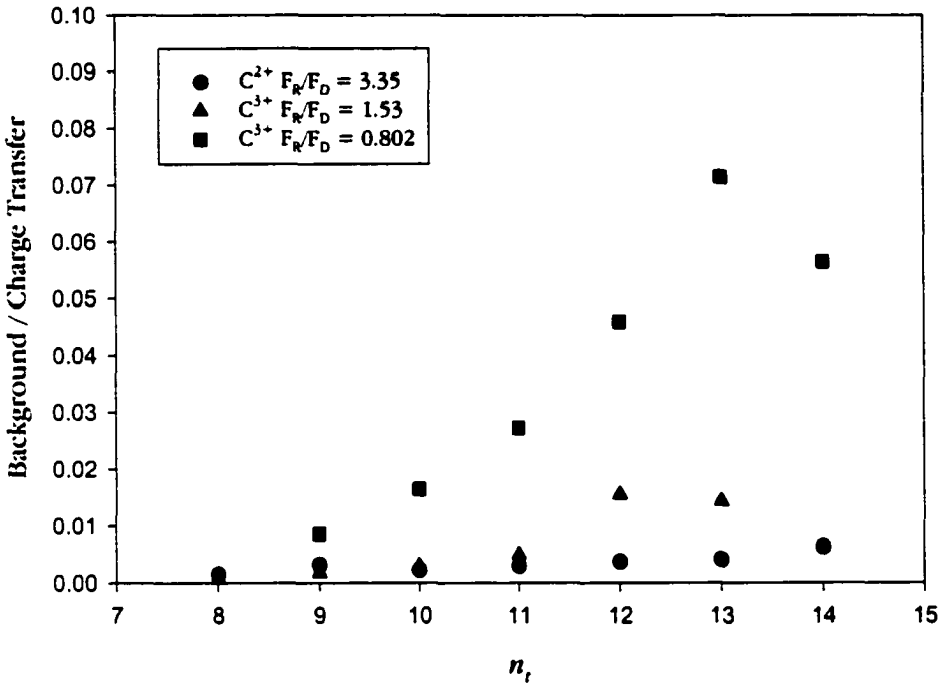

Figure (2.4.10) : **Ratio of background to charge transfer beam.** This shows the variation of the background with target for three different ratios of the repeller and detector fields. Two of these are for the C III 29-71 laser transition. The squares show the ratios for case A in the text and the triangles show the ratios for case B. The third is for the C II 19-51 laser transition and has a window which is completely closed.

increases the background is seen to rise in the two C III cases. However, when the window is closed, as in the case of the C II data, this increase is not seen. There is however a non-zero background seen in the C II data not explained by the model, and not strongly dependant on the target state. The source of this background is not clear but could be from a variety of sources, including a small amount of primary ion beam not fully blocked or separated from the signal, or perhaps repopulation of states near the upper state from lower states through n changing collisions.

2.4.4 Limitation on the field to prevent population mixing

It is important to consider effects of the fields on the populations being measured, because this experiment probes the population of a specific energy state. Of particular interest is what field mixes the measured population with nearby states. By applying a field in the repeller to ionize the background near the upper state of the laser resonance, it is possible to mix the lower state of the resonance with nearby states. The Stark structure of the state being measured along with the slew rate of the field and the critical slew rate, described in the section above on Stark ionization, all play a role in determining whether the population of the state being measured will be mixed with neighboring state's populations.

The field at which it becomes possible for adjacent states to mix is determined by the energy difference between adjacent states. When the extreme blue Stark state of the state being measured and the extreme red Stark state of the level above reach an avoided crossing, in a non-hydrogenic system, there is a possibility that the two states can mix. The energy difference between adjacent levels in a Rydberg ion is given by,

$$\Delta E(n,n+1) = \frac{q^2}{2}\left(\frac{1}{n^2} - \frac{1}{(n+1)^2}\right) \tag{2.4.26}$$

and the separation of an extreme Stark state from the original energy level in a Rydberg ion is given by,

$$\Delta E_{\text{Stark}} = \frac{3Fn(n-1)}{2q} \underset{\text{for high } n}{\approx} \frac{3Fn^2}{2q} \tag{2.4.27}$$

given these two equations for sufficiently high n the field at which adjacent states

will reach an avoided crossing is given by,

$$F_{\text{Mix}} \cong \frac{q^3}{3n^5} \tag{2.4.28}$$

If this field is not exceeded in the repeller, then the population between different n-states will not be exchanged. When this field is exceeded, the populations of the two states might mix, but whether they do depends on the detailed conditions of entry and exit from the field. Specifically whether they mix depends on the slew rate at the time of the crossing and the critical slew rate of the state involved , as defined in Eqn. 2.4.9. If the avoided crossing is passed in both directions entirely adiabatically or diabatically the state is preserved and no mixing between the n-states occurs. Only when the slew rate is near the critical slew rate is there a chance that an n-state will go out on one manifold and come back along a state of a different manifold. This is because near the critical slew rate there is a probability of passing through each avoided crossing differently, adiabatically or diabatically, each time it is crossed.

2.4.5 Combining all repeller functions

At this point we have found two conditions that ideally should be fulfilled by the electric field in the repeller, (a) F_R should be large enough to eliminate the background in detection of the upper state of the laser transition and (b) F_R should be small enough to avoid mixing the lower state of the laser transition.

We will now consider the extent to which both of these conditions can be simultaneously satisfied. First we will determine what limits are set on the upper

and lower states of the laser transition (n_l and n_u) by the requirement that the background be eliminated in the repeller. These limits are expressed in terms of the repeller electric field, F_R. To completely ionize the state n_u in the detector requires that

$$F_D \geq \frac{2}{9}\frac{q^3}{n_u^4} \tag{2.4.29}$$

For the repeller to completely eliminate the background as described in section 2.4.3, the field in the repeller must be twice this large,

$$F_R \geq \frac{4}{9}\frac{q^3}{n_u^4} \tag{2.4.30}$$

or equivalently in terms of the binding energy,

$$\left|E_B(n_u)\right| \leq \frac{3}{4}\sqrt{qF_R} \tag{2.4.31}$$

The lower state of the laser transition, n_l, has a binding energy that is larger than n_u by the approximately constant energy of one CO_2 photon,

$$\left|E_B(n_l)\right| \approx \left|E_B(n_u)\right| + h\nu_{CO_2} \tag{2.4.32}$$

So the requirement on the lower state set by the absence of background is:

$$\left|E_B(n_l)\right| \leq \frac{3}{4}\sqrt{qF_R} + h\nu_{CO_2}(a.u.) \tag{2.4.33}$$

This is illustrated for $q=1$ by the dashed curve in Fig. 2.4.11. The lower state energy must lie above this curve.

The requirement that the field in the repeller is low enough that the Stark levels associated with the $n_l \pm 1$ states do not cross the n_l state is:

$$F_R \leq \frac{1}{3}\frac{q^3}{n_l^5} \tag{2.4.34}$$

or,

$$\left|E_B(n_l)\right| \geq \frac{1}{2}\left[3q^2F_R\right]^{\frac{2}{5}}(a.u.). \tag{2.4.35}$$

This is illustrated for $q=1$ by the solid curve in Fig. 2.4.11. The lower state energy

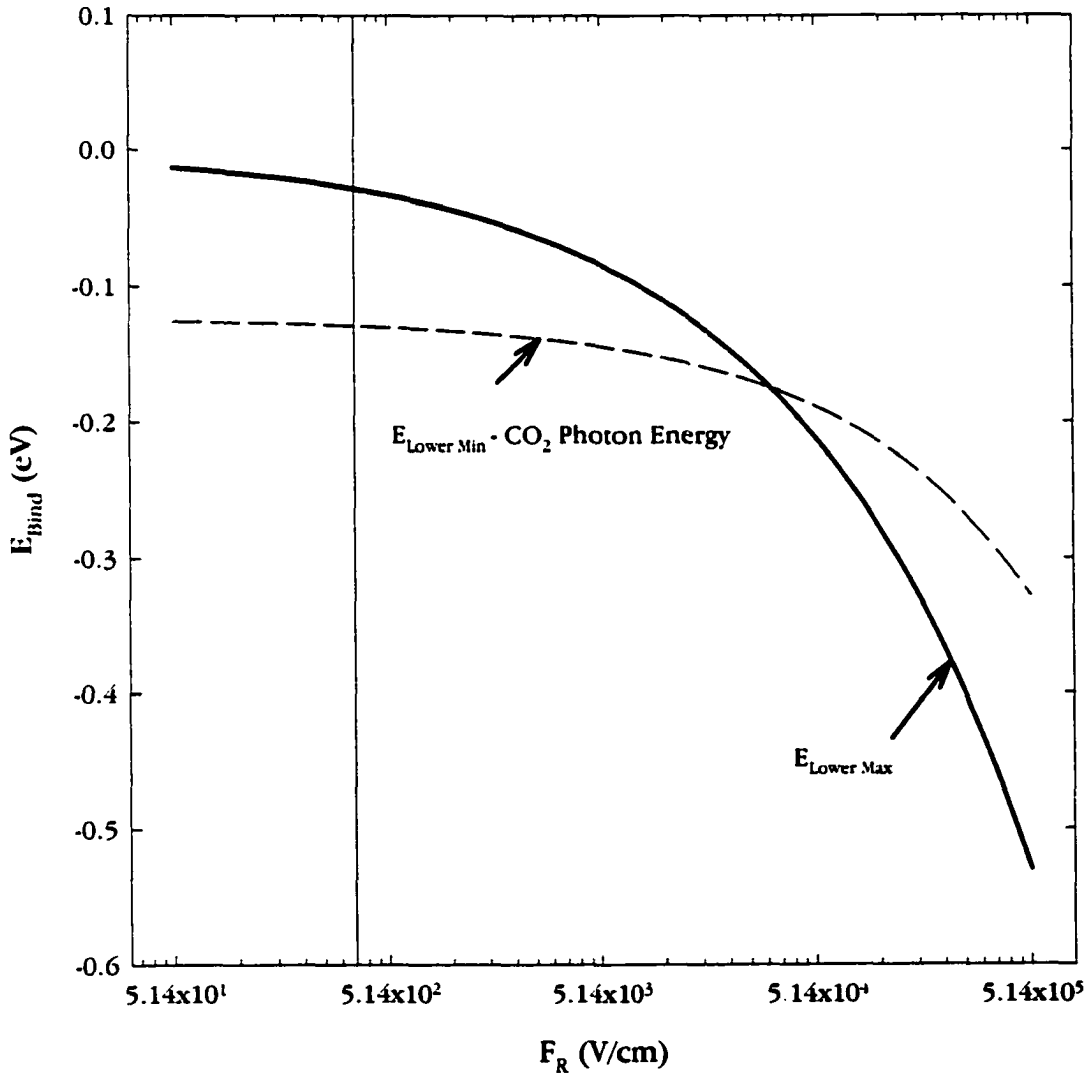

Figure (2.4.11) : **Limits on the usable lower states.** This shows the limits placed on the lower states (for $q=1$) by requiring the background to be removed and the lower state not to be mixed.

must lie below this curve to satisfy this requirement. Clearly there is a maximum value of the repeller field which allows both conditions to be met.

With the existing detector design, there is a minimum value of V_D and hence F_D and F_R, which allows separation of the "signal" ions from residual primary ion beam. The value of this minimum V_D is determined by using $q=1$ measurements for which the highest upper state successfully separated from the residual primary ion beam was an $n=50$ state which could be detected marginally. This gives an optimistic estimate of the minimum detectable upper state binding energy of approximately 0.0054 eV and a minimum F_R of 360 V cm^{-1}. This restriction is represented by the solid vertical line in Fig. 2.4.11. Acceptable conditions are to the right of this line and for this case ($q=1$) there are a wide range of acceptable lower states. The shaded area in Fig. 2.4.11 illustrates the range of lower states which satisfy all of these requirements for $q=1$. An example of an acceptable transition which satisfies all of these requirements is:

$n_l = 10$ to $n_u = 30$

$|E_B| = 0.136$ eV, $F_R = 2821$ V cm^{-1}

For increasing values of q satisfying these conditions become progressively more difficult.

Fig. 2.4.12 (a)-(d) shows the same curves as Fig. 2.4.11 but for $q=1$, 3, 6, and 10. The shaded area again represents the range of lower states which satisfy all of the described requirements for each q. By $q=7$ there are no states that satisfy all of the requirements. This is the case in Fig. 2.4.12 (d), which shows the curves described for q=10. With these restrictions in place it is not possible with CO_2 laser

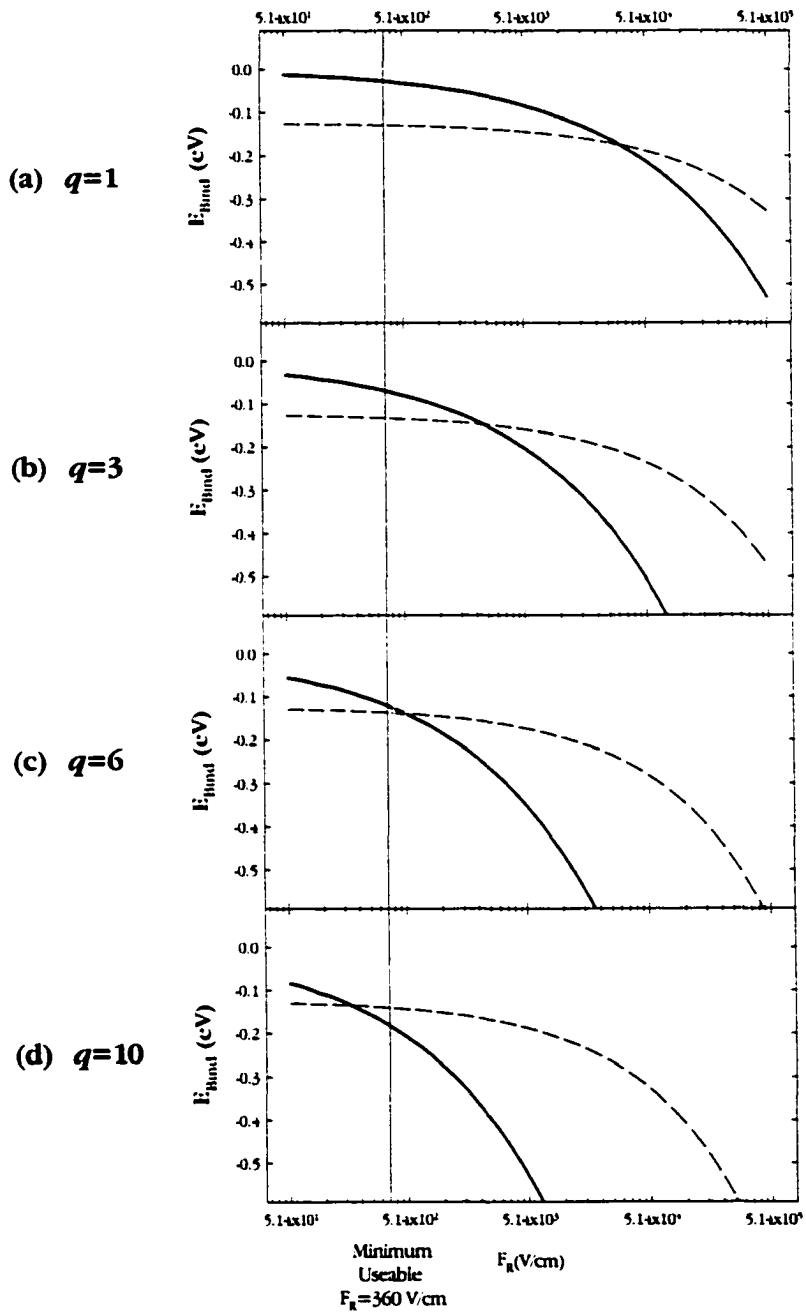

Figure (2.4.12) : **Limits on the upper and lower states for various charges.** This shows the limits and how they change with charge.

excitation energy and any repeller geometry to go above q=7. However, it is possible to go above this limit by relaxing the above restrictions. There are two conditions, thus two different restrictions, which can be eased to make it possible to make measurements above q=7.

The first restriction which can be relaxed is on the upper state, specifically the requirement that the field in the repeller must be high enough to ionize all of the background population. Relaxing this restriction comes at the cost of a reduced signal to noise ratio. Thus this condition can be relaxed if there is sufficient signal to noise that additional background will not render the signal unmeasurable in a reasonable period of time. If the repeller is instead set to a field equal to the detection field, the minimum upper state changes and the minimum usable field in the repeller changes from F_R=360 V cm^{-1} to F_R=180 V cm^{-1}. This moves the vertical line in Fig. 2.4.12 to the left and shifts the dashed curve downward so that more states satisfy this new requirement including a small number of q = 10 states. Setting the repeller in this way removes nearly these same amount of background as the original requirement. Fig. 2.4.9 shows that this adjusted requirement still removes approximately 90% of the background. This adjusted requirement was used for numerous ions in this experiment with an adequate signal to noise.

The other restriction that can be eased is the mixing of the lower state with neighboring states. Relaxing this restriction permits the population of the measured state to possibly mix with that of nearby states. The number of states it can mix with is determined by how large a field is applied to the beam when this restriction is relaxed. Equations 2.4.26 can be extended to determine the field at

(a) q=1

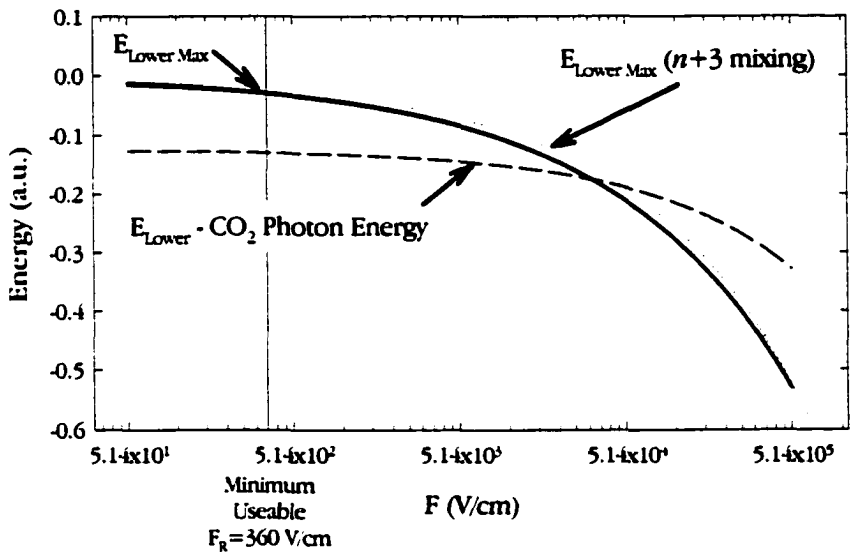

(b) q=10

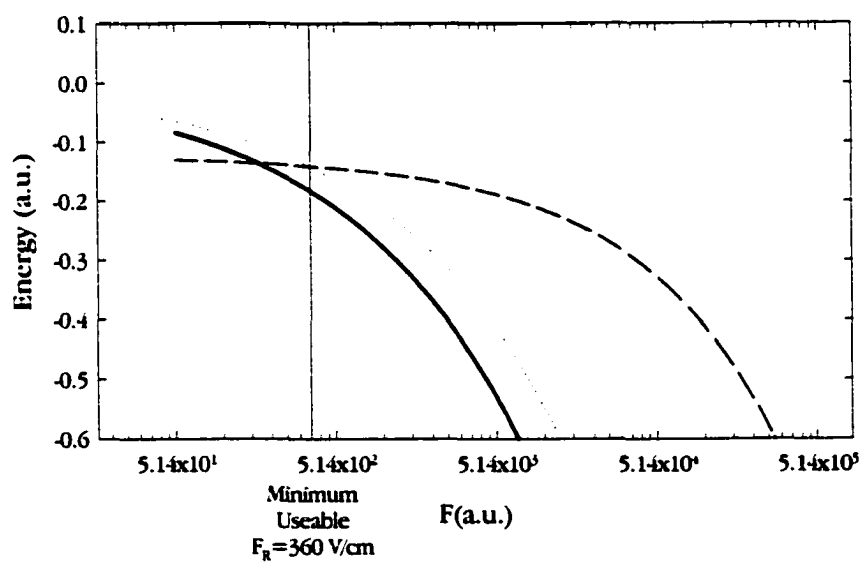

Figure (2.4.13) : **Effect of relaxing no mixing requirement.** This shows the effect of relaxing the requirement that the lower state of the transition does not mix.

which a state can mix with a state an arbitrary number of states away giving the result,

$$F_r = \frac{q^3}{3n_{Lower}^2}\left(\frac{1}{n_{Lower}^2} - \frac{1}{(n+i)^2}\right) \qquad (2.4.36)$$

where i is the number of states away from measured state which for which the field for mixing is being calculated. Using this equation we can relax the requirement for mixing and find the field at which the measured state can mix with a state $n+2$, or $n+3$ away from it. The effects of the relaxing of this restriction on the states which can be used in the measurement are shown in Fig. 2.4.13 (a) and (b) for $q=1$ and 10 respectively for mixing with a state $n+3$ away from the measured state. In the $q=10$ plot the lower state maximum moves to the right sufficiently, so that there is a transition by a CO_2 photon energy between the lower and upper states fulfilling the requirements of completely ionizing the background and mixing no further than a state three states away from the measured state. Note that this changes the lower state curve more dramatically as q is increased. Thus combining the relaxing of the mixing restriction with the reduction of the repeller field many more states become available at higher q. Allowing this mixing of the population was considered an acceptable compromise for some ions because it allowed the measurement of higher charge states than would have been possible without modifying the apparatus, at the expense of possibly mixing the population with levels very close in energy to the level being probed (no more than three states away for high charges (e.g. an energy difference for an $n=102$ measured state in $q=11$ of 0.00066 a.u. or 0.0089 eV) thus having nearly the same population as the state measured

(the width of the measured resonance is ~0.04 eV), so mixing the two populations should only affect the measured population slightly, however in the analysis effects of this mixing should be considered.

2.4.6 Conclusions

Thus while significant background existed for most of the measurements made, because the window was left partially open, the signal to noise was sufficient to allow successful measurements for q=2-6. For charges q>=6 it was necessary to allow the lower state of the transition to possibly mix with neighboring states, although the population difference between these states is believed to be small. The window model does not include all the sources of background but it can be used to determine how to effectively eliminate a significant source of background, states populated in the capture near the upper state being detected. In future experiments investigation of the background sources not from this ionization window might be necessary to achieve an acceptable level of signal to noise.

2.5 Laser interaction region

2.5.1 Introduction

After the repeller the state whose population is being probed is resonantly excited to a very high upper state in the laser interaction region, or LIR. The laser excitation is the first step in the RESIS detection of the population being measured. A CO_2 laser is used to excite the resonant transition in the LIR. The discrete lines of the CO_2 laser are spaced by approximately 1 cm^{-1} with a wide range of energies, from 894 cm^{-1} to 1100 cm^{-1} or equivalently 0.111 eV to 0.136 eV. The most populated states in collisions with the Rydberg target are closely matched to this range of energies. The CO_2 laser used in this study has a typical power of 15 W.

2.5.2 LIR construction

The laser interaction region is shown in Fig. 2.5.1. It is a four-way stainless steel Dependex cross with a small Cajon fitting making a fifth opening to the chamber. A 1" ZeSe window is mounted in a holder inserted into the Cajon fitting. The CO_2 laser enters the chamber through the ZeSe window and is incident on a small first surface gold mirror mounted opposite the window. The CO_2 laser has a waist of 0.45 cm and a spot diameter at the entrance window of approximately 1.5 cm. The ion beam enters from the left in the figure after exiting the repeller, intersects the CO_2 laser, and exits to the right entering the detector. The maximum possible angular spread of the ion beam is approximately 8 mrad as calculated from the limiting apertures in the repeller and the detector which define the ion beam path.

The mirror is mounted on a post attached to a precision rotation stage outside

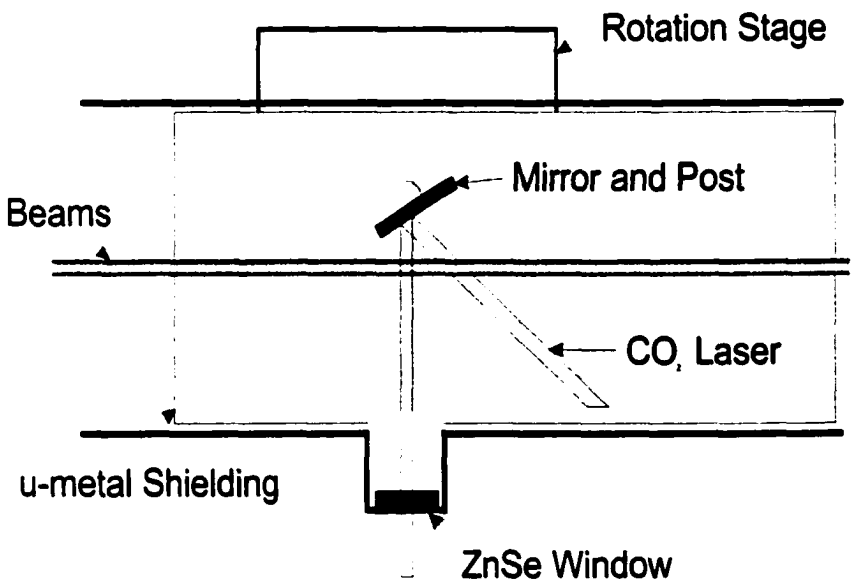

Figure (2.5.1) : **Schematic of the laser interaction region.** This shows the general construction of the LIR. Note the rotation stage is behind the chamber in this picture with the mirror post coming out of the page.

of the chamber, which controls the angle of the mirror to the window. This allows the angle between the reflected laser and the ion beams to be varied. A small angle of metal is placed opposite the mirror to deflect the reflected laser away from the interaction plane to prevent any further reflections from interacting with the Rydberg ion beam.

By the adjustment of the angle between the laser and the Rydberg ion beam the discrete frequency of a particular line of the CO_2 laser can be Doppler-tuned continuously over a range of frequencies. This makes it possible to match exactly the resonance frequency of a particular transition of the Rydberg ion being studied. The frequency of the laser in the rest frame of the ion beam is,

$$\nu' = \nu_L \gamma \left(1 + \beta \cos(\theta)\right) \qquad (2.5.1)$$

where ν_L is the laser frequency, θ is the angle between the laser and the beam measured from anti-parallel, β is the scaled velocity (v/c), and $\gamma = (1-\beta^2)^{-1/2}$. Thus the velocity of the ion beam also plays a role in which transitions in the ion are available, because less Doppler tuning can be done at lower velocities. At very low velocities only transitions very near the frequency of a discrete CO_2 line can be excited. Conversely at a velocity of about 0.4 a.u., or β = 0.003, the excitation energy is continuously tunable through the entire range of the CO_2 spectrum.

After choosing a particular transition to study, the CO_2 laser is tuned to the nearest discrete line. The angle of the mirror, measured on the rotary stage, is then scanned over the angle required for the Doppler tuned frequency to be resonant with the Rydberg ion's rest frame transition frequency. This results in the resonance being excited and detected as an ion signal dependant on the angle of

the mirror.

The chamber in which the laser excitation takes place is carefully designed to reduce the electric and magnetic fields in the interaction region because of the sensitivity of Rydberg states to even small fields. Any fields present in the interaction region can affect the excitation significantly, by Stark broadening the laser resonance. To prevent uncontrolled electric fields in the chamber the interior is coated with Aquadag, a commercially available mixture that leaves a coating of graphite on treated surfaces. This coating reduces charging on insulating oxide surfaces which form on many components in the LIR. The interaction region is also shielded from electric fields produced by the repeller steering plates. To provide this shielding a wire mesh screen, with a small aperture at the center to allow the beams to pass through, is placed at the entrance of the LIR.

The magnetic field in the LIR must also be reduced, as a fraction of the earth's field can induce a motional electric field strong enough to broaden the resonance unacceptably. To shield the interior of the chamber from external magnetic fields a cylindrical μ-metal shield that extends well beyond the region where the excitation takes place reduces the magnetic field inside the LIR to less than 50mG. Additionally the materials used in the construction of the LIR are chosen carefully. The use of materials with a residual magnetic field should be avoided in the interaction region, for example any ferromagnetic, steel, hardware used in the construction of the interaction region, for this reason the interaction chamber is constructed entirely out of non-magnetic materials including aluminum, brass, copper, Delrin, and gold, and only aluminum and brass bolts and connecting

hardware is used to connect the chamber to the rest of the system. Stainless steel should be used with caution since even stainless steels which are "non-magnetic" often have residual fields large enough to pose a problem for more sensitive transitions. Any aluminum used in the interaction region must be coated with Aquadag or a similar compound to reduce the possibility of charging by ions and electrons impacting the surface because of the insulating oxide formed when aluminum is exposed to air. It was discovered in the course of this experiment that the use of dissimilar materials should also be avoided if possible, as the contact potential between them may be a source of fields in the interaction region. This will be discussed further in the section describing the width of the resonance.

2.5.3 Structure of the transition

A large number of different transitions in the Rydberg ion are available because of the number of discrete CO_2 frequencies. The transition energy between any two particular Rydberg states of the ion is approximately equal to the hydrogenic energy difference between the two states, or

$$\Delta E = \frac{R_\infty}{1+\frac{m_e}{M_N}} q^2 \left(\frac{1}{n_{\text{Lower}}^2} - \frac{1}{n_{\text{Upper}}^2} \right) \tag{2.5.2}$$

where R_∞ is the Rydberg, m_e is the electron mass, M_N is the nuclear mass of the core ion, q is the charge of the ion core, n_{Lower} is the lower state of the resonant transition and n_{Upper} is the upper state of the transition. Examples of some of the many possible transitions for a q = 3 ion core are shown in Fig. 2.5.2 with the CO_2 spectrum below. Each of the short lines in the upper portion of the figure indicates

the hydrogenic energy difference between the state listed at the left and a particular final state. The range of CO_2 frequencies is indicated in the lower portion of the

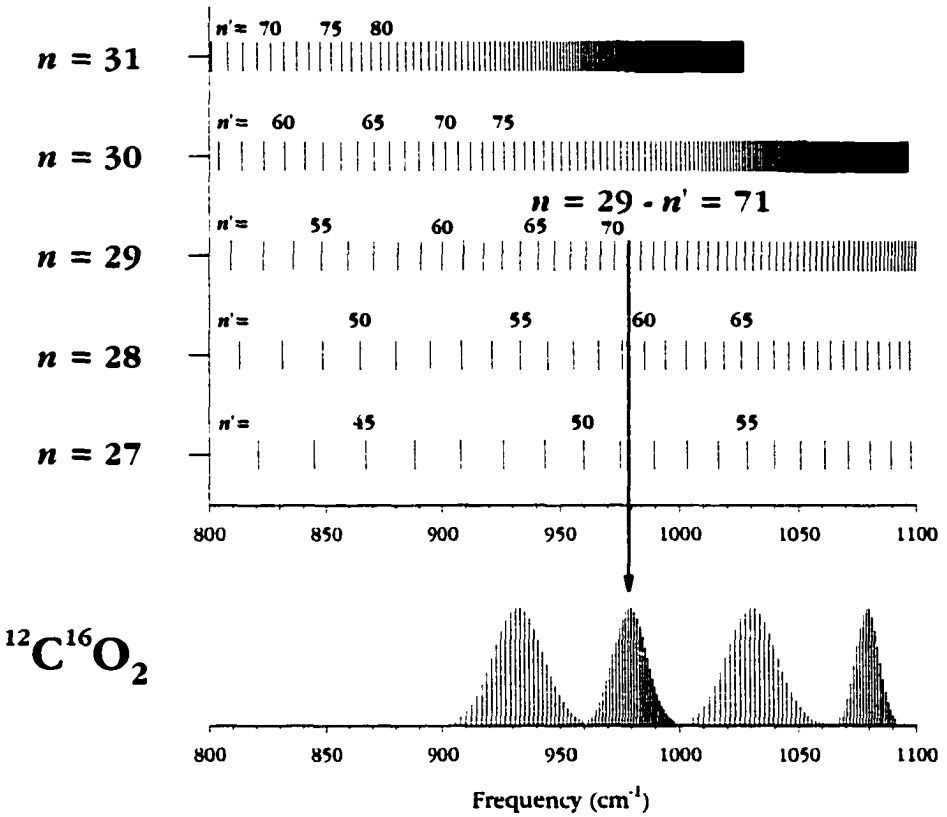

Figure (2.5.2) : **CO_2 spectrum and C III transitions.** **CO_2 spectrum and C III transitions.** The upper part of this figure shows the energies of various transitions of C III. The lower state of the transition is listed to the right and each line indicates the energy of a transition to an upper state n'. A few of these upper states are labeled for each lower state. The lower part of the figure shows the energies of CO_2 laser lines available. Note that the CO_2 laser energies overlap a number of the transitions shown. One particular transition of C III is indicated, the $n=29-n'=71$ transition. Note that this lies near the energy of one of the CO_2 laser lines.

figure. The available CO_2 frequencies make transitions to a wide range of upper states possible from a relatively small range of lower states.

A measurement of a typical transition of C II, n=19 - n'=51 is shown in Fig. 2.5.3. The transition shown corresponds to the C II n = 19 to n' = 51 transition, Rydberg levels bound to the q = 2 ion. The angle has been converted to a frequency difference from the hydrogenic energy using the Doppler tuning equation, Eqn. 2.5.1, and the calculated intersection angle between the CO_2 laser

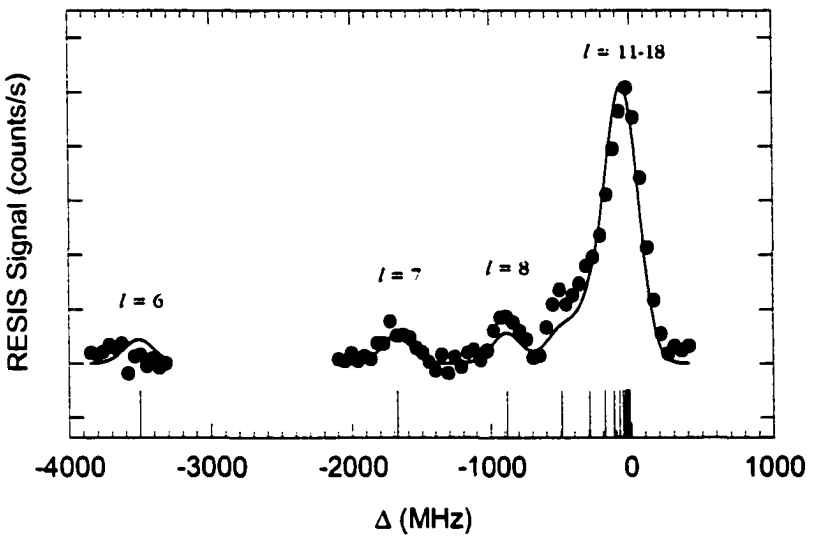

Figure (2.5.3) : <u>C II spectrum.</u> This shows the n = 19 to n' = 51 transition of C II. The large peak on the right is the combination of a number of l-states, l = 11-18, the next isolated peak to the left is the l = 8 peak, the next the l = 7 peak, and the peak furthest left is l = 6. In between the high-l peak and the l = 8 peak are l = 9 and 10 which are unresolved from the high-l peak but do not contribute more than half their amplitude to the center. The solid curve under the data points is a simulated line shape using an l-structure as calculated using Eqn. 2.5.4 derived below, with α_s=3.56 a_0^3. The full width at half max of the isolated lines is 270(33) MHz.

and the ion beam. However, Fig. 2.5.3 shows more than a simple single peak. It shows a number of peaks partially resolving the *l*-structure of the transition. This structure was in fact only visible as a set of isolated lines for CII. The signal to noise

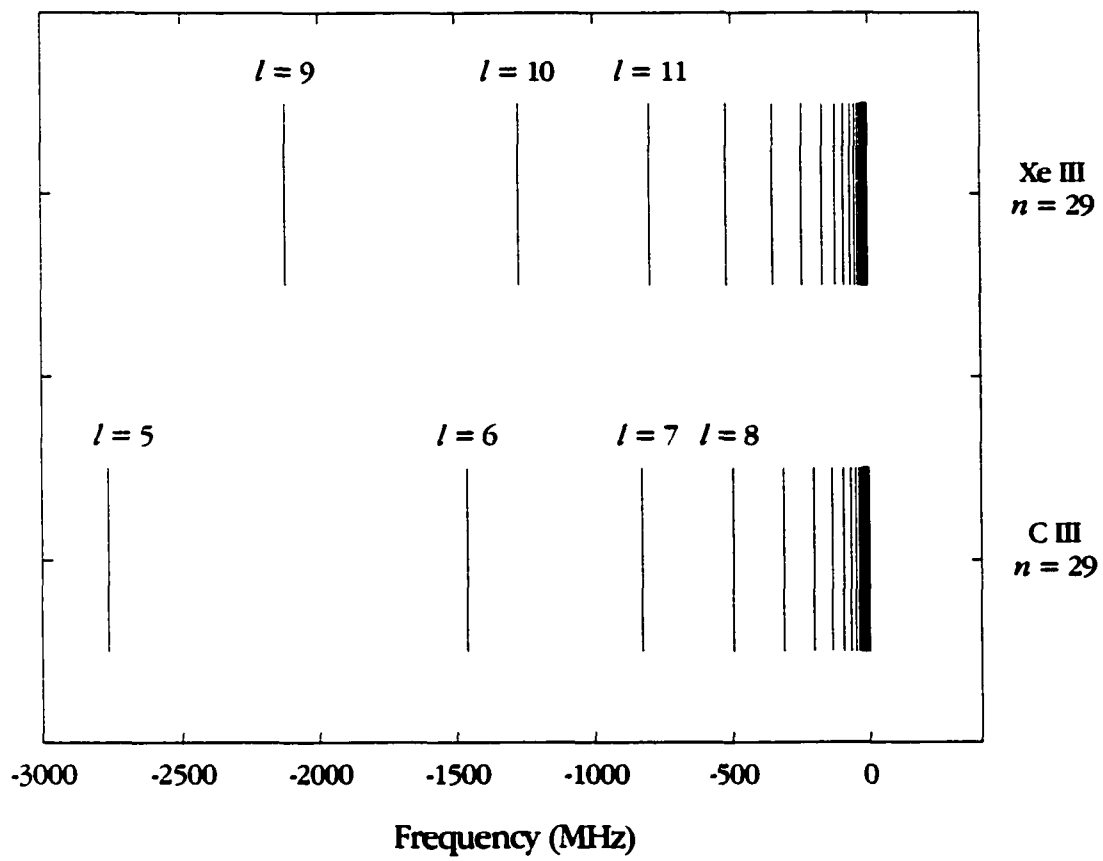

Figure (2.5.4) : **Calculated fine structure for two ions.** This shows the calculated fine structure for two ions for the *n* states used in this experiment. Note the much larger separation of the Xe III states because of the larger α_s.

was insufficient to see the isolated *l*-structure for the other ions measured in this study. By modeling the non-Coulombic potential to first order as a scalar polarizability of the ion core, one can calculate this energy fine structure. The

non-Coulombic potential perturbing the Coulombic potential is equal to,

$$V_{eff} = -\frac{\alpha_s e^2}{2r^4} \tag{2.5.3}$$

where α_s is the scalar polarizability of the ionic core. This gives an energy correction E^1 to the hydrogenic energy level of,

$$E^1 = -\frac{\alpha_s e^2}{2}\langle nl|r^{-4}|nl\rangle \tag{2.5.4}$$

Table 2.5.1 : **Values of α_S for the ions used in the measurement.** This table lists the values used for α_S for the ions used in this measurement. The Z_{eff}^{-4} scaling uses Z_{eff} = Atomic number - number of closed shell electrons.

Ion core	α_S (a_0^3)	Source
C^{2+}	3.56	Fit of measured spectrum
C^{2+}	3.86	From 7G value from C II spectral table [23]
C^{3+}	4.0	From 5,6,7G State values from C III spectral table [23]
C^{4+}	0.009	Extrapolation of Bhatia and Drachman table[25]
Ne^{6+}	0.428	Charlotte Fischer private communication
Ar^{8+}	0.062	From Na^+ using Z_{eff}^{-4} scaling
Ar^{11+}	0.019	From Ne^{3+}=0.550 (Charlotte Fischer private communication) using Z_{eff}^{-4} scaling
Ar^{3+}	3.52	Charlotte Fischer private communication
Xe^{3+}	10.25	Charlotte Fischer private communication

for a particular n_l state. This breaks the degeneracy in l and results in multiple peaks for the laser excitation of a single n-state. The calculated structure for C II is shown as a solid curve in Fig. 2.5.3 superimposed on the measured signal points for a value of a = 3.56 a_0^3. The positions of the individual l-state components are shown in the figure as small vertical lines under the curve. Note that although the high-l states are not resolved they do affect the shape and width of the laser resonance measured. Since the unresolved high-l peak is the largest feature in this (and all other) spectra, we used it to indicate the population of the n_p state. As Fig. 2.5.3 illustrates, only a subset of the l-states in the n_p level is actually included under this peak. In order to estimate which l-states are included one needs to know both a_S, the ion polarizability, and the resolution or lineshape of the laser excitation. A list of a_S for all of the ions used in this experiment is given in Table 2.5.1. These values are all theoretically calculated except for the a_S value for the C^{2+} core, which is calculated from the spectrum above. The source for each a_S is listed next to the value and include calculation from spectral tables [26], extrapolation of a value reported by Drachman [27, 28], and from private communications with Charlotte Fischer. To give an idea of how different values of a_S affect the structure of the resonance a two examples are given in Fig. 2.5.4. This figure shows the calculated structure for C III n = 29 and Xe III n = 29 and the large difference between their l-structure.

2.5.4 Width of the resonance

The width of the resonance consists of two separate types of width. The homogeneous width, or the width that would be present for an individual atom,

and the inhomogeneous width, the width due to the fact that different atoms are excited differently. The homogeneous width includes a number of different sources of width including, the spectral width of the excitation laser, the natural linewidth of the transition, the width due to the finite interaction time or transit width, and the width from Stark broadening of the resonance. Of these widths only the transit width and the Stark width are of sufficient size to be significant to this measurement as the line widths seen are 100's of MHz. Sources of inhomogeneous width include the width due to the velocity and angular spread of the beam, of which only the angular spread of the beam will be shown to be significant.

The transit width can be estimated using a two state time dependant pertubation theory, or TDPT, model of the excitation. This gives an estimate of the full width at half max of,

$$\Delta\nu_{FWHM}(\mathrm{Hz}) = \frac{1}{\pi}\sqrt{2\ln 2}\,\frac{v\sin(\theta)}{w_o} \tag{2.5.5}$$

where v is the velocity of the beam and w_0 is the waist size of the laser, 0.45 cm for the laser used in this experiment. For beams with a velocity of 0.100 a.u. this width is about 18 MHz at perpendicular. It is of interest to note that the width of the transition from the finite interaction time and the shape of the beam does not change with the spot size of the laser beam at the interaction point, only with the waist size of the Gaussian laser beam.

The other possibly significant source of homogeneous width is the Stark broadening of the Rydberg levels of the ion by external electric or magnetic fields. The upper state is extremely sensitive to any external fields at the interaction point.

The lower state is less sensitive to these fields by about a factor of $(n_l/n_u)^2$. Thus, the major contribution to the width of the resonance by the Stark effect is from the upper state of the transition. The separation of the two extreme Stark levels in a particular n-state manifold can be determined approximately by treating the states as if they were states of a hydrogen like ion. This gives the approximate width for the high-l state line at a given field due to the linear Stark effect as,

$$\Delta E_{FWHM} \approx \frac{3n(n-1)}{2q} F \tag{2.5.6}$$

where ΔE_{FWHM} is the full width at half max in atomic units of energy, n is the upper state's principal quantum number, q is the charge of the Rydberg core, and F is the field in the interaction region.

Since the ion beam has a substantial velocity, any magnetic fields present at the interaction point will also cause a Stark width in the resonance due to the induced motional field. The induced field can be calculated using the following formula,

$$E = \vec{v} \otimes \vec{B} \tag{2.5.7}$$

The width due to this induced electric field can be substantial if the interaction region is improperly shielded from the Earth's magnetic field or fields from the experimental equipment near or in the interaction region.

As can be seen in Eqn. 2.5.6 the Stark effect is highly dependant on the n-state. The width due to the Stark effect can be measured by choosing transitions from the same or neighboring lower states to a wide range of upper states and determining how the width of the resonance varies with the n of the upper state. If these transitions are selected so that the laser angle to the ion beam is nearly the same

only the linear Stark effect and the structure of the upper state vary, allowing the separation of these effects from the inhomogeneous widths. This width can become quite substantial for even small stray fields within the LIR. For example the hydrogenic Stark width due to a stray electric or induced electric field of only 50 mV cm^{-1} for a q = 3 ion core, n_l = 29 to n_u = 71 transition is about 160 MHz.

The velocity and angular spread of the beam both contribute to the inhomogeneous width and can be estimated using the Doppler equation. The velocity spread of the beam causes a frequency width because ions traveling with different velocities will experience different frequencies according to the following equation when $\gamma \sim 1$,

$$\Delta \nu_v = \nu_L \frac{\Delta v}{c} |\cos(\theta)| \tag{2.5.8}$$

where ν_L is the laser frequency, θ is the intersection angle of the laser and the ion beam, and Δv is the velocity spread of the beam. This source of width is controlled mostly by the ion source, if the ion source is a nearly monoenergetic source of ions then this width will be small, however if the source poorly controls the energy of the accelerated ions this width can be quite large. For most accelerators this width contributes, but is not the major source of width, because ion accelerators are generally quite good at producing a nearly monoenergetic beam. The CryEBIS has a measured energy spread of 2 eV/q, this gives a maximum expected width from this source to be approximately 25 MHz when the beams are colinear, at a typical angle for our measurements, 100°, the maximum width from this source is only 4 MHz and is not significant.

The angular spread of the beam also causes a frequency width because ions experience different frequencies, but now it is because they are traveling at different angles to the laser beam. The width in frequency due to the angular spread of the beam is expressed as the following equation when $\gamma \sim 1$,

$$\Delta \nu_{\theta} = \nu_{L} \beta \Delta\theta |\sin(\theta)| \qquad (2.5.9)$$

where $\Delta\theta$ is the angular spread of the ion beam in the laser ion beam interaction plane. Thus the collimation of the ion beam at the point of interaction with the laser is the critical source of this width. This width can be controlled somewhat with careful design of the ion optics, and/or collimating slits. In this experiment very little was done to control this source of width, the maximum angular spread given above, 8 mrads, gives an estimate of the maximum width possible from this source of 175 MHz at a perpendicular intersection angle and 172 MHz at a typical intersection angle of 100°.

Table 2.5.2: **Stark width study.** This table shows the width for various transitions of C IV in particular a wide range of upper states with the original grounded mirror. Also shown is the width scaled by the upper state $n(n\text{-}1)$ to account for the width due to the Stark effect. Also shown is the stray field calculated assuming the entire width is from the Stark width of the upper state.

Transition	FWHM (MHz)	FWHM/n(n-1)	Calculated Stray Field (mV cm^{-1})
35-71	162	0.033	136
37-85	265	0.037	155
37-94	317	0.036	151
40-101	376	0.037	155

A study of how the width varied for a wide range of upper states for nearly the same angle gave convincing evidence of the presence of a significant Stark width. The measurements from this study for C IV at v=0.100 a.u. are shown in Table 2.5.2. The width due to the Stark effect should scale as $n(n\text{-}1)$ for the same q as shown in Eqn. 2.5.6, and the last column in Table 2.5.2 shows that in fact the width seen in the measurement does show this dependance, thus the width due to the Stark effect was dominant during this study. To make an estimate of the upper limit of the stray field in the LIR we can assume the entire width is due to the Stark effect. This calculation gives a stray field of approximately 70 mV cm^{-1}. After realizing that there was a significant field in the LIR chamber we isolated the mirror post and found that we could null this field by applying a small potential to the

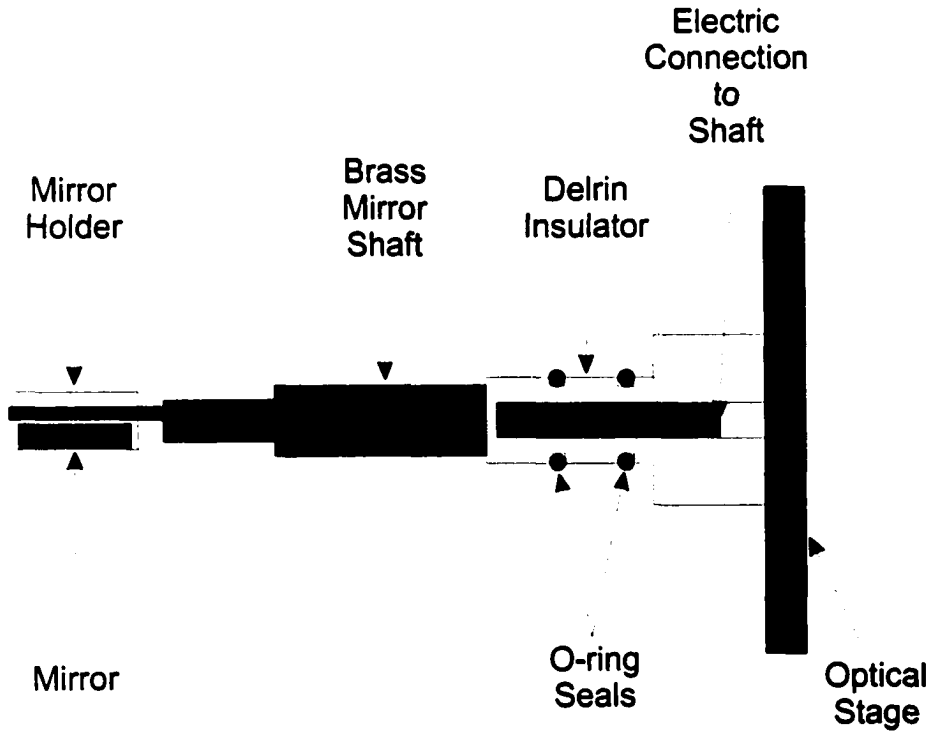

Figure (2.5.5) : **LIR post design.** This shows the modified LIR post used to electrically isolate the post from the chamber and provide an electrical connection so a controlled voltage could be applied to the post.

post. After this was recognized, the post mounting the mirror to the rotation stage was modified to completely electrically isolate it and allow the voltage on it to be controlled carefully, the new design of the post is shown in Fig. 2.5.5. Grounding the new post to the vacuum chamber did not significantly reduce the width of the resonance so we decided that there was still a voltage somewhere in the LIR that was not corrected by simply grounding the post, possibly a contact potential between the mirror and the post. However we could now control the voltage on the post and possibly compensate for any other potentials in the LIR. To determine what voltage to apply to the post, we varied the voltage on the post and set it to minimize the width of a C III 31-100 transition at a velocity of 0.081 a.u. by measuring the resonance signal slightly off the peak and determining the minimum. This study is shown in Fig. 2.5.6 the voltage on the post was varied using a 9 V battery across a variable resistance. The narrowest resonance appeared to be for a voltage of 0.100 V. This study was repeated with less detail later for a different transition (Ne VI 55-133) and the voltage for the minimum resonance width was

Table 2.5.3: **Second Stark width study.** This table shows the width for various transitions of C IV for a wide range of upper states with a 0.2 V potential on the mirror post.

Transition	FWHM (MHz)	FWHM/n(n-1)
35-71	110	0.022
37-85	112	0.016
40-101	84	0.008

adjusted to 0.200 V. After this adjustment the widths of various upper state transitions of C IV were measured again and this time they did not scale with n as expected if the Stark width were the dominant width. The measurements from this study are given in Table 2.5.3. The widths in Table 2.5.3 are essentially constant for the same range of states that previously showed a clear increase consistent with Stark broadening. Thus the Stark width of the resonance could be controlled using a small voltage applied to the post and mirror in the interaction region. The remaining width is not larger than the width due to the angular spread of the beam,

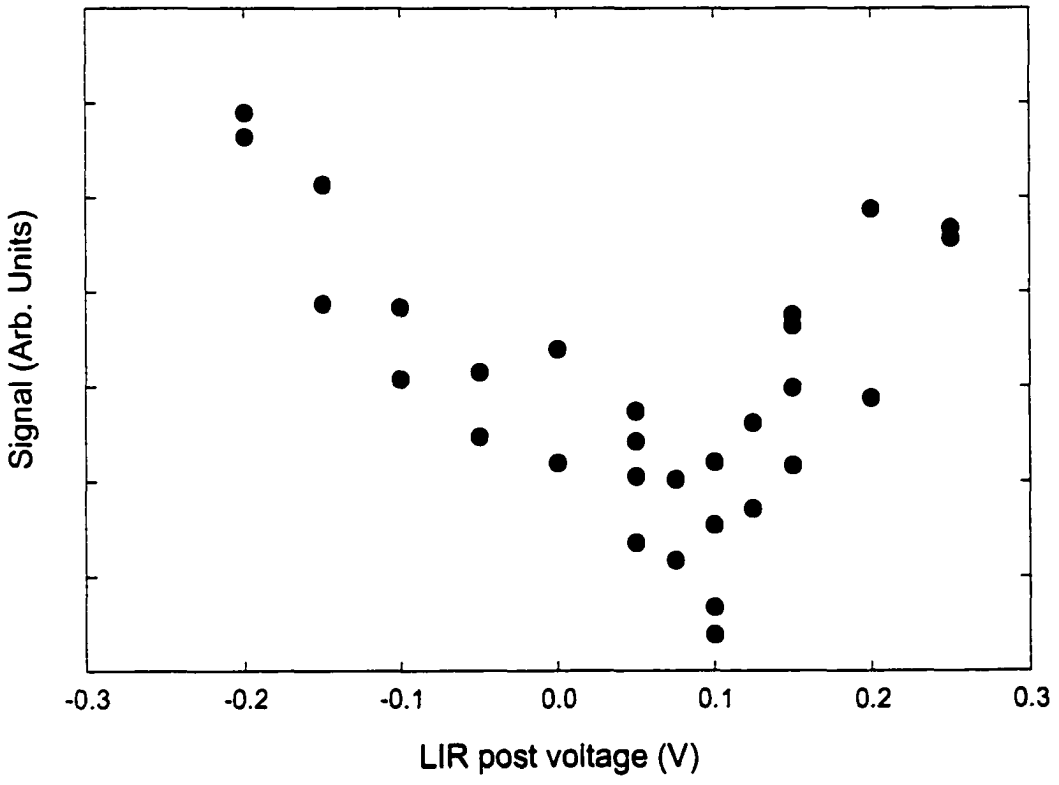

Figure (2.5.6) : **Variation of the off resonance signal with the applied post voltage.** These four plots show the variation in the signal slightly off the center of the resonant signal. Where this is at a minimum the width is expected to also be at a minimum.

which has a maximum possible width of approximately 175 MHz. This is the only source of width which is not well reasonably controlled after the residual post voltage was corrected.

A source of width which also affects the composition of the signal is the fine structure of the transition. This is dependant on the ion being used and the specific transition being measured and can create significant width to the resonance because the signal is actually made of a number of transitions from a number of different l-states in the lower state to the upper state. The determination of which l-states contribute to the measured signal peak necessary to comparing our experimental results to theoretical calculations that account for the distribution of the population in l, specifically in comparison to CTMC calculations. The determination of which l-states contribute significantly to the measured signal was done by using the estimated scalar dipole polarizability for each ion core, as given earlier in this section, to calculate the position relative to hydrogenic of each of the l-states of the lower state. Each l-state was then given a Gaussian peak at that position all of the individual peaks having the same width and amplitude. The Gaussians were summed and this was fit to a carefully measured scan of signal with angle. Any of the l-states which contributed more than half of their amplitude to the center frequency of the measured signal were considered to be part of the measurement while those which did not were excluded in the CTMC calculation. The fit, the transition used, the contributing l-states, and the full width at half maximum used for the individual peaks are shown in Fig. 2.5.7 for each of the signals used in the measurement.

2.5.5 The amplitude of the resonance

Another aspect of the signal which is of interest in the laser excitation is the amplitude of the signal. This was significant to us when we were beginning the experiment. There are many transitions available in the charged Rydberg states but the question we needed to answer was whether or not we could excite them effectively. Additionally some information on the excitation efficiencies of different transitions would be useful in choosing which of the many possible transitions to use. To this end a reasonable theoretical method of determining the signal amplitude was needed. The induced transition rate can be written as,

$$W = \frac{4\pi^2}{3}\left(\frac{I}{h\nu}\right)\alpha|r_{n'n}|^2\nu \cdot g(\nu) \qquad (2.5.10)$$

where I is in J/m^2 and,

$$\oint g(\nu)d\nu \equiv 1 \qquad (2.5.11)$$

from Yariv[29] and Bethe and Salpeter[30] where $|r_{n'n}|$ may be approximated (by averaging over all *m* and *l* states) using Bethe and Salpeter [31] to be,

$$|r_{n'n}| \approx 2\left(\frac{n}{n'}\right)^{3/2}\left[1-\left(\frac{n}{n'}\right)^2\right]^{-2}\left(\frac{a_0}{q}\right) \qquad (2.5.12)$$

as an order of magnitude estimate. This model predicts a transition probability that is proportional to q^{-2} which can be seen from Eqns. 2.5.10 and 2.5.12. Thus the transition will become saturated at much lower powers for lower charge states and as the charge increases the power required to get the same transition strength should increase dramatically. One way to see this increase is to look at how the

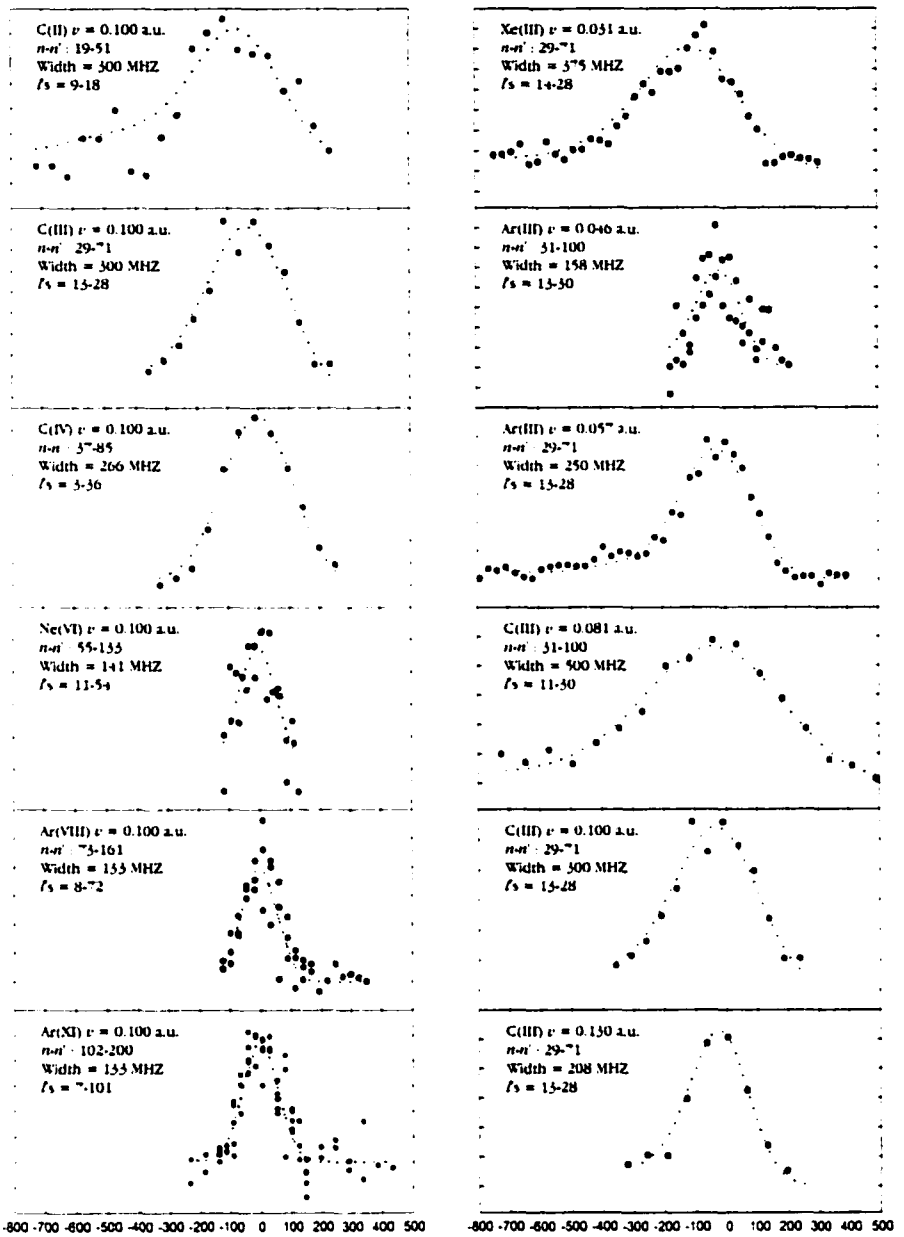

Figure (2.5.7) : **Measurements and fits of CO_2 signals.** These are the CO_2 signals measured for each of the ions used for this experiment. Each signal includes information on the transition used, the full width at half max of the individual Gaussians summed to generate the simulation, and the *l*-states included in the high-*l* peak.

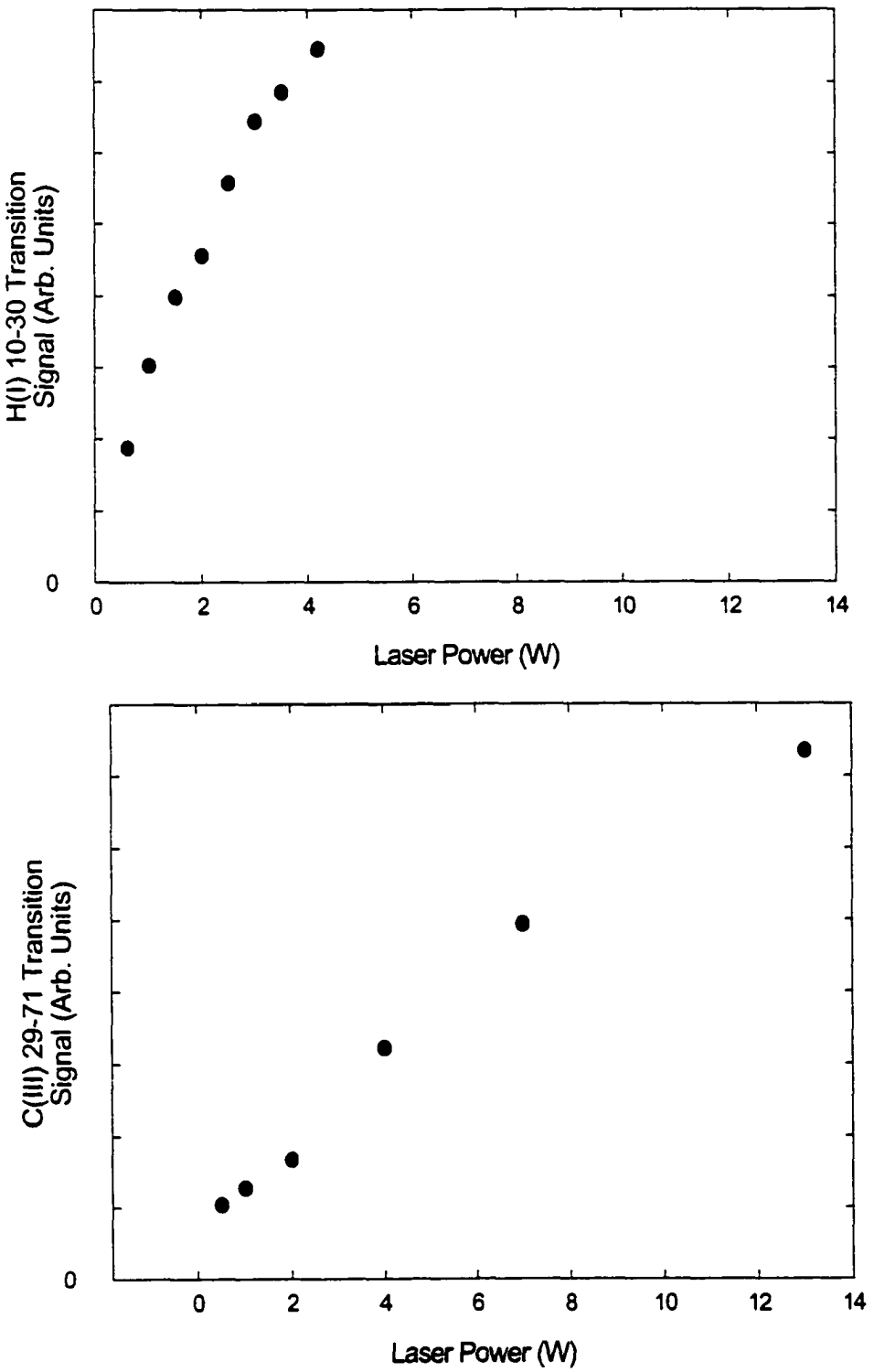

Figure (2.5.8) : **C III and He I Laser saturation curves.** This shows the signal size as a function of the laser power.

signal amplitude behaves with power for different charge states. Figure 2.5.8 shows the signal amplitude as a function of the laser power for both the H I and the C III transitions. It is obvious from the figure that the H I saturates much more quickly than the C III signal which is expected.

A second factor which may affect the signal amplitude is the amount of population in a particular final state as the charge varies. CTMC predicts that the width of the final state population in energy is approximately constant with charge. Since the energy width of the distribution remains constant the number of states in the distribution can be approximated by the energy width divided by the average separation between adjacent states. This can be written as,

$$\frac{W}{\Delta E} = \frac{E_p}{\Delta E}\frac{W}{E_p} \tag{2.5.13}$$

where W/E_p is nearly constant. This leaves the ratio $E_p/\Delta E$ which varies approximately proportionally to q. The result is that the number of states within a constant energy width increases approximately proportionally to q. Thus the amount of population in a particular state will be reduced by a factor of q. This combined with the reduced transition probability give an expected overall reduction in the signal size proportional to q^{-3} when there is no saturation and the laser power is constant. This is confirmed by comparison with predicted population distributions from CTMC calculations.

The data shown in Fig. 2.5.9 shows that indeed the signal does indeed fall off approximately as q^{-3} which is shown as the solid curve in the figure. The data in the figure is all with the same LIR post voltage after the Stark width was reduced to no

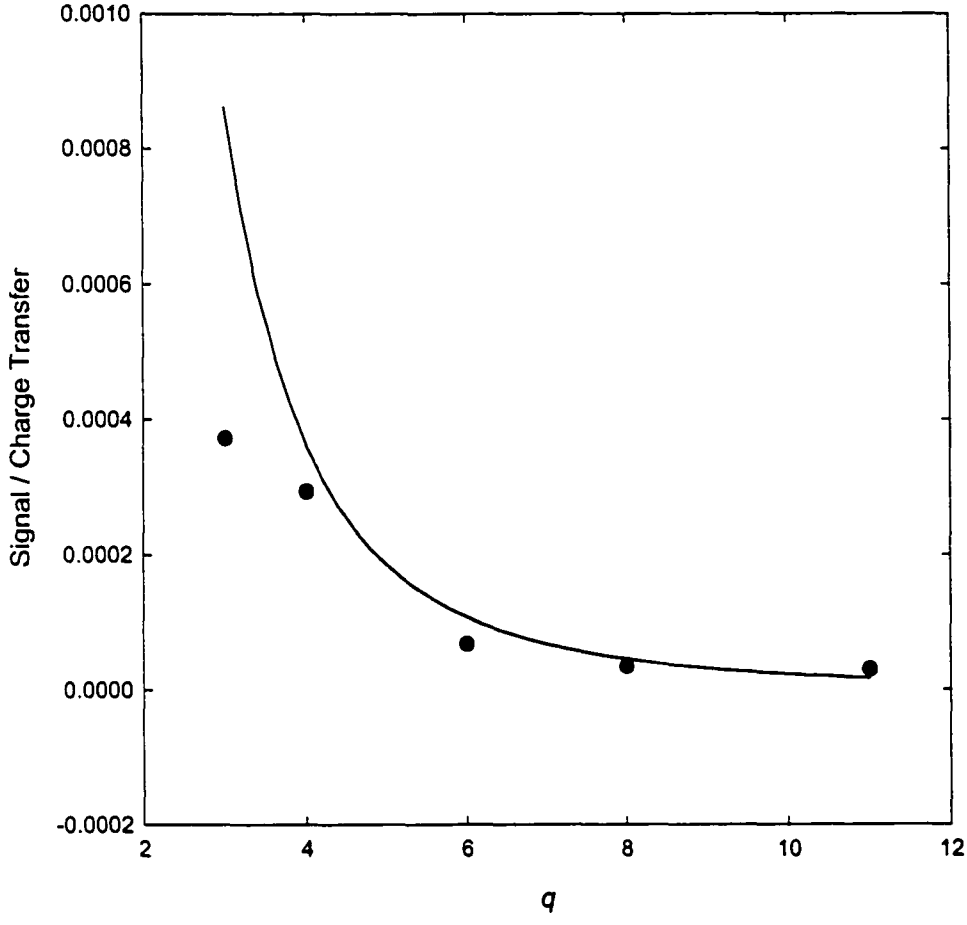

Figure (2.5.9) : **Signal to charge transfer versus charge.** This shows the dependance of the signal on charge note that the predicted q^3 dependance, shown as a solid line, is followed.

longer be the major source of width. This figure shows the ratio of the signal to the charge transfer beam for the target with the maximum population transfer to the observed state, to normalize the different ion beam intensities and to choose the center of the distribution for which the simple proportionality was made. Thus this confirms the predicted dependance on charge. The only point which does not

closely follow the predicted curve is for $q = 3$. This deviation is possibly because the signal for $q = 3$ is slightly saturated thus producing less signal per charge transfer beam than it would were the transition not saturated.

2.5.6 Conclusions

The LIR combined with the CO_2 laser allows a wide range of transitions in Rydberg ions to be available. Isolated fine structure lines were only visible in C II, however the high-l peak had sufficient signal to noise to allow measurement from $q = 2$-11. Careful examination of the width during the experiment revealed a stray field in the LIR chamber of approximately 70 mV cm-1. We believe this was from contact potentials generated by dissimilar materials in the mirror and post. This stray field was corrected by isolating the post and placing a small potential on it. After the stray field was corrected the dominant width appears to be from the angular spread of the ion beam. The variation of the amplitude of the signal with charge appears to agree with an estimate of the transition probability and the prediction of CTMC that the width of the product state resonance is approximately constant with charge.

2.6 The detector

2.6.1 Introduction

After exiting the LIR the ion beams enter the detector. The detector consists of a Stark ionizer, focusing and steering electrodes, and a set of detection electronics used to view and measure the ion beams. Our measurement requires the measurement of two different quantities, the charge transfer ion beam and the laser

resonant signal. The ratio of the signal to the charge transfer ion beam is proportional to the ratio of the population in the state being measured to the entire charge transfer population.

The charge transfer beam can be measured simply by collecting and measuring it, however the signal ions must be differentiated from the rest of the charge transfer beam and the remaining primary ion beam. As discussed in Chapter 1 and earlier in this chapter, in Section 2.4.3, the detector Stark ionizes the signal at a potential to increase or decrease its speed. This differentiates the signal from the other ion beams by giving it a unique kinetic energy to charge ratio. However, the Stark ionizer does more than differentiate the signal. There are focusing effects at each electrode with a potential for any ion beams, because of the non-uniform field at the aperture. Even for a neutral charge transfer beam the non-uniform field at the aperture affects the signal beam after it is ionized. The complications from this focusing are more pronounced as the charge of the primary ion beam is increased. The ion optics of the detector are considerably more difficult when all of the beams entering the detector are charged. For this reason the ion optics of the detector are discussed in some detail below.

2.6.2 Detector construction

The Stark ionizer is housed in a large 10" conflat tee. The ends of the tee have flanges with five 2.75" conflat ports on them and the bottom port of the tee is used to attach a pump to the chamber. The large number of ports on the front and back of the chamber give great flexibility in setting up the detection electronics. Mounted on the entry flange are all the high voltage feedthroughs used to apply

voltages to the plates of the Stark ionizer, lens, and deflector within the chamber. On the rear flange an ion beam viewing system and a Channeltron electron multiplier (Galileo model 4716) used for signal measurements are attached to two of the five 2.75" conflat ports in positions symmetric around the center axis. A second Channeltron electron multiplier is mounted on the center port for ion beam current measurements, to both monitor the primary ion beam current during measurements with the detection voltages off and to allow the initial tuning of the primary ion beam. Pictures of the chamber and the front and rear flanges are shown in Figs. 2.6.1 and 2.6.2. The ion beam viewing system is mounted symmetrically across from the Channeltron so that the ions being measured can be tuned on the beam viewer and then by changing the polarity of the deflection plates

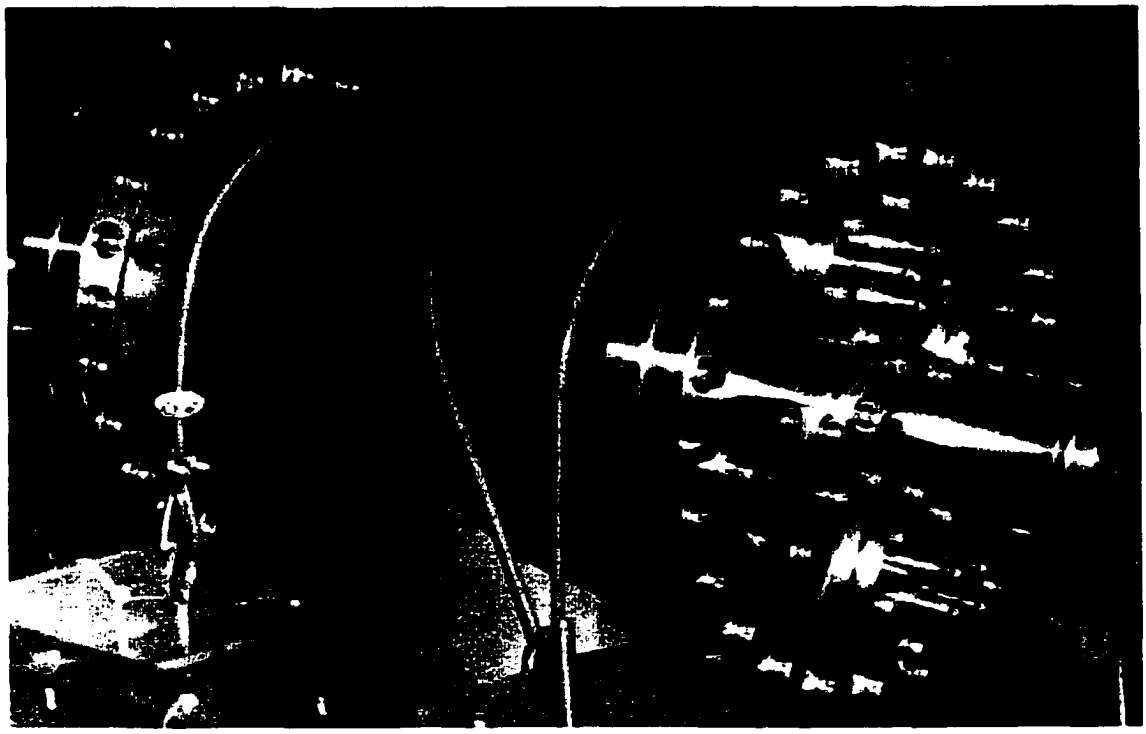

Figure (2.6.1) : **Outside of detector (front).** This shows the outside of the detector chamber from the front side. The high voltage feedthroughs seen on the flange are used to supply voltages to the electrodes for the Stark ionizer, lens and deflectors.

can be easily tuned onto the Channeltron to make quantitative measurements of the beam currents not possible with the beam viewer.

The parts used for the electrostatic optical elements in the detector were obtained from Kimbal Physics as separate pieces which are designed as a kind of electrostatic optics erector set. The Stark ionizer and the aperture lens which immediately follows it are built using square stainless steel (SS304) plates for their

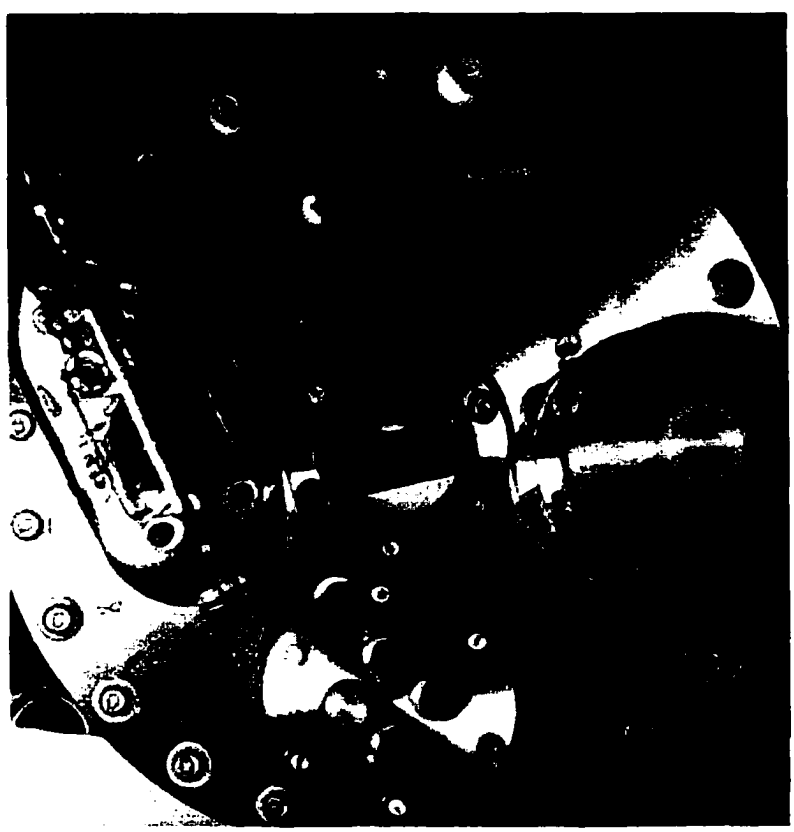

Figure (2.6.2) : **Rear flange of detector.** This shows the rear flange of the detector. The bottom port has a Channeltron electron multiplier mounted to it and the top port has the Colutron ion beam viewing system mounted. The center viewport was replaced with a Channeltron for the measurement, and the rotary feedthrough shown on the right port was removed for the measurement.

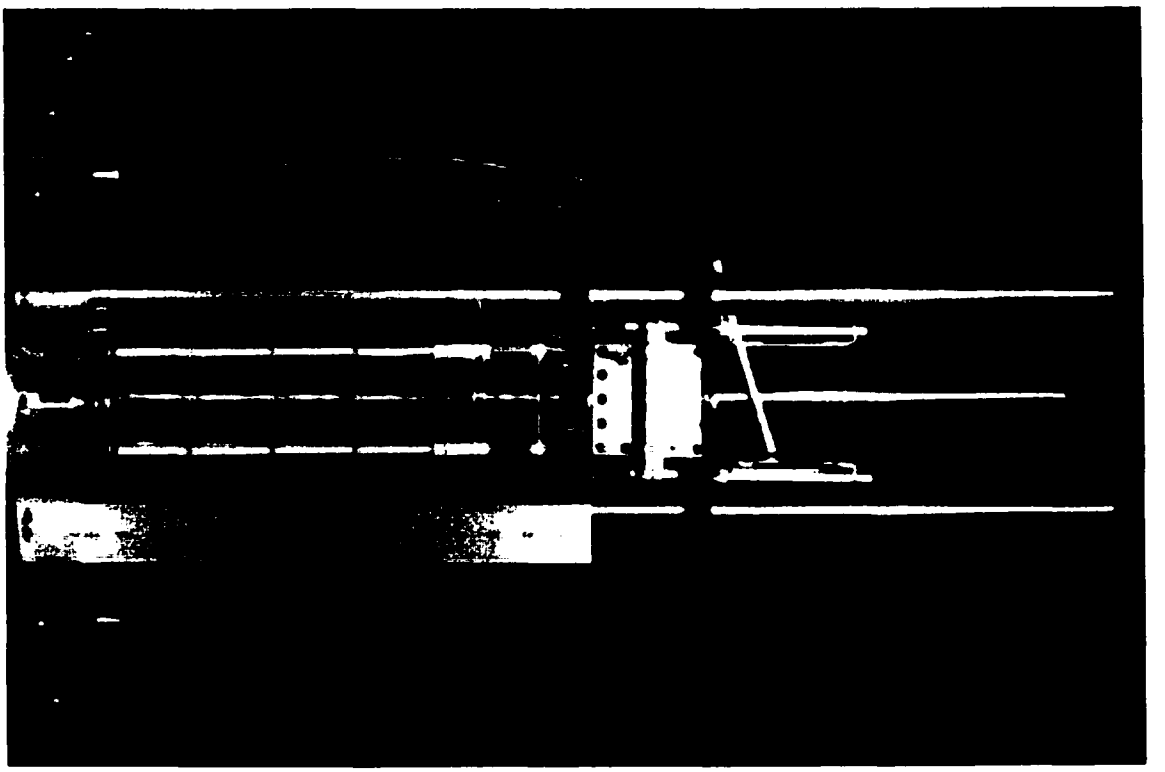

Figure (2.6.3) : **Stark ionizer, lens, and deflectors.** This shows the electrode stack inside the detector the Stark ionizer, the lens and the deflectors.

electrodes. The plates are manufactured without apertures so the desired size for each aperture is drilled into the plates. Stainless steel wires with a diameter of 0.050" are welded to the edge of the plates to connect to the feedthroughs on the front flange of the detector chamber. The Stark ionizer and lens are assembled on a circular stainless steel plate significantly larger than the square plates with four holes for mounting the alumina supporting rods around a 6 mm entrance aperture at the center. The plates are then assembled in order on the alumina rods with alumina spacers added to separate the plates to the proper distance. The plates are mounted through the holes in the corners on alumina rods. The entire stack of

plates is secured with split ring clamps that fit over the alumina rods. The spacers were not used for the large separations of the first three plates. These plates were positioned using the split ring clamps to secure their positions. The Stark ionizer and lens stack is attached to the front flange by three vented bolts holding the circular bottom plate of the assembly. The electrodes are positioned and supported by three 0.5" stainless steel rods mounted with an inside diameter between them equal to the size of the bottom plate of the Stark ionizer and lens stack. The

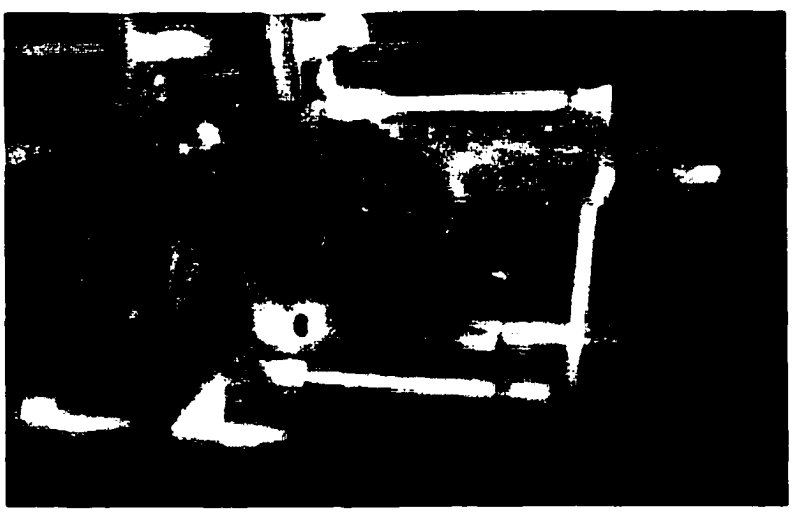

Figure (2.6.4) : **Close-up of deflector assembly.** This is a close-up of the deflector assemby in the detector.

structure is supported by attaching another circular stainless plate, shown at the left of Fig. 2.6.4, which is grounded and the same diameter as the bottom plate to the assembly and attaching it to the three stainless steel rods. A picture of this assembly is shown in Fig. 2.6.3.

The deflector assembly is assembled on another circular stainless plate, with the same diameter as the circular plates in the Stark ionizer, with the horizontal plates on one side and the vertical plates on the other. The plates are mounted using

clamps around another set of four alumina rods with the same spacing as the Stark ionizer and lens stack. The final deflector assembly is then attached to the three stainless steel rods with the horizontal deflectors to the front and the vertical deflectors to the rear. Stainless steel wires with a diameter of 0.050" are welded to the backs of the plates to connect to the feedthroughs on the front flange of the detector chamber. A picture of the assembled deflector assembly is shown in Fig. 2.6.4. The entire electrostatic optical stack of the detector is shown in Fig. 2.6.3. The position and aperture size where appropriate for each of the

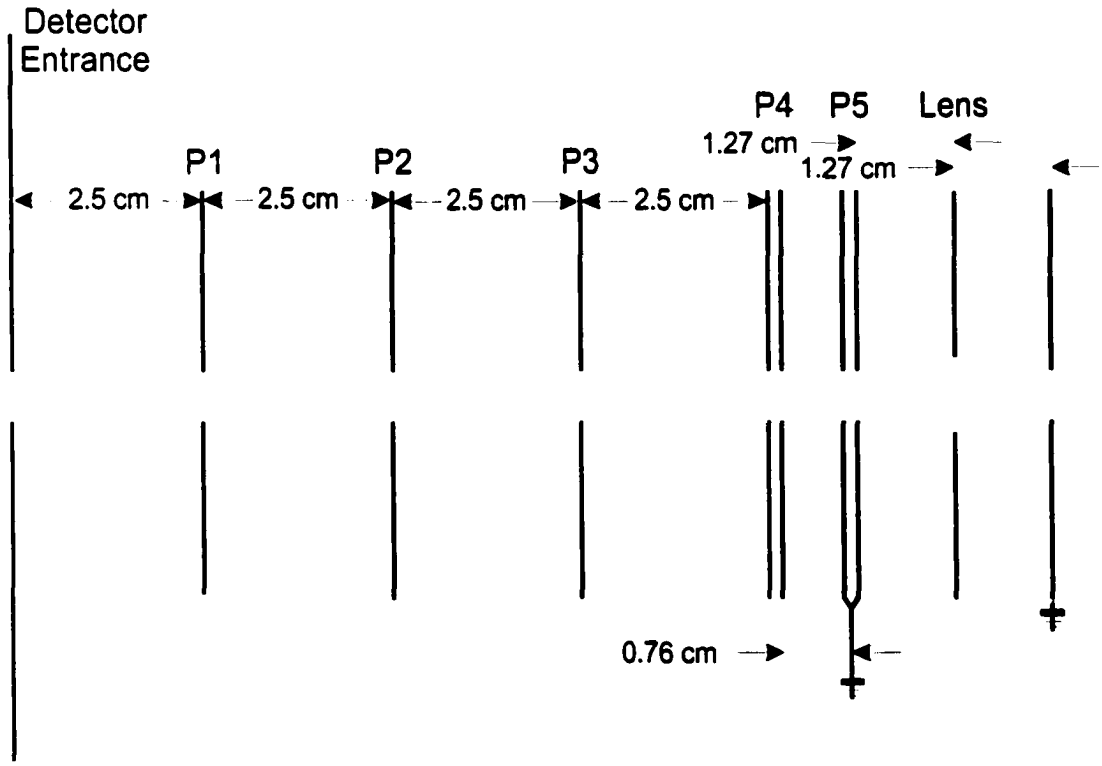

Figure (2.6.5) : **Stark ionizer dimensions.** This shows the dimensions and positions of the elements in the detector. All of the apertures are 6.4 cm in diameter except for the lens element which has a 9.5 cm diameter aperture. P5 and the final plate are both grounded inside of the detector chamber and have no external connections.

electrostatic elements is shown in Fig. 2.6.5.

The detection electronics are mounted on the rear flange. The ion beam viewing system, or BVS, is an elegant device produced by Colutron which has two microchannel plates in a chevron configuration with a phosphor screen and a small glass view port behind them. The dual microchannel plates provide enough gain to image single ions. The size of the viewport and imaging area is approximately 2 cm in diameter. A small video camera is mounted observing this viewport and transmitting a magnified image to a monitor. This allows one to see in real time the shape of an ion beam incident on the viewer from the multiplied electron beam being accelerated and impacting the phosphor. This device has proved to be critical to being able to find and tune the signal from various states and primary ion beam charges and velocities examined in this experiment.

The Channeltron is mounted in a support structure shown in Fig. 2.6.6. The plate directly in front of the Channeltron is held at a potential equal to the potential on the front of the Channeltron, which is held at negative high voltage. This is to ensure that secondary electrons from ions impacting the surface of the Channeltron are collected properly. The entrance aperture to the Channeltron electron multiplier can be replaced with different sized apertures so that a physically large signal can be completely collected, or for a physically small well focused signal can be collected and exclude as much background as possible.

The power supplies providing voltages for the various deflection, ionizing, and focusing plates are designed using modular supplies from Ultravolt. These supplies were chosen for their relatively low cost, high voltage output, ease of control, and

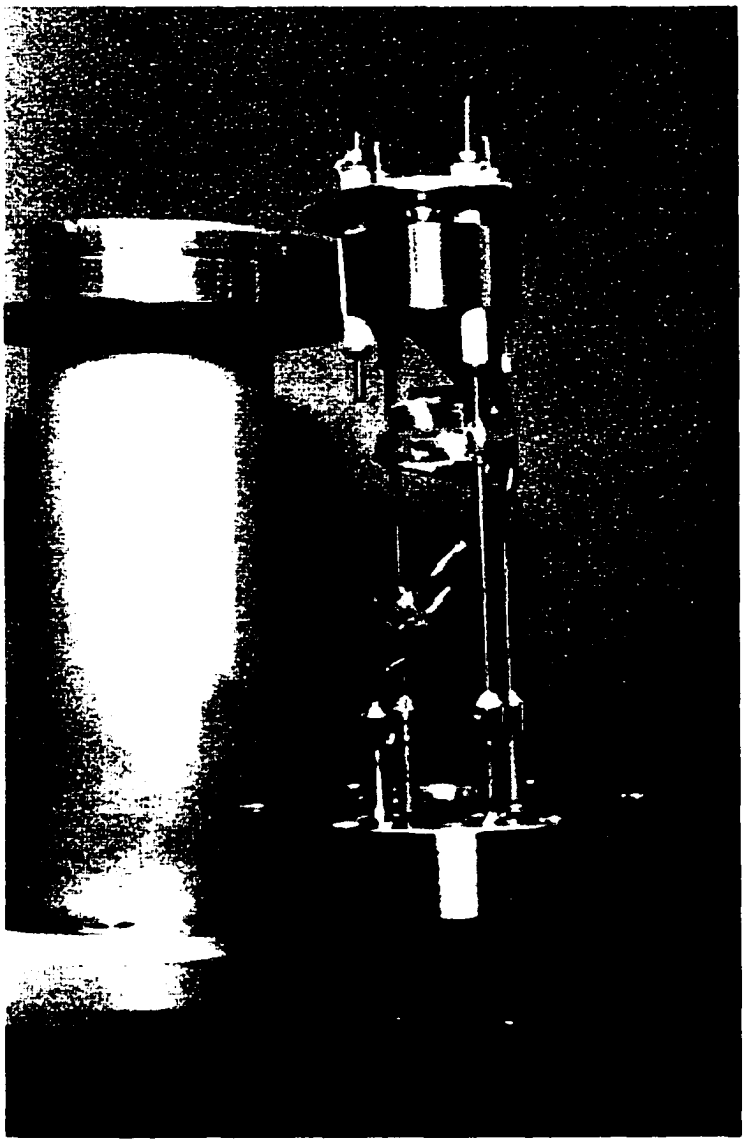

Figure (2.6.6) : **Picture of the Channeltron mounting structure.** This shows the Channeltron (Galileo model 4716) the mounting structure, and the vacuum nipple in which it is housed.

voltage stability. The modular supplies are enclosed in a rack mounted case and controlled with settings from the front panel or a set of voltage inputs. To optimize the collection of either the signal or the charge transfer beam it was necessary to frequently change between two sets of detector voltages. This made it very useful

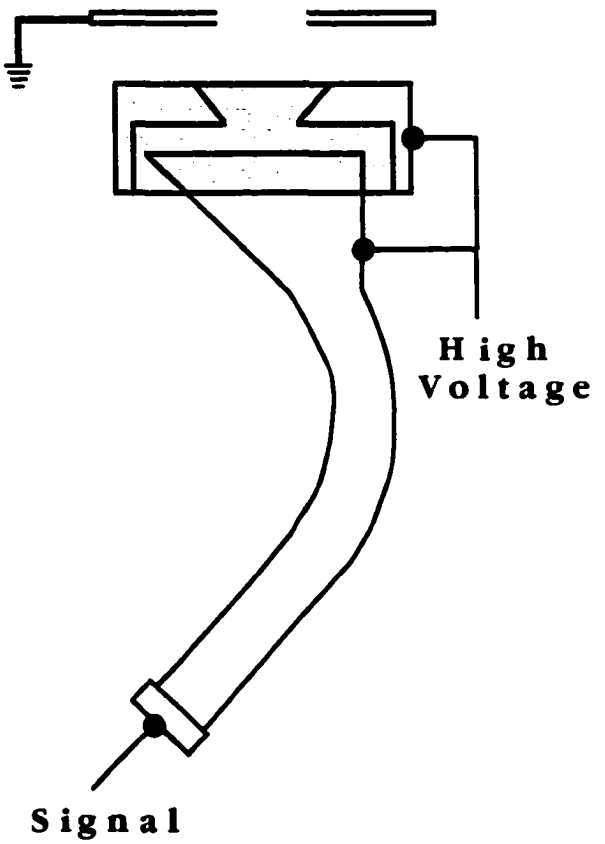

Figure (2.6.7) : **Schematic of Channeltron mounting structure.** This shows the connections to the Channeltron mounting structure pictured in Fig. 2.6.6. The grey rectangle is the metal piece placed over the entrance of the Channeltron and is held at the same voltage as the front of the Channeltron. This is to insure the secondary electrons are collected properly.

to have two easily switched sets of controls. So the power supply was designed to have two distinct settings, one from the front panel dials and another from voltages supplied through a set of BNC inputs. These can be switched by simply flipping a switch on the front panel. The design of this power supply and the control unit

which supplies the input voltages for the second setting are shown in detail in Appendix C.

2.6.3 Ion optics of the detector

The basic purpose of the detector is to ionize the signal, collect and measure it. As described earlier in this chapter and in Chapter 1 three electrodes can be used to perform this task, an electrode held at potential V_D between two grounded electrodes. The ratio of the two separations is three to one. The separation between the first and center plate is the larger of the two separations and is referred to as the large gap, and the second smaller separation is referred to as the small gap. This is so the field in the first region is low enough not to ionize any of the resonantly excited population, while the field in the second region is high enough to ionize all of the resonantly excited population. Any states ionizing in a field of,

$$F_{Large} = \frac{V_D}{3a} \tag{2.6.1}$$

where V_D is the center plate potential and a is the small gap distance, will ionize as soon as they enter the large gap where the potential is approximately zero. These ions will leave the ionizer at about the same speed at which they entered. On the other hand, states which only ionize at the higher field,

$$F_{Small} = \frac{V_D}{a} \tag{2.6.2}$$

will ionize as soon as they enter the small gap. There the potential is $\pm V_D$ and when these ions leave the ionizer their kinetic energy will be increased or decreased by,

$$\Delta KE = qV_D \tag{2.6.3}$$

and this difference in speed differentiates the signal from the other ions that remain after the repeller or which may have formed from other processes.

An example to illustrate this design is shown in Fig. 2.6.8 for a C^{3+} primary ion beam. The three beams that enter the detector, the remaining primary ion beam, the charge transfer beam and the signal beam and their respective energies, are shown with the plates and the ideal fields and voltages along the ion beam path in Fig. 2.6.8. The remaining primary ion beam and the non-excited charge transfer beam have the same charge throughout the Stark ionizer and thus they have the same energy when they leave as when they enter. However, the resonantly excited

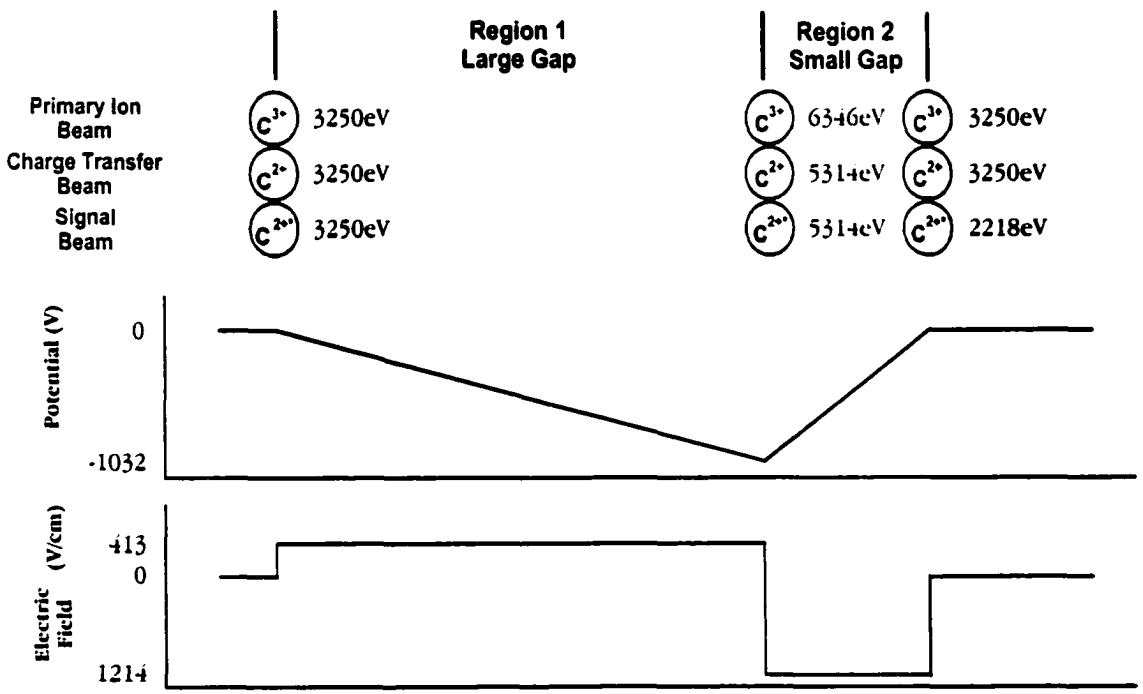

Figure (2.6.8) : **Illustration of Stark ionizer concept.** This shows a C^{3+} ion beam to illustrate the concept of the Strak ionizer in the detector.

Rydberg ions are ionized as they enter the second region of the Stark ionizer and are reduced in energy by $\Delta KE = e V_D = 1032$ eV because of the difference in charge

of the signal beam in the two regions of the ionizer. These ions have a unique energy per charge in the system and can thus be differentiated by their deflection in the field following the Stark ionizer.

The Stark ionizer, as can be seen in the earlier Fig. 2.6.3 and schematically in Fig. 2.6.5, has a large number of plates with apertures which apply fields to the ions in the longitudinal direction when held at differing potentials. The original purpose of the elements shown in Fig. 2.6.3 was to form two interchangeable Stark ionizers which could be used to detect Rydberg states over a wide range of ionization fields. The first of these Stark ionizers is what we call the large gap Stark ionizer which uses the circular plate holding the Stark ionizer stack at the entrance of the detector tee as the first grounded plate, P3 as the high voltage plate and P4 as the grounded exit plate with P5 also grounded. The other plates in the device are used to make the field in the entry region more uniform by holding P1 and P2 at 1/3 and 2/3 the voltage on P3 respectively. This prevents distortion of the fields by the grounded stainless rods supporting the device. The second configuration is what we call the small gap Stark ionizer which uses P3 as the first grounded plate, P4 as the high voltage plate, and P5 which is grounded internally as the exit plate. The primary difference between the two configurations is the scale of the geometry. The long gap Stark ionizer has a final gap effective distance of 2.51 cm and thus has a much lower field for the same applied voltage than the short gap Stark ionizer which has a physical gap of 0.76 cm and an effective distance of 0.88 cm. The effective distances for each of the ionizers is determined in the same way as for the repeller earlier in this chapter. A SIMION simulation of the field along the center

axis for a 1000 V potential on the center plate of the ionizer, this calculation along with the maximum field is shown in Fig. 2.6.9. The effective distances reported are simply,

$$d_{eff} = \frac{V_D}{F_{Max}} = \frac{1000\,\mathrm{V}}{F_{Max}} \tag{2.6.4}$$

where d_{eff} is the effective distance and F_{Max} is the maximum field reached in the simulation. Thus the short gap Stark ionizer can be used to apply a much higher field without exceeding the maximum voltage for which the feedthroughs are rated, 5000 V.

The first consideration in the ion optics of the detector needs to be the voltage applied creating the field in the ionization region. This needs to be considered first because it is determined by the state being measured and the rest of the elements need to be set so the signal can be collected with this field being applied to the ionizer. The field at which a state begins to ionize is,

$$F_D = \frac{1}{9}\frac{q^3}{n^4}\,\mathrm{a.u.} = 5.71\mathrm{x}10^8\,\frac{q^3}{n^4}\,\frac{\mathrm{V}}{\mathrm{cm}} \tag{2.6.5}$$

and the field needed to completely ionize a particular state is.

$$F_D = \frac{2}{9}\frac{q^3}{n^4}\,\mathrm{a.u.} = 1.14\mathrm{x}10^9\,\frac{q^3}{n^4}\,\frac{\mathrm{V}}{\mathrm{cm}} \tag{2.6.6}$$

as derived in section 2.4.3. The setting of the voltage on the center plate of the Stark ionizer for each of the states measured was set above the point at which all of the state is ionized.

The field at which the state completely ionizes can be measured by carefully

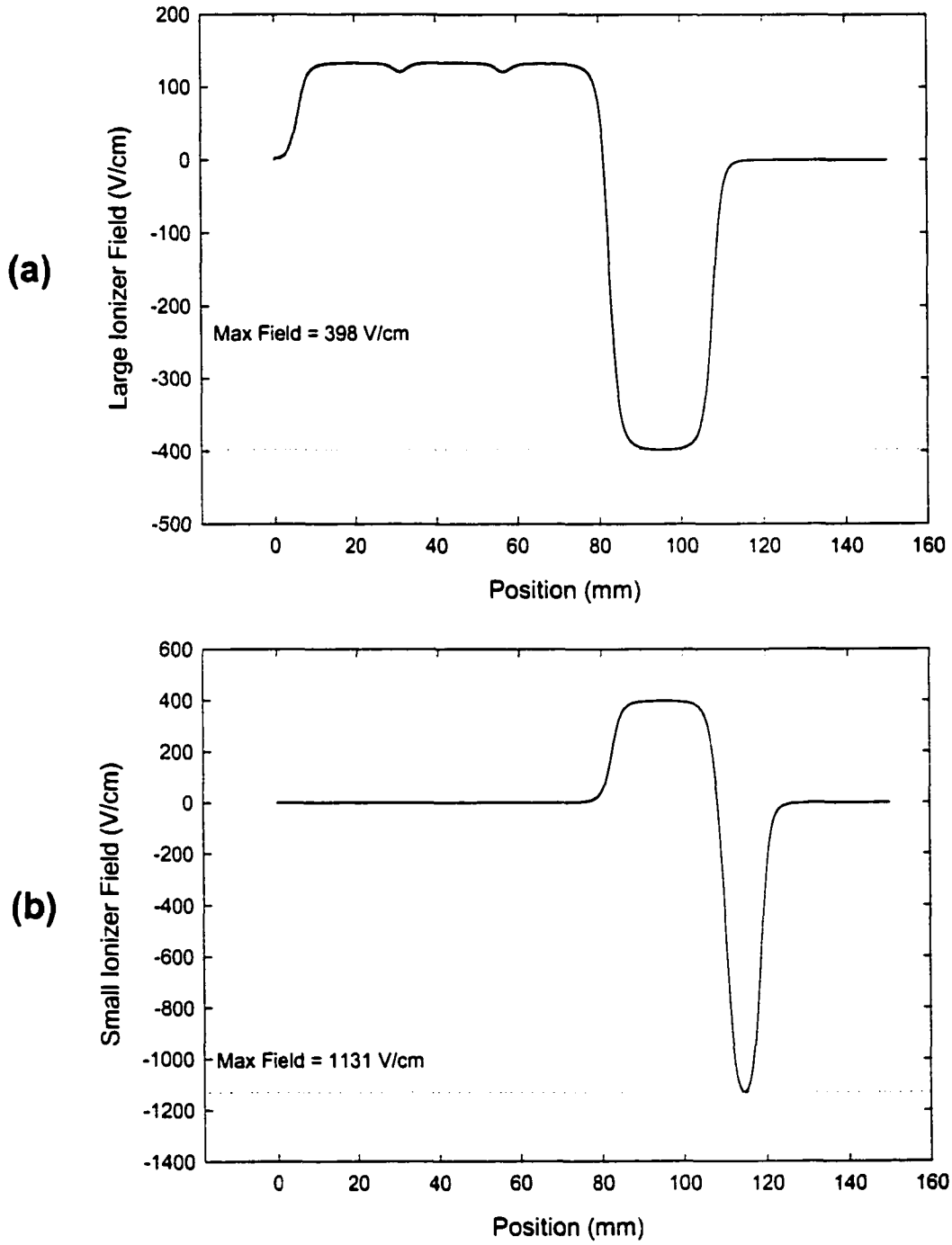

Figure (2.6.9) : **Field profile of detector large and small Stark ionizers.** These are the SIMION simulation results for the field resulting from a potential of 1000 V applied to the middle plate of the ionizers used to calculate the effective distances. The effective distances are 2.51 cm for the large Stark ionizer panel (a), and 0.88 cm for the small Stark ionizer panel (b).

tuning the Stark ionizer and the detector for a range of fields and determining when the detected signal amplitude flattens as a function of field. At this point increasing the field does not increase the laser resonant signal thus at this field all the signal is being ionized. As the field increases further another check can be made by examining when the signal begins to decrease. This can be interpreted as the point at which the state being measured begins to be ionized in the pre-ionization region. The signal versus the field in the ionization region for both H I n=10-30 and C III n=29-71 signals are shown in Fig. 2.6.10. This figure shows the predicted values of the field for which the state is completely ionized and the field at which the state begins to ionize in the pre-ionization region. These are shown by dotted vertical lines and agree quite well for when the small gap begins and completely ionizes the upper state, but poorly for when the states are removed by the large gap. The reason for disagreement on the high field side is not understood but could possibly be due to focusing effects in the Stark ionizer when these relatively large fields are applied. This is a speculation however, and the data we have for this does not give any direct information on why the disagreement between measurement and Stark ionization theory occurs on the high field side. However, this is not relevant to the measurement since settings near point B were used, and the absolute signal size does not matter as long as the signal to noise is usable.

2.6.4 Application to charged Rydberg states

This relatively simple process of ionizing the laser excited Rydberg state becomes considerably more difficult to implement when all of the beams entering the detector are charged. The short gap Stark ionizer was used for nearly all of the

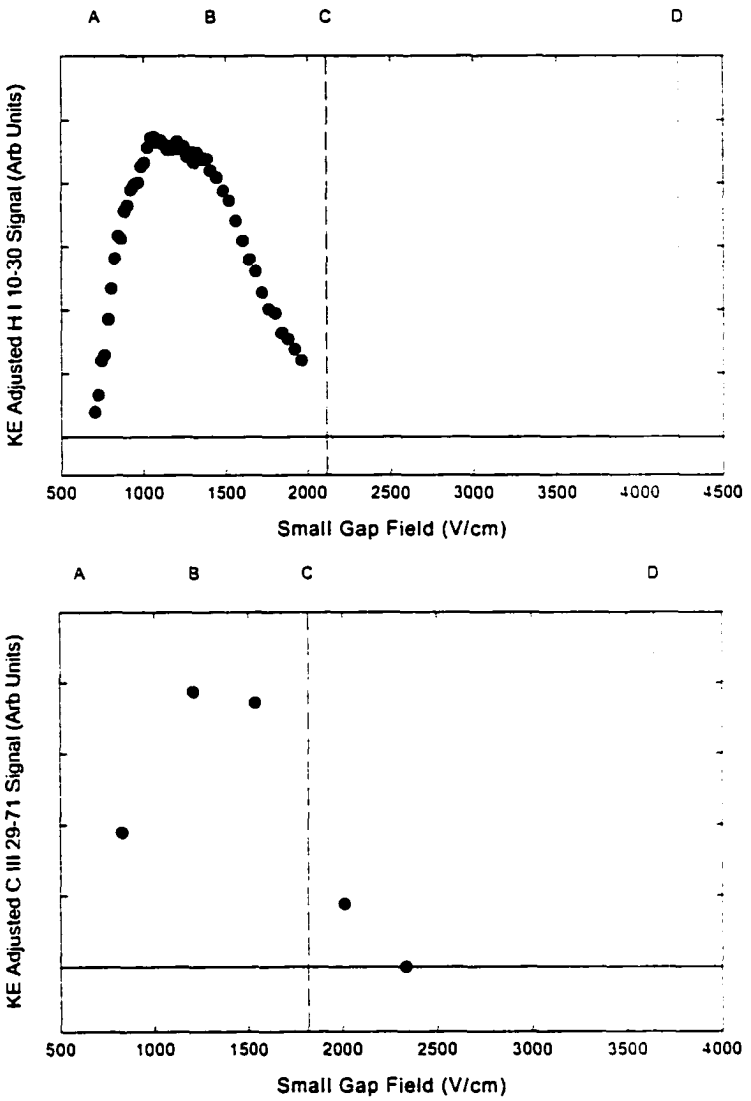

Figure (2.6.10) : **Signal versus ionization field.** These plots show the relationship between the signal and the ionization field applied in the Stark ionizer. The vertical lines show important fields relating to the ionization of Rydberg states, A is where the small gap field theoretically begins to ionize the upper state of the laser transition, B is where the small gap completely ionizes the upper state, C is where the large gap begins to ionize the upper state and D is where the large gap completely ionizes the upper state. The signals are adjusted to correct for the difference in detection efficiency of ions with different kinetic energy.

measurements made in this experiment. The short gap was chosen so that the ratio between the upper and lower state could be kept as low as possible so the transition probability would be as high as possible as calculated using Eqn. 2.5.10. The ion optics involved with the multiply charged signal ions created in the Stark ionizer become critical for the signals observed in this experiment. In the device the fields are not uniform at the apertures and thus at each aperture focusing of the ions will occur and must be taken into account. Particularly at the plate where the ionization of the signal (the resonantly excited states) takes place the uniformity, or non-uniformity of the field is of critical importance to both how the ionization takes place and how the ions are focused. Specifically the ionizing region of the Stark ionizer was designed to have fields as uniform as possible while keeping an angular acceptance as large as possible, to allow as much ion beam as possible into the detector. The compromise between these two competing concerns was to make the apertures in the plates are no larger than the spacing between the plates and if possible much smaller than the spacing between plates. This compromise was chosen because the field non-uniformity as simulated by SIMION was found to increase dramatically when the ratio of the aperture size to the distance to the next grounded plate increased particularly if the aperture is larger than the spacing between the plates. To reduce the focusing effect of the non-uniform field on all of the ions and in particular the signal ions a negative voltage is applied to the plate controlling the ionization field. This reduces the focusing power of the non-uniform field at the aperture because the ions are at their highest velocity at the aperture.

A simple aperture lens was incorporated after the ionizing region to refocus the signal ions to as small a spot size as possible. However, while the placement of the lens was not of great importance when the charge transfer beam was neutral, the placement proved critical when all of the beams entering the detector were charged. The lens was placed close to the end of the Stark ionizer both for the convenience of mounting and to get the largest acceptance of the beam from the ionizer. However when the charge transfer beam is charged the focusing effects of the short gap ionizer focus the signal ions to a point well before the detection plane. This can be seen in Fig. 2.6.11, a SIMION simulation of the small gap Stark ionizer for a C III signal beam which is ionized in the Stark ionizer. Since a simple electrostatic lens can only be used as a converging focusing element and not as a diverging element, the single lens in this design cannot focus the signal at the detection plane when the charge transfer beam is charged. The flexibility of the Stark ionizer design with the additional electrodes allowed a solution to this problem. To focus the signal correctly using the short gap ionizer, the large gap plates are used to pre-focus the ions before they enter the short gap Stark ionizer. Specifically, P1 in Fig. 2.6.11 is raised to a potential to focus the ions into the short gap Stark ionizer while the entrance plane, P3, and P2 are at ground and with P1 create a simple aperture lens. The pre-focused beam signal ions have a focus before the lens element and thus can be refocused at the detector plane for a wide range of charges, beam energies and applied ionization fields.

Starting points for tuning the detector using the short gap ionizer in the manner described above for a particular charge and energy beam are given by the

following rules of thumb. The first lens with P1 as the center element is set by the following rule of thumb,

$$V_{P1} = 0.62\frac{KE}{q-1} \tag{2.6.7}$$

with P2 grounded. A comparison of this rule of thumb and the final settings for a

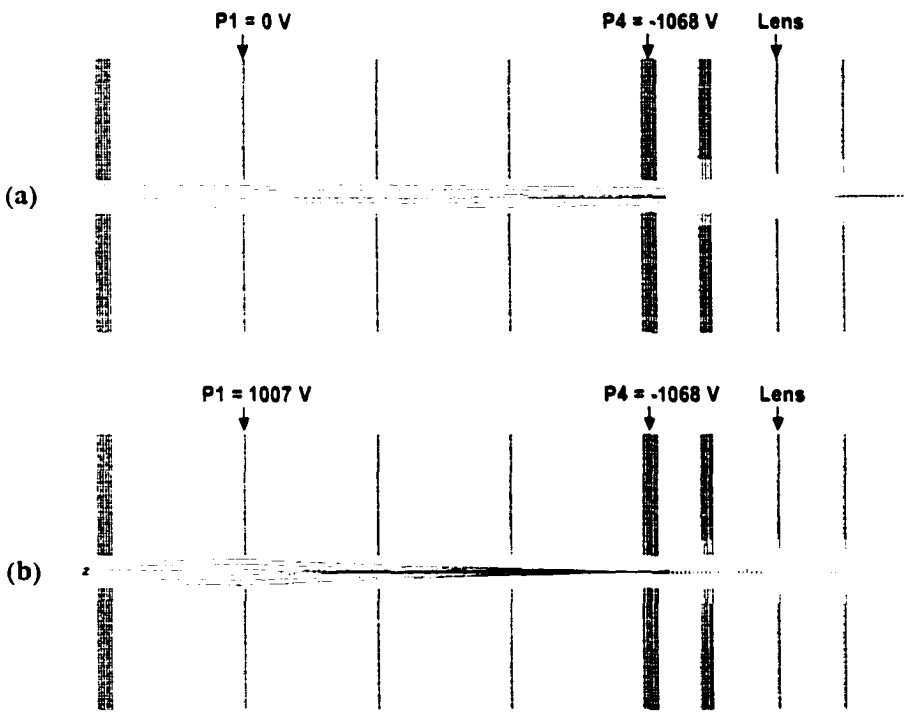

Figure (2.6.11) : **SIMION simulation of C III, n=71 being ionized in detector.** This shows a SIMION simulation of the behavior of a C III, n=71 ion beam being ionized in the detector. Panel (a) shows the effect with voltage only on P4. Panel (b) shows the effect of adding the rule of thumb voltage to P1. The change from solid lines to dotted lines occurs at the point where the C III, n=71 signal is ionized and becomes a C^{3+} beam. Note the focus of the beam in panel (a) occurs after the lens but before the CEM (off the page to the right), while in panel (b) the focus occurs before the lens, so can be refocussed at the CEM.

wide range of ions is given in Table 2.6.1 and shown in Fig. 2.6.12. P3 is grounded to create the entry to the short gap Stark ionizer and P4 is set so the field in the short gap ionizes the resonantly excited state. The final lens voltage is then set by the following rule of thumb,

$$V_{Lens} = 0.63\frac{KE + V_{P4}}{q} \tag{2.6.8}$$

where V(P4) is the voltage on the short gap Stark ionizer and it is multiplied by the

Table 2.6.1 : **Measured values of applied voltages to P1, P4 and Lens.** This table lists the values of P1, P4, and Lens used to measure a signal and compared to the rule of thumb values in Fig. 2.6.12.

Ion	n_l - n_u	KE_{Total}	P1 (V)	P4 (V)	Lens (V)
C^{2+}	19-51	3250	1936	-1291	720
C^{3+}	29-71	3250	917	-1225	376
Ar^{3+}	29-71	3250	917	-1225	376
Xe^{3+}	29-71	3250	917	-1225	376
C^{4+}	37-85	3250	605	-1440	342
Ne^{6+}	55-133	5500	742	-894	324
Ar^{7+}	64-119	10000	1110	-1896	742
Ar^{8+}	73-161	10000	1017	-950	594
Ar^{9+}	80-169	10000	843	-1008	473
Ar^{11+}	102-200	10000	668	-1349	253

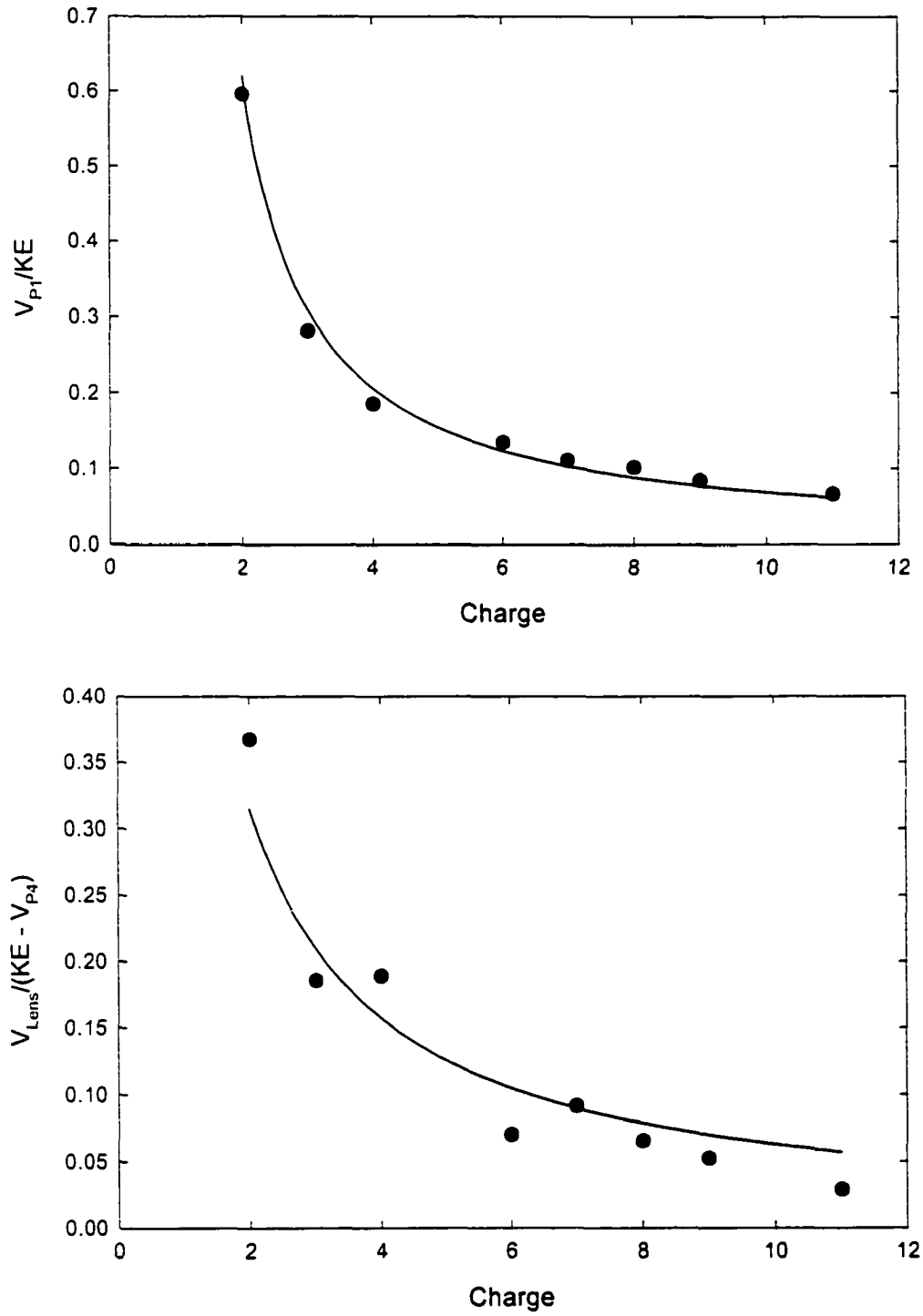

Figure (2.6.12) : **Comparison of rule of thumb and measured values for detector voltages.** These plots show the comparison between the rule of thumb calculated values and the final values used for the measurement for P1 and Lens in the detector for a number of ions and velocities, as listed in Table 2.6.1.

one for the single charge change in the Stark ionizer to make it an energy. A comparison of this rule of thumb and the final settings for a wide range of ions is given in Table 2.6.1. These settings will only be close to the final settings if the voltage on P4 is within a range that fully separates the signal ions from the remaining primary ion beam, but is not so large that the ion optics set in this way cannot compensate for the focusing effects of the Stark ionizer, this is usually a large range of voltages from about -800V to about -2000V.

2.6.5 Detection of the signal and charge transfer ions

As stated before the detector is required to perform two different measurements on the ion beams, the laser resonant signal and the charge transfer beam. This is to allow the measurement of the ratio of these two quantities for the range of targets being investigated. Thus, two sets of voltages are used in the detector. The best way to get an acceptable focus for the charge transfer beam and the signal beam is to tune the voltages while viewing each of the beams at the detector position. This is done using the BVS and setting the voltages individually for each beam using the switch in the power supply to change between beams and settings. This is reasonably simple to do for the charge transfer beam since it has a relatively high current. The signal ions, however, have a low enough current that was not possible to make out the shape of the beam on the BVS. To allow the signal ions to be focused optimally an alternate method of tuning the focus was found. This method involved turning off the repeller, which caused a substantial background to enter the detection region. This background for a target such as 14F was substantial enough that the background could be viewed on the BVS and optimally

focused. The repeller was then turned back on and the majority of the background was eliminated. Using this method to tune the detector worked very successfully for the entire range of charges and velocities investigated. The final settings for the measurement were then determined by reversing the voltages to the deflection plates so that the signal was incident on the CEM and then scanning the signal over a range of deflection voltages in the horizontal and vertical directions and choosing the peak in each direction.

Any fluctuation in the measurement of either the signal ions or the charge transfer beam, which does not affect the other beam, is critically damaging to the measurement being made, so all efforts were made to keep these measurements from varying independently. One concern was the gain response of the Channeltron across its face. If this was not uniform it could affect the measurement of the "signal" and the charge transfer if the position on the entrance of the Channeltron varied during the measurements over the full range of target states. This was found to be a problem for the original orientation of the CEM, as seen in Fig. 2.6.13 (a). This was corrected by rotating the orientation of the Channeltron by 180°. The original and final orientation of the Channeltron in relation to the incident signal ions is shown in Fig. 2.6.14. The final positional sensitivity was of the Channeltron is shown in Fig. 2.6.13 (b), which was measured using a C^{2+} primary ion beam focused to a 0.2 cm diameter spot and measuring the DC signal from the CEM versus the deflection voltages to map the detector sensitivity. This is important to the measurement because if there is a non uniformity of the response with the position of the ions entering the Channeltron then a small

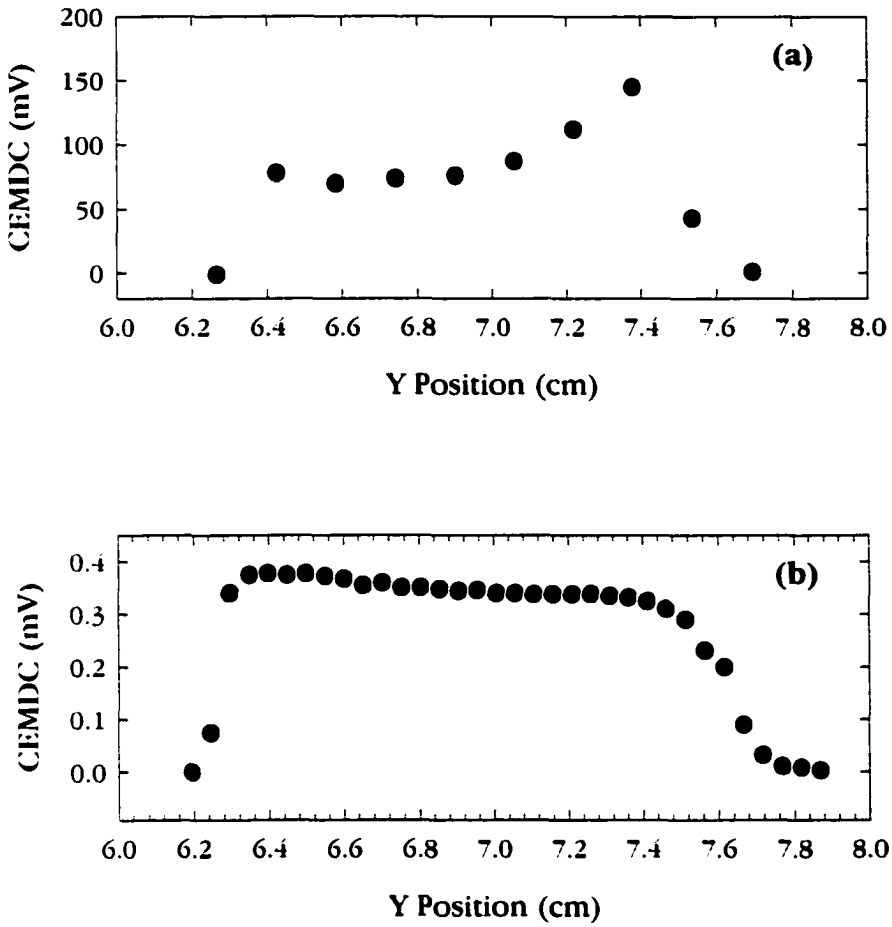

Figure (2.6.13) : **Positional sensitivity of the CEM used for measurement.** This shows the measured DC signal as a function of vertical and horizontal deflection for a C^{2+} ion beam focused to a 0.2 cm spot size. Panel (a) is in the original orientation, which shows the variation across the face of the Channeltron. Panel (b) is in the final orientation after the Channeltron was rotated. This shows the improvement in the uniformity of the detector in the final orientation.

change in the position can change the signal size disproportionately.

2.6.6 Conclusions

The flexibility of the detector electrode arrangement allows it to measure the

RESIS signals for a wide range of beam energies and charges. The design also allows the detection of a wide range of upper states (from about n = 20 to 50 in q = 1). This flexibility allowed a mode of operation to overcome the position of the lens element and operate using the small gap ionizer for primary ion beams with

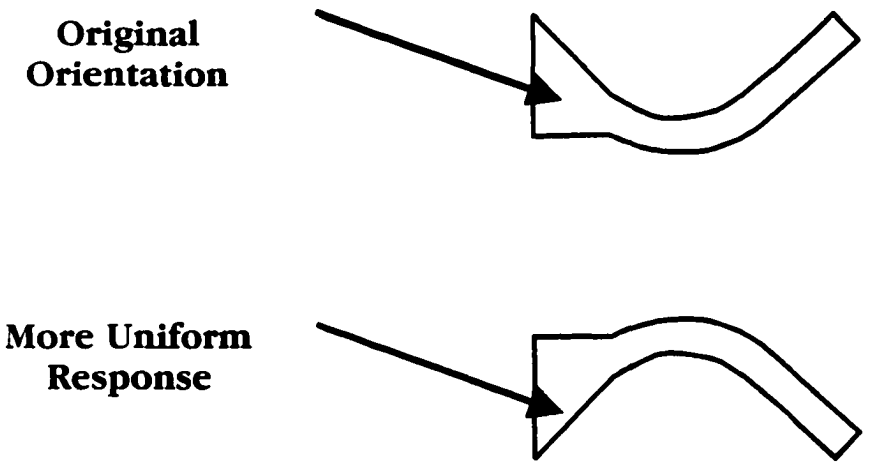

Figure (2.6.14) : **Original and final orientation of Channeltron.** This shows the original orientation of the Channeltron which led to the non-uniform response seen in Fig. 2.6.13 (a). The final orientation is shown in the bottom figure which has a much more uniform response as seen in Fig. 2.6.13 (b).

$q>1$. Using this arrangement of electrodes the detector succeeded in making measurements of q=1-11 ions with a wide range of velocities at q=3. The addition of the beam viewing system assisted greatly in visualizing how the ion optics affected the various beams and allowed the easy focusing of the signal and charge

transfer beams which would have been extremely difficult without such a device. The ability to focus and isolate the signal allowed measurements of RESIS signals when the primary ion beam transported to the detector was only on the order of 1 nA.

Chapter 3 : Measurement and comparison to theory

3.1 Introduction

At this point it is helpful to review the general procedure used to measure the charge capture resonance in this experiment. A primary ion beam of charge q with velocity v is directed through the rubidium Rydberg target where a charge capture collision can occur. Most of the remaining primary ion beam is blocked by the repeller and the q-1 charge transfer beam continues to the laser interaction region, or LIR. The single product state being measured in the charge transfer beam, n_p, is excited to a very highly excited state, and that laser excited state is Stark ionized to produce a "signal" ion current. That signal current and the charge transfer beam are measured in quick succession and their ratio is taken. This is the fundamental measured quantity in this experiment. Measurement of this ratio as a function of the Rydberg target binding energy reveals the "energy resonance" characterizing the capture process.

3.2 The measurement process

In order to clarify the specific procedure used to measure the signal to charge transfer ratio, it will be described in detail for a specific ion, $^{13}C^{3+}$ at v=0.100 a.u (having a total kinetic energy of 3250 eV). First, the charge transfer beam is deflected onto the BVS (Beam viewing system) in the detector. The repeller lenses are then set to the rule of thumb voltages described earlier, in section 2.4.2. For

our example, with a C^{3+} primary ion beam, these voltages are 975V for the first lens and 1333V for the second repeller lens element. The deflectors immediately following the repeller are used to redirect the beam if necessary, so it is again visible on the BVS. The repeller voltages are then carefully adjusted to provide the brightest and best focused charge transfer beam possible while keeping the voltage of one of the lenses high enough to repel the primary ion beam. For this measurement the voltages after this adjustment for this example were 1125 V for the first and 1275 V for the second repeller lens element. The deflectors immediately after the repeller were set to -63.7 V on the top plate, 0.9 V on the bottom plate, 0.9 V on the left plate, and -25 V on the right plate to steer the beam into the detector.

After the repeller has been adjusted, all the repeller voltages are turned off and the detector power supply is switched to the signal control settings. The "signal" voltages are optimized using the "background" of highly excited Rydberg states created directly by charge transfer collisions with the Rydberg target. The "background" was used to optimize the detector focusing because the laser-excited signals were too weak to view directly on the beam viewing system. The "background" states are normally ionized and blocked by the repeller, but with the repeller off they have sufficient intensity to allow the adjustment of the detector voltages for an optimal focus. An additional advantage of this method is that it does not require the laser to be tuned to a resonance before tuning the detector. Higher target ($n_t \geq 14$) states work best for tuning the detector using this method because they produce a larger "background" due to their larger portion of capture

population in states near the upper state of the laser resonance.

To begin the tuning of the detector, the voltages are set to the rule of thumb values described in section 2.6.4 for the detection of the signal. For our example these values are P1=1008V, P2=P3=0V, P4=-1044V and Lens=441V the x- and y-deflection are adjusted so the background signal which is being tuned is near the center of the BVS. During the tuning process the ionization plate voltage, P4 in Fig. 2.6.5, is fixed at the value calculated to provide complete ionization of the upper state of the laser resonance by Eqn 2.6.6. The first plate, P1 in Fig. 2.6.5, and the lens voltages are then used to optimize the focus of the "background" starting from the rule-of-thumb settings above. Once the final values for these voltages are set then the detector power supply is switched back to the charge transfer settings. The P4 voltage remains unchanged by the switch. The charge transfer beam is re-tuned to a tight focus using the first plate and lens voltages to compensate for the P4 voltage. This tuning process results in the selection of two alternate sets of detector voltages P1, V_L, V_x, and V_y which can be selected using a switch on the power supply unit.

The connections to the vertical deflection plates in the detector are then reversed in polarity to deflect the charge transfer ions onto the CEM rather than the BVS. The *x*- and *y*-deflections are then adjusted to maximize the signal from the CEM. The detector controls are switched back to the signal controls and the *x*- and *y*-deflections are adjusted to maximize the background signal which is syncronous to the target chopping. This step completes the tuning of the detector for the signal and charge transfer signal measurements.

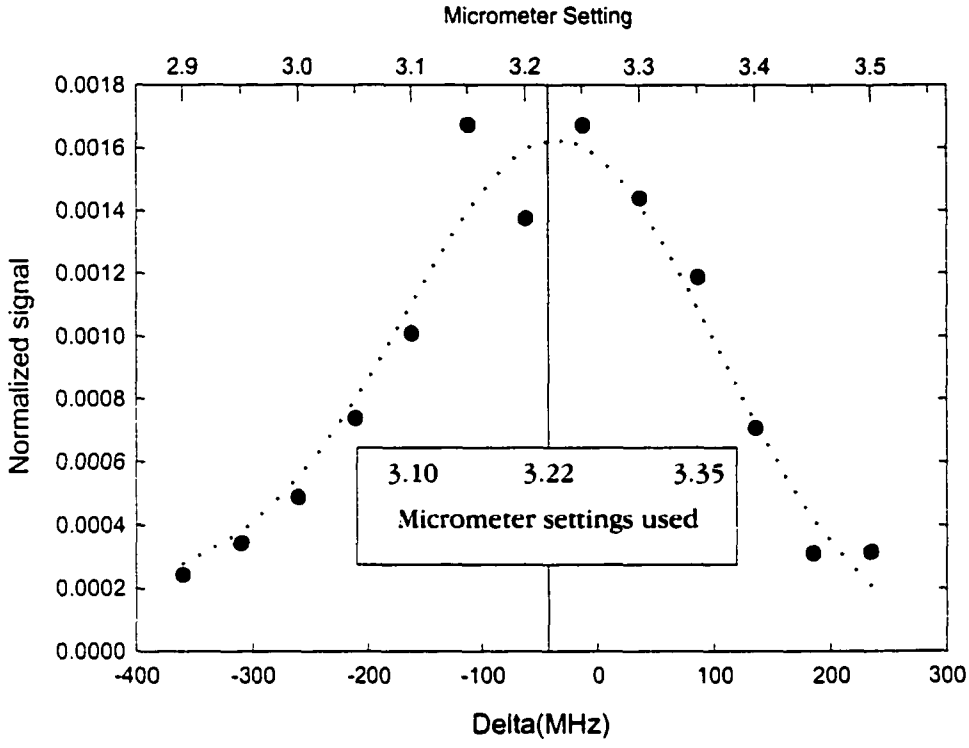

Figure (3.2.1) : **Scan of laser resonance used to determine data collection positions.** This shows a scan of the laser resonance for the n-n' = 29-71 transition in C III which was used to decide where to take the data points used to monitor the signal size. The three vertical lines show the three positions where the data was taken. The dotted curve is a fit of the data to guide the eye. Delta measures the frequency difference from line center.

The repeller voltages are then turned on to reduce the primary ion beam and the background signal ions. The angle of the mirror in the LIR is adjusted to be near the predicted resonance angle and the CO_2 laser shutter is opened. The intersection angle of the laser and the charge transfer beam is scanned by small increments until a signal is measured by the CEM. The signal, in this case, is the CEM current synchronous with chopping the CO_2 laser. The laser resonance signal is then carefully measured versus the micrometer setting of the rotary stage drive (directly related to the stage angle). Three micrometer settings are chosen for

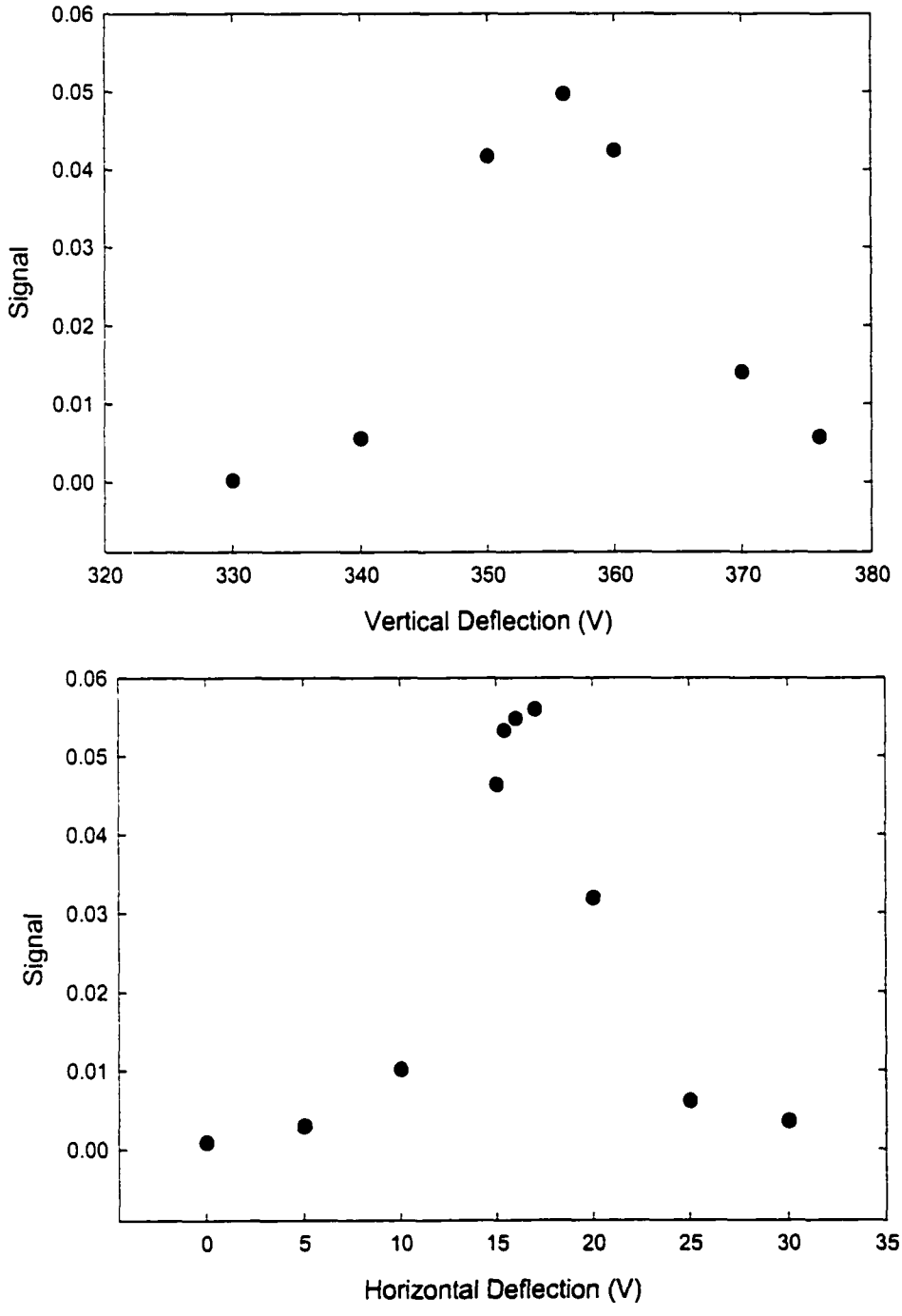

Figure (3.2.2) : **Signal versus deflection voltage.** This shows a typical scan of the horizontal and vertical deflection voltages for the signal. The signal shown is the 29-71 resonance in C III.

measurement of the laser signal to check the stability of its position during the ratio measurement. The detailed measurement of the C III n-n' = 29-71 laser resonance and the three positions chosen are shown in Fig. 3.2.1. The angle is then set to the peak of the laser resonance and scans of the x- and y-deflection voltages are taken to set them optimally for the signal. These scans for the C III measurement are shown in Fig. 3.2.2.

After these set-up procedures are complete, the measurement of the ratio is made using the following procedure. The charge transfer beam and the blue fluorescence of the Rydberg target are measured twice on lock-in amplifiers, connected to the amplified output of the CEM and the PMT monitoring the target fluorescence, using the reference from the chopper on the second laser of the target excitation (172 Hz). Each measurement is an average over 10 seconds. The CO_2 laser power is noted and recorded at the same time. The voltage applied to the CEM is set at a particular value for the charge transfer measurement, in the case of C III this voltage is -800 V. The laser is then directed into the LIR at the first of the selected monitoring angles and the detector voltages are switched to the signal settings. The reference to the lock-in is changed to the CO_2 laser chopper (510 Hz), and the voltage on the CEM is increased, in the case of C III to -1100 V. The increase of the CEM voltage is necessary because the laser excitation signal is much smaller than the charge transfer signal and requires more gain. A measurement of the signal and the blue fluorescence was made and recorded twice for each of the three monitoring angles. The detector and CEM voltages were then switched back to the charge transfer beam settings and two additional

measurements were made and recorded while the laser power was again noted and recorded. An example of one of these measurement sets, which we will denote a "data set", for C III and n_t = 14 is shown in Fig. 3.2.3.

To determine the ratio from this "data set" first each measured signal is divided by the corresponding blue fluorescence signal to correct for fluctuations in the target density. The laser signal amplitude was then determined by fitting the six data points, taken at the three angles, to a Gaussian of fixed width. The fixed width

```
dfcf5p18a.out
04/05/00
07:58:15 1
File: dfcf5p18.a
Target: 14F
Charge Capture
--------------
Xsig -8.7511e-04 , Ysig -1.0531e-02 , Blue 242.49 , Red 19.46 #pts: 10
Xsig -9.0903e-04 , Ysig -1.0280e-02 , Blue 239.61 , Red 19.13 #pts: 10
Signal
------
Angle[1], 3.35 : Xsig 7.7162e-04 , Ysig 2.4892e-04 , Blue 239.44 , Red 19.26 #pts: 10
Angle[1], 3.35 : Xsig 8.6551e-04 , Ysig 1.1882e-04 , Blue 238.55 , Red 19.28 #pts: 10
Angle[2], 3.22 : Xsig 1.1011e-03 , Ysig 1.5706e-04 , Blue 229.90 , Red 18.40 #pts: 10
Angle[2], 3.22 : Xsig 1.1650e-03 , Ysig 7.4058e-05 , Blue 231.18 , Red 18.12 #pts: 10
Angle[3], 3.10 : Xsig 4.7249e-04 , Ysig 1.8314e-05 , Blue 222.20 , Red 17.67 #pts: 10
Angle[3], 3.10 : Xsig 4.4701e-04 , Ysig -5.1205e-05 , Blue 220.82 , Red 17.52 #pts: 10
Charge Capture
--------------
Xsig -9.4565e-04 , Ysig -8.2689e-03 , Blue 210.69 , Red 16.52 #pts: 10
Xsig -8.1428e-04 , Ysig -7.9072e-03 , Blue 205.51 , Red 15.83 #pts: 10
```

Figure (3.2.3) : **Example of a typical data set.** This is an example of a typical data set. This particular set is for a C III 29-71 transition for a collision with a n_t=14 target. The charge capture signal is the YSig value under the Charge Capture heading (XSig is 90° out of phase), and the laser resonance signal is the XSig under the Signal heading (and Ysig is 90° out of phase). Blue is always the blue fluorescence of the target. Red is the target fluorescence at the third laser wavelength and is not used. Note the reference to the lock-in amplifier is changed between the Charge Capture and Signal headings as described in the text.

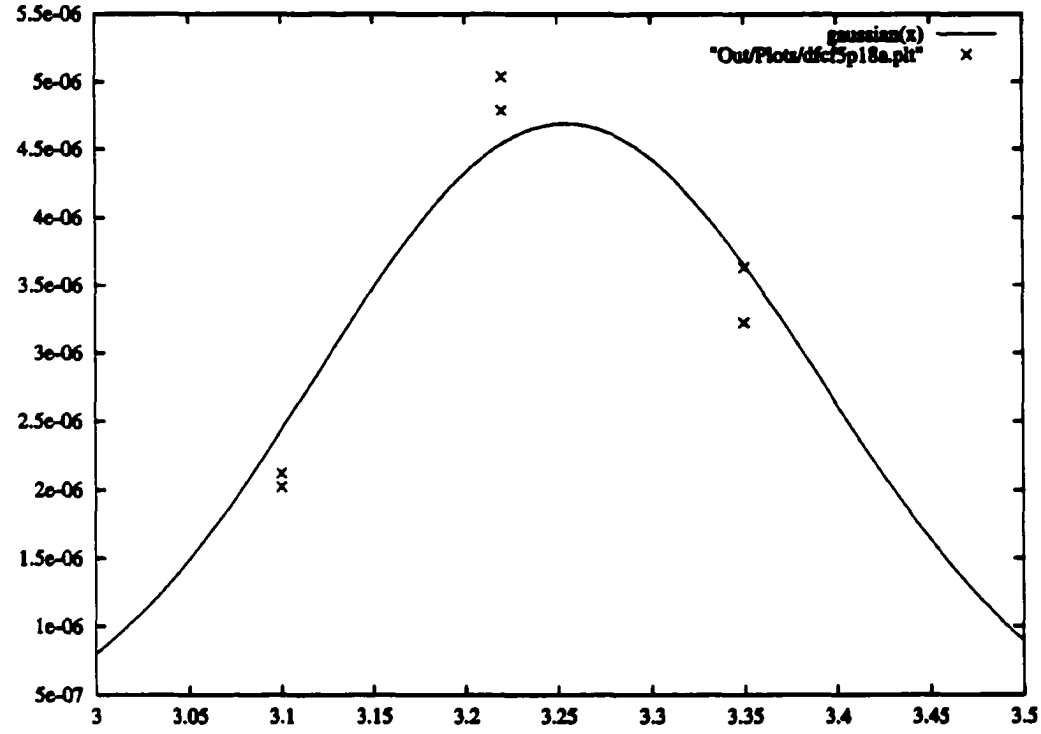

Figure (3.2.4) : **Typical fit of a single "data set".** This shows the fit and data points for a typical C III 29-71 laser transition "data set". This set is for $n_t = 14$.

used for the fit is determined by the fitted width of the detailed scans taken at the beginning and end of the measurement of each ion. Thus the fit of the laser signal for each measurement gives two parameters, the position and the amplitude of the resonance. If the position was more than two standard deviations from the average position of the fits, due to noise in the data, the curve is refit fixing the position of the resonance and fitting only the amplitude. The position used in the refit was the average position of the other fits of the resonance. An example of a typical fit for a set of C III $n_t = 14$ data is shown in Fig. 3.2.4. The amplitude from this fit (4.69×10^{-6} in this case) is then divided by the average of the four normalized charge transfer measurements (4.10×10^{-5} in this case). This is the ratio of the signal to

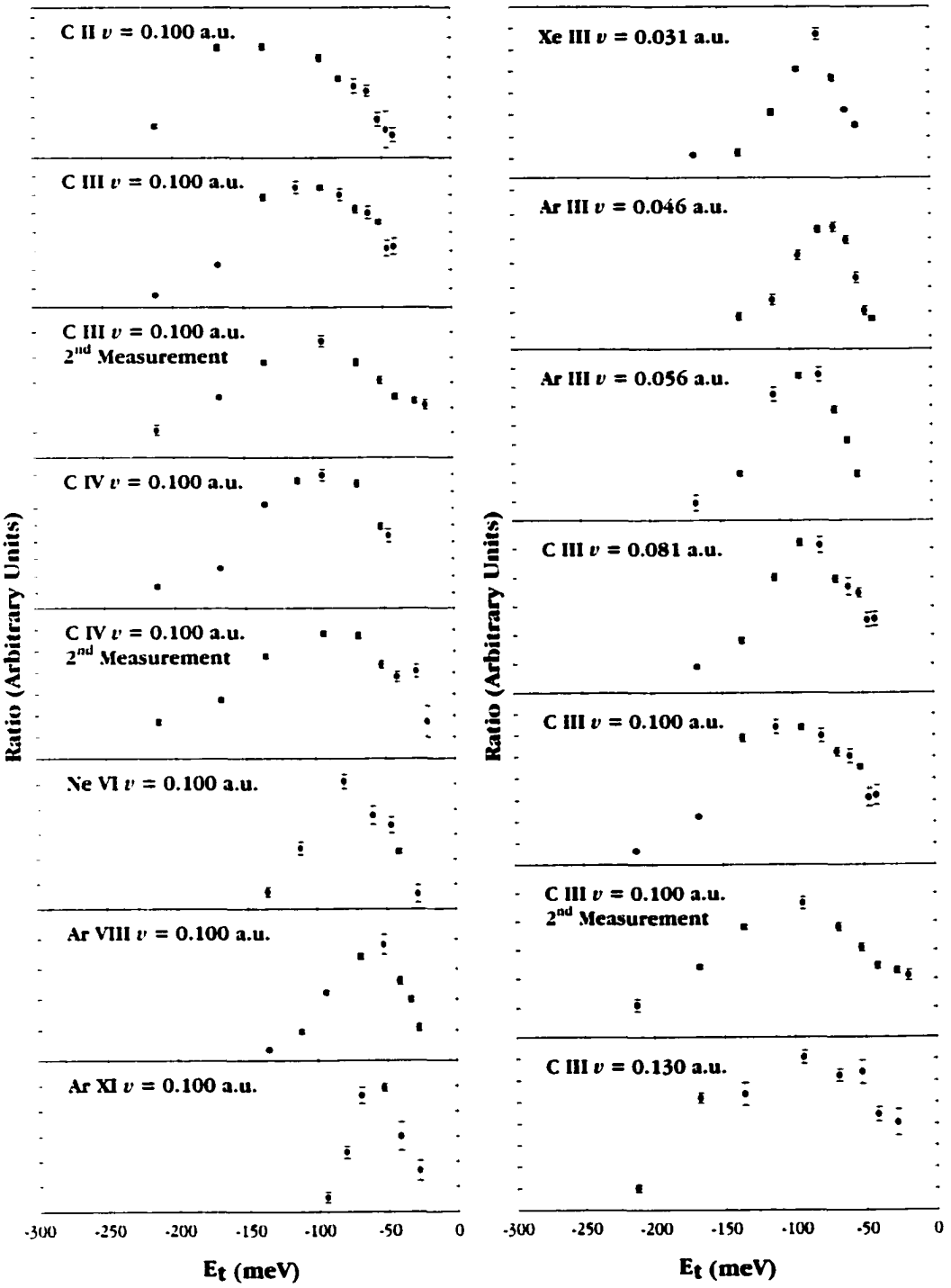

Figure (3.2.5) : **Raw results of all measurements.** This shows the raw results for all the ions measured as calculated from the individual data sets as described in the text.

charge transfer used for each measurement of a particular target state. For this example the resulting ratio is 0.114. A minimum of four of these "data sets" were taken for each target and repeated for a range of target states. The measurements were then repeated, without changing the detector tuning, for the target states in a different order to check for reproducibility. Since each "data set" gives one value of the signal to charge transfer ratio, at least eight ratio measurements were obtained in this manner for each target.

To determine the best value of the signal to charge transfer ratio for a particular ion and target, the results from all of the data sets were averaged and the error for the point was determined by the scatter of the individual data sets. We will designate this ratio R_{Meas}. The repeated measurements in most cases agreed extremely well with the original measurements. Thus, the average of all of the points taken was used as the best estimate of the ratio with the quoted error equal to the standard deviation of the mean. For the C III n_t=14 measurement R_{Meas}=0.105(4). Appendix D lists the results for R_{Meas} obtained for all ions and targets studied. Fig. 3.2.5 plots R_{Meas} for all measurements.

3.3 Comparing the measured ratio to CTMC calculations

Neglecting any change in populations between the Rydberg target and the laser, the measured ratio is directly related to the ratio of the partial cross section into a particular product state, σ_p, to the total cross section of the charge capture, σ_T. More precisely the measured ratio is proportional to the ratio between σ_p', the total cross section for capture into a subset of l-states in the n_p level, and σ_T' the total

cross section for capture into states which are not ionized in the repeller. Both σ_p' and σ_T' can be calculated by CTMC. The ratio of these cross sections differ from the measured signal to charge transfer ratio by a constant factor due to the relative efficiencies of the signal and charge transfer measurements. However, there are population changes between the Rydberg target and the laser and these must be modeled to make a proper comparison between theory and observations.

In what follows we will compare our measurements to CTMC theory (as we have calculated using the CTMC code provided by Brett DePaola, originally written by Olson[12]) in two distinct ways. First we will compare the measured ratios directly to the CTMC calculated ratio of σ_p' to σ_T'; after accounting for the population changes between the Rydberg target and the laser and the difference in the relative detection efficiencies. This is the most direct method of comparison between the CTMC calculations and the measured data. However, comparing the CTMC model to the measurement in this way obscures the physics of the capture process. The physics of the capture into a particular state in the collision is better understood by looking directly at the partial cross sections into the specific state at the target rather than the ratio of σ_p to σ_T at a later time. To estimate σ_p from the measurement of the ratio we multiply the measured ratio by the total cross sections determined by the CTMC calculations. This allows us to compare σ_p from the measurement and the CTMC calculations. The partial cross sections are nearly symmetric peaks, as opposed to the very non-symmetric peaks formed by the ratio of σ_p to σ_T. This allows the position and width of the partial cross section peaks to be parameterized by a rather simple function and any trends in these quantities

with charge and velocity can be carefully analyzed to try to understand the physics involved in the collision. This is only slightly more dependant on theory than the first more direct comparison. Looking at the partial cross section also allows comparison of the measurement with the Classical Over Barrier model which only predicts the position of the maximum partial cross section and does not predict the total cross sections necessary for a comparison with the measured ratio.

3.3.1 Factors applied to raw CTMC calculations to make comparison with measured ratios

To make the first more direct comparison a number of correction factors need to be applied to the raw CTMC calculations. First we must decide what should be included in σ_p' and σ_T'. The laser excitation signal is only sensitive to a subset of

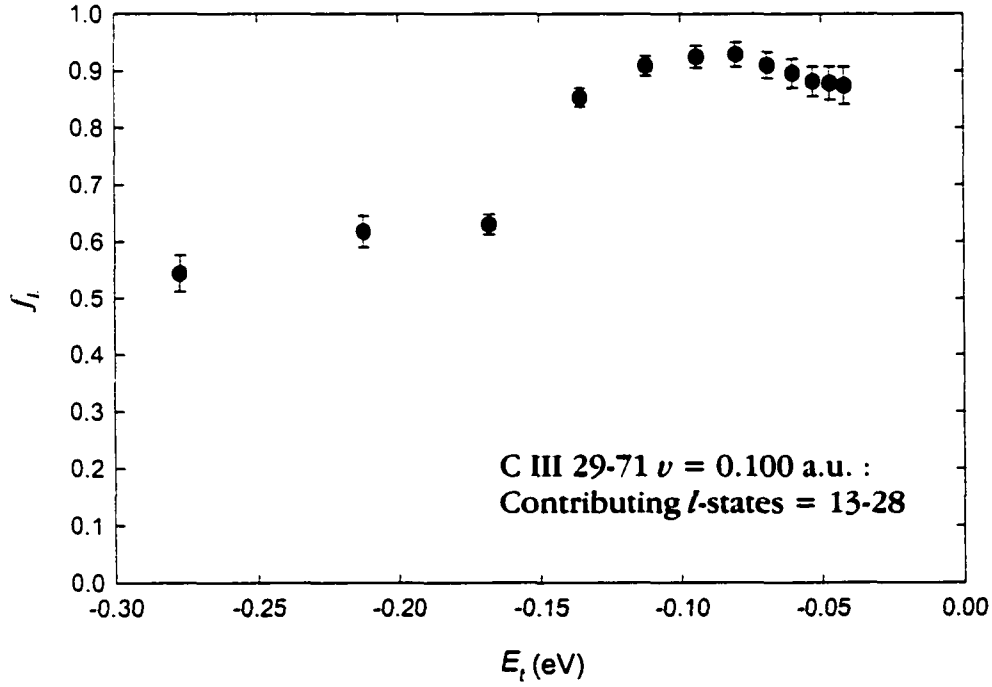

Figure (3.3.1) : **Effect of l-state contribution, f_L.** Effect on partial cross section from including only states measured. The factor f_L is the fraction of the population in the high l-states measured.

l-states in the n_p level. For this reason, the effective partial cross section, σ_p', should only include those l-states. To determine which l-states to include in the calculation, the detailed angle scans of the laser resonance were studied. A simulation of the l-structure of the resonance was then made using the scalar polarizabilities given for each ion in Table 2.5.1. The simulation used Gaussian curves with equal amplitudes and widths at each l-state position and added these individual curves together to get an overall lineshape. The common amplitude and width of these individual curves was adjusted to give the best agreement to the measured laser resonance lineshape. The l-states included in the calculation of σ_p from the complete CTMC results (which give the capture cross sections into all of the individual n,l states) were the states of the simulated line shape which contributed half or more of their amplitude at the center of the main resonance. The fits of the l-state simulations to the angle data are shown in Appendix E Figs. E.1-E.3 for all of the ions used. Only the l-states determined to be contributing to the resonance in this manner were included in σ_p'. This range of l-states is given in Table 3.3.1 for all the transitions used. The effect on the partial cross section calculated for C^{3+} (n_p=29, l=13-28) at v=0.100 a.u. is shown in Fig. 3.3.1 as f_L, the fraction of the population in the measured l-states where $\sigma_p' = f_L \sigma_p$. The fraction f_L is shown for the rest of the ions in Appendix F Figs. F.1. The change in the shape of the resonance from the total partial cross section is rather small because the included fraction, f_L, does not have a strong dependance on the target state particularly near the center of the capture resonance. The largest effect is seen in the lowest target states, which have a small cross section into the measured state.

For more highly charged ions, or ions with small scalar polarizabilities, a much larger fraction of the l-states are included and this correction becomes negligible.

The effective total cross section, σ_T', is also affected by conditions of the experimental measurement. The repeller voltages were left on during the measurement of the charge transfer beam, and we later realized that this reduced the measured charge transfer beam by ionizing population in high n-states. Since the fraction of the population formed in these ionizable levels varies with n_t, this results in a distortion of the measured ratio versus n_t when compared with the complete total cross section. To properly compare with the measurements, σ_T' must only include n-states which were not ionized by the repeller in the measurement. The cutoff n-state, above which population was ionized, was determined by using a Stark ionization field midway between the extreme red and blue Stark states. This gives an ionization field,

$$F = \frac{q^3}{6n^4} \tag{3.3.1}$$

which for a particular field gives an n_{Cutoff} of,

$$n_{Cutoff} = \left(\frac{q^3}{6F}\right)^{1/4} \tag{3.3.2}$$

For each of the ions and velocities the n_{Cutoff} used for the calculation of σ_T' is given in Table 3.3.1. Figure 3.3.4 shows the effect of the ionization of high n-states on σ_T' for C^{3+} at v=0.100 a.u by looking at f_R, the fraction of product states which survive the repeller fields without ionization, where $\sigma_T' = f_R\,\sigma_T$. The quantity σ_T' is shown

for all targets and ions in Appendix F, Fig. F.3. This affects the apparent total cross section at high n_t targets most, since they produce a substantial population in states ionized by the repeller. This effect is also strongly dependent on the field in the repeller, and thus indirectly on the energy of the ion beam.

Now that we have examined how the repeller affects σ_T we need to answer a question first raised in section 2.3. How much and in what way is the charge capture beam affected by capture from the lower excited states of the target with large populations, $5P_{3,2}$ and $4D_{5,2}$? The capture cross sections from these states are quite small compared to that from the exited states. For example, one of the smallest capture cross sections from a "final" excited state is 29×10^{-13} cm^2, while the cross sections from the $5P_{3,2}$ and $4D_{5,2}$ states are only 10^{-15} cm^2. Appendix D gives values of σ_T' for all targets and ions. Although the cross sections from the lower excited states are small, if the population is significantly larger than the "final" excited state even these small cross sections may be significant to the charge capture beam measured.

If the capture from the lower states in the target excitation is significant, the measured capture beam will be increased by the capture from these states. The small relative cross section from these lower excited states means that any effect on the charge capture beam will be greatest when the capture cross section and population of the "final" excited state are smallest. For example, σ_T' for C III at v = 0.130 a.u. is shown versus target binding energy in Fig. 3.3.2. The general features for σ_T' are similar in the other ions, but σ_T' is smallest in this ion. Thus, the largest fractional effect from lower state capture will occur at the highest and lowest

targets and will increase the measured capture from what would be expected if only capture from the "final" excited state were significant.

To determine more quantitatively what effect these states have on the charge transfer beam we develop a crude model below. Earlier in this chapter we described the measurement of the charge transfer beam. That measurement is made by measuring the current synchronous to the chopping of the second laser of the Rydberg target excitation, the $5P_{3/2}$ to $4D_{5/2}$ transition. Thus by measuring the signal synchronous to this chopper we are measuring the difference between,

$$\begin{aligned} Capture = {} & \sigma_{5S}N_{5S} + \sigma_{5P}N_{5P} \\ & + \sigma_{4D}N_{4D} + \sigma_{n_t F}N_{n_t F} + \sigma_{(n_t-1)D}N_{(n_t-1)D} \end{aligned} \tag{3.3.3}$$

when the second laser is on and,

$$Capture(Off) = \sigma_{5S}N_{5S}^{Off} + \sigma_{5P}N_{5P}^{Off} \tag{3.3.4}$$

when the second laser is off. N is the population of the state in the subscript, σ is

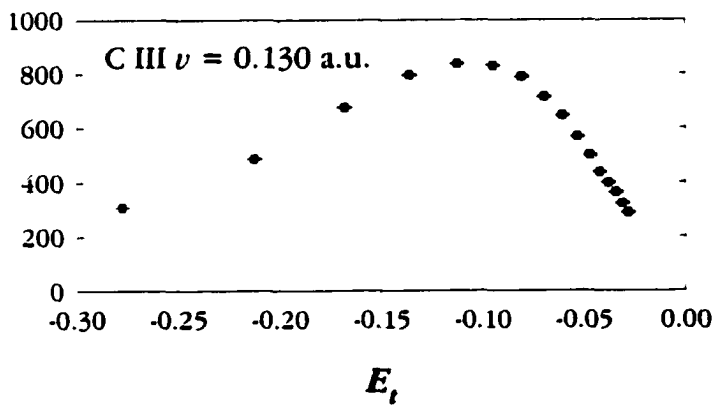

Figure (3.3.2) : σ_T' versus E_t. This figure shows the variation of the capture cross section after removal of population above n_{Cutoff} for C III at v = 0.130 a.u. n_{Cutoff} = 57 for this ion.

the total capture cross section of the subscript state, and N^{Off} is the population of the given state with the second laser off. To simplify this model, we will neglect capture from the ground state ($\sigma_{5S} \approx 0$) and assume that the capture cross sections from the two "final" excited states, n_tF and $(nt+1)D$ are equal. Then, by defining,

$$p \equiv \frac{N_{n_tF} + N_{(n_t+1)D}}{N_{4D}} \tag{3.3.5}$$

we can rewrite the above as,

$$Capture = \sigma_{5P}N_{5P} + \sigma_{4D}N_{4D} + \sigma_{n_t}pN_{4D} \tag{3.3.6}$$

with σ_{n_tF} and $\sigma_{(n_t+1)D}$ now indicated by σ_{n_t}. If we further assume that the population increase in the $4D$, n_tF, and $(n_t+1)D$ states comes equally from the $5S_{1/2}$ and $5P_{3/2}$ states, this gives a difference between the charge transfer signal with the second laser on and off of,

$$\Delta Capture = N_{4D}\left[\sigma_{4D} - \left(\frac{1+p}{2}\right)\sigma_{5P} + p\sigma_{n_t}\right] \tag{3.3.7}$$

In the ideal case where capture from the lower states, $4D_{5/2}$ and $5P_{3/2}$ is zero($\sigma_{4D} = \sigma_{5P} = 0$), then the charge capture signal would be,

$$\Delta Capture(Ideal) = p\sigma_{n_t}N_{4D} \tag{3.3.8}$$

Thus the fractional change due to capture from the lower excited states within this simple model is,

$$f_{Lown} = \frac{\Delta Capture}{\Delta Capture(Ideal)} = 1 + \frac{\sigma_{4D}}{p\sigma_{n_t}} - \left(\frac{1+p}{2p}\right)\frac{\sigma_{5P}}{\sigma_{n_t}} \tag{3.3.9}$$

If we further assume $\sigma_{4D} \approx \sigma_{5P}$, this becomes,

$$f_{Lown} \approx 1+\left(\frac{1-p}{2p}\right)\frac{\sigma_{4D}}{\sigma_{n_t}} \tag{3.3.10}$$

The last factor, σ_{4D}/σ_{n_t}, is smaller than 0.03 and can be calculated for all the ions and targets. However, the factor p can't be calculated theoretically. We can estimate the variation of p with target state by examining the target density as a function of target (see Fig. 2.3.9). However, we only have one measurement the absolute ratio of the final excited state capture to the $5P$ and $4D$ state population

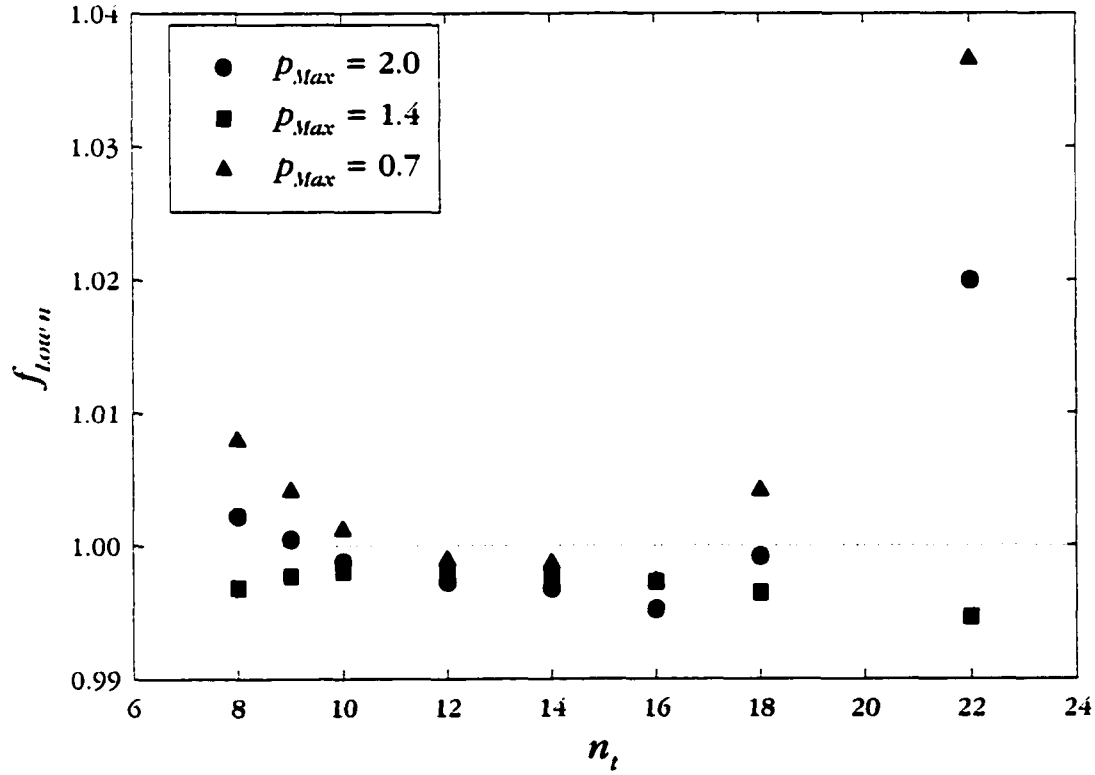

Figure (3.3.3): $f_{Low\ n}$ **for C III at v = 0.130 a.u.** This shows the variation of $f_{Low\ n}$ as a function of target state for p_{Max} = 2, 0.2, and 0.02. Note that this is not a significant correction for p_{Max} = 2 or 0.2.

capture. This measurement made with our target in a previous experiment [32] gives a value of p=0.7 for n_t = 10. However, a precise evaluation of this factor for this experiment was not made.

The maximum possible ratio, p, of the final excited state population to the $4D$ state population is 2.0. This would correspond to equal population of all five states ($5S$, $5P$, $4D$, n_tF, and $(n_t+1)D$) on the primary excitation path. However, it is certainly possible that p is less than 2.0, since the excitation may not be that efficient. Indeed we see from Fig. 2.3.9 that the excited state population varies by almost an order of magnitude for different targets, indicating that p is certainly much less than 2.0 for some targets.

In the absence of better information, we can try to assess the importance of this effect, lower state capture, by assuming a range of values for the maximum of parameter p and using Fig. 2.3.9 to evaluate p for the other targets. Figure 3.3.3 plots the factor, $f_{Low\ n}$ calculated in Eqn. 3.3.10, for p_{Max} = 2.0, the maximum possible value, and the smaller values p_{Max} = 1.4 and 0.7. The figure is for the case C III at v = 0.130 a.u., where we expect the effect to be most severe. Note that, as expected, the effect is most significant for the targets with the smallest cross sections. None of these values affect the charge transfer beam measurement a great deal amounting to less than a 5% correction in the worst case. Although we have made no measurements of the ratio of the excited state to the $4D$ state population in this experiment, we believe at the peak target density a substantial fraction of the population is being excited to the n_t state as suggested by the capture measured in the earlier experiment. Consequently, we believe this correction will have a

minimal effect on the capture beam measurement even for the targets with the lowest "final" state capture cross sections and populations.

Another correction that must be applied to the CTMC calculation is the correction for the change in the population between the target and the

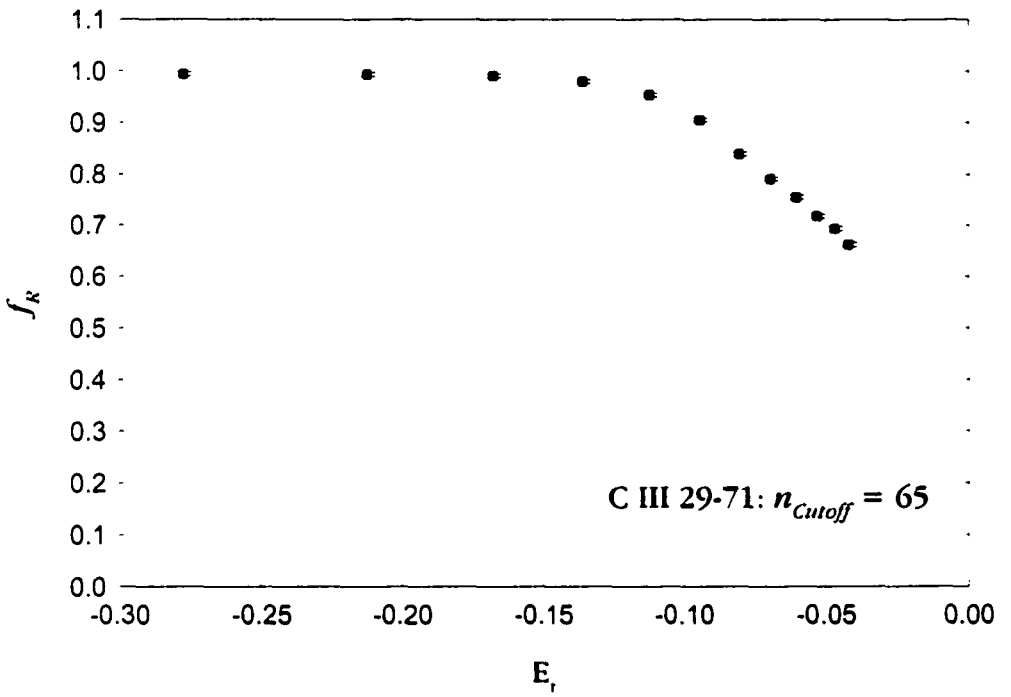

Figure (3.3.4) : **Effect of repeller ionization, f_R.** This shows the effect of ionization of high n-states by the repeller on σ_T' as a function of target energy. The factor f_R is the ratio of σ_T' to σ_T.

measurement position. To estimate this change we calculated the effects of cascades and black body radiation at 300 K during the time of flight from the target to the position of the CO_2 laser, starting with initial populations given by the CTMC results. An additional complication to this calculation was the field in the repeller. The distribution of the l-state populations can be affected by the detailed conditions of entry and exit from the fields in the repeller. To estimate the effect, calculations

were made for two extreme cases. The first extreme was to assume that the l-state populations were completely unaffected by the fields in the repeller (no mixing of

Table 3.3.1: **n_{Cutoff} and contributing l states for each ion.** This shows n_{Cutoff} and the contributing l-states for each ion, the transition used for each is also given.

Ion	Velocity (a.u.)	Transition	n_{Cutoff}	Contributing l-states
C II	0.100	19-51	46	9-18
C III	0.100	29-71	65	13-28
C III Second Set	0.100	29-71	55	15-28
C IV	0.100	37-85	78	3-36
C IV Second Set	0.100	37-85	78	3-36
Ne VI	0.100	55-133	106	11-54
Ar VIII	0.100	73-161	118	8-72
Ar XI	0.100	102-200	171	7-101
Xe III	0.031	29-71	65	14-28
Ar III	0.046	31-100	62	13-30
Ar III	0.057	29-71	65	13-28
C III	0.081	31-100	63	11-30
C III	0.130	29-71	57	13-28

the population). The second extreme was to assume that the l-state populations were completely and evenly redistributed among all of the l-states by the repeller fields (a complete mixing of the population). The correction factor calculated is simply the ratio of calculated population (of the selected n_p, l_p levels) at the measurement position to the initial population at the target. We call this correction

factor $f_{Cascade}$. The cascade correction factors to the partial cross sections, for both extremes, no mixing and complete mixing, are shown for all the ions and targets used in this experiment in Fig. F.4-F.5 in Appendix F.

The different effect of the two extreme cases can be seen quite clearly by examining the population in the n_p, high-l state as a function of time after the target. This is shown in Fig. 3.3.5 for a C III, n = 29 state l = 13-28 for n_t = 14. At the repeller position, 1.1 μs, the population in the measured state drops very sharply for the case where complete mixing occurs. This drop is from population being

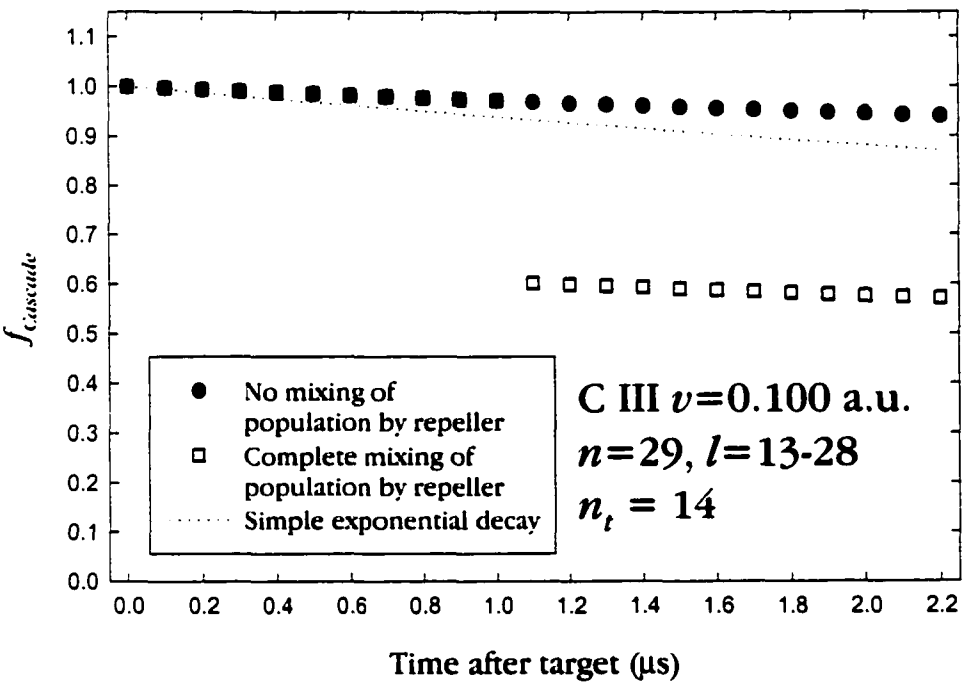

Figure (3.3.5) : **Population change with time.** This figure shows the effects of different types of calculations of population change from target to measured position of population in measured state. The solid points show the change in population with no mixing of the population at the repeller. The open squares show the change if the repeller completely mixes the l-state population. Finally the dotted line shows the effect on the population by simple exponential decay at the average decay rate of the initial population.

redistributed to lower *l*-states which are not measured, but have largely decayed away before reaching the repeller because of their shorter lifetimes. Also shown in this figure is a dotted line representing the population in the measured state as a function of time if only simple exponential decay at the average decay rate of the initial population was considered. The effective lifetime of the state is increased by cascade repopulation, as illustrated by the dotted line, which drops more quickly than the points. For low target *n*-states the simple decay and the more complete calculation including blackbody radiation and repopulation of the state from states above it are almost identical.

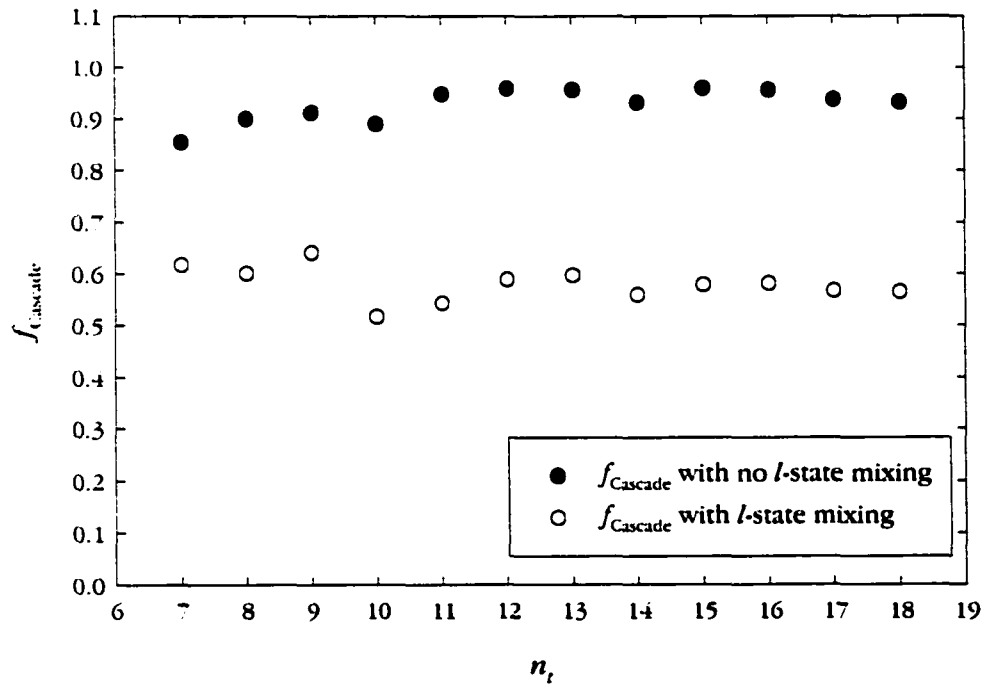

Figure (3.3.6) : **Comparison of $f_{Cascade}$ with and without *l*-state mixing.** This figure shows that the correction with and without *l*-state mixing has nearly no difference in shape. The small exception at low target states doesn't affect the shape of the corrected data substantially because of the small value of the partial cross section for these states.

The cascade correction factor at the observation point is illustrated in Fig. 3.2.5. The factor without any mixing of the l-states are shown as solid points and with complete mixing of the l-states as open points. This figure shows that the corrections are only a weak function of target state, relatively flat over the entire range of target energies studied. This is true for all of the ions studied except at the lowest velocities studied (Ar III at v = 0.046 a.u. and Xe III at v = 0.031 a.u.). For these ions the cascade corrections are quite large at high n_t because the increased time of flight between the target and the measurement and a large capture population above the measured state. The corrections for these two cases do significantly affect the shape of the resonance. The cascade corrections for all of the ions used are shown in Figs. F.4-F.5 in Appendix F. There is no significant difference in the shape of the corrections with the l-states mixed or unmixed. Thus the correction we will apply to correct for the change in population will simply be the average of the complete mixing and no mixing.

3.3.2 Comparison of the measured ratios with CTMC predictions

The three correction factors, f_L, f_R, and $f_{Cascade}$ are applied to the CTMC calculations of σ_p and σ_T to give the predicted ratio up to an overall constant,

$$R_{CTMC} = C\, f_{Cascade} \frac{\sigma_p'}{\sigma_T'} = C\left(\frac{f_L f_{Cascade}}{f_R}\right)\frac{\sigma_p}{\sigma_T} \qquad (3.3.11)$$

The constant factor C is determined by a fit of all the predicted ratios to the measured ratios for a particular ion and velocity. The R_{CTMC} and the measured ratios

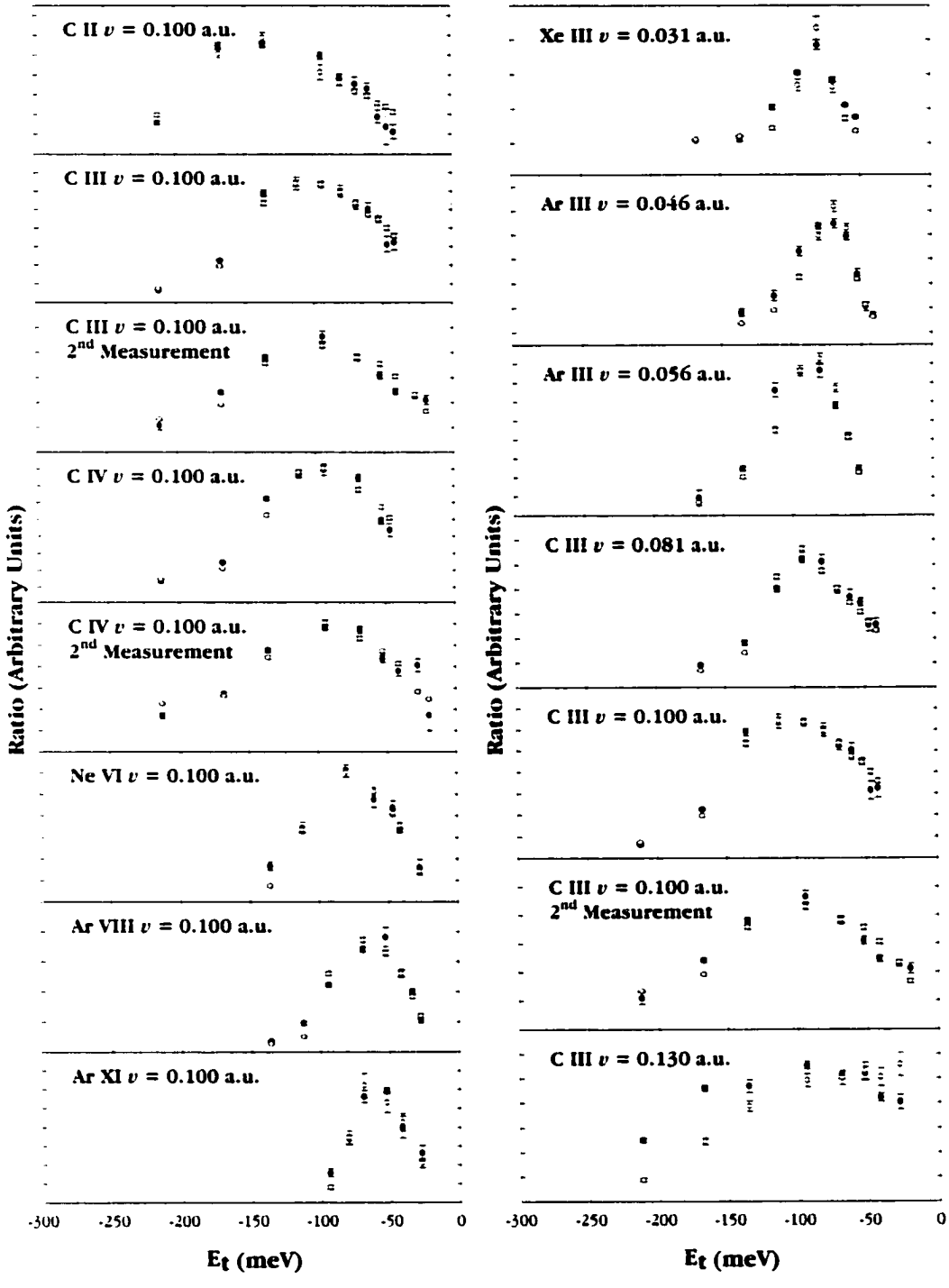

Figure (3.3.7) : **Comparison of measured and predicted ratios of signal to charge transfer.** This shows the most direct comparison of the measurement, solid points, and the CTMC calculations, open squares. The CTMC calculations account for the partial ionization in the repeller, the *l*-states which contribute, and are corrected for population transfer by spontaneous and blackbody transitions.

are shown versus the target state binding energy in Fig. 3.3.7. The values used in the figure are given in Tables D.1-D.13 in Appendix D. The figures show generally good agreement between the measured and the calculated values of the ratio and very good agreement between the shapes and positions of the resonances. The shapes of both the calculated ratios and the measured ratios are changing substantially with both charge and velocity and they agree with each other in the shape and position of the peak for nearly the entire range measured.

This good agreement between the measurement and the CTMC calculations seen in our measurement disagrees with the conclusions of previous measurements of the product state distribution on the projectile following collision with a Rydberg target [5, 13, 14]. MacAdam measured the collision of Na^+ and Ar^+ with a sodium Rydberg target inferring the n-distribution by selective field ionization [5]. Pascale *et. al.* [13, 14] compared this measurement to CTMC calculations and found a difference between the peak of the n-distribution of the measurement (n_{max} = 26.2) and the peak calculated by CTMC (n_{max} = 33 for v = 0.046 a.u. and n_t = 25). MacAdam later analyzed the measurement again [33] and this second analysis was in agreement with the CTMC calculations of Pascale *et. al.* [34]. Pesnelle *et. al.* [13, 14] measured the collision of Kr^{8+} with a Rb Rydberg target. Again this experiment inferred the final state population from the ionization field. They compared their measurement to CTMC calculations and found that the width of the CTMC n-distributions was about twice that of their measurement (see Fig. 1.3.1), and that position of the distributions also disagreed.

The only exceptions to the generally good agreement between our measured

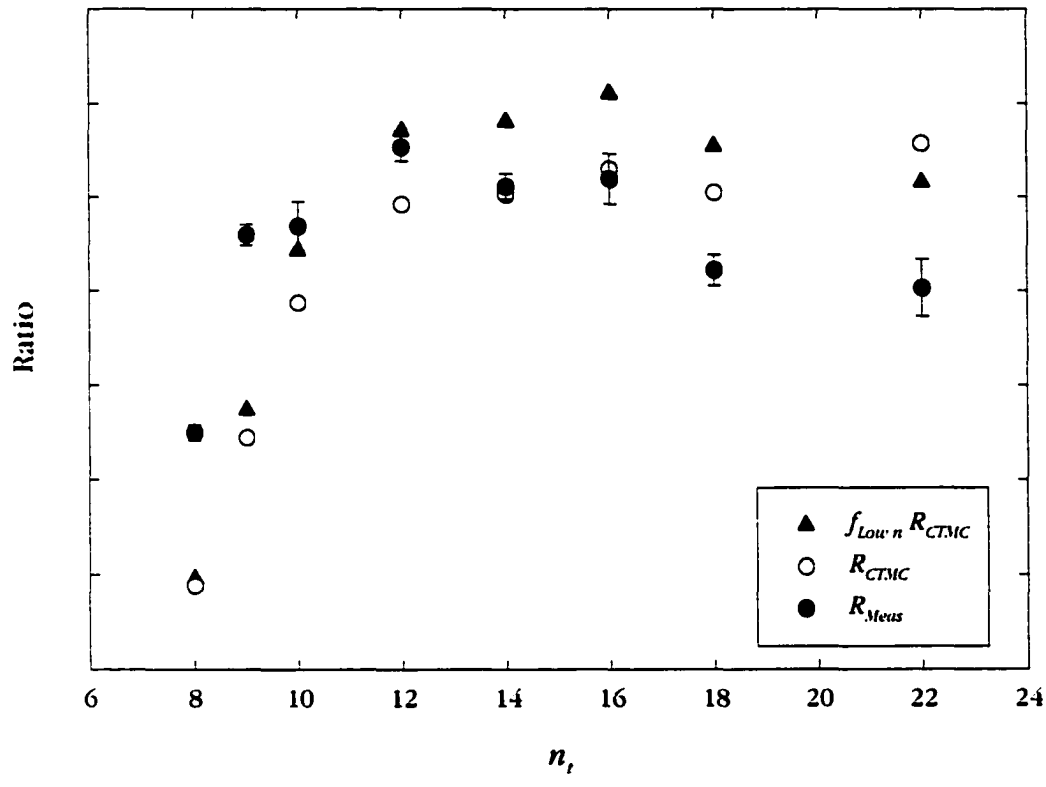

Figure (3.3.8): **Comparison of R_{Meas} and R_{CTMC} and R_{CTMC} with low n capture from target.** This figure shows the minimal improvement in the agreement of R_{CTMC} with R_{Meas} when the factor $f_{Low\ n}$ is applied with p_{Max} = 0.3, the best fit of this parameter to the measurement.

and calculated ratios are at the lowest and highest velocities. At the lowest velocities it is apparent that the width of the measured peak is wider than the CTMC calculations. The disagreement at the highest velocity, v = 0.130 a.u., is less clear. The measured peak does not match in position with the peak from the CTMC calculations very well, but it is difficult to tell how their respective widths compare because only part of the peak is visible. To further examine this disagreement, we will look in detail at what makes up the CTMC calculations. To generate the CTMC ratio a number of factors were combined to generate the ratio of the partial to the total cross section at the measurement position. The factors making up the ratio are

shown in Eqn. 3.3.11 above. We will examine whether any of these factors is qualitatively different from the other ions which might explain the disagreement at seen at this velocity. First, the factor f_R is rather unremarkable when compared to the f_R's of the other ions. It slowly drops at high target states reducing σ_T' and increasing R_{CTMC}. The next factor is f_L, this factor varies substantially more than seen for the other ions rising at least a factor of two more than any other ion. The strong dependance on the l-state capture of f_L at this velocity tests the l-state predictions more strongly than the other ions. This difference is seen again in $f_{Cascade}$. The shape of $f_{Cascade}$ without allowing l-state mixing is rather unremarkable compared to other ions. However, $f_{Cascade}$ when l-state mixing is allowed at the repeller position shows a large increase at low l, when the fraction of the population in the high l-states is at a minimum as seen in the f_L factor. Thus since for this ion alone there are substantial corrections due to the l-state structure calculated by CTMC it would be advantageous to have direct measurements of the l-state population distribution for comparison.

We also must consider the effect of the additional capture from the lower excited states populated in the target. Allowing the factor p_{Max} to vary we find that p_{Max} = 0.3 gives the best fit to the measurement. Figure 3.3.8 illustrates this by showing R_{Meas}, R_{CTMC}, and R_{CTMC} corrected for this effect by $f_{Low\,n}$. Since the fit is not much improved by this correction it seems unlikely that this is the only cause of the disagreement.

At the lowest velocities the disagreement is only in the width of the peak, the position of the peaks is in good agreement. This means that any change in the

factors would need to be symmetric around the peak to improve the agreement with the measurement. Since $f_L, f_{Cascade}, f_R$, and σ_T are all flat or increasing from left to right the most likely explanation for the disagreement is σ_p. The ability to observe these rather minor discrepancies illustrates the high level of quantitative precision of this measurement.

3.3.3 Comparing the estimated measured partial cross sections to CTMC calculations and COB theory

For a more physical picture of the collision it is useful to look at the partial cross sections into the particular state rather than the ratio. The curves seen for the partial cross section alone are nearly symmetric which allows them to be parameterized easily and the changes in the gross structure of the capture resonance can be examined as a function of charge and velocity. To get the most physical picture of the collision we look at the partial cross section at the point of the collision rather than the population at the laser interaction point. The measured ratios are multiplied by σ_T', the CTMC total cross section corrected for the partial ionization in the repeller. To compare at the target position the measured ratios are multiplied by the inverse of $f_{Cascade}$, the cascade and black body correction. This gives a measured "partial cross section", σ_p' of,

$$\sigma_p' = \frac{f_R \sigma_T}{f_{Cascade}} R_{Measured} \tag{3.3.12}$$

where f_R, σ_T, and $f_{Cascade}$ are as defined earlier and $R_{Measured}$ is the measured ratio.

To quantitatively compare the shape and positions of the curves they are fit to

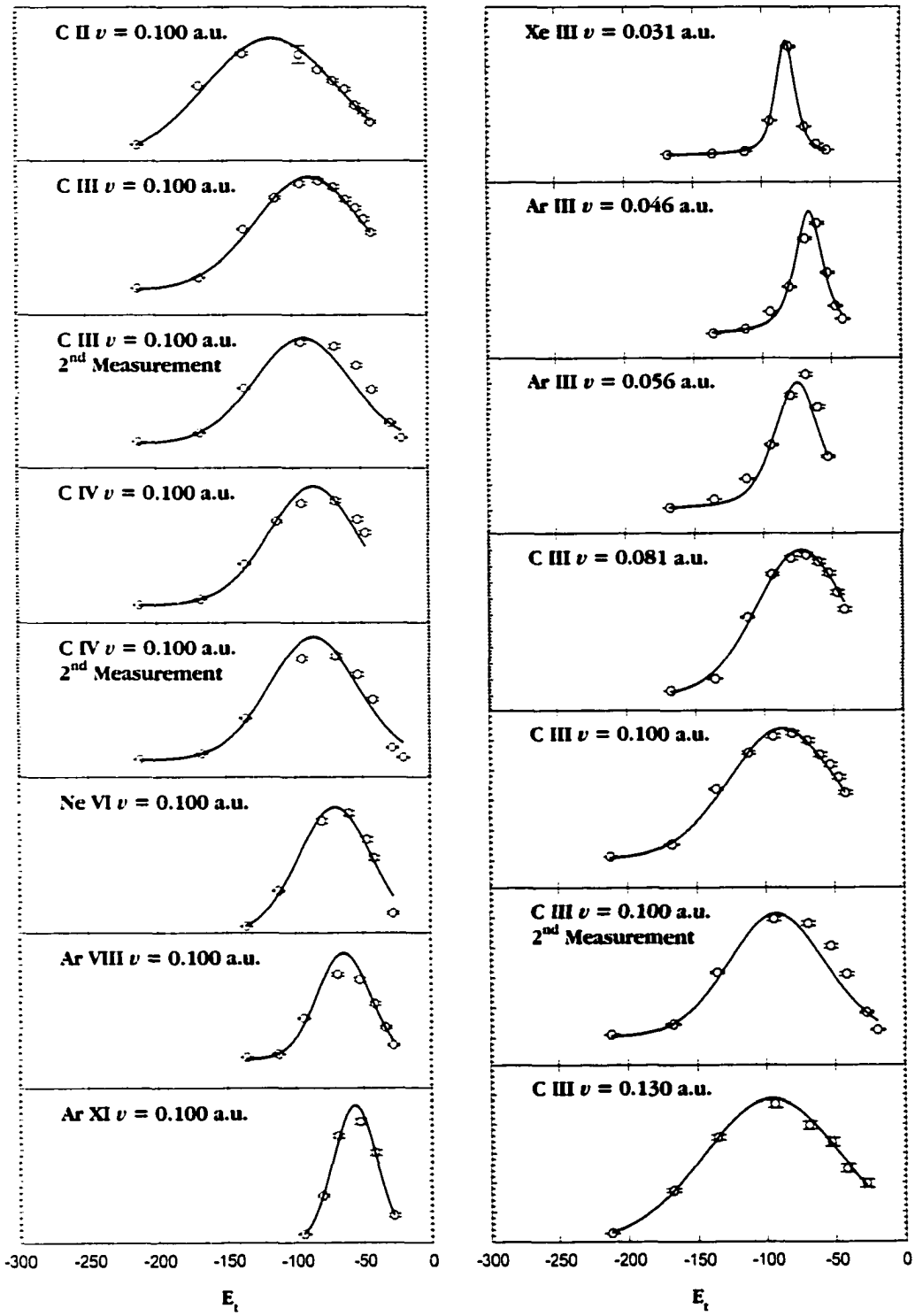

Figure (3.3.9) : **Fits of CTMC partial cross sections to a Psuedo-Voight parameterization.** This shows the fits of the calculated CTMC partial cross section to the Gaussian parameterization.

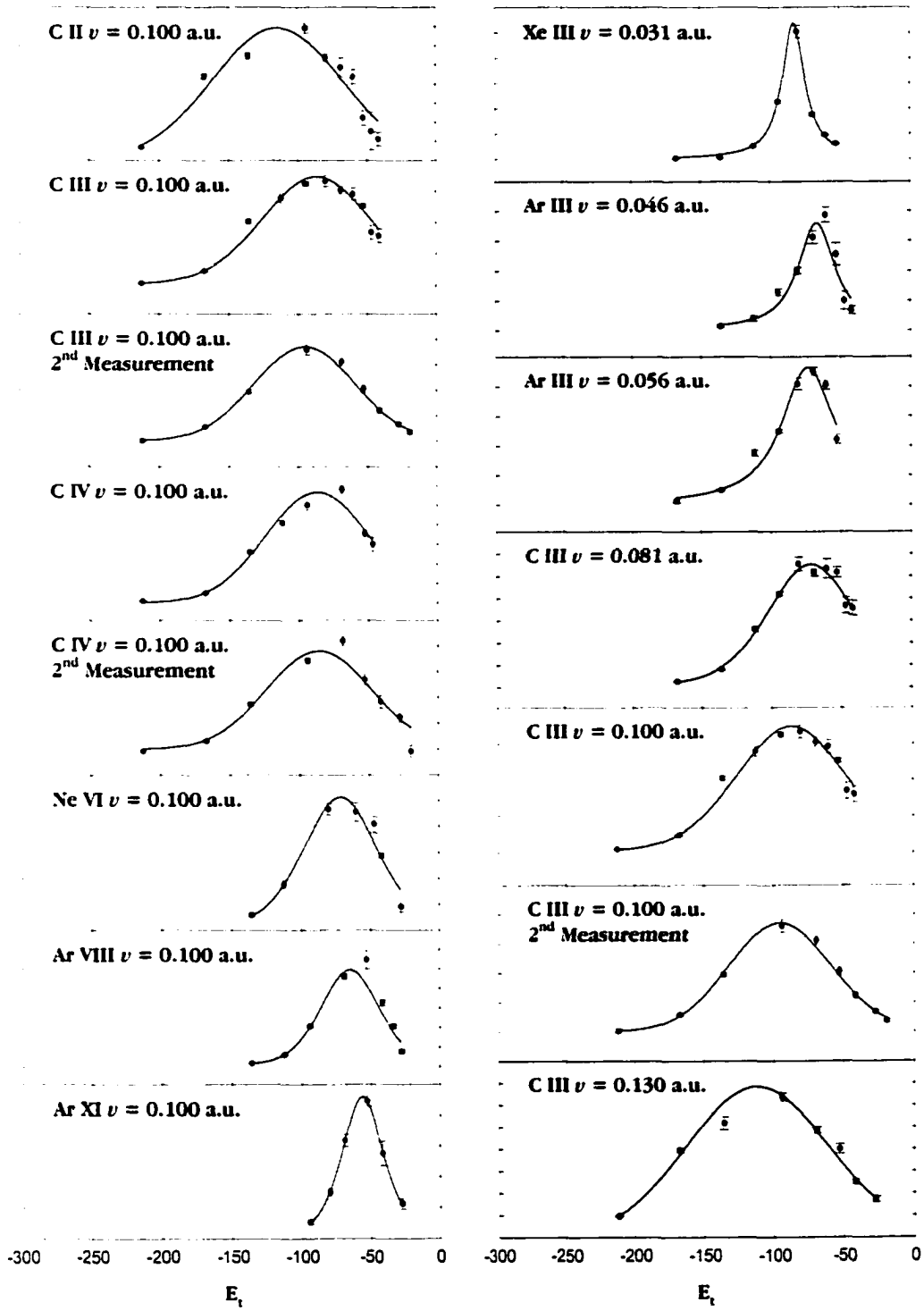

Figure (3.3.10) : **Fits of measured partial cross sections to a Pseudo-Voight parameterization.** This shows the fits of the measured ratio multiplied by the CTMC total cross sections to the Gaussian parameterization.

pseudo-Voight functions (a simple combination of a Gaussian and a Lorentzian). The function used for the fit is,

$$\sigma_p(E_t, E_p) = A\left\{c\left[\frac{1}{1+4\left(\frac{E_t-\kappa E_p}{W}\right)^2}\right]+(1-c)\left[e^{\left(-2.77\left(\frac{E_t-\kappa E_p}{W}\right)^2\right)}\right]\right\} \quad (3.3.13)$$

where E_p is the fixed binding energy of the detected state, E_t is the binding energy of the target, and A, κ, W, and c are fitting parameters. The parameter κ is the peak target energy divided by the fixed product energy, E_t/E_p. This allows comparison of the position of the peak even though E_p changes slightly for different ions and velocities. The parameter W measures the full width at half max of the peak. The parameter c measures the Lorentzian and Gaussian character of the curve, a c value of one is a pure Lorentzian and a c value of zero is a pure Gaussian. The parameter c is restricted to vary only in the range from zero to one. The parameter A is the amplitude of the peak and is not used in the comparison. These fitting parameters are used to compare the overall shape of the data and the CTMC calculation in a more quantitative way than was possible previously.

The fits to this pseudo-Voight parameterization of the data and CTMC calculations are shown in Figs. 3.3.10 and 3.3.9. As can be seen in the figure the change of the resonance shape with charge and velocity is substantial. As the charge is increased the resonance narrows and moves to a more loosely bound state. As the velocity is decreased the resonance narrows substantially and becomes more Lorentzian in shape, but remains nearly constant in position with the exception of

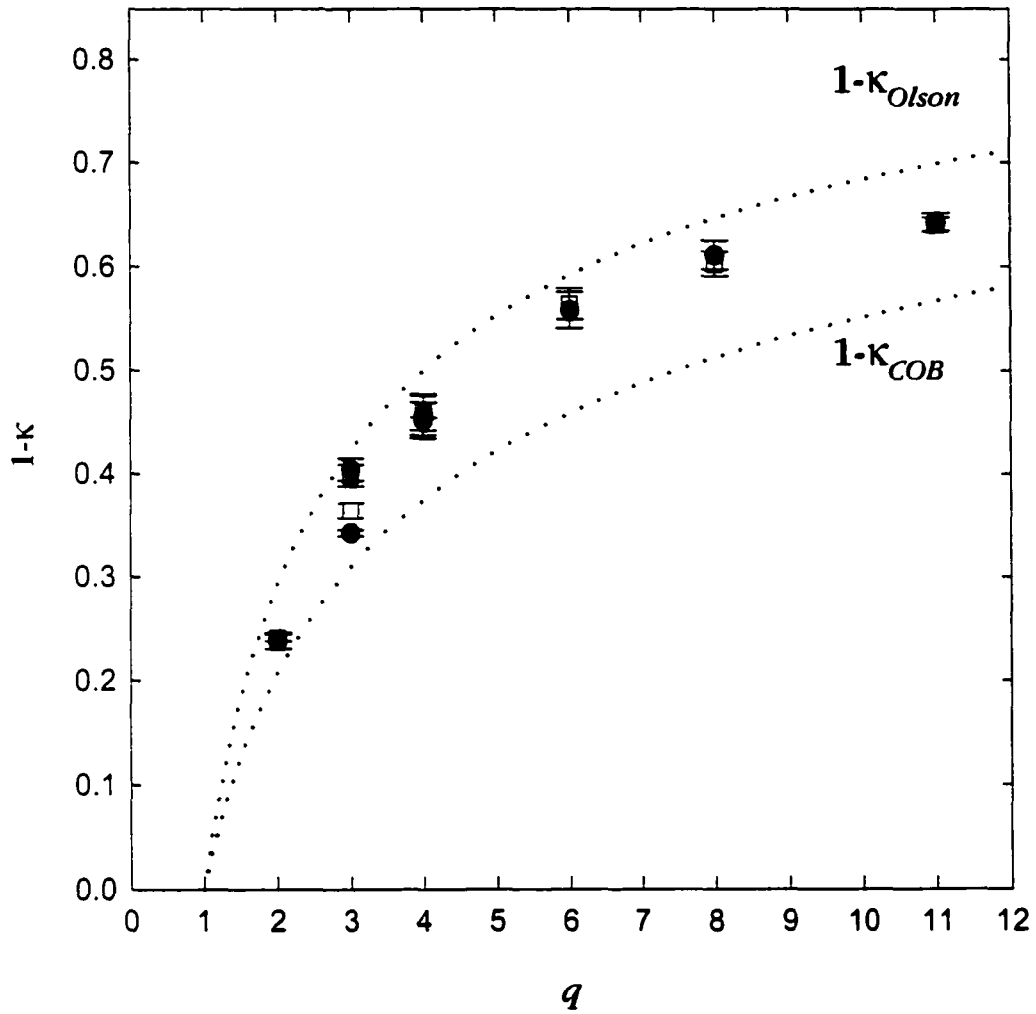

Figure (3.3.11) : **Plot of 1-κ versus *q*.** This shows the values of 1-κ from fits of the measured and CTMC partial cross sections as a function of charge at a fixed velocity of v = 0.100 a.u. The values from the measured resonances are shown as solid points and those from the CTMC calculations are shown as open squares. Also shown are two dotted curves, the prediction of the COB model and the empirical estimate by Olson from CTMC results.

the highest velocity ion. The fitting parameters, given in Table 3.3.2, show the same trends seen in the figures more quantitatively. These parameters again show exceptionally good agreement between CTMC and the measured data for nearly the

Table 3.3.2 : **Parameters of the fit.** This tabulates the parameters of the fits to the CTMC and measured partial cross sections for all of the measured ions.

		CTMC				Measurement			
Ion	v	κ	W	c	χ^2/dof	κ	W	c	χ^2/dof
C II	0.100	0.759(10)	0.118(8)	0.0(3)	3.55	0.76(3)	0.113(15)	0.0(5)	15.75
C III	0.100	0.601(15)	0.093(5)	0.11(10)	64.73	0.597(16)	0.093(4)	0.16(5)	10.47
C III 2nd Measurement	0.100	0.635(13)	0.083(5)	0.1(2)	187.83	0.658(6)	0.086(4)	0.04(16)	2.13
C IV	0.100	0.538(9)	0.078(4)	0.17(6)	51.37	0.55(2)	0.087(7)	0.01(15)	16.60
C IV 2nd Measurement	0.100	0.54(2)	0.077(7)	0.14(16)	555.29	0.54(2)	0.089(8)	0.0(3)	11.53
Ne VI	0.100	0.435(12)	0.064(5)	0.0(2)	45.27	0.442(14)	0.064(8)	0.3(4)	6.05
Ar VIII	0.100	0.396(8)	0.046(4)	0.05(14)	105.45	0.400(9)	0.051(4)	0.28(10)	16.52
Ar XI	0.100	0.359(4)	0.038(3)	0.0(2)	12.33	0.357(7)	0.037(2)	0.5(2)	0.06
Xe III	0.031	0.567(2)	0.0169(6)	0.61(6)	29.26	0.566(8)	0.019(5)	1.0(4)	12.94
Ar III	0.046	0.518(12)	0.025(6)	0.7(2)	341.02	0.524(15)	0.032(7)	1.0(5)	18.32
Ar III	0.057	0.516(6)	0.039(4)	0.49(10)	145.00	0.503(14)	0.047(8)	0.9(3)	14.64
C III	0.081	0.572(13)	0.078(5)	0.09(11)	130.69	0.562(14)	0.075(4)	0.29(7)	3.55
C III	0.130	0.717(8)	0.129(7)	0.0(3)	12.49	0.809(14)	0.130(12)	0.0(6)	7.20

entire range of data, as seen before in the more direct comparison of the ratios. The fitting function used however is only a guess of the true functional form of the data, and does not match well for all of the curves. Thus we will look in detail at the error bars of the parameters. At this point we must mention the inclusion of χ^2/dof, or the reduced chi-square, in the table. This was necessary to include because it affects the reported error bars of the fit parameters. There are two possible cases, the first is when $\chi^2/dof \leq 1$. In this case the function adequately describes the data and the errors on the parameters simply propagate the errors on the points. The second case is when $\chi^2/dof > 1$. In this case there are two possible causes, either the errors on the points are under estimated or the function is not a good representation of the data. The errors on the parameters reported assume that the error on the points has been underestimated and they are expanded by multiplication with a constant to achieve $\chi^2/dof = 1$, and then these enlarged error bars are propagated to the parameters. Thus the error bars reported for $\chi^2/dof > 1$ must be regarded with some skepticism as the functional form may not be quite correct.

A closer look at the variation of κ with q is given by Fig. 3.3.11 which plots $(1-\kappa)$ vs. q. Also shown in Fig. 3.3.11 are two classical predictions compared to the measured data. The parameter k allows a comparison to the Classical Over Barrier, or COB, model by comparing the position of the peak of the distribution with the COB predictions of the most probable final state energy. The COB model predicts

κ for the collision to be,

$$\kappa_{COB} = \frac{1+2\sqrt{q}}{q+2\sqrt{q}} \tag{3.3.14}$$

This leads to the lower of the two curves on Fig. 3.3.11, which plots $1-\kappa_{COB}$. It is clearly very different from the measurements. Another prediction shown on the figure is the empirical estimate obtained by examination of CTMC results for several values of q[6],

$$\kappa_{Olson} \cong \frac{1}{\sqrt{q}} \tag{3.3.15}$$

This leads to the other curve in Fig. 3.3.11, which plots $1-\kappa_{Olson}$, which does not fit our measurements or the calculated CTMC values particularly well, especially at high q. In contrast, the direct fits of CTMC calculations of σ_p' give values of κ which are in very good agreement for all charges.

One way of interpreting κ (the E_t to E_p ratio) is by looking at the qualitative picture of the energy exchange between the projectile and target during the collision as described in Chapter 1. In this picture the capture radius is expected to be closely related to the binding energy of the products. This is a consequence of conservation of the total energy in the collision. For $q > 1$, the collision products are both charged and gain kinetic energy as they repel each other after charge transfer. To conserve total energy the product state is more tightly bound than the

target state by the amount of kinetic energy gained,

$$E_p - E_t = \Delta E = \frac{e^2(q-1)}{R_c} \tag{3.3.16}$$

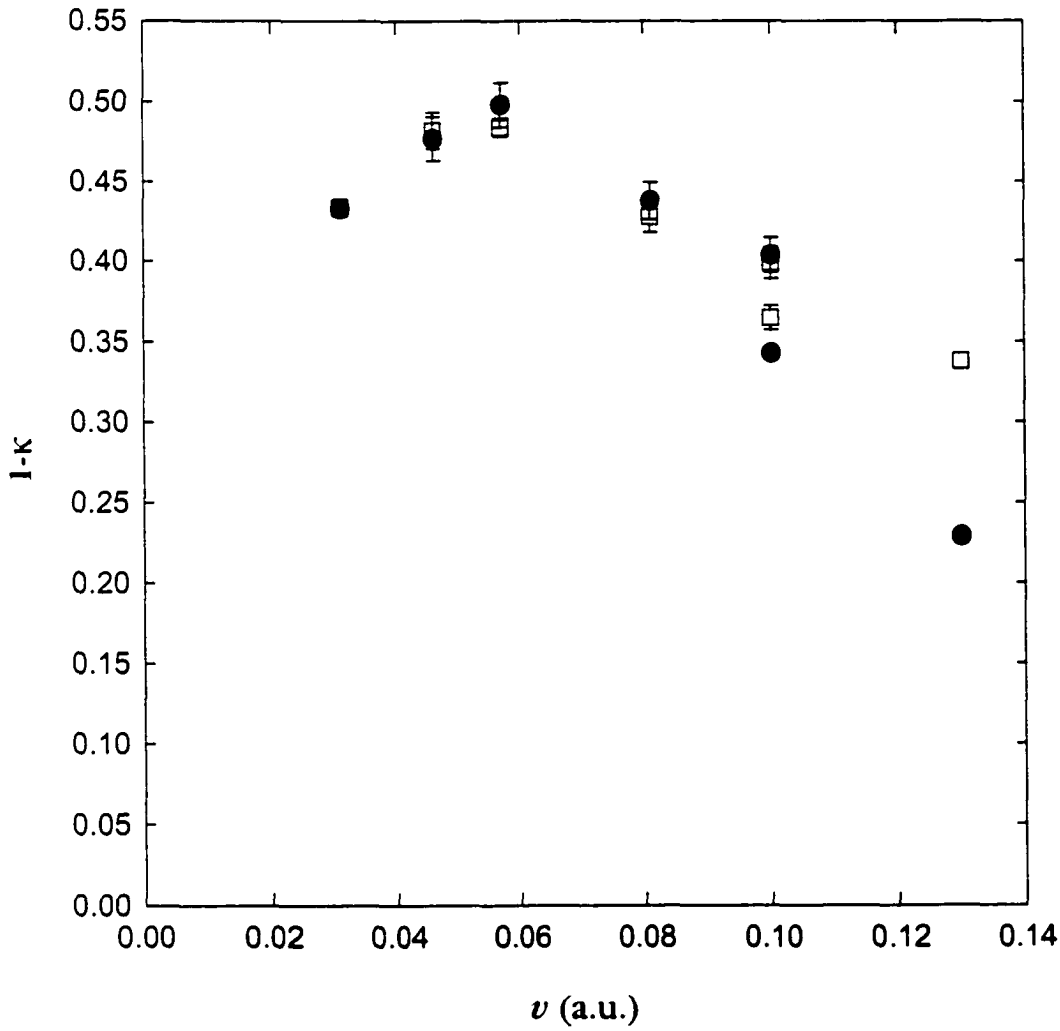

Figure (3.3.12) : **Plot of 1-κ versus *v*.** This shows the values of 1-κ from fits of the measured and CTMC partial cross sections, as a function of velocity at a fixed charge q = 3. The values from the measured resonances are shown as solid points and those from the CTMC calculations are shown as open squares.

where e is the electron charge, E_t is the target state binding energy, E_p is the product state binding energy and R_c is the radius at which capture occurs. This is directly related to 1-κ when E_p is constant, since, $1-\kappa = 1 - E_t/E_p$. Since E_p is approximately constant for all the ions in this experiment, we can use this examine the behavior of 1-κ.

The measured values of 1-κ as it varies with charge lead to some general conclusions about the internal energy transfer in ion-Rydberg charge transfer based on this simple energy conservation argument. First, the fact that 1-κ is not equal to zero for $q > 1$ shows that the most probable E_p is not equal to E_t, but rather increases with q for constant target energy. This is a widely anticipated result and appears to be in very good agreement with the specific predictions of CTMC theory. Some of the deviation of κ_{COB} from the measurements can also be explained using this energy conservation argument. The COB model is closely analogous to the simplest model of Stark ionization of atoms which predicts an ionizing field of $F = 1/16\ n^4$ a.u. (this calculation is reproduced in Appendix B). While this may be correct for atomic ground states, it is known to underestimate the diabatic ionization fields of Rydberg states by a factor of 1.8 to 3.6, depending on the Stark state. Therefore, we might expect the COB model to underestimate the field required to "ionize" the Rydberg target atom and cause capture by a similar factor. This would imply an over estimate of the capture radius by the square root of that factor or about 1.6. The COB model gives the same equation as the simple energy conservation argument above in its calculation of the capture radius. Thus if the COB model does overestimate the capture radius this will lead to an underestimate

of 1-κ by about the same factor. The COB model corrected in this manner (using a correction factor of 1.14) gives reasonable agreement with the measured 1-κ. However this correction factor is not nearly as large as expected. It is difficult to see how the COB model achieves the degree of agreement that it does, given its

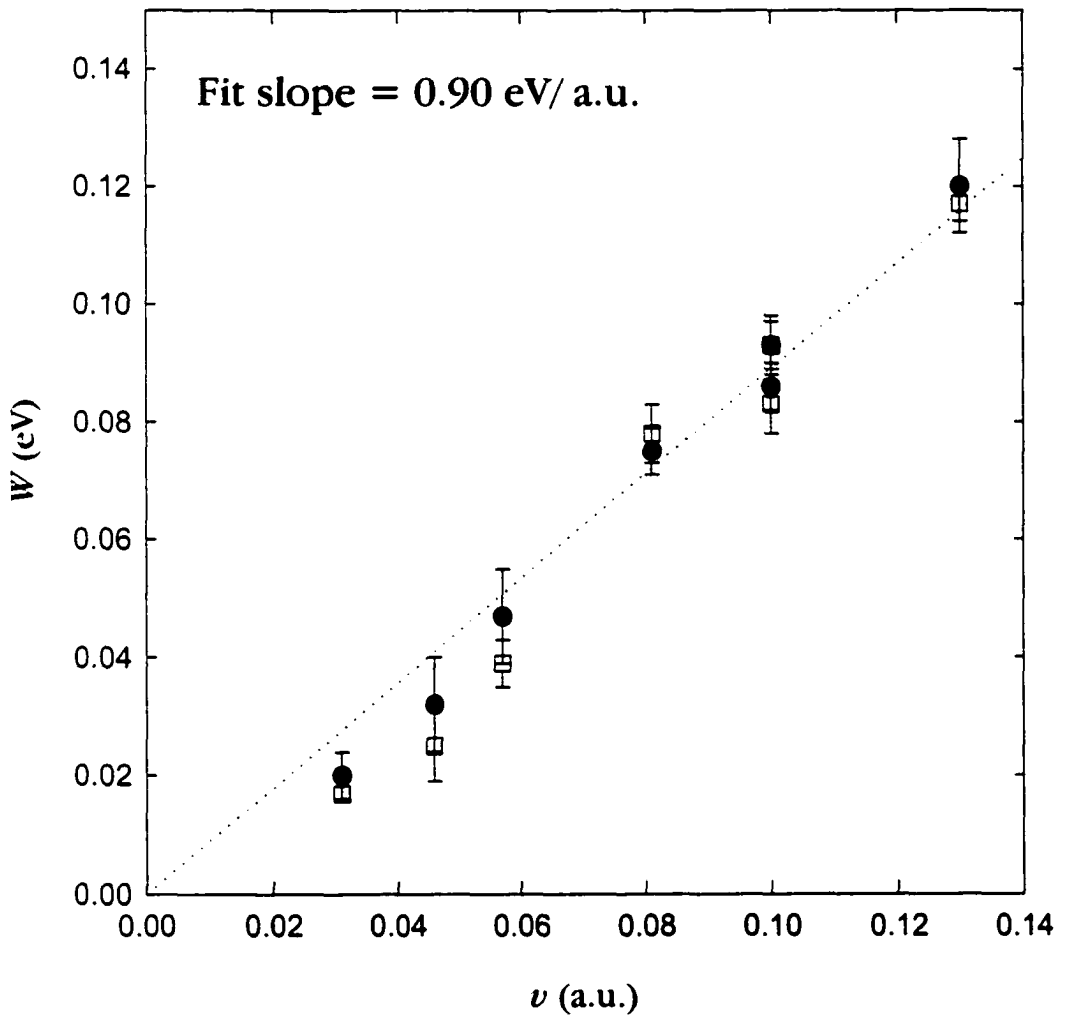

Figure (3.3.13) : **Plot of W versus v.** This shows the value of W from the fits of the measured and CTMC partial cross sections as a function of velocity at fixed charge q = 3. The values from the measured resonances are shown as solid points and those from the CTMC calculations are shown as open squares. The dotted line is a linear regression through the origin.

obviously unrealistic description of the "ionization" of the target. The agreement of the measured values with CTMC is excellent over the entire range of q which is likely at least partially due to its much more accurate modeling of the Rydberg

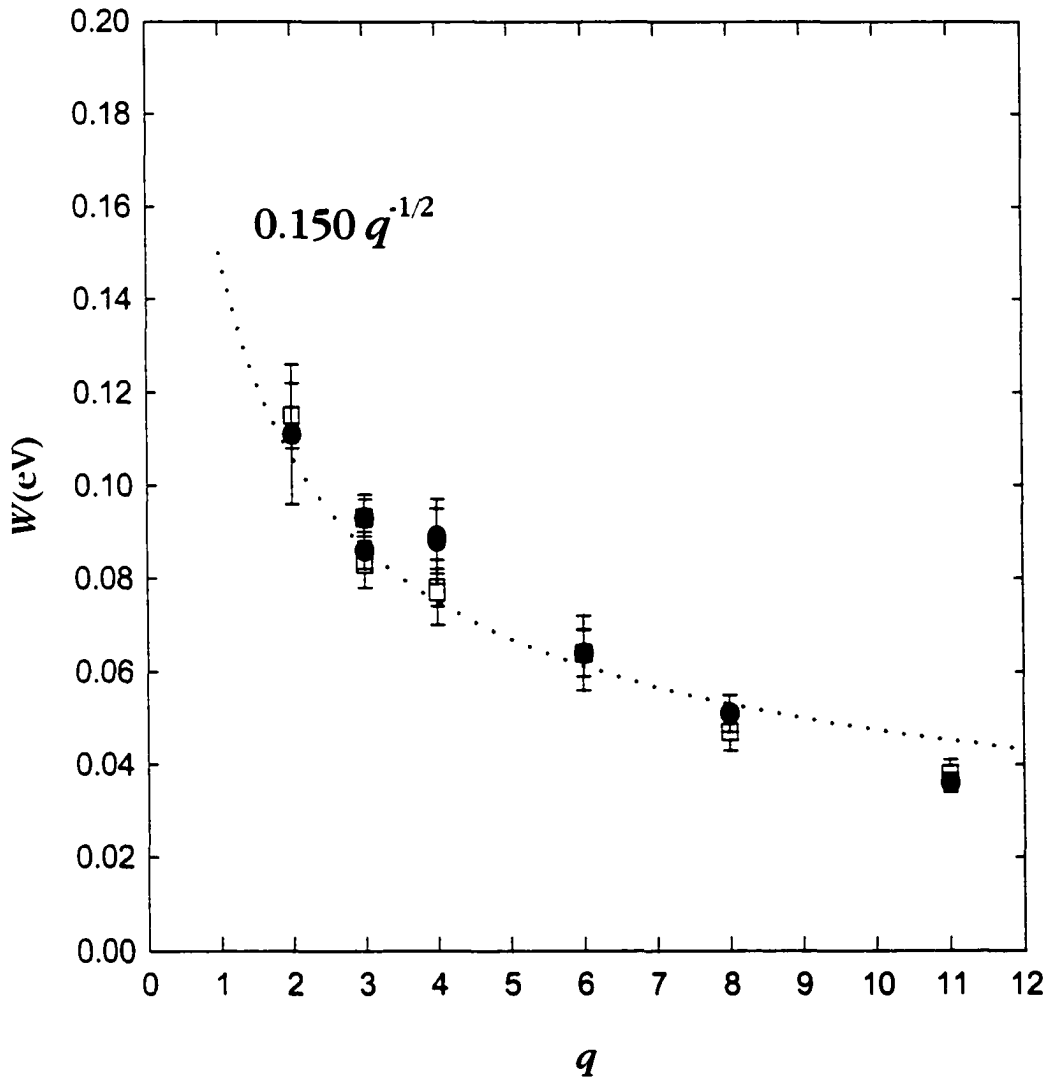

Figure (3.3.14) : **Plot of W versus q.** This shows the value of W from the fits of the measured and CTMC partial cross sections as a function of charge at a fixed velocity v = 0.100 a.u. The values from the measured resonances are shown as solid points and those from the CTMC calculations are shown as open squares. Also shown is a curve showing an empirical prediction based on the CTMC model.

ionization process. The one obvious limitation of the CTMC model, the neglect of tunneling does not seem to have a measurable effect in the comparison of the position of the resonances with charge. Tunneling would be expected to lead to capture at larger distances, with correspondingly lower values of 1-κ. Finally, we note that previous studies of charge capture by q=8 ions [13, 14] are not precise enough to discriminate between the COB and CTMC curves in Fig. 3.3.11.

These results and conclusions are different from our earlier reported results [17]. The disagreement between the results presented here and our earlier results is due to the factor f_R which was not taken into account in the previously reported results. Correcting σ_T to include the ionization in the repeller (the factor f_R) brings our measurement into very good agreement with CTMC.

The variation of 1-κ with velocity is shown in Fig. 3.3.12. These measurements are in good agreement with theory except for the single highest velocity point, which has been disscussed in section 3.2.2.

The variation of W with v is shown in detail in Fig. 3.3.13. For comparison a linear fit through zero of the measurement and the CTMC data is also shown, the regression results are also shown on the figure. The variation of W with q is shown in Fig. 3.3.14. Also shown in this figure is a fit to a simple $q^{1.2}$ dependance, which agrees very well with both the measurement and the CTMC calculation.

The form of the dependance of W on both q and v is similar to what would be expected from the energy-time uncertainty principle. In the case of W versus v, it is known that σ_T is approximately constant with velocity at sufficiently low velocities. Thus one can characterize the collisions as taking place over a time interval,

$$\Delta t \approx \frac{\sqrt{\sigma_T}}{v} \tag{3.3.17}$$

Then the energy-time uncertainty principle gives a width W (in energy) of,

$$W = A\frac{\hbar}{\Delta t} = A\hbar\frac{v}{\sqrt{\sigma_T}} \tag{3.3.18}$$

where $\hbar$ is Plank's constant, v is the ions velocity, and A is a dimensionless constant. The slope fit in Fig. 3.3.13 gives a value of A=40.2 using an average $\sigma_T = 38\text{x}10^{-12}$ cm^2. When σ_T is constant, the relationship between the width and velocity is linear as seen in Fig. 3.3.13. In the case of the relationship of W with q, σ_T is expected to be proportional to q, leading to W being proportional to $q^{1.2}$, which is similar to what is measured. Although no quantum mechanical theory of this process yet exists, one would expect a width of this form to result from such a calculation. On the other hand, CTMC a purely classical calculation, predicts widths in agreement with our measurements. This suggests that there may be an alternate explanation of the dependance of the width on q and v. Also, it seems inconsistent with the simple uncertainty principle argument that the energy widths in the "entrance channel" would depend so clearly on q while the widths predicted by CTMC for the "exit channel" (see Fig. 1.2.5) are nearly independent of q.

The final parameter of interest is the c parameter. The main feature of this parameter is its variation with velocity. As the velocity decreases the shape of the curve becomes much more Lorentzian, until it is almost entirely Lorentzian in character for the lowest two velocities. There is also some increase in the Lorentzian character of the resonance as the width decreases with increasing

charge. The reason for this rather clear variation in shape is not understood.

In summary, a number of general characteristics of the internal energy transfer in slow ion-Rydberg collisions have been determined in this study. First, the energy transfer was found to be highly selective at the lowest velocities studied resulting in a very narrow range of possible product state energies following capture. The measured resonance position shows an increase in binding energy of the product states, but differs slightly but significantly from the classical over barrier predictions. The predictions of CTMC are in excellent agreement with our measurements over nearly the entire range of our study with only small deviations at the lowest and highest velocities studied.

3.4 Discussion and conclusions

This is by far the most extensive and quantitative study of ion-Rydberg collisions to date. Earlier studies covered only singly charged ions over a range of velocities [5], or ions with q=8 at two velocities [14, 15]. In contrast this study covered both a wide range of charges and velocities. The previous studies analyzed the final state distribution using Selective Field Ionization, in both cases finding apparent disagreement with the details predicted by CTMC. This study uses lasers to fully define the energy of both the target and product states of the measurement, and finds virtually complete agreement with CTMC theory over the entire range studied.

It has often been assumed that the validity of CTMC is limited at low velocity to velocities, v, greater than the velocity of the target electron v_e, corresponding to a reduced velocity (v/v_e) greater than one [35]. However, the range of validity of

CTMC at low velocities is difficult to assess in the absence of experiments or other computational methods [34]. Recent experiments have suggested that CTMC predictions may be valid well below a reduced velocity of one [36]. Indeed, this study extends to reduced velocities as low as 0.3, with no apparent disagreement. One conclusion which can be drawn from the remarkably good agreement with CTMC seen in this study this study is that the description of the Rydberg-ion collision by CTMC theory appears to be completely satisfactory, within the precision of this measurement and over the range of parameters included. If there is a significant breakdown of CTMC at low velocities, as has been suggested, it occurs beyond the range of the present experiment.

It is true that the poorest agreement with CTMC observed in this experiment is at the extreme velocities studied. At the lowest velocities the observed $q=3$ resonances are slightly wider than predicted, and at the highest velocity there appears to be a disagreement in the resonance position. This suggests that further studies at these limits should be pursued. It would be interesting to know if the apparent disagreement at $v=0.130$ a.u. for $q=3$ would be confirmed by a repeated measurement, and if this disagreement persists at higher velocities. Even more interesting, would be extensions of these measurements to lower velocities. The fact that CTMC is expected to fail at sufficiently low velocity, because of the increasing importance of tunneling [37], makes this the region of greatest interest. Previous studies of the total charge exchange cross section in the region of reduced velocity below one have revealed oscillations which correlate with multiple "swapping" of the captured electron between the projectile and target [37]. This

suggests the onset of molecule-like behavior, which is expected to dominate the extremely low velocity behavior of charge exchange. Whether and how the swapping phenomenon is reflected in the energy distributions has yet to be explored.

Another direction that holds promise for further studies of ion-Rydberg charge transfer using the RESIS technique is a more detailed analysis of final state distributions. For example more demanding checks of CTMC theory could be made by exploring the detailed predictions of the l and m states populated within a particular n state in the collision. The l-distributions in the final states of neutral Rydberg atoms have been studied previously [38] using the RESIS technique. Similar studies should be possible for $q > 1$ although this will require a higher signal to noise than the present measurement.

One intriguing application of the Rydberg charge capture process might be in the selective formation of selected excited states of neutral or ionic Rydberg systems. At sufficiently low velocities, it might even be possible to selectively populate a single principal quantum state of such a system, and choose the final state by controlling the excitation state of the Rydberg target. For example, consider this for the case studied here, a q=3 ion. At v=0.031 a.u., we find a resonance width in target energy of,

$$W_T(v=0.031 \text{ a.u.})=0.020 \text{ eV}$$

If the linear relationship of the width to velocity continues to a velocity smaller by a factor of ten we might expect,

$$W_T(v=0.0031 \text{ a.u.})=0.002 \text{ eV}$$

This is much smaller than the energy difference between adjacent target states. For example,

$$E_T(n_t=10)\text{-}E_T(n_t=11) = 0.024 \text{ eV}$$

This suggests that only certain product states, those matched resonantly with one of the target states could be produced under these conditions. One factor which must be taken into account is that the CTMC calculations of the width of the exit channel show an approximately constant width as seen in Fig. 1.2.5, while both CTMC and our measurement show the width decreasing in the entrance channel as $q^{-1/2}$ as seen in Fig. 3.3.14. This result in a width in the exit channel about $q^{1/2}$ larger than the width in the entrance channel. Thus if we assume for simplicity that,

$$E_p = \sqrt{q}E_t \quad \text{and} \quad W_p = \sqrt{q}W_t \tag{3.4.1}$$

then we might expect an $n_t=11$ target (E_t=-0.1124 eV) to produce products in a distribution centered at E_p=-0.1947 with a width W_p=0.0035 eV. Only one possible product state, $n_p=25$ at E_p=-0.1958 eV, satisfies this condition. Consequently, at this velocity, charge transfer from an $n_t=11$ target might produce the $n_p=25$ state uniquely. By the same token, other target states such as $n_t=10$, for which no suitable product state exists, might show a much reduced total cross section at this velocity. Of course this is only speculation. What the actual behavior would be at these very low velocities remains to be explored. Discrete energy resonances of this type could never be predicted by CTMC which only knows continuous classical energies. Thus, observations in the extreme low velocity regime could stimulate improved understanding of the transition from classical to quantum behavior in these systems.

Appendix A : Rydberg target fluorescence spectra

These are the spectra and line identifications of a selection of the Rydberg targets used in this experiment. The line identifications are for isolated lines in the range of wavelengths measured by the spectrometer, 200-900 nm. Lines not identified as transitions in Rb I are labeled with an asterisk and their positions are enumerated in the tables. The positions of the peaks reported are the wavelengths measured by the spectrometer at the position of the maximum intensity, not fits of the peak position. The two largest peaks of each target spectrum, the two peaks furthest to the right, saturate the detector over a range of wavelengths and as a consequence the position of the maximum is not as precise as for the smaller peaks.

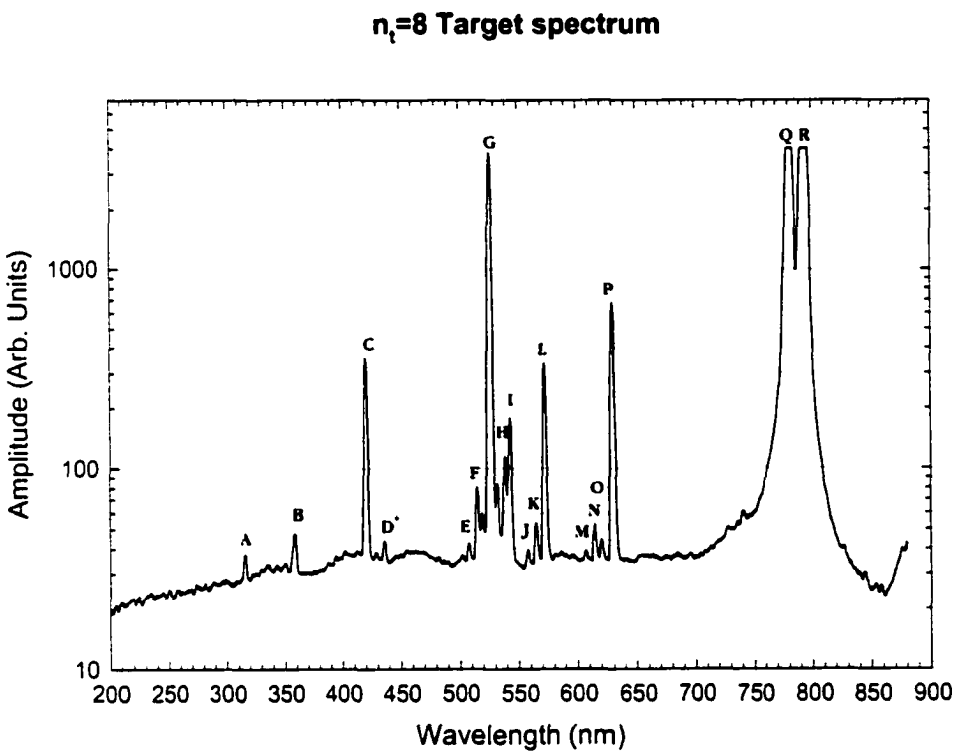

Figure (A.1): **The n_t = 8 target spectrum.**

Table A.1: Line identification of n_t=8 spectrum.

Label	Transition	Measured Wavelength(nm)	Tabulated Wavelength(nm)
A	$10P_{3/2}$-$5S_{1/2}$	315.7	315.8
B	$7P_{3/2}$-$5S_{1/2}$	358.5	358.8
C	$6P_{3/2}$-$5S_{1/2}$	420.1	420.3
D*	?	436.3	
E	$10D$-$5P_{1/2}$	507.2	508.9
F	$10D$-$5P_{3/2}$	515.2	515.2
G	$9D$-$5P_{1/2}$	525.9	526.2
H	$8D$-$5P_{1/2}$	538.7	536.4
I	$8D$-$5P_{3/2}$	542.8	543.3
J	$9S_{1/2}$-$5P_{1/2}$	557.9	558.0
K	$7D$-$5P_{1/2}$ $9S_{1/2}$-$5P_{3/2}$	564.8	564.9
L	$7D$-$5P_{3/2}$	572.3	572.6
M	$8S_{1/2}$-$5P_{1/2}$	606.8	607.2
N	$8S_{1/2}$-$5P_{3/2}$	614.8	616.1
O	$6D$-$5P_{1/2}$	620.5	620.8
P	$6D$-$5P_{3/2}$	629.2	630.1
Q	$5P_{3/2}$-$5S_{1/2}$	780.7	780.2
R	8F-4D	795.0	792.8

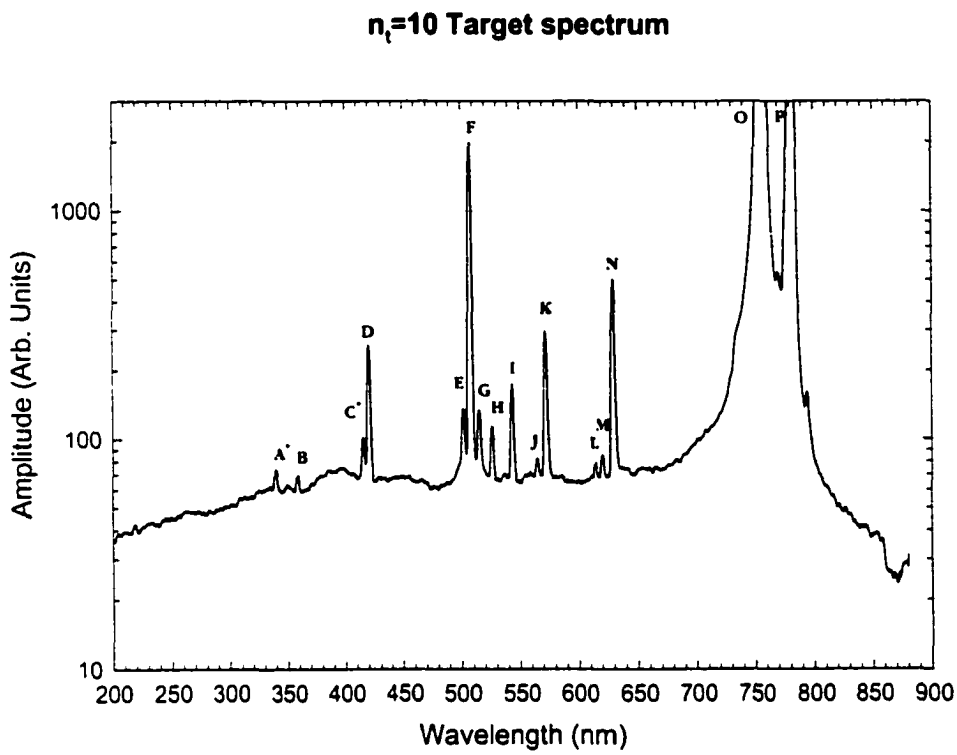

Figure (A.2): **The n_t=10 target spectrum.**

Table A.2: Line identification of $n_t = 10$ spectrum.

Label	Transition	Measured Wavelength(nm)	Tabulated Wavelength(nm)
A*	?	339.3	-
B	$7P_{3/2}$-$5S_{1/2}$	358.8	358.8
C*	?	415.1	-
D	$6P_{3/2}$-$5S_{1/2}$	420.1	420.3
E	$11D$-$5P_{1/2}$	501.6	501.6
F	$11D$-$5P_{3/2}$	507.5	507.7
G	$10D$-$5P_{3/2}$	514.8	515.2
H	$9D$-$5P_{3/2}$	525.9	526.2
I	$8D$-$5P_{3/2}$	542.8	543.3
J	$7D$-$5P_{1/2}$ $9S_{1/2}$-$5P_{3/2}$	564.4	564.9
K	$7D$-$5P_{3/2}$	572.3	572.6
L	$8S_{1/2}$-$5P_{3/2}$	614.8	616.1
M	$6D$-$5P_{1/2}$	620.2	620.8
N	$6D$-$5P_{3/2}$	629.2	630.1
O	10F-4D	758.0	755.6
P	$5P_{3/2}$-$5S_{1/2}$	782.2	780.2

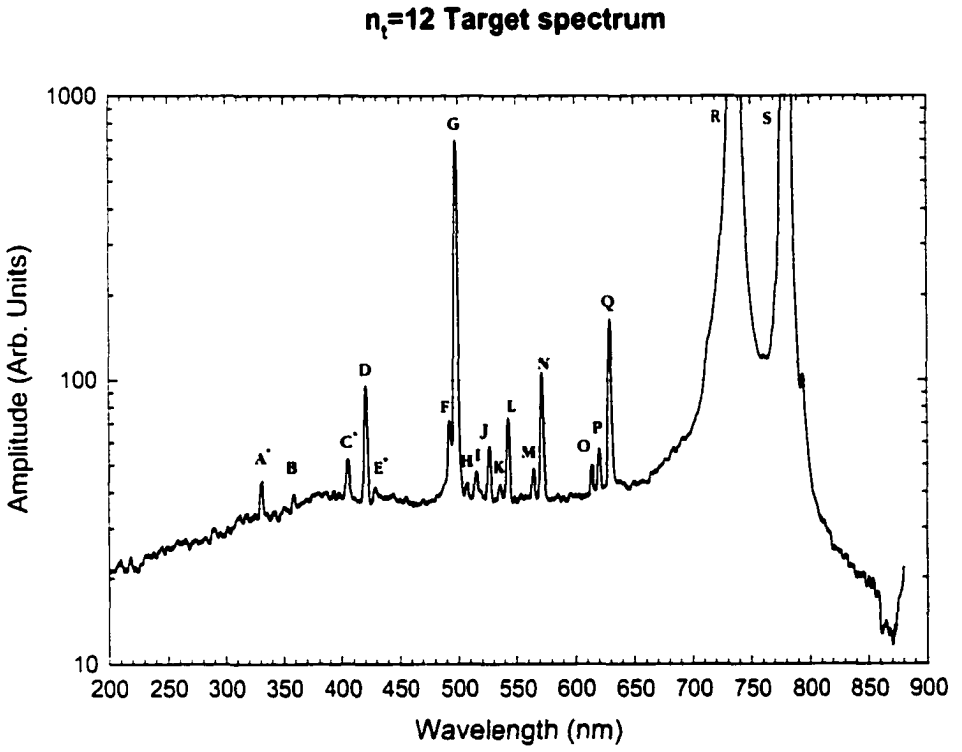

Figure (A.3): **The n_t=12 target spectrum.**

Table A.3: Line identification of n_t=12 spectrum.

Label	Transition	Measured Wavelength(nm)	Tabulated Wavelength(nm)
A*	?	330.9	-
B	$7P_{3/2}$-$5S_{1/2}$	358.8	358.8
C*	?	405.0	-
D	$6P_{3/2}$-$5S_{1/2}$	420.5	420.3
E*	?	428.0	-
F	$13D$-$5P_{1/2}$	492.1	492.5
G	$13D$-$5P_{3/2}$	498.1	498.3
H	$011D$-$5P_{3/2}$	507.5	507.7
I	$10D$-$5P_{3/2}$	515.2	515.2
J	$9D$-$5P_{3/2}$	525.9	526.2
K	$8D$-$5P_{1/2}$	536.0	536.4
L	$8D$-$5P_{3/2}$	542.8	543.3
M	$7D$-$5P_{1/2}$ $9S_{1/2}$-$5P_{3/2}$	564.4	564.9
N	$7D$-$5P_{3/2}$	571.9	572.6
O	$8S_{1/2}$-$5P_{3/2}$	614.2	616.1
P	$6D$-$5P_{1/2}$	620.2	620.8
Q	$6D$-$5P_{3/2}$	629.5	630.1
R	12F-4D	739.0	736.8
S	$5P_{3/2}$-$5S_{1/2}$	781.0	780.2

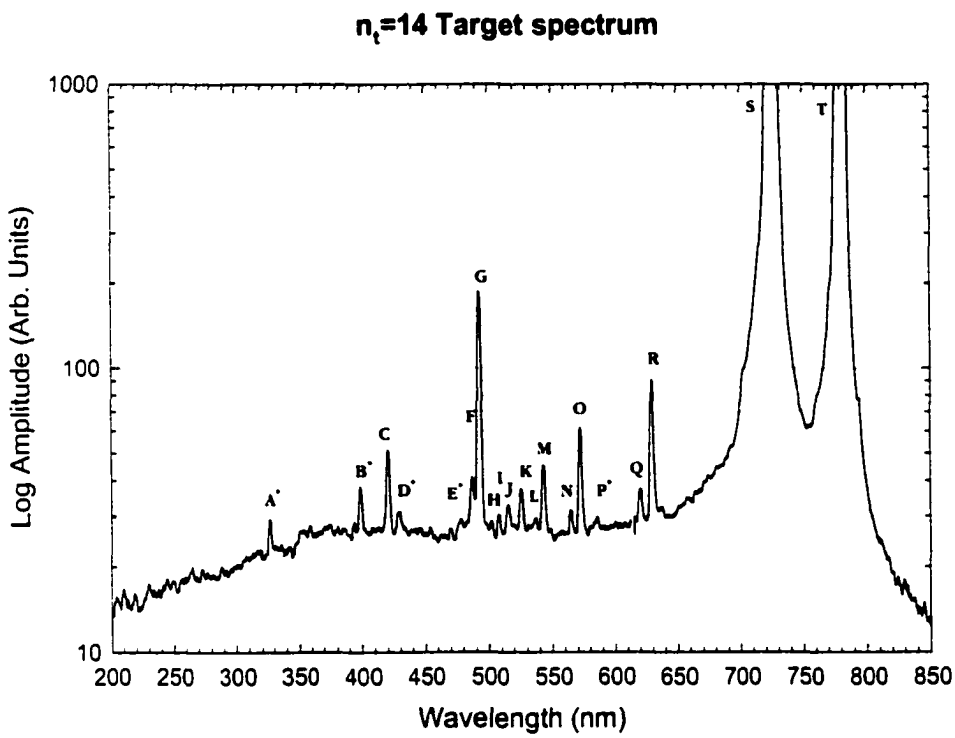

Figure (A.4): **The n_t=14 target spectrum.**

Table A.4: Line identification of n_t=14 spectrum.

Label	Transition	Measured Wavelength(nm)	Tabulated Wavelength(nm)
A*	?	325.7	-
B*	?	398.9	-
C	$6P_{3/2}$-$5S_{1/2}$	420.1	420.3
D*	?	429.1	-
E*	?	478.1	-
F	$15D$-$5P_{1/2}$	486.9	487.2
G	$15D$-$5P_{3/2}$	492.9	493.0
H	$11D$-$5P_{1/2}$	501.9	501.6
I	$11D$-$5P_{3/2}$	507.5	507.7
J	$10D$-$5P_{3/2}$	515.5	515.2
K	$9D$-$5P_{3/2}$	525.6	526.2
L	$8D$-$5P_{1/2}$	537.3	536.4
M	$8D$-$5P_{3/2}$	543.2	543.3
N	$7D$-$5P_{1/2}$ $9S_{1/2}$-$5P_{3/2}$	564.4	564.9
O	$7D$-$5P_{3/2}$	571.9	572.6
P*	?	585.5	-
Q	$6D$-$5P_{1/2}$	620.2	620.8
R	$6D$-$5P_{3/2}$	629.5	630.1
S	14F-4D	727.8	726.0
T	$5P_{3/2}$-$5S_{1/2}$	780.4	780.2

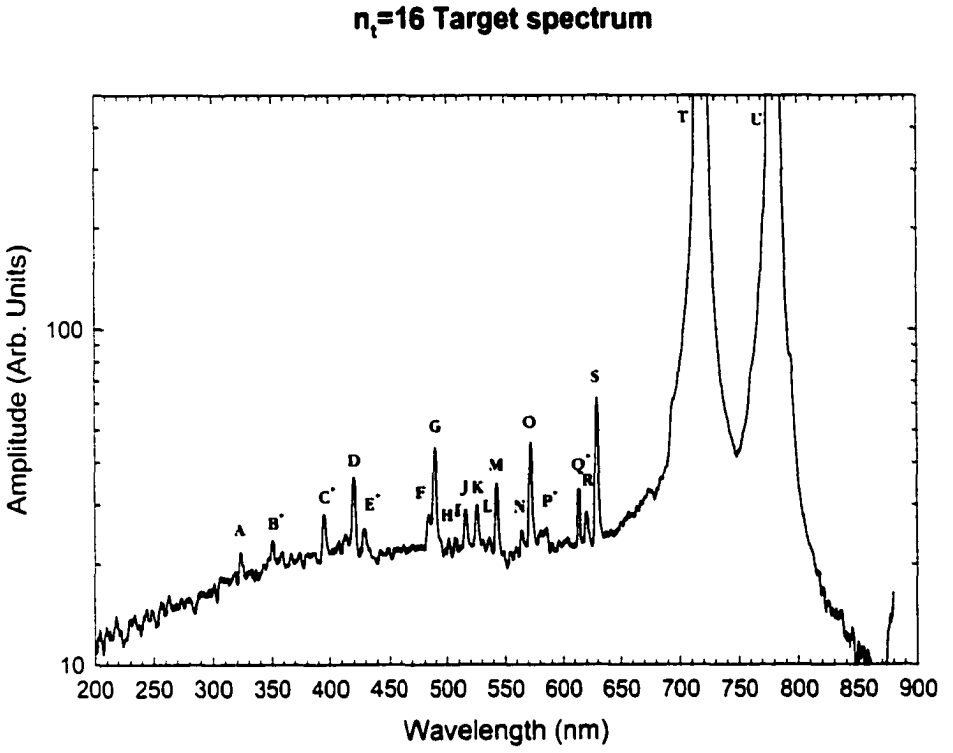

Figure (A.5): **The n_t=16 target spectrum.**

Table A.5: Line identification of $n_t = 16$ spectrum.

Label	Transition	Measured Wavelength(nm)	Tabulated Wavelength(nm)
A	$9P_{3/2}$-$5S_{1/2}$	323.1	322.9
B*	?	350.4	-
C*	?	394.9	-
D	$6P_{3/2}$-$5S_{1/2}$	420.1	420.3
E*	?	429.1	-
F	$17D$-$5P_{1/2}$	483.7	483.9
G	$17D$-$5P_{3/2}$	489.0	489.5
H	$11D$-$5P_{1/2}$	501.9	501.6
I	$11D$-$5P_{3/2}$	507.2	507.7
J	$10D$-$5P_{3/2}$	515.5	515.2
K	$9D$-$5P_{3/2}$	525.6	526.2
L	$8D$-$5P_{1/2}$	536.6	536.4
M	$8D$-$5P_{3/2}$	542.8	543.3
N	$7D$-$5P_{1/2}$ $9S_{1/2}$-$5P_{3/2}$	564.4	564.9
O	$7D$-$5P_{3/2}$	571.9	572.6
P*	?	585.5	-
Q*	?	613.8	-
R	$6D$-$5P_{1/2}$	620.2	620.8
S	$6D$-$5P_{3/2}$	629.5	630.1
T	16F-4D	717.9	719.1
U	$5P_{3/2}$-$5S_{1/2}$	781.0	780.2

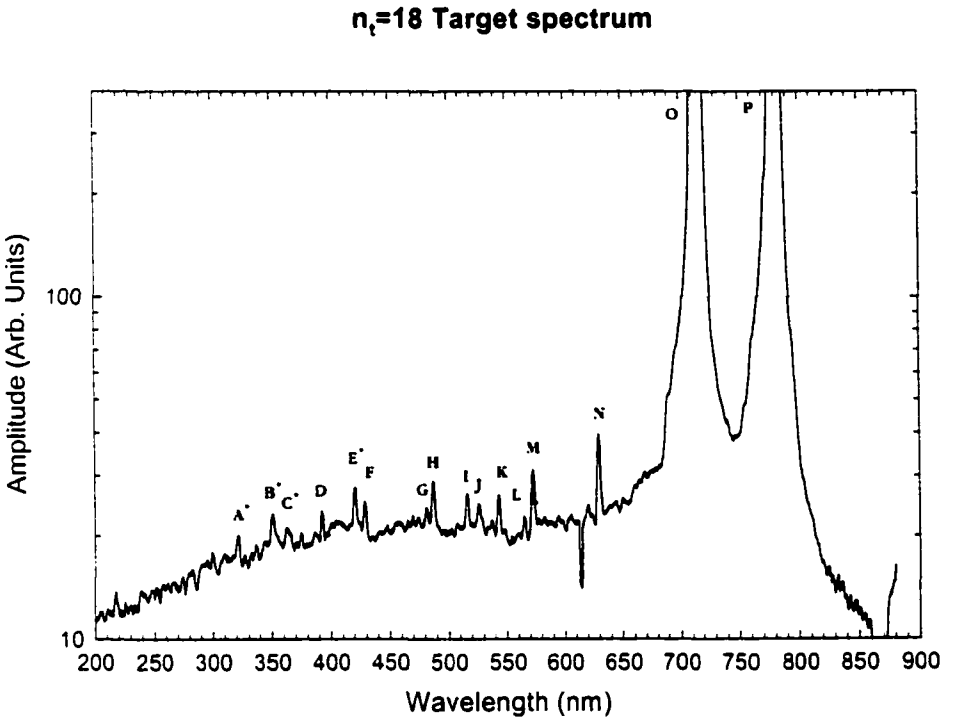

Figure (A.6): **The n_t=18 target spectrum.**

Table A.6: Line identification of $n_t = 18$ spectrum.

Label	Transition	Measured Wavelength(nm)	Tabulated Wavelength(nm)
A*	?	320.9	-
B*	?	350.8	-
C*	?	362.5	-
D	?	392.0	-
E	$6P_{3/2}$-$5S_{1/2}$	420.5	420.3
F*	?	428.4	-
G	$19D$-$5P_{1/2}$	481.3	481.6
H	$19D$-$5P_{3/2}$	486.9	487.3
I	$10D$-$5P_{3/2}$	515.9	515.2
J	$9D$-$5P_{3/2}$	525.6	526.2
K	$8D$-$5P_{3/2}$	542.8	543.3
L	$7D$-$5P_{1/2}$ $9S_{1/2}$-$5P_{3/2}$	564.4	564.9
M	$7D$-$5P_{3/2}$	572.3	572.6
N	$6D$-$5P_{3/2}$	629.5	630.1
O	18F-4D	714.3	714.5
P	$5P_{3/2}$-$5S_{1/2}$	780.4	780.2

There are some common features to all of the spectra. The first common feature is the series of *nD*-5*P* transitions. For example, peaks F, G, H, I, K, and N in the 10*F* spectrum. The largest peak of this series in each of the spectra is the $(n_t+1)D$-$5P_{3/2}$ transition. This is the visible transition from the population transfer from the mirrorless maser described briefly in Chapter 2 and in more detail in the paper referenced[17]. This transition is responsible for the blue glow seen when looking at the target directly. Also seen in this series is the set of smaller nD-$5P_{1/2}$ transitions to the left of the larger peaks. For example peak J is associated with peak K in the 10*F* spectrum. Any population making these transitions is coming from population not transferred along the desired excitation path, coming from an $nD_{3/2}$ rather than a $nD_{5/2}$ state. A second common feature to all the spectra is the $6P_{3/2}$-$5S_{1/2}$ transition. This is not surprising as the high-*n D* states are populated , as seen from the *nD*-5*P* transitions. The *nD*-6*P* transitions are not in the wavelength range measured by the spectrometer used, but it is likely the 6*P* state is populated by transitions similar to those seen in the *nD*-5*P* states. Finally all the spectra have two transitions on the excitation path, the $5P_{3/2}$-$5S_{1/2}$ and n_tF-4*D* transitions.

Appendix B : Stark ionization of Rydberg Ions

The following is an estimation of the field required for ionization of the Rydberg ion in an external electric field, generalizing the method used in the ionization of a Rydberg atom in an external field [7,39]. The combined Coulomb-Stark potential is used to determine when the zero field energy of a state in the Rydberg ion lies above the saddle point created by an external electric field. Thus starting with the potential,

$$V = -\frac{q}{r} - Fz \tag{B.1}$$

we set the gradient equal to zero to find the position of the saddle point. It is located on the z axis, at $z = -\sqrt{q/F}$ and has a potential of $V = -2\sqrt{qF}$. Setting this potential equal to the Rydberg energy of an arbitrary state,

$$E_{Rydberg} = -\frac{q^2}{2n^2} \tag{B.2}$$

this gives an ionization field for the Rydberg state of the ion of,

$$F = \frac{q^3}{16n^4}. \tag{B.3}$$

This simple picture has two serious flaws, first it neglects the Stark shift of the level due to the applied field and second it neglects the spatial distribution of the wavefunction. If the Stark shift of the level is taken into account the lowest lying

Stark state, or the extreme red Stark state, will have an energy of,

$$E_{\text{Stark}} = -\frac{q^2}{2n^2} - \frac{3Fn^2}{q} \tag{B.4}$$

for a sufficiently high n state. Using this energy and setting it equal to the potential of the saddle point gives an ionization field for the extreme red Stark state of,

$$F = \frac{q^3}{9n^4}. \tag{B.5}$$

Thus a significantly higher field than the most naive classical model is needed to ionize the lowest Stark state if the Stark shift is taken into account. Detailed quantum mechanical calculations confirm this estimate, but also predict that the ionization varies by up to a factor of two for other Stark states of the same n. The extreme red state is actually the first state to ionize. This is somewhat counter-intuitive since the states shifted up by the external field have less binding energy and thus would be expected to ionize at a lower field. The spatial distribution of the wavefunctions gives a physical argument for why the lowest energy Stark state is also the first to ionize. The lowest energy Stark state is shifted to lower energy because the electron is localized to the downfield side of the atom, or toward the saddle point, increasing the binding energy. Since the electron is localized by the field to a region near the saddle point, once the energy of the state is above the saddle point it is very likely the electron will leave the ion, and ionization will occur. However, the upshifted Stark states are localized to the

upfield side of the atom and thus are harder to ionize than the downshifted states even though their energy is well above the saddle point. This is because the electrons are localized well away from the saddle point, having a small probability of being near the saddle point position and ionizing. Thus, the spatial distribution of the Stark states causes the field required to ionize the highest energy state, or extreme blue state, to be approximately twice that of the lowest energy state, or extreme red state, in neutral hydrogen [7].

This result, calculated for neutral hydrogen can be shown to apply to a charged hydrogenic Rydberg ion as well, if an additional factor of q^3 is added, where q is the charge of the nucleus and is derived in detail in the following manner.

To scale the neutral hydrogen case first we write the Hamiltonian for the neutral hydrogen case as,

$$H = \frac{\left|\vec{p}_p\right|^2}{2m_p} + \frac{\left|\vec{p}_e\right|^2}{2m_e} - \frac{e^2}{\left|\vec{r}_e - \vec{r}_p\right|} + e\vec{F}\cdot\left(\vec{r}_e - \vec{r}_p\right) \tag{B.6}$$

where p_p, r_p, and m_p are the proton momentum, position, and mass, p_e, r_e, and m_e are the electron momentum, position, and mass, e is the electron charge and F is the field (all quantities are in a.u.). From this and the definitions,

$$\vec{R}_{CM} = \frac{m_p\vec{r}_p + m_e\vec{r}_e}{m_p + m_e}, \quad \vec{r} = \vec{r}_e - \vec{r}_p \tag{B.7}$$

where R_{cm} is the center of mass position and r is the position of the electron relative

to the proton, the Hamiltonian can be transformed to the center of mass frame of the system giving,

$$H = \frac{\left|\vec{P}_{CM}\right|^2}{2M_T} + \frac{\left|\vec{p}\right|^2}{2\mu} - \frac{e^2}{\vec{r}} + e\vec{F}\cdot(\vec{r}) \tag{B.8}$$

where,

$$M_T = m_p + m_e,\ \mu = \frac{m_e m_p}{m_e + m_p} \tag{B.9}$$

A similar transformation can be done for the Hamiltonian of the hydrogenic ion giving,

$$H = \frac{\left|\vec{p}_N\right|^2}{m_N} + \frac{\left|\vec{p}_e\right|^2}{m_e} - \frac{qe^2}{\left|\vec{r}_e - \vec{r}_N\right|} + e\vec{F}\cdot\left(\vec{r}_e - q\vec{r}_N\right) \tag{B.10}$$

where m_N, p_N, and r_N are the mass, momentum and position of the nucleus and q is the charge of the nucleus. Using the definitions,

$$\vec{R}_{CM} = \frac{m_N\vec{r}_N + m_e\vec{r}_e}{m_N + m_e},\ \vec{r} = \vec{r}_e - \vec{r}_N \tag{B.11}$$

the Hamiltonian after the change of coordinates to the center of mass frame for the system is,

$$H = \frac{\left|\vec{P}_{CM}\right|^2}{2M_T} + \frac{\left|\vec{p}\right|^2}{2\mu} - \frac{qe^2}{\vec{r}} - e(q-1)\vec{F}\cdot\vec{R}_{CM} - e\vec{F}\cdot\vec{r} - e(q-1)\frac{m_e}{m_N}\vec{F}\cdot\vec{r} \tag{B.12}$$

The last term is only a small correction when $m_N << m_e$ giving the approximate result,

$$H = \frac{|P_{CM}|^2}{2M_T} + \frac{|\vec{p}|^2}{2\mu} - \frac{qe^2}{\vec{r}} - e(q-1)\vec{F}\cdot\vec{R}_{CM} - e\vec{F}\cdot\vec{r} \qquad \text{(B.13)}$$

Looking only at the terms dependant on the relative positions of the nucleus and the electron, the terms that determine the behavior of the energy levels, and defining $e' \equiv e\sqrt{q}$ and substituting into Eqn. B.8 we get,

$$H = \frac{|\vec{p}|^2}{2\mu} - \frac{e'^2}{\vec{r}} + e'\left(\frac{\vec{F}}{\sqrt{q}}\right)\cdot\vec{r} \qquad \text{(B.14)}$$

which is identical to the equation for hydrogen if we let $F' = F/\sqrt{q}$. Thus for q > 1 the point at which the extreme blue state ionizes can be directly scaled from the hydrogen solution, approximately twice the point at which the extreme red state ionizes. This also gives a second way to calculate the ionization field of the extreme red Stark state by scaling the well known and tested solution,

$$F = \frac{1}{9n^4} \qquad \text{(B.15)}$$

to give,

$$F' = \frac{F}{\sqrt{q}} = \frac{1}{9n^4}\frac{e'}{a_o'^2} = \frac{1}{9n^4}\frac{e\sqrt{q}}{\frac{\hbar^4}{m^2e^4q^2}} = \frac{1}{9n^4}q^{\frac{5}{2}}\frac{e}{a_o^2} \qquad \text{(B.16)}$$

or,

$$F = \frac{q^3}{9n^4}\,(\text{a.u.}) \qquad \text{(B.17)}$$

the same ionization field given by the other method.

Thus hydrogenic Stark levels of ionic Rydberg states using this scaling of the hydrogenic case ionize at,

$$F = \frac{q^3}{9n^4}(\text{Extreme red}) \text{ to } F = \frac{2q^3}{9n^4}(\text{Extreme blue}). \qquad \text{(B.18)}$$

These results are only valid for states of a hydrogenic ion. The situation is more complex for non-hydrogenic atoms, such used in this experiment, where there is a non-Coulombic interaction between the Rydberg electron and the ion core. The Stark states in this case are coupled and do not cross as in the hydrogenic case, but instead have avoided crossings. In the non-hydrogenic ion, because of the coupling between Stark states and the associated avoided crossings between Stark states, ionization can occur in two ways. The first is diabatic ionization, which occurs exactly like hydrogenic ionization. The states proceed to ionization ignoring the avoided crossings as shown in Fig. B.1 as a dotted arrow. This yields the same fields

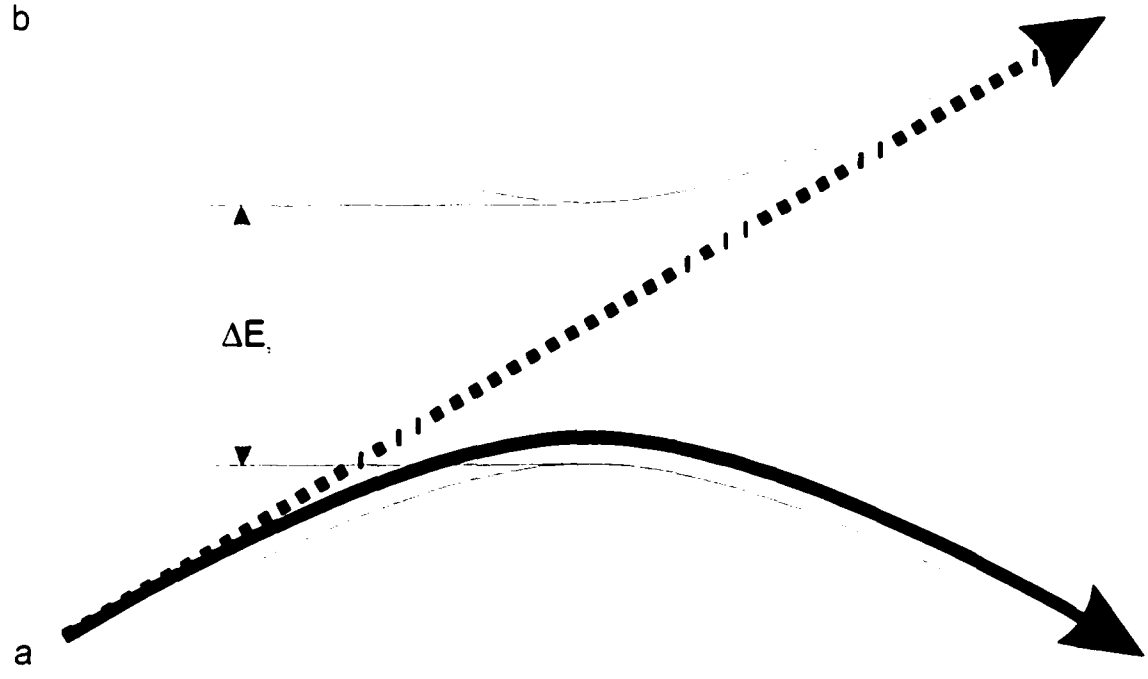

Figure (B.1): : **Diabatic and adiabatic ionization paths.** This shows the two different paths to ionization through one avoided crossing.

for ionization as Eqn. B.18. The second path to ionization in a non-hydrogenic system is more complicated and is called adiabatic ionization. In adiabatic ionization an electron follows a continuous path through the avoided crossing as shown in Fig. B.1 by the solid arrow. The route to adiabatic ionization may entail many such anti-crossings. In a remarkable coincidence, the net result is that ionization occurs at the classical ionization field predicted in Eqn. B.3 [28].

The slew rate S, how fast the electric field is changing with time, at the avoided crossing determines which type of ionization occurs. The critical slew rate, S_{Crit}, at the avoided crossing is determined by the separation energy, ΔE_0, at the avoided crossing and rate the energy of the state is changing with field, E_2-$E_1/\Delta F$. If $S >> S_{Crit}$ at the avoided crossing then the passage will be diabatic. If $S << S_{Crit}$ the passage will be adiabatic. If $S \cong S_{Crit}$ then the passage has some probability to be either diabatic or adiabatic.

The adiabatic theorem gives the criterion to determine the critical slew rate. If the field is changed slowly enough and the system begins in a Stark eigenstate, then according to the adiabatic theorem the system will remain in that Stark eigenstate. The rate that the field can change and remain in the original eigenstate requires that the energy separation between states divided by $\hbar$ is much larger than the rate of the parameter changes, or $E_0/\hbar >> 1/\Delta t$ where E_0 is the energy separation between the states. Thus, the critical slew rate is given when the relationship $\Delta E_0 \cdot \Delta t \approx \hbar$ is satisfied. Using this and rewriting Δt in terms of the slew rate and the energy separation gives,

$$\Delta t = \frac{\Delta E_o}{\frac{\Delta\left(E_2 - E_1\right)}{\Delta t}} \tag{B.19}$$

where E_1 and E_2 are the energies of states 1 and 2 respectively and $\Delta E_0 = E_2 - E_1$. This can be further rewritten in terms of the applied field as,

$$\Delta t = \frac{\Delta E_o}{\frac{\Delta\left(E_2 - E_1\right)}{\Delta F}\frac{\Delta F}{\Delta t}} \tag{B.20}$$

where ΔF is the change in the applied electric field. Thus the critical slew rate is calculated by substituting Δt into $\Delta E_0\ \Delta t \sim \hbar$ and solving for $\Delta F/\Delta t$ and the critical slew rate is,

$$S_{Critical} = \frac{1}{\hbar}\frac{\Delta E_o^2}{\frac{\Delta\left(E_2 - E_1\right)}{\Delta F}} \tag{B.21}$$

At the field at which the coulombic energies would cross, the non-colombic potential lifts the degeneracy giving the energy separation ΔE_0. This separation energy is equal to the following matrix element,

$$\Delta E_0 = 2\left|\left\langle nn_1n_2m\middle|V(r)\middle|n'n_1'n_2'm\right\rangle\right| \tag{B.22}$$

where $V(r)$ is the non-coulombic component of the potential. The value of this matrix element can be calculated in the following way,

$$\langle nn_1n_2m|V(r)|n'n_1'n_2'm\rangle = \sum_l \langle nn_1n_2m|nlm\rangle\langle nlm|V(r)|n'lm\rangle\langle n'lm|n'n_1'n_2'm\rangle \tag{B.23}$$

where,

$$\langle nlm|V(r)|n'lm\rangle = -\frac{q^2e^2}{2a_0}\frac{\delta_l}{\sqrt{n^3}\sqrt{n'^3}} \tag{B.24}$$

and,

$$|\langle nlm|nn_1n_2m\rangle|^2 = \frac{1}{(n-m)} \tag{B.25}$$

when averaged over l as shown by Gallager[7]. This reduces to,

$$\langle nlm|V(r)|n'lm\rangle \cong -\frac{q^2e^2}{2a_o}\frac{\delta_{l\min}}{n^3(n-m)} \tag{B.26}$$

exactly for transitions within a n-state manifold and approximately for adjacent n states for high n, where $\delta_{l\,min}$ is the quantum defect of the lowest l state of the m manifold being examined, because this has the largest effect on the matrix element. Using this value for ΔE_0 in Eqn. B.21, and the rate of change of energy of adjacent states calculated by differentiating Eqn. B.4,

$$\frac{\Delta(E_2 - E_1)}{\Delta F} = \frac{6n^2}{q}ea_o \tag{B.27}$$

gives an approximate critical slew rate of,

$$S_{Crit} \cong \frac{q^5 \delta_{l\min}^2}{24 n^{10}} \tag{B.28}$$

for $n >> m$. If the state has a slew rate smaller than the critical slew rate it will ionize at the adiabatic field as given by scaling Eqn. B.3 for the $q > 1$ ion core ($q^3/(16\,n^4)$). However if the slew rate is greater than the critical slew rate the state will not ionize unless the diabatic ionization field for the state, ($1/9$ & $2/9 q^3/n^4$), is exceeded. To determine which states are ionized in the repeller and how they are ionized it is necessary to determine the slew rate of the field in the repeller, and whether the states of interest are ionized diabaticly or adiabaticly.

Appendix C : Power supply and control unit schematics

These are the schematics for the power supply used to provide the voltages for the Stark ionizer, lens, and deflection plates in the detector. Note that the control voltages for the individual supplies can be switched between 0-5 V inputs and front panel potentiometers on the power supply for all the supplies except the -4 kV supply providing the voltage for the Stark ionization field (P4) in the short gap Stark ionizer. An additional control unit was required to allow the deflection plates to have the same voltage applied in opposite polarities, which allows for the least focusing effects from the deflection. This unit was necessary because for an output of 0 V the control voltage applied to the negative Ultravolt supplies must be about 5 V, and the output voltage increases as the control voltage is lowered. However, for the positive supplies it is opposite, for a 0 V output a 0 V control voltage is applied, and the output voltage increases as the control voltage increases. Thus the control unit supplies voltages from 5 V to 0 V for the negative supply and from 0 V to 5 V for the positive supply for each set of deflectors.

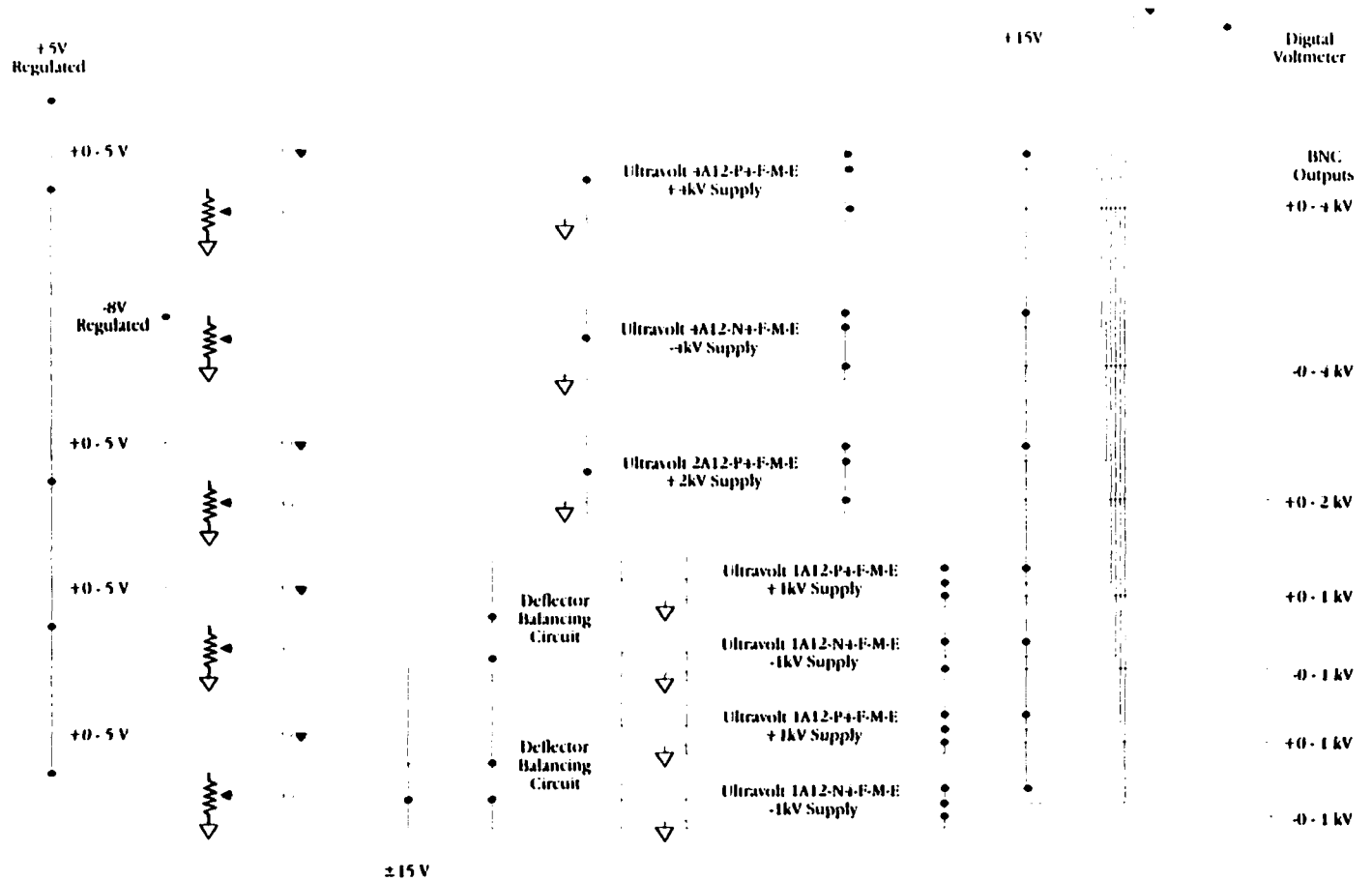

Figure (C.1):<u>Power supply shematic</u>. All the potentiometers shown are front panel controls and have a total resistance of 100kΩ. The deflector balancing controls are shown in detail in Fig. C.2.

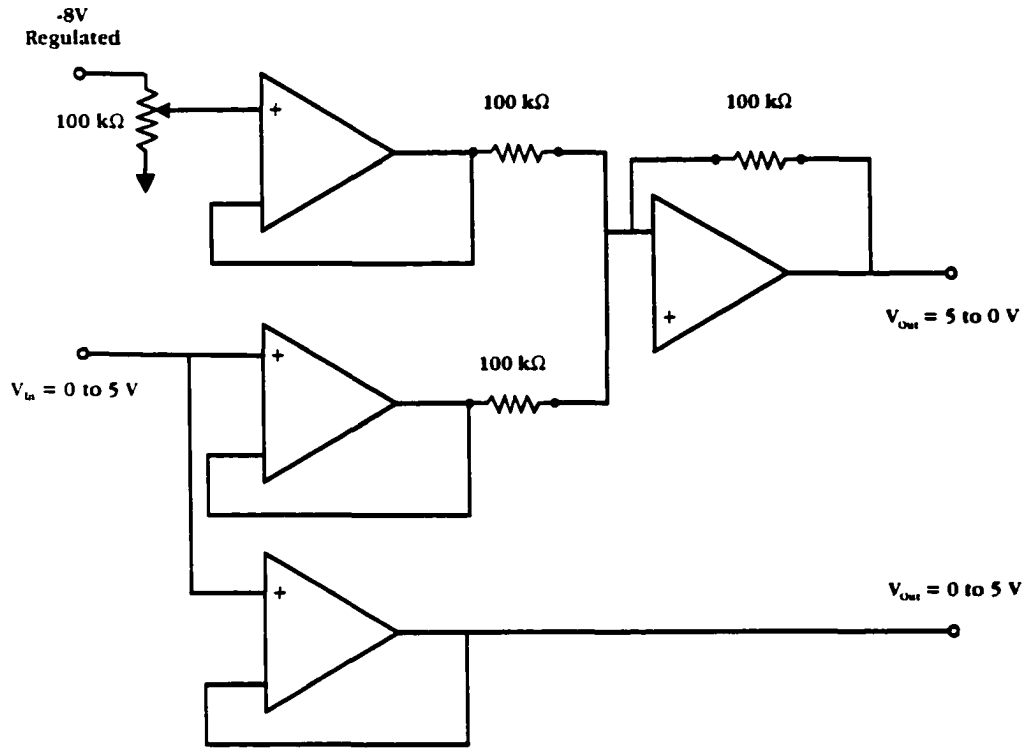

Figure (C.2): **Detail of detector balancing control.** This shows the detector balancing control. The regulated voltages are from regulators powered by the ±15 V supplied to the unit from the front panel. The potentiometer is a trim potentiometer inside the power supply cabinet. This is used to balance the control voltages so the output voltages the positive and negative supplies are equal.

Appendix D : Tabulated measured and theoretical ratios

The following tables give the measured ratios, R_{Meas}, and the ratios theoretically calculated using the CTMC method, R_{CTMC}, for all of the ions and velocities used in this experiment. Also given are all of the factors used to calculate R_{CTMC}. As a reminder Eqn. 3.3.11 specifies these factors as,

$$R_{CTMC} = C\, f_{Cascade} \frac{\sigma_p'}{\sigma_T'} = C\left(\frac{f_L f_{Cascade}}{f_R}\right)\frac{\sigma_p}{\sigma_T} \qquad \text{(D.1)}$$

where C is an overall constant determined by a fit of R_{CTMC} to R_{Meas} for all of the targets measured, $f_{Cascade}$ is the factor representing changes in the population between the target and the CO_2 excitation from cascades and black body radiation, f_L is the factor representing the fraction of the partial cross section in the measured l-state, f_R is the factor representing the fraction of the capture population which is not ionized in the repeller, σ_p is the partial cross section calculated by CTMC, and σ_T is the total capture cross section calculated by CTMC. The order of the measurements is indicated by giving the lab book and page number of the starting page of the measurement in parentheses for each of the sets of measurements. One important event was the replacement of the LIR post, this occurred in lab book DFCF7 on page 18.

Table D.1: C^{2+} v = 0.100 a.u. : Measured ratios (Lab book : DFCF5p60)

Target n_t	R_{Meas}
8	0.032(2)
9	0.110(3)
10	0.111(3)
12	0.099(3)
13	0.079(2)
14	0.071(7)
15	0.066(6)
16	0.038(7)
17	0.028(18)
18	0.022(7)

Table D.2: C^{2+} v = 0.100 a.u. : Calculated quantities

Target n_t	R_{CTMC}	$\sigma_p(10^{-14}cm^2)$	f_L	$f_{Cascade}$	$\sigma_T(10^{-14}\ cm^2)$	f_R
8	0.0166(6)	14.19	0.56	0.66	317.05	0.99
9	0.0424(15)	41.50	0.81	0.61	499.27	0.98
10	0.0474(18)	55.18	0.84	0.70	717.34	0.96
12	0.0341(3)	58.91	0.80	0.70	1135.50	0.84
13	0.0297(11)	54.11	0.75	0.71	1211.98	0.81
14	0.0260(10)	47.67	0.76	0.70	1250.77	0.78
15	0.0250(10)	43.81	0.76	0.69	1223.73	0.75
16	0.0215(9)	33.38	0.77	0.71	1166.32	0.73
17	0.0210(9)	28.90	0.78	0.71	1131.55	0.70
18	0.0182(8)	24.26	0.77	0.71	1074.37	0.68

Table D.3:: C^{3+} v = 0.100 a.u. : Measured ratios (Lab book : DFCF5p13)

Target n_t	R_{Meas}
8	0.0130(7)
9	0.0451(6)
10	0.118(3)
11	0.128(7)
12	0.128(2)
13	0.120(6)
14	0.105(4)
15	0.101(6)
16	0.091(2)
17	0.063(8)
18	0.065(9)

Table D.4: C^{3+} v = 0.100 a.u. : Calculated quantities

Target n_t	R_{CTMC}	$\sigma_p(10^{-14}cm^2)$	f_L	$f_{Cascade}$	$\sigma_T(10^{-14}\ cm^2)$	f_R
8	0.0039(2)	4.32	0.62	0.76	532.02	0.99
9	0.0101(3)	17.05	0.63	0.78	844.93	0.99
10	0.0273(7)	55.51	0.85	0.70	1243.93	0.98
11	0.0328(9)	78.63	0.91	0.74	1696.63	0.95
12	0.0324(9)	89.30	0.93	0.77	2159.63	0.91
13	0.0305(9)	91.14	0.93	0.77	2552.32	0.84
14	0.0274(8)	87.67	0.91	0.76	2794.30	0.79
15	0.0242(7)	78.44	0.90	0.76	2908.28	0.76
16	0.0228(7)	72.21	0.88	0.75	2929.02	0.72
17	0.0205(7)	62.84	0.88	0.75	2921.17	0.69
18	0.0183(7)	51.22	0.87	0.75	2767.22	0.66

Table D.5: C^{3+} v = 0.100 a.u. : 2nd Measurement Measured ratios

(Lab book : DFCF11p3)

Target n_t	R_{Meas}
8	0.02(4)
9	0.282(12)
10	0.562(18)
12	0.73(4)
14	0.56(3)
16	0.42(3)
18	0.29(2)
22	0.26(2)
26	0.22(4)

Table D.6: C^{3+} v = 0.100 a.u. : 2nd Measurement Calculated quantities

Target n_t	R_{CTMC}	$\sigma_p(10^{-14}cm^2)$	f_L	$f_{Cascade}$	$\sigma_T(10^{-14}\ cm^2)$	f_R
8	0.0033(2)	4.32	0.53	0.76	532.02	0.99
9	0.0089(3)	17.05	0.54	0.81	844.93	0.99
10	0.0251(8)	55.51	0.78	0.70	1243.93	0.97
12	0.0320(10)	89.30	0.88	0.75	2159.63	0.86
14	0.0274(9)	87.67	0.87	0.72	2794.30	0.72
16	0.0249(9)	72.21	0.85	0.75	2929.02	0.63
18	0.0200(8)	51.22	0.83	0.73	2767.22	0.56
22	0.0128(7)	23.04	0.73	0.78	2176.03	0.47
26	0.0065(6)	7.80	0.68	0.85	1641.22	0.42

Table D.7: C^{4+} v = 0.100 a.u. : Measured ratios (Lab book : DFCF5p89)

Target n_t	R_{Meas}
8	0.0073(19)
9	0.0293(8)
10	0.1046(18)
11	0.133(3)
12	0.139(7)
14	0.129(4)
16	0.078(4)
17	0.067(8)

Table D.8: C^{4+} v = 0.100 a.u. : Calculated quantities

Target n_t	R_{CTMC}	$\sigma_p(10^{-14}cm^2)$	f_L	$f_{Cascade}$	$\sigma_T(10^{-14}$ cm$^2)$	f_R
8	0.00227(10)	2.63	0.98	0.65	749.41	0.99
9	0.00517(17)	9.16	0.99	0.68	1198.23	0.99
10	0.0199(4)	49.76	1.00	0.69	1748.70	0.99
11	0.0318(7)	98.18	1.00	0.77	2459.38	0.97
12	0.0330(7)	118.78	1.00	0.85	3261.70	0.93
14	0.0270(7)	121.78	1.00	0.83	4687.52	0.79
16	0.0222(6)	100.63	1.00	0.80	5325.23	0.68
17	0.0192(6)	85.12	1.00	0.78	5329.92	0.65

Table D.9: C^{4+} v = 0.100 a.u. : 2nd Measurement Measured ratios

(Lab book : DFCF11p51)

Target n_t	R_{Meas}
8	-0.015(6)
9	0.037(5)
10	0.138(5)
12	0.191(5)
14	0.186(8)
16	0.119(8)
18	0.090(12)
22	0.103(15)
26	-0.014(36)

Table D.10: C^{4+} v = 0.100 a.u. : 2nd Measurement Calculated quantities

Target n_t	R_{CTMC}	$\sigma_p(10^{-14}cm^2)$	f_L	$f_{Cascade}$	$\sigma_T(10^{-14}\ cm^2)$	f_R
8	0.00228(11)	2.63	0.98	0.65	749.41	0.99
9	0.0052(2)	9.16	0.99	0.68	1198.23	0.99
10	0.0198(6)	49.76	1.00	0.69	1748.70	0.99
12	0.033(10)	118.78	1.00	0.85	3261.70	0.93
14	0.0270(8)	121.78	1.00	0.82	4687.52	0.79
16	0.0222(7)	100.63	1.00	0.80	5325.23	0.68
18	0.0174(7)	71.66	1.00	0.79	5261.45	0.62
22	0.0068(4)	16.21	1.00	0.87	4163.13	0.50
26	0.0039(5)	4.82	1.00	1.04	2953.05	0.43

Table D.11: Ne^{6+} v = 0.100 a.u. : Measured ratios (Lab book : DFCF9p61)

Target n_t	R_{Meas}
10	0.084(9)
11	0.172(13)
13	0.304(14)
15	0.238(19)
17	0.219(16)
18	0.166(5)
22	0.081(18)

Table D.12: Ne^{6+} v = 0.100 a.u. : Calculated quantities

Target n_t	R_{CTMC}	$\sigma_p(10^{-14}cm^2)$	f_L	$f_{Cascade}$	$\sigma_T(10^{-14}\ cm^2)$	f_R
10	0.0030(2)	10.64	0.97	0.80	2808.87	0.99
11	0.0130(5)	68.61	0.98	0.76	3987.72	0.99
13	0.0235(8)	180.33	1.00	0.87	7104.42	0.94
15	0.0200(7)	192.09	1.00	0.83	10368.83	0.77
17	0.0160(6)	150.51	1.00	0.82	12100.67	0.64
18	0.0138(6)	121.48	0.99	0.81	12213.50	0.58
22	0.0056(4)	32.35	0.97	0.89	11083.83	0.45

Table D.13: Ar^{8+} v = 0.100 a.u. : Measured ratios (Lab book : DFCF10p10)

Target n_t	R_{Meas}
10	0.036(2)
11	0.095(6)
12	0.222(6)
14	0.341(9)
16	0.38(3)
18	0.260(12)
20	0.199(9)
22	0.108(11)

Table D.14: Ar^{8+} v = 0.100 a.u. : Calculated quantities

Target n_t	R_{CTMC}	$\sigma_p(10^{-14}cm^2)$	f_L	$f_{Cascade}$	$\sigma_T(10^{-14}$ cm$^2)$	f_R
10	0.00153(11)	7.66	0.98	0.77	3846.43	0.99
11	0.00268(14)	17.65	0.99	0.83	5479.52	0.99
12	0.0139(3)	129.94	0.99	0.79	7546.47	0.98
14	0.0199(5)	269.07	1.00	0.87	13062.50	0.89
16	0.0176(5)	252.76	1.00	0.85	18737.50	0.65
18	0.0139(5)	176.75	1.00	0.85	21839.33	0.49
20	0.0099(4)	102.71	0.99	0.83	21926.50	0.39
22	0.0064(4)	46.19	0.99	0.91	20295.67	0.32

Table D.15: Ar^{11+} $v = 0.100$ a.u. : Measured Ratios (Lab book : DFCF10p64)

Target n_t	R_{Meas}
12	0.0079(10)
13	0.0168(12)
14	0.0281(16)
16	0.0297(7)
18	0.020(3)
22	0.013(2)

Table D.16: Ar^{11+} v = 0.100 a.u. : Calculated quantities

Target n_t	R_{CTMC}	$\sigma_p(10^{-14}cm^2)$	f_L	$f_{Cascade}$	$\sigma_T(10^{-14}\ cm^2)$	f_R
12	0.0020(2)	26.71	1.00	0.79	10837.33	0.99
13	0.0085(9)	150.74	1.00	0.81	14576.67	0.98
14	0.0153(16)	345.55	1.00	0.83	19065.50	0.96
16	0.0131(13)	391.51	1.00	0.86	30016.67	0.83
18	0.0105(11)	290.35	1.00	0.88	39874.83	0.59
22	0.0051(6)	87.49	1.00	0.90	40498.67	0.38

Table D.17: Xe^{3+} v = 0.031 a.u. : Measured ratios (Lab book : DFCF4p116)

Target n_t	R_{Meas}
9	0.009(2)
10	0.013(7)
11	0.105(7)
12	0.205(4)
13	0.286(13)
14	0.185(7)
15	0.111(2)
16	0.076(3)

Table D.18: Xe^{3+} v = 0.031 a.u. : Calculated quantities

Target n_t	R_{CTMC}	$\sigma_p(10^{-14}cm^2)$	f_L	$f_{Cascade}$	$\sigma_T(10^{-14}\ cm^2)$	f_R
9	0.0029(3)	6.21	0.77	0.55	908.84	1.00
10	0.0051(5)	19.43	0.63	0.59	1405.50	1.00
11	0.0109(11)	46.45	0.58	0.87	2116.18	1.00
12	0.042(4)	335.82	0.69	0.54	3003.58	1.00
13	0.083(8)	824.45	0.89	0.46	4096.80	1.00
14	0.041(4)	229.27	0.85	1.11	5346.05	1.00
15	0.0181(19)	96.46	0.80	1.58	6807.88	0.99
16	0.0091(9)	46.74	0.78	2.09	8447.88	0.98

Table D.19: Ar^{3+} v = 0.046 a.u. : Measured Ratios (Lab book : DFCF7p29)

Target n_t	R_{Meas}
10	0.16(3)
11	0.30(4)
12	0.66(4)
13	0.87(3)
14	0.89(4)
15	0.79(3)
16	0.48(4)
17	0.21(3)
18	0.146(16)

Table D.20: Ar^{3+} v = 0.046 a.u. : Calculated quantities

Target n_t	R_{CTMC}	$\sigma_p(10^{-14}cm^2)$	f_L	$f_{Cascade}$	$\sigma_T(10^{-14}\ cm^2)$	f_R
10	0.0039(2)	11.28	0.63	0.73	1326.65	1.00
11	0.0095(4)	38.54	0.65	0.70	1868.45	1.00
12	0.0237(10)	109.48	0.85	0.68	2671.53	0.99
13	0.0414(18)	226.79	0.84	0.76	3550.47	0.98
14	0.054(2)	421.70	0.90	0.62	4495.37	0.97
15	0.0447(19)	469.34	0.94	0.60	6138.43	0.96
16	0.0232(10)	292.92	0.84	0.76	8407.88	0.96
17	0.0120(6)	141.13	0.82	1.08	10974.67	0.95
18	0.0068(3)	76.94	0.84	1.37	13792.50	0.93

Table D.21: Ar^{3+} v = 0.057 a.u. : Measured ratios (Lab book : DFCF4p21)

Target n_t	R_{Meas}
9	0.019(8)
10	0.049(2)
11	0.132(7)
12	0.152(3)
13	0.153(7)
14	0.116(3)
15	0.084(3)
16	0.049(3)

Table D.22: Ar^{3+} v = 0.057 a.u. : Calculated quantities

Target n_t	R_{CTMC}	$\sigma_p(10^{-14}cm^2)$	f_L	$f_{Cascade}$	$\sigma_T(10^{-14}\ cm^2)$	f_R
9	0.00360(16)	9.48	0.51	0.62	842.25	1.00
10	0.0104(4)	31.05	0.68	0.63	1292.98	1.00
11	0.0230(8)	78.00	0.79	0.65	1767.58	0.99
12	0.0391(14)	152.58	0.84	0.74	2480.48	0.98
13	0.0424(15)	251.08	0.90	0.66	3611.00	0.98
14	0.0346(12)	287.81	0.93	0.63	5013.97	0.98
15	0.0212(8)	249.38	0.82	0.67	6627.93	0.97
16	0.0117(5)	146.58	0.72	0.89	8488.73	0.95

Table D.23: C^{3+} v = 0.081 a.u. : Measured ratios (Lab book : DFCF6p71)

Target n_t	R_{Meas}
9	0.046(3)
10	0.091(5)
11	0.201(6)
12	0.261(6)
13	0.257(14)
14	0.198(6)
15	0.185(15)
16	0.174(8)
17	0.127(12)
18	0.129(12)

Table D.24: C^{3+} v = 0.081 a.u. : Calculated quantities

Target n_t	R_{CTMC}	$\sigma_p(10^{-14}cm^2)$	f_L	$f_{Cascade}$	$\sigma_T(10^{-14}$ cm$^2)$	f_R
9	0.00564(19)	8.36	0.78	0.70	816.06	0.99
10	0.0118(3)	25.33	0.84	0.72	1299.75	0.99
11	0.0373(8)	104.80	0.93	0.72	1906.97	0.99
12	0.0465(10)	156.76	0.96	0.78	2607.63	0.97
13	0.0392(9)	175.08	0.97	0.74	3423.72	0.94
14	0.0334(8)	178.87	0.97	0.73	4276.63	0.89
15	0.0286(7)	170.12	0.97	0.73	5164.33	0.81
16	0.0254(7)	157.12	0.96	0.73	5898.95	0.74
17	0.0219(6)	136.17	0.94	0.75	6333.22	0.69
18	0.0192(6)	117.45	0.91	0.77	6665.60	0.64

Table D.25: C^{3+} v = 0.130 a.u. : Measured ratios (Lab book : DFCF7p120)

Target n_t	R_{Meas}
8	0.250(8)
9	0.459(11)
10	0.46(3)
12	0.553(15)
14	0.511(14)
16	0.52(3)
18	0.422(16)
22	0.40(3)

Table D.26: C^{3+} v = 0.130 a.u. : Calculated quantities

Target n_t	R_{CTMC}	$\sigma_p(10^{-14}cm^2)$	f_L	$f_{Cascade}$	$\sigma_T(10^{-14}$ cm$^2)$	f_R
8	0.0068(4)	9.24	0.44	0.81	497.49	0.98
9	0.0177(6)	20.81	0.79	0.73	712.57	0.95
10	0.0226(8)	28.98	0.84	0.74	905.87	0.88
12	0.0267(10)	33.42	0.88	0.75	1049.95	0.79
14	0.0268(14)	28.07	0.86	0.80	980.94	0.73
16	0.0273(19)	22.28	0.89	0.78	831.96	0.68
18	0.026(2)	15.28	0.93	0.80	678.27	0.65
22	0.028(3)	11.93	0.92	0.73	479.15	0.60

Appendix E : Fits of measured data to determine *l*-states included

These figures show the detailed scans of the laser resonance for each ion and velocity used in this experiment. The scans are fit to a Gaussian curve and to a simulation of equal amplitude Gaussians at each *l*-state position. The simulation full width at half max, FWHM, is reported. This is the FWHM of the individual Gaussians at each *l*-state position. Also reported are the *l*-states which contribute more than half of their amplitude to the high-*l* peak used for the measurement of the ratio. These are the *l*-states used to calculate the f_L used to correct the CTMC calculations to compare to the measurements.

Xe III v = 0.031 a.u.

n=29 to n'=71

l = 14-28 contribute 1/2 or more of their strength to the center frequency

Simulation FWHM = 375 MHz

Ar III v = 0.046 a.u.

n=31 to n'=100

l = 13-30 contribute 1/2 or more of their strength to the center frequency

Simulation FWHM = 158 MHz

Ar III v = 0.057 a.u.

n=29 to n'=71

l = 13-28 contribute 1/2 or more of their strength to the center frequency

Simulation FWHM = 250 MHz

C III v = 0.081 a.u.

n=31 to n'=100

l = 11-30 contribute 1/2 or more of their strength to the center frequency

Simulation FWHM = 500 MHz

C III v = 0.130 a.u.

n=29 to n'=71

l = 13-28 contribute 1/2 or more of their strength to the center frequency

Simulation FWHM = 208 MHz

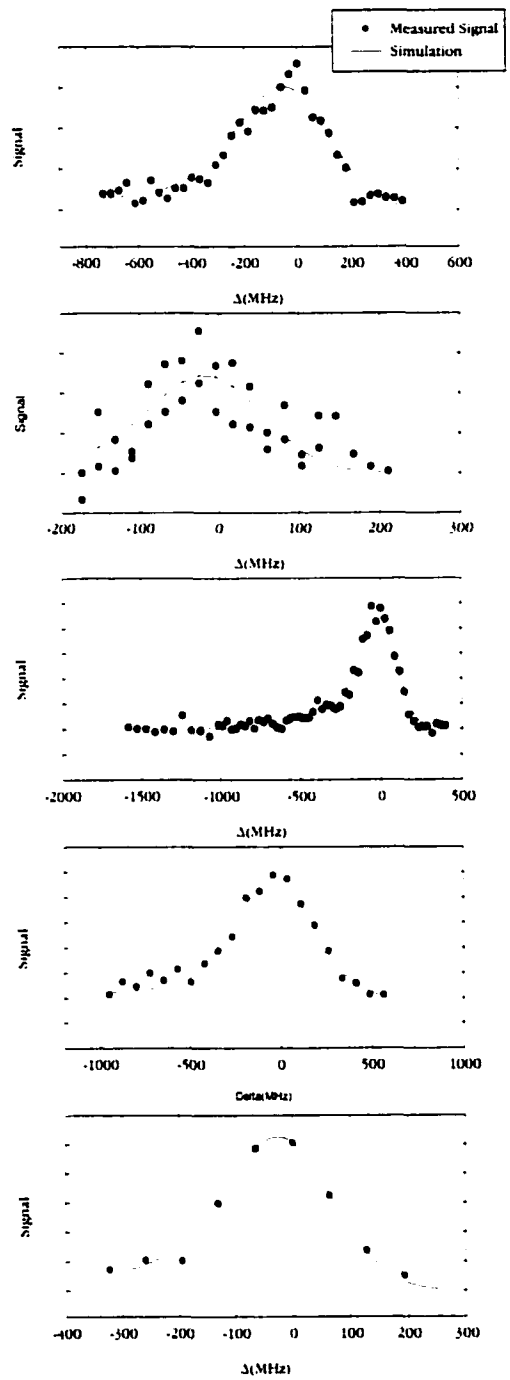

Figure (E.1): **Determination of *l*-states included in the laser resonance.** These figures show the fits of a Gaussian and a simulation of the *l*-state structure to the detailed scans of the laser resonances for each of the ions and velocities studied.

C II v = 0.100 a.u.

n=19 to n'=51

l = 9-18 contribute 1/2 or more
of their strength to the center frequency

Simulation FWHM = 300 MHz

C III v = 0.100 a.u.

n=29 to n'=71

l = 13-28 contribute 1/2 or more
of their strength to the center frequency

Simulation FWHM = 300 MHz

C III v = 0.100 a.u. 2nd Measurement

n=29 to n'=71

l = 15-28 contribute 1/2 or more
of their strength to the center frequency

Simulation FWHM = 167 MHz

C IV v = 0.100 a.u.

n=37 to n'=85

l = 3-36 contribute 1/2 or more
of their strength to the center frequency

Simulation FWHM = 266 MHz

Ne VI v = 0.100 a.u.

n=55 to n'=133

l = 11-54 contribute 1/2 or more
of their strength to the center frequency

Simulation FWHM = 142 MHz

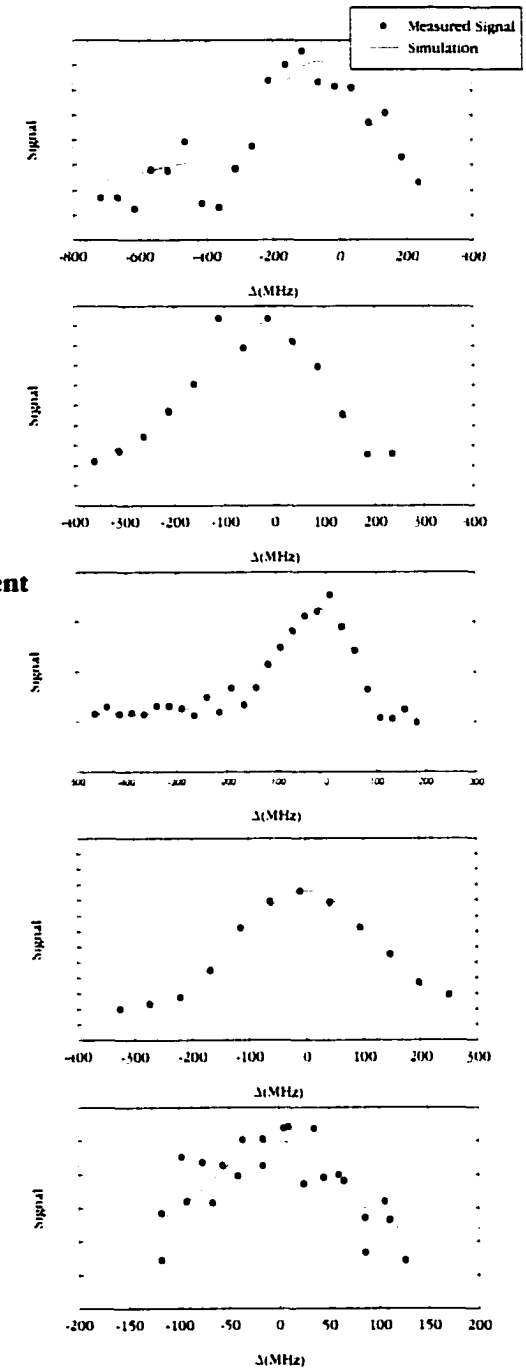

Figure (E.2):**Continuation of figure E.1.**

Ar VIII v = 0.100 a.u.

n=~3 to n'=161

l = 8-~2 contribute 1.2 or more
of their strength to the center frequency

Simulation FWHM = 133 MHz

Ar XI v = 0.100 a.u.

n=102 to n'=200

l = ~101 contribute 1.2 or more
of their strength to the center frequency

Simulation FWHM = 133 MHz

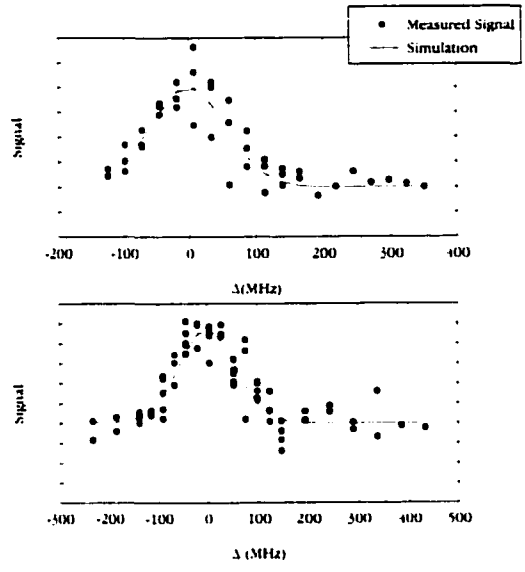

Figure (E.3): **Continuation of figure E.1.**

Appendix F: f_L, f_R, σ_T', and $f_{Cascade}$

These figures plot the factors used to correct the CTMC calculations in order to properly compare to the measured ratios. They show the factors for all of the ions and velocities studied in this experiment.

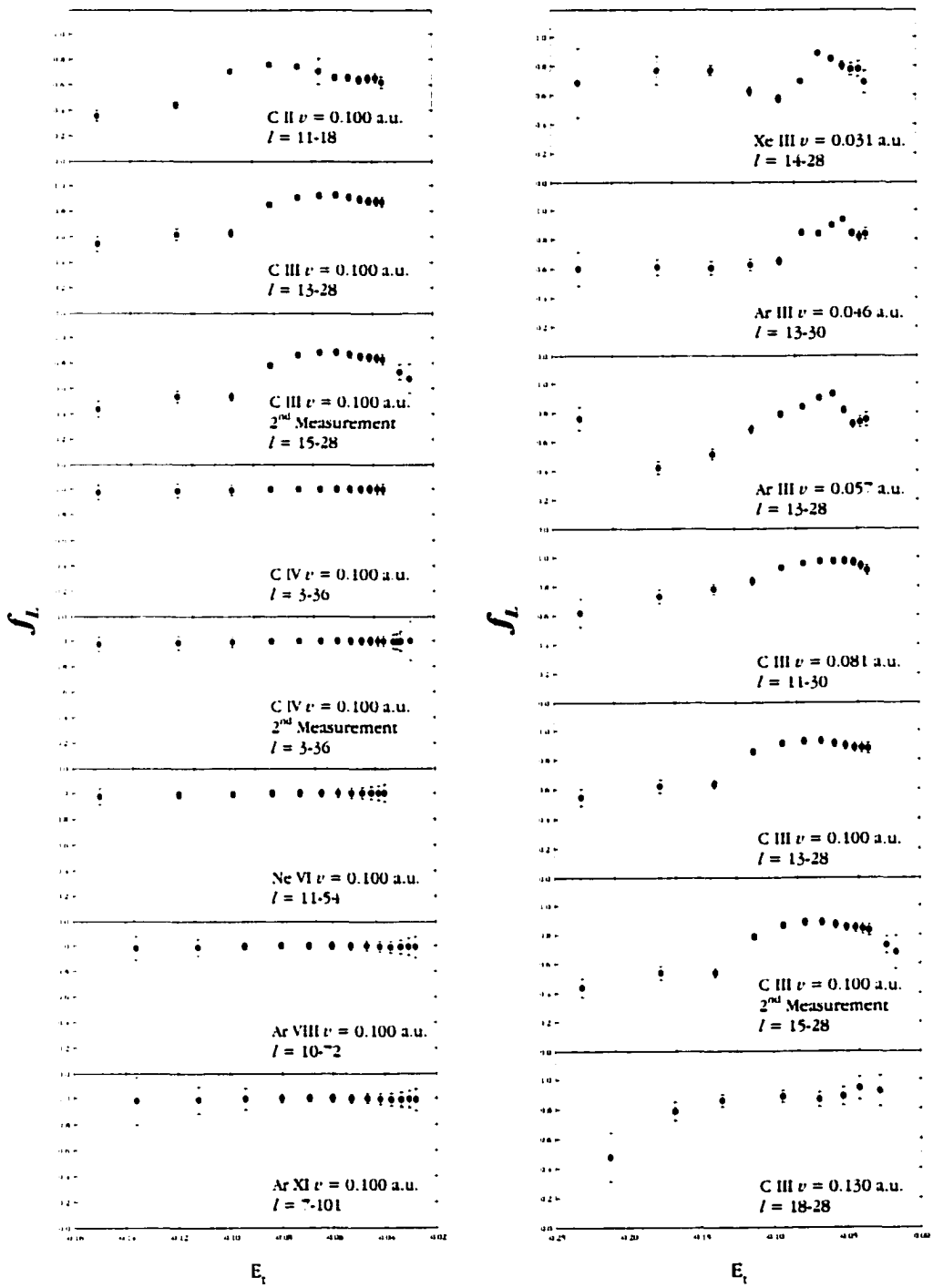

Figure (F.1): **f_L as a function of target binding energy.** These show the factor f_L as a function of the target binding energy. Note that for states where nearly all the l-states are included, $q \geq 4$, this is essentially flat.

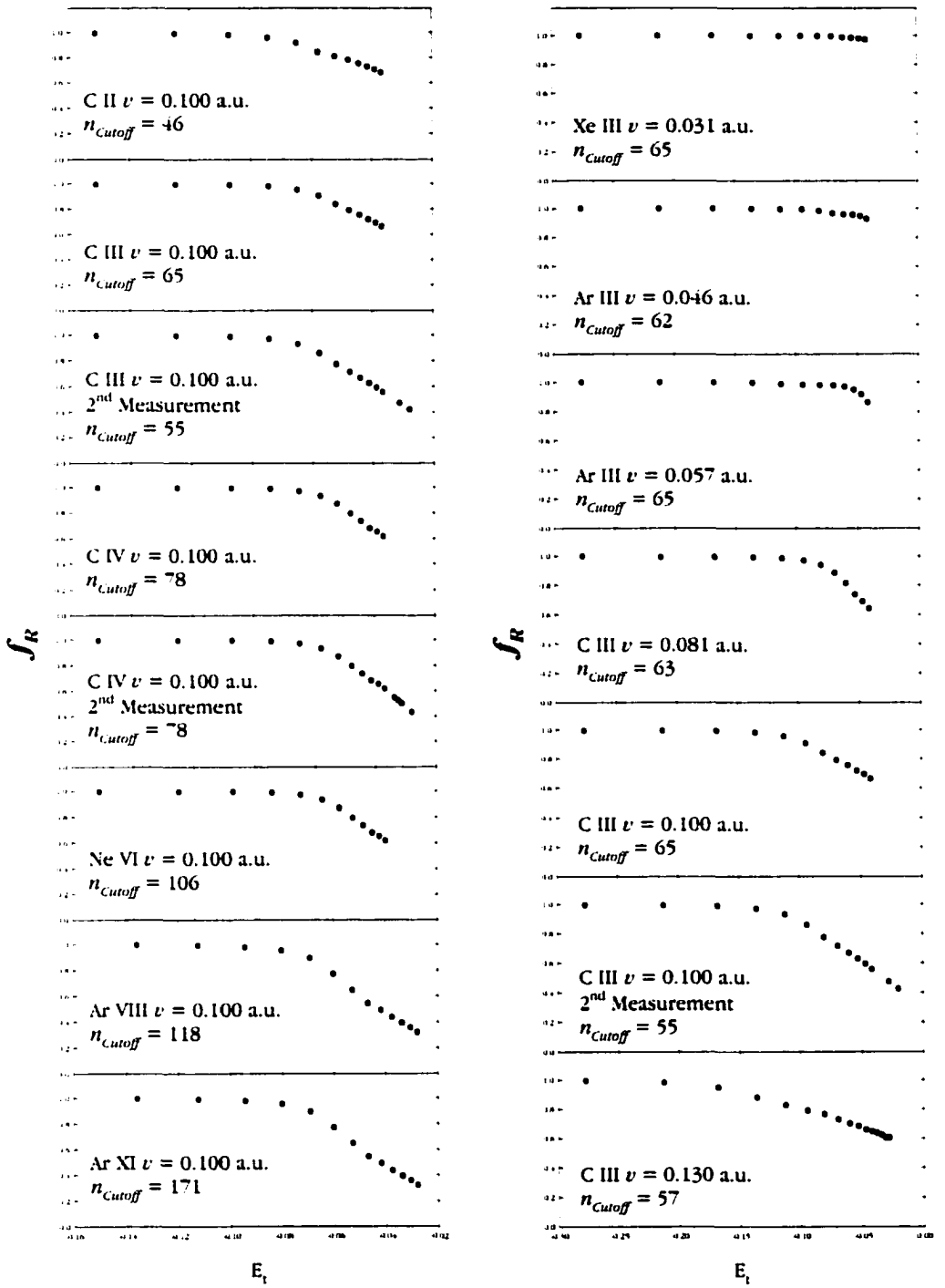

Figure (F.2): **f_R as a function of target binding energy.** This shows how f_R as a function of binding energy. Note this is quite flat at lower velocities. This is because the fields in the repeller for these is significantly smaller than for the other ions and velocities.

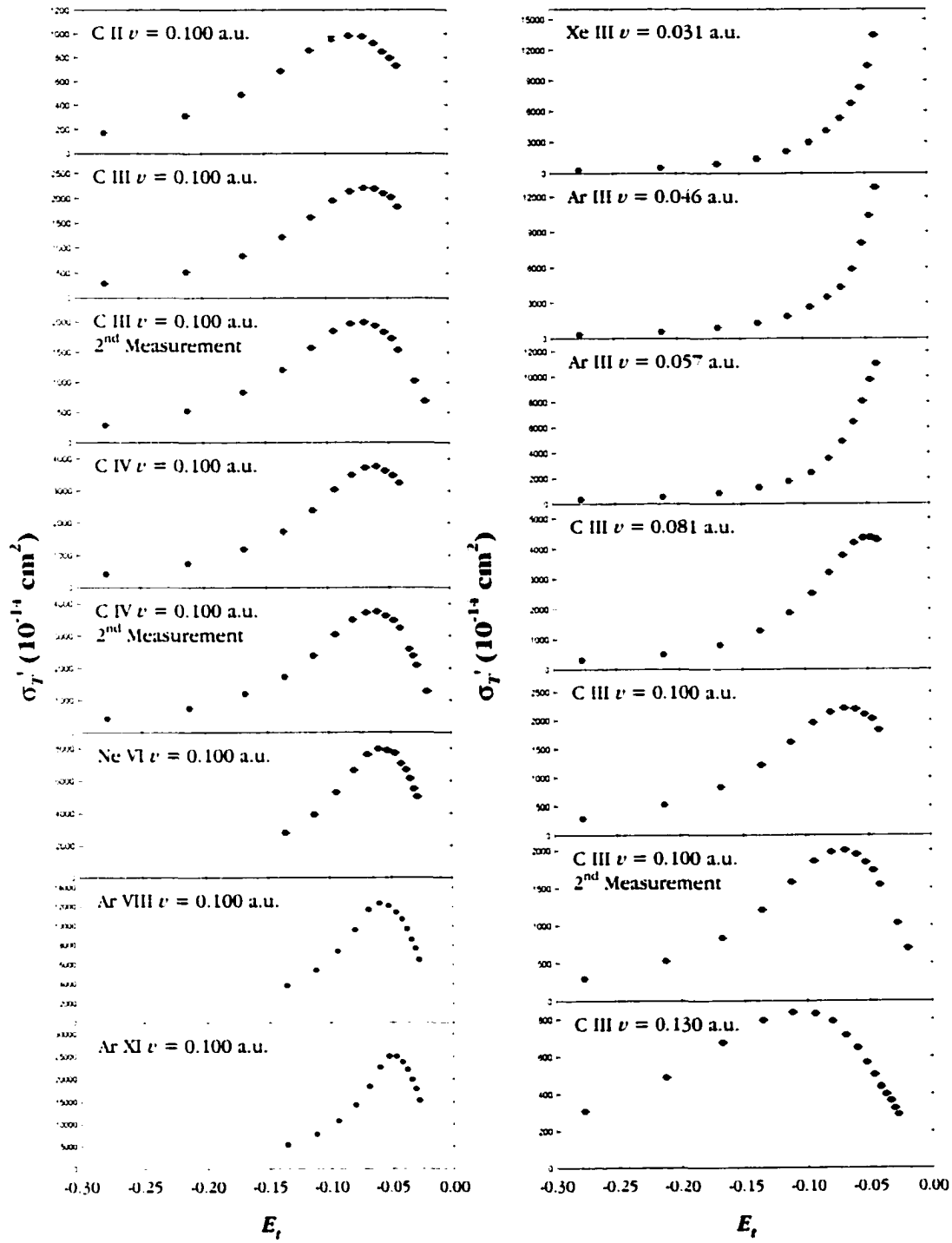

Figure (F.3): **σ_T' as a function of target binding energy.** This figure shows how σ_T' varies as a function of target binding energy.

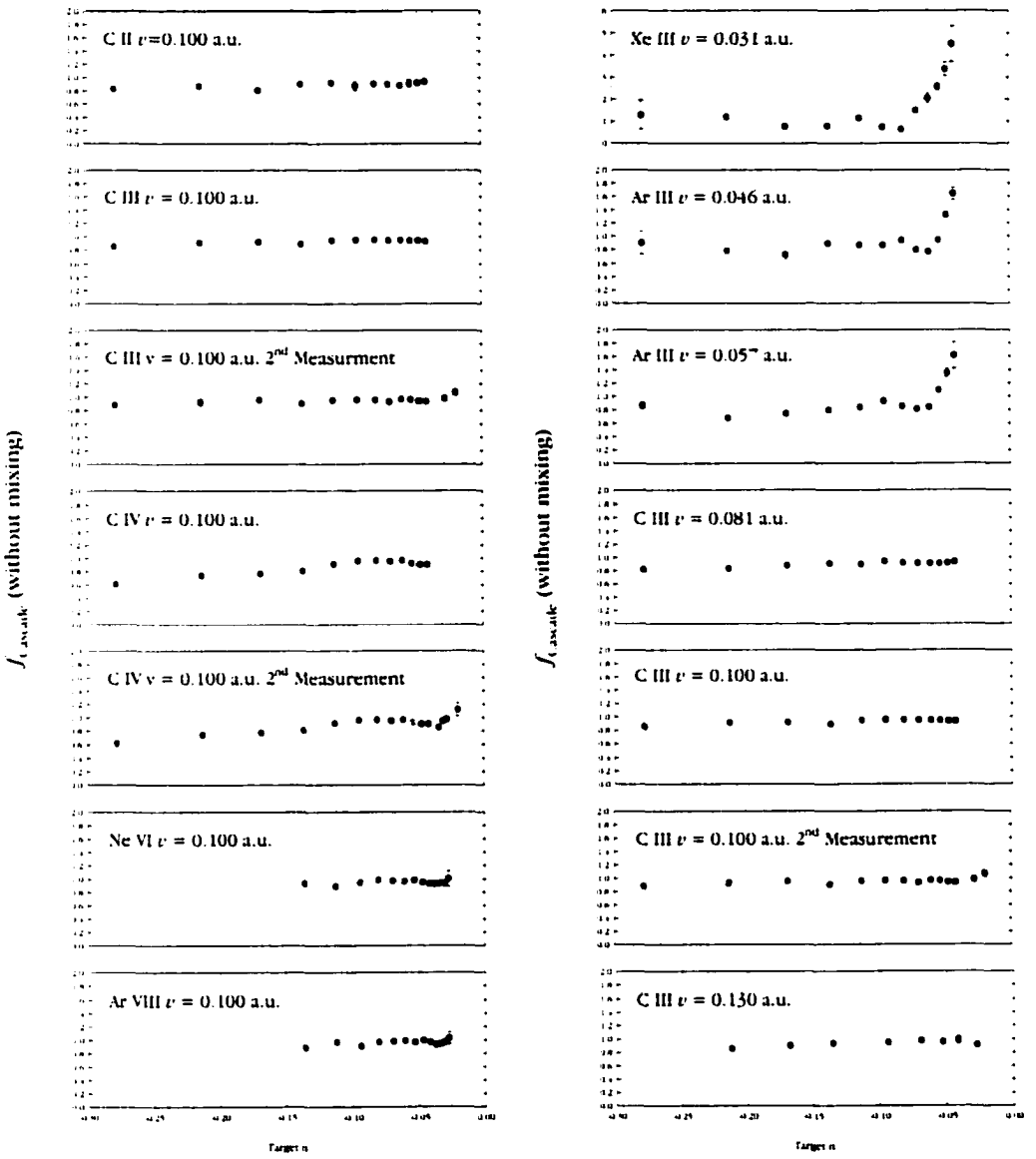

Figure (F.4): $f_{Cascade}$ **without mixing at repeller.** This shows $f_{Cascade}$ calculated without any l-state mixing at the repeller position.

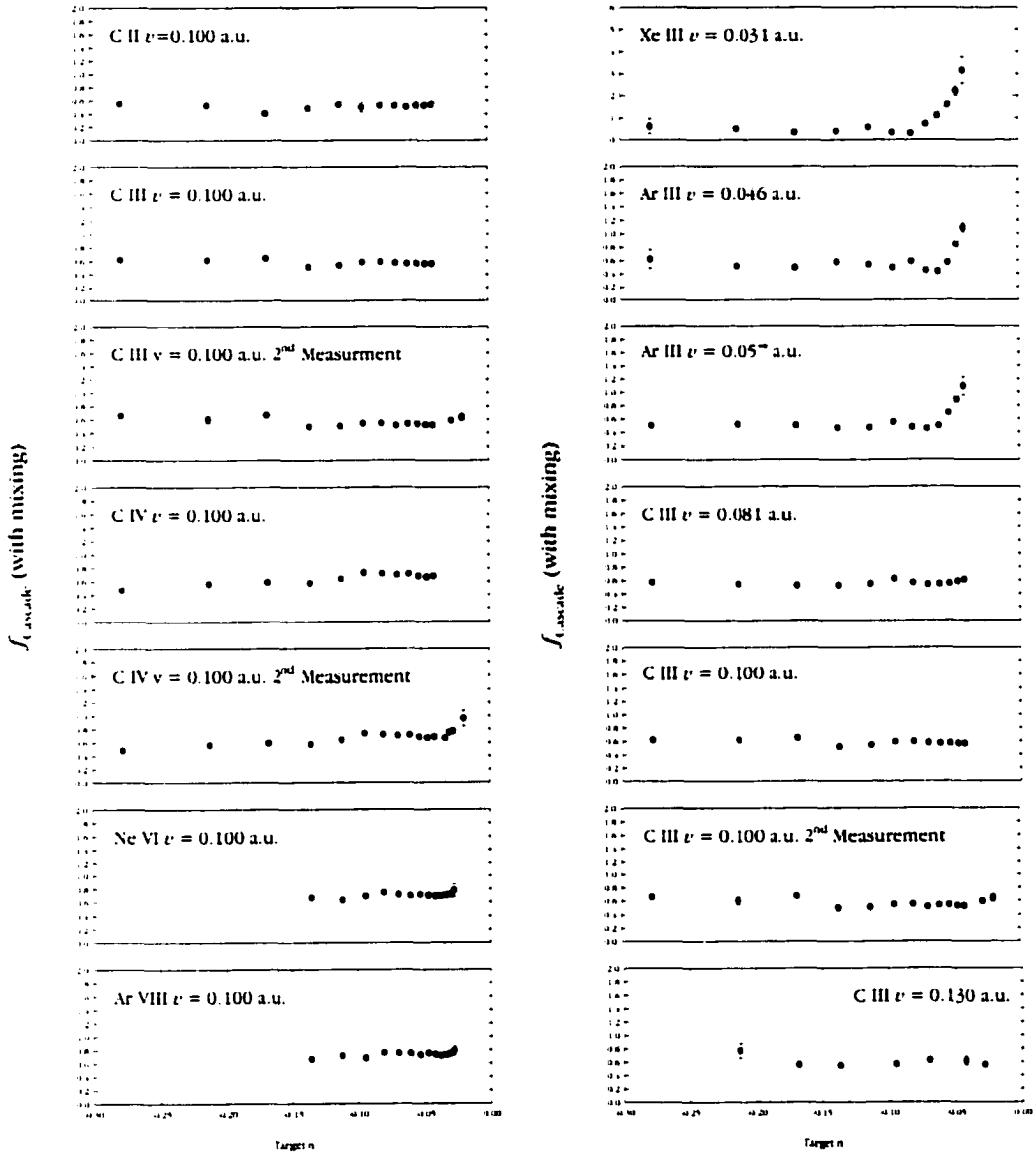

Figure (F.5): $f_{Cascade}$ **with mixing at repeller.** This shows $f_{Cascade}$ calculated with l-state mixing at the repeller position.

References

[1]. R. K. Janev and H. Winter, *Physics Reports*, **117** 266 (1985).

[2]. M. A. Abdallah, *et al.*, *Phys. Rev. A*, **58** 2911 (1998).

[3]. R. H. Dixon and R. C. Elton, *Phys. Rev. Lett.*, **38** 1072 (1977).

[4]. P. A. Naik, P. D. Gupta, and S. R. Kumbhare, *Phys. Rev. A*, **43** 4540 (1991).

[5]. K. B. MacAdam, L. G. Gray, and R. G. Rolfes, *Phys. Rev. A*, **42** 5269 (1990).

[6]. R. E. Olson, in *Rydberg States of Atoms and Molecules*, ed. R. F. Stebbings and F. B. Dunning (Cambridge University Press 1983).

[7]. T. F. Gallagher, *Rydberg Atoms* (Cambridge University Press 1994).

[8]. G. B. Rybicki and A. P. Lightman, in *Radiative Processes in Astrophysics*, 260 (John Wiley & Sons 1979).

[9]. J. Weisheit, in *Atomic, Molecular, & Optical Physics Handbook*, ed. G. W. F. Drake 979 (AIP Press 1996).

[10]. H. Ryufuku and K. Sasaki, *Phys. Rev. A*, **21** 745 (1980).

[11]. M. Karplus, R. N. Porter, and R. D. Sharma, *J. Chem. Phys.*, **43** 3259 (1965).

[12]. R. E. Olson and A. Salop, *Phys. Rev. A*, **16** 531 (1977).

[13]. P. M. Koch and J. E. Bayfield, *Phys. Rev. Lett.*, **34** 448 (1975).

[14]. A. Pesnelle *et al.*, *Phys. Rev. Lett.*, **74** 4169 (1995).

[15]. A. Pesnelle *et al.*, *Phys. Rev. A*, **54** 4051 (1996).

[16]. D. S. Fisher *et al.*. *Phys. Rev. A*, **56** 4656 (1997).

[17]. D. S. Fisher, C. W. Fehrenbach, and S. R. Lundeen, *Phys. Rev. Lett.*, **81** 1817 (1998).

[18]. M. P. Stöckli *et. al.*, Phys. Scr. **T71** 188 (1997).

[19]. F. J. Deck, Dissertation, Unpublished (University of Notre Dame 1993).

[20]. C. W. Fehrenbach, S. R. Lundeen, and O. L. Weaver, *Phys. Rev. A*, **51** R910 (1995).

[21]. M. T. Huang, Dissertation, Unpublished (Kansas State University 1998).

[22]. B. D. DePaola *et al.*, *Phys. Rev. A*, **52** 2136 (1995).

[23]. M. T. Huang *et al.*, *J. Phys. B: At. Mol. Opt. Phys.*, **30** 2425 (1997).

[24]. J. Farely and R. Gupta, *Phys. Rev. A*, **15** 1952 (1977).

[25]."SIMION 3D Version 6.0" by David A. Dahl 43ed ASMS Conference on Mass Spectrometry and Allied Topics, May 21-26 1995, Atlanta, Georgia, pg 717.

[26]. C. E. Moore, *Tables of spectra of hydrogen, carbon, nitrogen, and oxygen atoms and ions*, ed. J. W. Gallagher (CRC Press 1993)

[27]. A. K. Bhatia and R. J. Drachman, *Phys. Rev. A*, **60** 2848 (1999).

[28]. A. K. Bhatia and R. J. Drachman, *Can. J. Phys.*, **75** 11 (1997).

[29]. A. Yariv, *An Introduction to Theory and Applications of Quantum Mechanics*, Eqn. 5.2.12 (John Wiley & Sons 1982).

[30]. H. A. Bethe and E. E. Salpeter, *Quantum Mechanics of One- and Two-Electron Atoms*, Eqn. 59.11 (Springer-Verlag 1957)

[31]. H. A. Bethe and E. E. Salpeter, *Quantum Mechanics of One- and Two-Electron Atoms*, Eqns. 59.14 and 63.11 (Springer-Verlag 1957)

[32]. B. D. DePaola *et al.*, *Phys. Rev. A*, **52** 2136 (1995)

[33]. K. B. MacAdam, in *The Physics of Electronic and Atomic Collisions*, ed. T. Andersen, *et al.*, AIP Conf. Proc. No. 295 (AIP, New York, 1993), p. 183.

[34]. J. Pascale, R. E. Olson, and C. O. Reinhold *Phys. Rev. A*, **42** 5305 (1990).

[35]. R. E. Olson, *J. Phys. B*, **13** 483 (1980).

[36]. K. B. MacAdam, *Phys. Rev. Lett.*, **75** 1723 (1995).

[37]. D. Banks, K. S. Barnes, J. M. Wilson, *J. Phys. B*, **9** L141 (1976).

[38]. F. J. Deck, E. A. Hessels, S. R. Lundeen, *Phys. Rev. A*, **48** 4400 (1993).

[39]. M. G. Littman, M. M. Kash, and D. Kleppner, *Phys. Rev. Lett.*, **41** 103 (1978).